COMPREHENSIVE CHARACTERIZATION OF NANOTRANSFER PRINTING SYSTEM FOR ORGANIC ELECTRONIC DEVICES

COMPREHENSIVE CHARACTERIZATION OF NANOTRANSFER PRINTING SYSTEM FOR ORGANIC ELECTRONIC DEVICES

By L. S. Hui, B.A. Sc.

A THESIS SUBMITTED TO THE DEPARTMENT OF ENGINEERING PHYSICS AND THE SCHOOL OF GRADUATE STUDIES OF MCMASTER UNIVERSITY IN PARTIAL FULFILMENT OF THE REQUIREMENTS FOR THE DEGREE OF PhD

McMaster University Master of Applied Science (2018) Hamilton, Ontario (Engineering Physics)

TITLE: Comprehensive Characterization of Nanotransfer Printing System for Organic Electronic Devices AUTHOR: Lok Shu Hui SUPERVISOR: Dr. Ayse Z. Turak NUMBER OF PAGES: ix, 248

Abstract

This thesis presents a universal transfer printing method to introduce a thin layer of interlayer nanoparticle material in the cathode-organic layer interface in organic device. The use of reverse micelles for making nanoparticles restricts the nanoparticles to be directly synthesized on the organic active layer , therefore a transfer printing method using graphene was derived and a characterization method was needed to detect the transfer of nanoparticles in the whole device system.

Raman spectroscopy was found to be the best candidate in studying these organic systems. The oxidation behavior and interaction of CVD graphene on Cu with oxygen plasma and mild annealing was monitored closely by a detailed Raman trilogy studies. Raman results also show evidence of graphene oxide successfully transferred to the target organic layer.

Raman spectroscopy was further explored to understand all material in the transferred system including the micelles, type of nanoparticles and the organic layer, which then provides valuable insights to the evolution of the different phases of nanoparticle material formed by the reverse micelles technique. Raman was also used to confirm the first-reported formation of the hot-topic perovskites materials in reverse micelles. An extended Raman technique, the unconventional inverted-TERS, was used to detect a monolayer of micelles which was otherwise impossible for a normal Raman setting. The underlying mechanisms of this technique with high-resolution were also proposed.

In order to understand and explore the tunability of reverse micelles on nanoparticle synthesis, a study with the pervovskite material was performed. There were evidence of precursors interacting with the pyridine group in the micelles core, which affects nanoparticle formation. The size of nanoparticles is also found to be tunable by using micelles of different block lengths and different solvents.

All these findings contribute to future optimization on the nanoparticles to be transfer printed into devices interlayer and ultimately to benefit on the improvement on organic photovoltaics.

Nomenclature

α	Polarizability
γ	Surface energy
μTP	Microcontact printing
A	Electron-acceptor
AFM	Atomic Force Microscopy
AT	Annealing Time
ATR-FTIR	Attenuated Total Reflection- Fourier Transform Infrared Spectroscopy
BCP	Bathocuproine
BHJ	Bulk Heterojunction
bipy	Bipyridine
C_{60}	Fullerenes
CB	Conduction Band
CET	Critical Etching Time
CIGS	$CuInGaSe_2$
CuPc	Copper phthalocyanine
CVD	Chemical Vapour Deposition
D	Electron-donor
DFT	Density Functional Theory
DMF	N,N-Dimethylformamide
DMT	Derjaguin-Muller-Toporov
DRIFTS	Diffused Reflectance Infrared Fourier Transform Spectroscopy
DS	Donor Substrate
E	Young's Modulus
EDX	Energy-dispersive X-ray spectroscopy
EELS	Electron Energy Loss Spectrum
EM	Electromagnetic
EPBT	Energy Payback Time
ET	Etching Time
ETL	Electron Transport Layer
F	Total Modification Factor

FA	Formamidinium
$FAPbI_3$	Formamidinium lead iodide
FEG	Field Emission Gun
FG	Full Graphene
FIB	Focused Ion Beam
FWHM	Full Wave Half Maximum
GO	Graphene Oxide
Gr	Graphene
HOMO	Highest Occupied Molecular Orbital
HRTEM	High Resolution Transimssion Electron Microscopy
HTL	Hole Transport Layer
IERS	Interference Enhanced Raman Scattering
IPCC	Intergovernmental Panel on Climate Change
IR	Infrared
ITO	Indium Tin Oxide
LCST	Lower Critical Solution Temperature
LUMO	Lowest Unoccupied Molecular Orbital
M_s	Saturation magnetization
MA	Methylammonium
$MAPbBr_3$	Methylammonium lead bromide
$MAPbI_3$	Methylammonium lead iodide
M-H	Magnetization applied magnetic field
NEMS	Nanoelectromechanical systems
NFA	Non-fullerene acceptors
NIR	Near-Infrared
NP	Nanoparticles
NR	Normal Raman
NREL	National Renewable Energy Laboratory
nTP	Nanotransfer Printing
OA	Optical Adhesive
OFET	Organic Field-Effect Transistors
OLED	Organic Light Emitting Diode
OPV	Organic Photovoltaics
P2VP	Poly(2-vinyl pyridine)

P3HT	Poly(3-hexyl thiophene)
PAA	Polyacrylic acid
PCBM	[6,6]-phenyl C_{61} -butyric acid methyl ester
PCE	Power Conversion Efficiency
PCF	Pair Correlation Function
PDI	Polydispersity Index
PDMS	Polydimethylsiloxane
PEDOT:PSS	Poly(3,4-ethylenedioxythiophene):poly(styrenesulfonate)
PET	Polyethylene terephthalate
PFPE	Perfluropolyether
PG	Partial Graphene
PL	Photoluminescence
PMMA	Polymethacrylate
pNIPAAm	Poly-N-isopropylacrylamide
PS	Polystrene
PV	Photovoltavics
PVD	Physical Vapour Deposition
q_6	Hexagonal symmetry basis
QNM	Quantitive Nanomechanical Property Mapping
R_s	Series resistance
rGO	Reduced Graphene Oxide
RMD	Reverse Micelles Deposition
RS	Receiver Substrate
SEM	Scanning Electron Microscopy
SERS	Surface-enhanced Raman Scattering
SHG	Second-harmonic generation
SO	Surface assisted optical modes
SPP	Surface Plasmon Polaritons
SPR	Surface Plasmon Resonance
SQUID	Superconducting quantum interference device
STEM	Scanning transmission electron microscopy
STM	Scanning tunneling microscopy
TEM	Transmission Electron Microscopy
TERS	Tip-enhanced Raman Scattering

TR	Triple Resonance
TRT	Thermal-release Tape
TS	Template Stripping
UV	Ultraviolet
UV-O_3	Ultraviolet-ozone
V_{OC}	Open circuit voltage
VB	Valence Band
VOC	Volatile Organic Compounds
VP	Pyridine
XPS	X-ray Photoelectron Spectroscopy
XRD	X-ray Diffraction

Acknowledgements

This work is dedicated to my most supportive, ever-loving parents.

First of all, I would like to thank my supervisor, Dr. Turak, for her guidance and supervision throughout my graduate studies. When I first joined as a Master student, I have never dreamt of being as a PhD student, but one day she asked me to continue as a PhD student in her group when we were walking outside JHE. I remember saying very explicitly to my family and friends that I am not a PhD material, but I am very glad that I changed my mind. I thank for all the trust my supervisor has on me. I am grateful for all the group meetings and group dinners. I guess I will not be convinced again to work in the academia though, I am not a professor material. For now.

Now for my family.

My perseverance comes from the training my father has given me, to accept challenges ever since I was a kid– from small things such as figuring out how to connect a DVD player to the TV to making big plans for family vacations. This trait holds me down throughout my research career as a PhD candidate.

I have always find new things and topics fascinating and yearn to learn more about them. It is important to stay open-minded and curious as a scientist and that probably comes from my mother. My mother constantly encourages me to try everything, again, since I was a kid. She would sign up a number of diverse courses for me and my sister that ordinary kids in Hong Kong would not have experienced and let us learn and have fun. Even now, if time allows, I still keep going to all sorts of seminars even though they are not related to anything I work on (and Dr. Turak can prove that) because I enjoy doing so.

I thank my parents for shaping me the way I am now and all the countless Skype and Whatsapp video chats throughout the years, which gave me strength to carry on. I would also need to thank my sister, whom I always fought with, but without her, I probably would never have considered coming to Canada to do my PhD studies.

I also wholeheartedly thank my grandparents, Uncle James, my dear grandpa-in-heaven for the greatest support and love one can ever have. My sister and I are very much badly spoiled by them and that is something I miss most every year I visit Hong Kong during Christmas.

There are still a list of friends (groups) to be thanked, without them, I would not have survived the life in Grad school. They are the Caffeineds, Thursday Burrito, Diamond Lattice, Okonomiyaki Party, Tile Hile Club and etc. I also need to thank the following musicians whom I have played their pieces countless times on my iTunes when I am writing: Bach, Dvorak, Rachmaninoff, Stokowski, Bernstein, Itzhak Perlman, SHINee and BTOB.

Last but not least, I would attribute all these blessings and great people I have to my God. My thank you note for Him will be attached in my evening prayers.

List of publications

1. Lok Shu Hui, Eric Whiteway, Micheal Hilke, and Ayse Turak, "Effect of Post-Annealing on Plasma Etching of graphene- coated-copper", Faraday Discuss.,2014, 173,79. (DOI: 10.1039/C4FD00118D)

2. Jonathan Heidkamp, Minh Nguyen, Peter Lienerth, Felix Maye, Lok Shu Hui and Ayse Turak, "Interfacial Structure Modifying Interlayers Equalize Substrate Performance: The Case of PEDOT: PSS", Science of Advanced Materials, 2016, 8, 2, 414-420. (DOI: 10.1166/sam.2016.2503)

3. Lok Shu Hui, Eric Whiteway, Micheal Hilke, and Ayse Turak, "Synergistic oxidation of CVD graphene on Cu by oxygen plasma etching", Carbon, 2017, 125, 500-508. (DOI: 10.1016/j.carbon.2017.09.076)

4. Matt Bumstead, Kunyu Liang, Gregory Hanta, Lok Shu Hui and Ayse Turak, "disLocate: tools to rapidly quantify local intermolecular structure to assess two-dimensional order in self-assembled systems", Scientific reports, 2018, 1, 1554. (DOI: 10.1038/s41598-017-18894-7)

5. Seung Il Lee, Geum Jae Yun, Jin Wook Kim, Gregory Hanta, Kunyu Liang, Lazar Kojvic, Lok Shu Hui, Ayse Turak and Woo Young Kim, "Improved hole injection for blue phosphorescent organic light-emitting diodes using solution deposited tin oxide nano-particles decorated ITO anodes", under review by Scientific Reports, [Paper SREP-18-20858].

6. Lok Shu Hui, Eric Whiteway, Micheal Hilke and Ayse Turak, "Tuning Reduced Graphene Oxide by Low Temperature Annealing". Submitted to Thin Solid Films (TSF-D-18-01040).

Contents

List of Figures

Part I

Motivation

The need to strive for cleaner renewable energy sources has grown more and more over the years. The latest fifth assessment of the United Nations Intergovernmental Panel on Climate Change (IPCC) was just released, highlighting an urgent call to keep the Global Warming under 1.5°C that beyond which would result in a devastating global ecosystem damage.[1] Researchers and experts have been working towards the goal of achieving more efficient renewal energy sources, hoping to replace the use of fossil fuel one day and reduce the green house gas emission. Photovoltavics (PV) technology has been a strong contender among with other renewal energy sources in replacing the fossil fuels. The field experienced a rapid growth since its emergence in the early 2000s, and the global annual PV installed capacity increased over 29% last year.[2]

Organic photovoltaics (OPVs) is classified as the third generation solar cells in the PV family.[3] It addresses the energy demanding manufacturing costs of inorganic solar cells and uses the carbon-based conjugated semiconductive polymer instead of the III-IV inorganic semiconductors, which nevertheless is toxic to the environment. The tunable bandgap of the organic polymer is a big advantage when compared with the inorganic ones; the flexible nature of the polymer allows the OPVs to be bendable and be put on any surfaces, which is also not achievable otherwise by the inorganic solar cells. The PV industry would have been long replaced by OPVs if its efficiency and the device lifetime were competitive with the inorganic PVs that is now commercially available.

The polymeric nature of the OPVs intrinsically limits the lifetime of the OPVs, but the efficiency can be improved by engineering various aspects of the cell such as the structure and the components, which after optimization, can improve the lifetime of the device as well. The current goal of the industry is to achieve high efficiency at a low cost even though the lifetime is limited, so that it can be made competitive with the current inorganic solar cells.

With the goal of making efficient organic devices, this thesis looks into manipulating the thin interlayer specifically between the metal cathode and the organic active layer using nanoparticles. We use the reverse micelles technique to synthesize the various nanoparticles for its superior controllability on size and dispersion. Ultimately, we would like to see the different effects of interlayer on the device due to the nanoparticle size, dispersion and types of nanoparticles. However, there are two challenges associated with this notion– moving the nanoparticles onto the target layer

and detecting them. When it comes to nanoparticles of ultrathin layer, unless using a synchrotron, most characterization techniques is be incapable for detection due to the small volume of materials for interaction. An ideal characterization method would meet the requirements for detecting the nanoparticles integrated as the interlayer in the device and at the same time also able to detect other components in the device.

Among various characterization methods, Raman spectroscopy is the closest to being ideal and comprehensive for this purpose. In particular, the transfer method developed for moving nanoparticles to the target layer involves the use of the famous 2D material, graphene, Raman is an excellent choice for characterization the nanoparticles, the target organic layer and graphene simultaneously. On top of that, Raman can also provide valuable insights for furthering understanding the micelles system used for making nanoparticles.

The thesis is divided into three parts: i. the method for relocating the nanoparticles to the target layer; ii. the pursue of using various Raman techniques to characterize the components (nanoparticles, graphene) in the device; and iii. understanding the reverse micelles technique and interaction with the nanoparticles.

An overview of PVs including organic, graphene-based and perovskites will be covered in the Literature Review part, Chapter 1, in which the roles of interlayers will be discussed. The chapter that follows (Chapter 2) reviews the methods practiced in general to produce nanoparticles and at the same time introduce the reverse micelles technique in Chapter 2.3. Next chapter (Chapter 3) explores various transfer printing methods attempted in literature, which will introduce the idea of using graphene. Chapter 4 discusses the basics plasma as the RMD method involves the use of plasma etching in order to expose the nanoparticles inside. The last chapter of the Literature Review will focus on the characterization part of the project, which is the Raman spectroscopy. It starts with the basics of Raman in Chapter 5.1, which the Physics of Raman will be investigated. Then the next chapter (Chapter 5.2) will focus on the extended techniques of Raman. Finally, the various Raman spectrum of materials employed in this project will be discussed one by one in Chapter 5.3, so that one can interpret the spectrum fully.

The experimental details will be discussed in Part III, followed by the Results, findings and discussions made up of publications in journals and publications ready to be submitted. This part is divided into three parts, the first section (Chapter 6) will cover a universal transfer method for nanoparticles using graphene into devices

for which preliminary results shows success transfer was achieved. The next section discussed why Raman spectroscopy is helpful for this study, as supported by examples from the tip enhanced Raman scattering technique in Chapter 8; its ability to detect iron oxides formed by RMD in different phases (Chapter 9); the detection of perovskites nanoparticles by RMD in Chapter 10 and 11; and finally a trilogy detailed study on the graphene oxidation due to oxygen plasma and annealing treatment in Chapter 12.2, 12.1 and 12.3. The final Chapter (13 is on undertanding the micelles system as we discovered the ability to tune the nanoparticles by different parameters, again with the help of Raman.

The transfer method and micelles open up a lot more interesting topics to be investigated. These will be discussed in the Part of Future Work (Chapter VII). The thesis will be summarized in the Conclusion and supplemented with Appendix for readers' perusal.

0.1 Co-Authorship Statement

Chapter 6 is co-authored by Lok Shu Hui, Kunyu Liang and Ayse Turak. Lok Shu Hui prepared the ingredients for the graphene transfer process and did the Raman measurement. Kunyu Liang performed the SEM measurement. CVD graphene was prepared and provided by Eric Whiteway, advised by Micheal Hilke at McGill University. The study was lead and supervised by Ayse Turak.

Chapter 8 is co-authored by Lok Shu Hui, Maria Dittrich and Ayse Turak. Lok Shu Hui prepared the samples and performed the measurements for TERS, SERS, and Raman. The TERS measurements were advised by Maria Dittrich at the University of Toronto (Scarborough). The study was lead and supervised by Ayse Turak.

Chapter 9 is co-authored by Kunyu Liang, Lok Shu Hui and Ayse Turak. Kunyu Liang made the samples, performed TEM and SQUID measurements. Lok Shu Hui performed the Raman measurements. The study was lead and supervised by Ayse Turak.

Chapter 10 is co-authored by Lok Shu Hui, Colin Beswick, Kunyu Liang, Nebile Isik, Ray LaPierre and Ayse Turak. Lok Shu Hui and Colin Beswick prepared the samples together and performed the AFM measurements. Lok Shu Hui performed the Raman measurement and did the analysis. The PL measurements were assisted by Nebile Isik in Ray LaPierre's group. Kunyu Liang performed the TEM measurements.

The study was lead and supervised by Ayse Turak.

Chapter 11 is co-authored by Lok Shu Hui, Herwig Heilbrunner, Niyazi Serdar Sariciftci and Ayse Turak. Lok Shu Hui prepared the samples and performed the Raman and AFM measurements. The PL measurements were performed by Herwig Heilbrunner in Niyazi Serdar Sariciftci's group in the Johannes Kepler University. The study was lead by Ayse Turak.

Chapter 12.1 is a co-authored publication by by Lok Shu Hui, Eric Whiteway, Micheal Hilke, and Ayse Turak. Lok Shu Hui performed the graphene post-production annealing treatment, plasma etching of CVD graphene and the Raman measurement. Preparation of CVD graphene was done by Eric Whiteway, advised by Micheal Hilke at McGill University. This publication was lead and supervised by Ayse Turak. This chapter is based on the publication: Lok Shu Hui, Eric Whiteway, Micheal Hilke, and Ayse Turak, "Effect of Post-Annealing on Plasma Etching of graphene- coated-copper", Faraday Discuss.,2014, 173,79. (DOI: 10.1039/C4FD00118D)

Chapter 12.2 is a co-authored publication by by Lok Shu Hui, Eric Whiteway, Micheal Hilke, and Ayse Turak. Lok Shu Hui performed the graphene post-production annealing treatment, plasma etching of CVD graphene and the Raman measurement. Preparation of CVD graphene was done by Eric Whiteway, advised by Micheal Hilke at McGill University. This publication was lead and supervised by Ayse Turak.

Chapter 12.3 is a co-authored by by Lok Shu Hui, Eric Whiteway, Micheal Hilke, and Ayse Turak. Lok Shu Hui performed the graphene post-production annealing treatment, plasma etching of CVD graphene and the Raman measurement, ATR-FTIR analysis and contact angle measurements. Preparation of CVD graphene was done by Eric Whiteway, advised by Micheal Hilke at McGill University. This publication was lead and supervised by Ayse Turak. This chapter is based on the publications: Lok Shu Hui, Eric Whiteway, Micheal Hilke, and Ayse Turak, "Effect of Post-Annealing on Plasma Etching of graphene- coated-copper", Faraday Discuss.,2014, 173,79. (DOI: 10.1039/C4FD00118D); and Lok Shu Hui, Eric Whiteway, Micheal Hilke, and Ayse Turak, "Synergistic oxidation of CVD graphene on Cu by oxygen plasma etching", Carbon, 2017, 125, 500-508. (10.1016/j.carbon.2017.09.076)

Chapter 13 is co-authored by Lok Shu Hui, Colin Beswick, Adam Getachew, Herwig Heilbrunner, Kunyu Liang, Gregory Hanta, Hani Dawood, Marcus Scharber, Nebile Isik, Ray LaPierre, Niyazi Serdar Sariciftci and Ayse Turak. Lok Shu Hui, Colin Beswick and Adam Getachew developed the sample parameters together. Herwig

Heilbrunner provided the ligand-assisted samples for comparison and performed the PL measurements with Marcus Scharber's supervision. Kunyu Liang prepared the iodine-staining samples and performed the SEM and TEM measurements. Gregory Hanta performed the QNM measurements and analysis. Lok Shu Hui, Colin Beswick and Gregory Hanta contributed to the AFM measurements equally. Niyazi Serdar Sariciftci provided valuable insights and supervisions for the study. The study was lead and directed by Ayse Turak.

Article ("disLocate: tools to rapidly quantify local intermolecular structure to assess two-dimensional order in self-assembled systems") is co-authored by Matt Bumstead, Kunyu Liang, Gregory Hanta, Lok Shu Hui and Ayse Turak. Samples were provided by Lok Shu Hui, Kunyu Liang and Gregory Hanta together. The AFM resulst were provided by Lok Shu Hui and Gregory Hanta. Matt Bumstead developed the program tool for dispersion analysis. The study was lead and supervised by Ayse Turak.

Article("Interfacial Structure Modifying Interlayers Equalize Substrate Performance: The Case of PEDOT: PSS") is co-authored by Jonathan Heidkamp, Minh Nguyen, Peter Lienerth, Felix Maye, Lok Shu Hui and Ayse Turak. Lok Shu Hui contributed in providing AFM results of ITO substrates.

Manuscript-under-review ("Improved hole injection for blue phosphorescent organic light-emitting diodes using solution deposited tin oxide nano-particles decorated ITO anodes") is co-authored by Seung Il Lee, Geum Jae Yun, Jin Wook Kim, Gregory Hanta, Kunyu Liang, Lazar Kojvic, Lok Shu Hui, Ayse Turak, and Woo Young Kim. Samples were prepared by the Ayse Turak's group at McMaster University and the device characterization was done by Woo Young Kim's group at Hoseo University.

Part II

Literature Review

Chapter 1

Generic interlayer effect in OPVs and perovskites PVs

1.1 General Organic device overview

The inorganic photovoltaic technologies though manage to achieve high efficiency exceeding 46%, the industry suffers from production limitations such as the high production cost from vacuum processing and material toxicity.[4] Organic semiconductor technologies, on the other hand, can be manufactured at a much lower cost through solution processing and use more eco-friendly organic polymers.[4] The organic electronics has been a growing field since the past two decades with devices including the organic field-effect transistors (OFETs), organic photodiodes, organic light-emitting diodes (OLEDs) and organic photovoltaics (OPVs). While OLEDs technology is now well-commercialized, OPVs technology is still focusing on improving its efficiency and device lifetime to be comparable to the inorganic photovoltaics. The latest National Renewable Energy Laboratory (NREL) to-date has a new record Power Conversion Efficiency (PCE) of 12.6% for the OPV developed by Yang's group.[5] Despite of the lower PCE of OPVs than their inorganic counterpart, the energy payback time (EPBT) (the time required for energy production to break even with the device production and decommission costs) of OPVs is only on the order of days, while the inorganic ones are in the order of years.[4]

The inorganic photovoltaic industry has been evolving since the first silicon based single p-n junction photovoltaic device invented in 1954 with the PCE of 6% as

the first-generation photovoltaics.[6,7] The second-generation photovoltaics soon came into market after almost 50 years in early 2000s using the thin-film semiconductors technology in micron scale thickness.[8] Instead of using crystalline silicon wafers in the first-generation, the second-generation was made use of amphorous silicon, II-VI semiconductors so as to improve the PCE and reduce the material needed for light absorption and thus reduce the cost of manufacturing. One of the best performing second-generation photovoltaics $CuInGaSe_2$ (CIGS) has a reported PCE of 19.2%.[9]

OPVs technology finally emerged as the organic semiconducting polymers were synthesized and the first single heterojunction OPV was invented in 1986 using copper phthalocyanine (CuPc) and perylene tetracarboxylic derivative as the active layer by physical vapor deposition.[10] This OPV developed by Tang's group has achieved a PCE of 1%.[10] As the polymer industry advanced, the semiconducting polymers could be synthesized in high purity. Since OPVs can be produced under low temperature using solution processing, which greatly reduced the production cost in making photovoltaic devices and also allows the deposition to take place in a variety of substrates, even on flexible ones.

The structure of an OPV consists of a low work function Ψ metal cathode with Al being most commonly used.[4] The anode has to be transparent and conductive for light transmission, so a high work function transparent oxide such as the Indium Tin oxide (ITO), is vastly used as the anode in OPVs.[4] In between the cathode and anode is where an organic semiconductive active layer system made up of an electron-donor (D) and electron-acceptor (A) can be found for photon absorbing.[11] Unlike the inorganic semiconductor which generates free charge carriers, the organic semiconductor material has a low dielectric constant which allows couloumbically bound electron-hole pairs called the exciton. The exciton which typically has a diffusion length of 10 nm, diffuses across to the D/A interface and dissociates to free charge carriers.[11] Therefore, a bulk heterojunction (BHJ) system was introduced to OPV so that the interface surface area can be increased to result in more exciton dissociations.[11] The free charge carriers can be extracted at the electrodes finally and the maximum open circuit voltage (V_{OC}) can be obtained, which is the difference between the donor Highest Occupied Molecular Orbital (HOMO) and acceptor Lowest Unoccupied Molecular Orbital (LUMO) energies levels. Figure 1.1 illustrates (a) the structure of a BHJ OPV and (b) its working mechanism of an OPV.

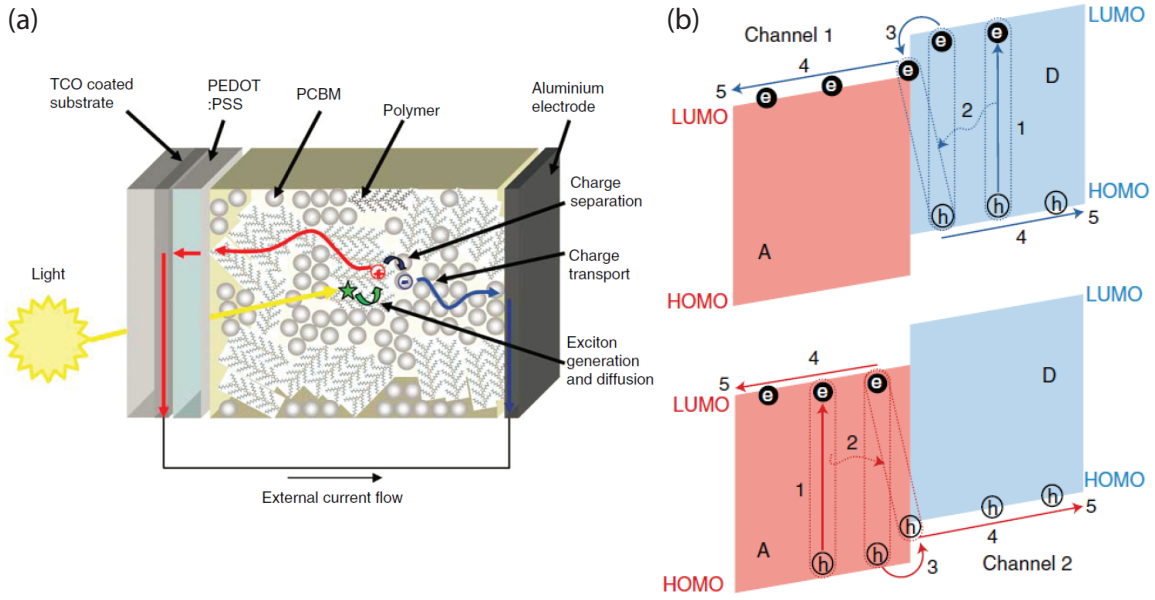

Figure 1.1: (a) Schematic layout of the function of a typical organic solar cell. Brabec, C. J., Durrant, J. R., Solution-Processed Organic Solar Cells Advances in Device Efficiency, MRS Bulletin, 33, July 2008, 670-675, reproduced with permission. (b) The operating mechanism of OPVs: (1) absorption of photons and creation of excitons; (2) diffusion of excitons to D/A interfaces; (3) dissociation of excitons to free charge carriers (holes and electrons) at D/A interfaces; (4) transportation of the charge carriers to electrodes; (5) extraction of the charge carriers at the electrodes. Reprinted by permission from Springer Nature: Nature Photonics Next-generation organic photovoltaics based on non-fullerene acceptors, Pei Cheng et al., 2018.

Poly(3-hexyl thiophene) (P3HT) and the fullerene derivative acceptor [6,6]-phenyl C_{61}-butyric acid methyl ester (PCBM) was a popular polymer blend at the early stages of BHJ OPV development.[12–14] These molecules consist of carbon backbones which are sp^2-hybridized with delocalized π orbitals, making them semiconductive. The "bandgap" of these organic semiconductors is determined by the highest occupied molecular orbital (HOMO) and the lowest unoccupied molecular orbital (LUMO), equivalent to the valence band (VB) and the conduction band (CB) in inorganic solid states respectively. The mobility of the system is governed by the hopping of excitons (polarons) because of the charge-carrier localization. Unlike inorganic systems, the charge mobility is much less and varies for many orders for different systems ranging from 10 cm^{-6} to 1 $cm^2V^{-1}s^{-1}$, whereas inorganic systems is at least 100 times faster.[7] Regardless of the low mobility and high binding energy (0.2-0.4eV) of excitons, there is a still high tendency for recombination to occur within the organic active layer and

results in non-radiative loss for the OPV.[15] One particular challenge with using PCBM is its weak absorption in the visible and near-infrared (NIR) region because of its high molecular symmetry.[13] The spherical structure of the fullerene derivative also tends to crystallize and cause aggregations that lowers the stability of the device.[13] Therefore, the OPV technology is moving towards using non-fullerene acceptors (NFAs) recently to benefit from its tunability in areas such as the bandgap, energy level alignment, molecular planarity and crystalinity.[13]

There are a number of ways to optimize efficiency and improve the stability of an OPV including modifying the design of active layer components and morphology, changing the device architecture to inverted BHJ or tandem devices, implementing interlayers in the device and finding alternatives for electrodes.[4,11,13,16] For the main interest of transfer printing, this chapter will only focus on the latter two aspects, where the roles of interlayers will be further discussed in Chapter 1.2.

1.2 Roles of interlayer material

Surface modification of OPV interlayers has been practiced in conventional OPVs. Ultrathin layers of fullerenes (C_{60}, bathocuproine (BCP)), transition metal oxides (V_2O_5, MoO_3, TiO_2 and ZnO) and metal fluorides such as lithium fluoride (LiF) are common examples of interlayers. They all have beneficial effects on the OPVs devices but the mechanism for each interlayer material serves differently.

For ITO anodes, a thin layer of poly(3,4-ethylenedioxythiophe- ne):poly(styrenesulfonate) (PEDOT:PSS) is usually included as a hole transporting layer (HTL), which has a work function of 5.2 eV to promote hole extraction and smooth the ITO. However, due to the acidic nature of PEDOT:PSS, it has been shown to cause chemical and morphological degradation to the ITO.[4,16] Therefore, buffer layers have to be implemented to physically block In diffusion into the PEDOT:PSS layer, which can then enhance lifetime of the device.[16]

Other approaches are to replace the HTL to other materials and refrain from using PEDOT:PSS for the device.[16] MoO_3 is found to be very successful in improving device stability by preventing moisture and oxygen in the interlayer. However, MoO_3 can form an unstable interface with P3HT:PCBM, so it is still not an ideal solution for HTL.[16] There has been much research on introducing buffer layers to promote adhesion between the anode and the HTL. Organic material is also susceptible to dewetting on

hydrophilic ITO.[16] An ideal HTL should also be able to stabilize against dewetting. A number of oxides such as TiO_2, ZnO, SnO_2, CuO_x, Fe_2O_3 and NiO, have been found to exhibit stabilizing behaviour for the anode and BHJ interface.

The back electrode (cathode) of a standard OPV, is typically made of a low work function metal like Al so as to line up with the LUMO of the acceptor to increase the built-in potential of the electrodes.[16] However, also because of its low work function, it is extremely prone to oxidation and reaction with the active layer, which then leads to irreversible degradation at this interface.[16] The inverted OPV architecture can avoid this problem entirely by avoid using the low work function metal. Instead, a high work function metal such as Ag or Au is used as anode, overtaking the role of ITO, while the ITO is typically coated with n-typed nanoporous metal oxide such to lower its work function to facilitate as the cathode. These metal oxides include ZnO, TiO_x, CrO_x and Cs_2O.[16]

For conventional standard OPV architecture, the other approach is to use a metal oxide based ETL. These ETLs are also widely recognized for its oxygen and moisture scavenging nature, which is important for device stability and longevity.[17] Some typical examples of these ETLs include TiO_2, CsCl, CrO_x, ZnO, LiF and etc.[16]

Among the interlayers, LiF has shown extremely high performance with OPVs and OLEDs.[16] LiF is a large band gap dielectric material which is insulating in bulk properties. On Al cathodes, submonolayer LiF can slow down the oxidation rate and stabilize the OPV series resistance.[16] However, the underlying mechanism is still under debate.

LiF interlayer is usually deposited by physical vapor deposition (PVD), which can easily segregate along the grain boundaries and form clusters, changing the morphology of the electrodes and the contacts. Studies show that by controlling the thickness of the LiF layer, the PCE changes until the thickness reached certain critical point.[16] For example, a 0.5 nm thick LiF shows no protection to Al at all, but as the thickness increases, the lifetime of the device also increases. This improvement of lifetime increases until the LiF thickness reaches 2 nm, for which a complete coverage of cathode occurs.[16] Like the metal oxides ETL, LiF is also scavenging oxygen from the Al cathode to prevent oxidation at the BHJ/cathode interface. However, this is not a universal effect as it does the exact opposite for Mg cathode, likely due to the nature of oxidation of these two metals.[16]

LiF can also tune the work function of the cathode because of its highly ionic

characteristic that a dipole moment is formed on the surface which lowers the energy barrier at the interface. When used on the ITO interface, however, the OPV also shows similar improvements with the work function of ITO is raised instead.[18]

1.3 Graphene-based OPVs

There has been demands to make OPV more flexible, the most commonly employed structure involves the use of ITO, which is brittle in nature.[19] Also due to the limited In source and their reactivity with the organic layer, there is a need to find an alternative to replace ITO.[19] Graphene has drawn a lot of attention ever since its discovery because of its excellent physically strength and electrical properties.[14,17,19–30] It is conductive, transparent and flexible, thus, it can be used to replace ITO as the anode in OPVs. A number of groups demonstrated using reduced graphene oxide (rGO) to produce flexible OPVs.[19,24,25] The work function of graphene is 4.3 eV, compared to ITO, which ranges from 4.5eV to 5eV, is not a good match for the HOMO of the acceptor (P3HT: 5.2eV).[25] The graphene work function, however, is tunable by doping its surface.[19,28,30] The rGO measured by Lin et al., has a work function of 4.7 eV, making it suitable to be the anode of OPV.[19] They deposited rGO on flexible substrates such as polyethylene terephthalate (PET) and by varying the thickness of the rGO, the sheet resistance can be manipulated.[19] As the thickness of the rGO increases, the sheet resistance of the rGO also decreases, which results in a lower series resistance (R_s), a higher current density and an overall improvement in PCE.[19]

rGO was also used as transparent cathode in an inverted hybrid photovoltaic as reported by Yin et al..[20] In such an inverted structure, a metal layer is still used as one of the electrodes, usually a high work function metal such as Au or Ag is used as the anode. The structure Yin et al. used is quartz/rGO/ZnO NRs/P3HT/PEDOT:PSS/Au which achieved a PCE of 0.31%.[20] There is a nice review by Yin et al. who listed out a good number of graphene-based OPVs.[20] From that table, graphene and its derivatives have been applied in every single layer in the OPV.

As mentioned earlier, the back electrode (cathode) of a standard conventional OPV, is typically made of a low work function metal so as to line up with the LUMO of the acceptor to increase the built-in potential of the electrodes.[16] However, also because of its low work function, it is extremely prone to oxidation and reaction with the active layer, which then leads to irreversible degradation at this interface.[16] Al

can naturally form a self-passivating oxide layer when in contact with air so that it is resistant to further oxidation, however, it is also very porous to oxygen and moisture.[16] Poor injection efficiency was developed as a result of increased series resistance of the OPV from cathode oxidation.[16] Feng et al. found that by putting a layer of graphene as the interlayer between the Al cathode and active layer successfully stabilize the device and stops the Al from diffusing into the active layer and react.[31]

On top of being a physical barrier, graphene derivatives have been used extensively as an electron transport layer (ETL) under the cathode in OPVs to improve charge transport and charge extraction.[14,17,26–28,30] Wang et al. took advantage of the work function tunability of GO and used thermal release tapes to stamp the GO onto the BHJ before evaporating the Al cathode. The work function of GO (4.3eV) was close to the LUMO of the fullerene acceptor, therefore, an efficient charge transport was achieved with a PCE of 6.72%.[26] They found that the role of GO is very similar to TiO_x as ETL that because of the interfacial dipole generated at the BHJ/ETL interface, the hole injection barrier increases while the electron injection barrier decreases. Thus, the electrons can be transported more efficiently to the cathode with the presence of the GO ETL.[26]

Like any graphene-based OPV mentioned above, the thickness of the graphene derivative and contact of the layer is very important to optimize the R_s.[26]

Another group doped GO with Li to obtain a similar work function of 4.3 eV and used it as the ETL.[27] The Go-Li ETL OPV device achieved a PCE of 6.29% better than the OPV with the GO-Li layer of just 5.51% PCE.[27] They also see an improvement in stability as the GO-Li act as physical barrier against moisture and oxygen.[27]

Alternatively, when the GO is doped with Cl, its work function is increased to 5.16 eV, which makes it suitable as an HTL.[28] This in turn tuned the work function to match with the HOMO of the donor. Konios et al. found that by incorporating both the GO-Cl HTL and GO-Li ETL, the charge carrier mobilities were increased and more importantly balanced which prevented charge accumulation in the device.[28] Their HTL only device has a measured PCE of 8.28% and the combined effect of the GO-Cl HTL and GO-Li ETL led to an impressive PCE of 9.14%.[28]

The tunability of work function for graphene and its derivatives makes it incredibly versatile to be applied to essentially any layer of an OPV.

1.4 Perovskite-based PVs

Perovskites have been the most promising candidate in photovoltaics for its low cost and high performance since its emergence in 2009 as perovskite-sensitized solar cells reported by Miyasaka's group with a PCE of 3.81%.[32–35]

In only less than a decade, the latest PCE delivered by these perovskites PVs have achieved 23.3%.[36–38] The perovskites material benefits from both the characteristics of organic and inorganic semiconductors, that their optoelectric properties can be tuned chemically, being processable in solution and at low temperature like the organics; and their high charge carrier mobility, long diffusion length and radiative lifetime like the inorganics.[39] These perovskite PVs, even though are not produced at the highest quality, can still offer high open-circuit voltages with low charge recombination.[32,34,39] In-depth studies on the fundamentals of perovskites have been performed by numerous groups to understand the superior efficiency of these new PVs, whereas new applications on other devices are already underway.[32,38–40]

The nomenclature of perovskites comes from the crystal structure of calcium titanate, in the form of ABX_3.[34] A is the large cation, which is usually Cs in inorganic perovskites and methylammonium (MA) or formamidinium (FA) in hybrid-organic perovskites.[38] B is the smaller cation with a 2^+ oxidation state, which is typically Pb^{2+}.[39] Though recent development has been trying to eliminate the toxic Pb content in perovskites and replace the B site with elements from the same group of Pb in the periodic table such as Ge and Sn.[39] These candidates are however, less stable in their 2^+ oxidation state. Other transition metals such as Mn, Ni and Zn were also tried, but Pb still is the major candidate in the field.[39] X is the halide anion, which can be I^-, Cl^-, Br^- or a mixture of them.[39] Figure 1.2 a shows the crystal structure of hybrid organic perovskites in the form of ABX_3.

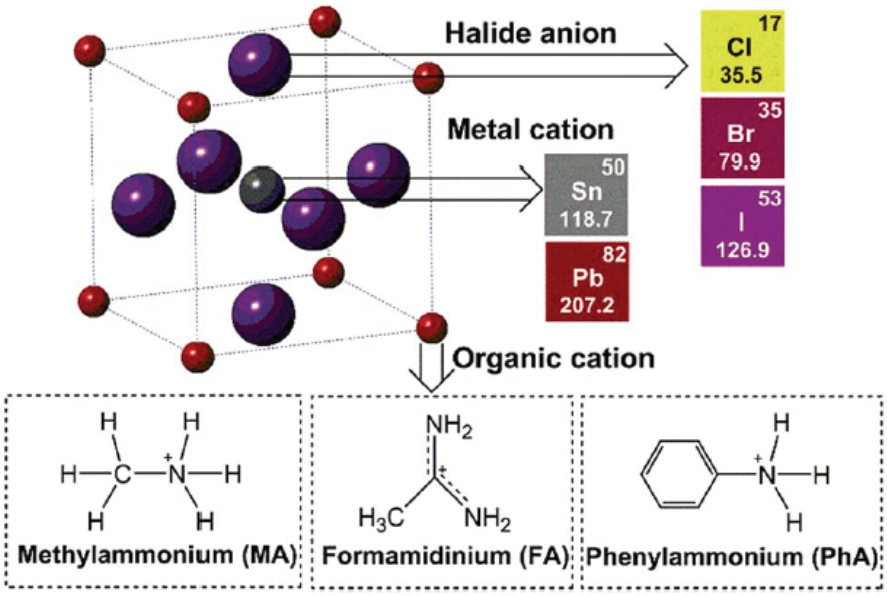

Figure 1.2: Schematic crystal structure of organo-metal halide perovskites Figure reproduced with permission from reference [35].

The wide tunable optical band gap (the entire UV-vis-IR) of the hybrid-organic perovskite PV is made possible by varying the choice of halide anion and the composition ratio.[32] The inorganic octahedron structure determines the valence band and conduction band of the perovskite band structure. The hybridized Pb *6s* orbital and the halide *p* orbital are responsible for the valence band.[39] Whereas, the conduction band is made mostly of the Pb *6p* orbital and little from the halide *s* orbital.[39] This can be seen from the difference of photoluminescence (PL) peaks of the hybrid organic perovskites with $MAPbCl_3$ at 402 nm, $MAPbBr_3$ at 537 nm and $MAPbI_3$ at 784 nm.[32] The organic cation only is responsible in modulating the band gap by varying the lead-halide bond distance.[39,41] For instance, switching the MA to FA cation can change the band gap from 1.51 eV to 1.4 eV.[42] The band gap tunability is particular useful for applications like the tandem PVs, which can be used as the top cell and tandem stacked light-emitting diodes for making white light source.

The organic cation is also responsible for the hysteresis phenomena exhibited in the Methylammonium lead iodide ($MAPbI_3$) perovskite PVs, which originates from the reorientation of the MA cation upon applied electric field.[35] The $MAPbX_3$ crystal begins from a cubic structure at high temperatures and transforms through tetragonal phases to ultimately the orthorhombic phases at low temperatures.[39] It has been

captured by neutron diffraction, infrared (IR) and Raman spectroscopy, and nuclear magnetic resonance that the MA cations rotate freely in the picosecond order in the structure.[39,41] This results in ferroelectricity which is hypothesized to aid with charge separation in the device for good performances.[35,39]

The architecture of perovskite PVs is similar to an OPV, where a perovskite layer is sandwiched in between a metal cathode with its ETL and a transparent conductive anode with its HTL. Unlike the organic semiconductor which forms Frenkel excitons, the perovskite forms Wannier-type excitons with a Bohr radius of 30 Å.[35,43–45] The Frenkel excitons have high binding energy of 100 meV while it is only 20-50 meV for Mott-Wannier type excitons.[35,39] The small binding energy of Mott-Wannier type excitons are comparable to the thermal energy of 26 meV at room temperature which allows for a great number of free charge carriers to dissociate quickly at the interfaces and be collected at the electrodes.[35,39,40] The differences of exciton binding energies between the organic semiconductors and perovskites are due to the dielectric constants of the material, with perovskites having a dielectric constant of 32, ten times more than a typical organic semiconductor.[35] High dielectric constant leads to strong dielectric screening effect and hence low binding energy.[35]

It was also measured by experimental studies that the perovskites have long-range ambipolar transport properties– the transport properties of electrons and holes are balanced, which is uncommon in semiconductors.[35,45] This is essential for charge transport and collection for the efficient PV device. Moreover, the charge carrier diffusion lengths of high quality single-crystalline $MAPbI_3$ are measured to be near 175 um, which is much larger than the 10 nm diffusion lengths of charge carriers in organic semiconductors.[32,35] In fact, the electron mobility of polycrystalline $MAPbI_3$ films are found comparable to other inorganic PV light absorber materials.[39] Though it also depends on the perovskite preparation process, an n-type $MAPbI_3$ film was reported to have an electron mobility of 66 $cm^2V^{-1}s^{-1}$, while that of a polycrystalline Si is around 40 $cm^2V^{-1}s^{-1}$.[39] The long diffusion length and high charge mobility are again beneficial to device performance for avoiding charge recombination and allowing more charge collection to take place. Liu et al. recently summarized a useful list of critical optoelectronic parameters of single-crystalline perovskites achieved by various groups.[32]

Like OPVs, selective transport layers of ETL and HTL are applied to perovskites PVs for further device optimization such as adjusting band alignment for charge carrier

flow and blockage; promoting chemical stability of the perovskites layer; tuning the predominant charge carrier type in the perovskites layer and modifying the binding energies of excitons.[35,39] These ETL and HTL should also be able to conformal and homogeneous contact with the perovskite layer, have a similar charge carrier mobility as the perovskite and for whichever layer is on the transparent electrode side depending on the design of the PV, it should also be transparent for light absorption.[39]

Most interlayer materials used for OPVs (see Chapter 1.2) have been tried on the perovskite PVs. Metal oxides are favourable as ETLs because they have high charge mobilities and are stable in air.[39] The examples include ZnO and even the organic acceptor material PCBM.[39] Metal sulfides are sometimes employed as ETL as well in the pervoskites, however, except for ZnS, these sulfides do absorb visible light.[39]

For the HTL, high work function organic semiconductors are often used for highly efficient perovskite PVs.[39] It is not surprising that these organic HTLs have lower hole mobilities than the perovskite material, only with the exception of PEDOT:PSS. However, as discussed in Chapter 1.2, PEDOT:PSS is acidic, reacts with the ITO, absorbs water and does not block electrons, which then causes degradation as evident in OPVs as well. Therefore, recent approaches have moved on to using metal oxides and metal sulfides such as MoS_2, NiO, MoO_x, V_2O_5 and WO_3 for their favourable higher valence bands, charge mobilities and better chemical stability.[39]

Like OPVs, the major challenge of perovskite PVs remains with the long-term stability issue. The mostly ionic perovskite is unstable in polar solvents, so water is detrimental to the device. However, the actual degradation process is still unknown because its phenomenon is not universal. For example, $MAPbI_3$ degrades in high humidity (>50%) , while such degradation is not observed for $MAPbBr_3$ and $MAPb(I_{0.8}Br_{0.2})_3$.[39] Moreover, the $MAPbX_3$ is also not tolerant to heat that they start decomposing at 200°C even under vacuum conditions.[39] It is because the MA halide portion volatilizes. Though switching MA to FA have shown better thermal stability, replacing the organic cation with inorganic metal such as Cs can avoid the thermal stability issue altogether.[32,42] Ironically, since the perovskite crystal is mostly ionic bounded, it also makes the perovskite material defect-tolerant.[38,39] The principle of defects is still a field too new to be explored. Much research is focused on chemical stabilization and efficiency of the perovskite PVs. There are still a lot of open questions in the field.

Chapter 2

Nanoparticles synthesis

The crystal size and dispersion of nanoparticles are important aspects for devices as they influence the efficacy and reliability. There are numerous ways to improve the degree of control for these aspects to put them into applications.

2.1 Ligands

A popular way of synthesizing nanoparticles is by using ligands, often with oleic and octylamine acids, which are long molecules that cannot be integrated into the crystal structure of the nanoparticles.[46] The ligands are a popular choice because they can prevent agglomeration and promote salt solubility; in particular, for the generous surface defect tolerance of perovskites discussed in Chapter 1.4, the ligands do not required surface passivation as opposed to most quantum dot nanocrystal systems.[47,48]

Hot injection is an example of ligand mediated approach. In this process, ligated precursors are injected into a hot solvent with a high boiling point which containing the ligands to stabilize the nanoparticles.[43,49–51]

Another example of ligand mediated approach is called the ligand assisted recrystallization. The recrystallization process takes place as the ligated precursors are injected drop-wise into non-polar, insoluble solvents with the help of non-equilibrium triggers such as impurities or vigorous stirring.[48,52–56] A similar method is called the emulsion-demulsion in which rapidly precipitation takes place by introducing a demulsifier to an emulsion solution of two immiscible solvents with ligated precursors in it.[57,58]

The last example of ligand mediated approach is by ion-exchange, where one

type of nanocrystal is transformed into another or a mixed-phase version by using ligand-mediated anion or cation.[58–60]

The limitations of these ligand mediated approaches are the restriction of large scale application. The extremely fast reaction kinetics with the ligand does not allow for a delicate external control for the nanoparticles.[46,54,61,62] Such fast kinetics typically will induce random nucleation, leading to inhomogeneous structures with large variations in particle size. For the case of perovskites, it has been possible to exert some level of size tunability, with even monodisperse nanoparticles observed for the inorganic ones through temperature, precursor concentration and ligand mixtures.[48,51,55,57] However, particularly for the case of organic hybrid perovskite nanoparticles synthesis, control of size dispersion has proven to be more challenging, due to their lower stability and sensitivity to moisture.[52,63–65] Additionally, ligand assisted synthesis has a tendency to form 1D nanowire structures or 2D nanoplatelets rather than true dimensionless nanoparticles.[48,54,56,66–68]

2.2 Evaporating

Direct synthesis of a thin layer of nanoparticles is possible by vapour deposition or vacuum evaporation. The precursors can be sequentially or simultaneously layered on the surface. However, random nucleations of crystals on the surface often lead to inhomogeneous, polycrystalline films with large variations in particle size.

2.3 Reverse Micelles Deposition

A very promising way to form nanoparticles is to use reverse-micelles as a template, thereby creating a non-polar environment in which the crystallization process can take place. The approach is called the reverse micelles deposition (RMD) technique. RMD gives a greater degree of control over the size and shape of the nano-materials being formed in solution, and does not require the addition of ligands. These also allow for a greater level of size control, locational dispersion and consistency.

The facile, room temperature RMD approach has been widely used to make a variety of NPs.[69–72] It takes advantage of the amphiphilic diblock copolymer to form a spherical micelle when dissolved in a solvent. Due to the amphiphilic nature, the copolymer block with the same polarity as the solvent will shield its constituent with

opposite polarity in the core of the sphere. For the reverse micelles, the hydrophobic tails of the diblock copolymer stick out to shield the inner core hydrophilic heads when dissolved in a non-polar solvent.[73] Hydrophilic ionic salts can form inside the reverse micelles through an acid-base redox reaction where the micelle medium is a reactor for the reaction. The resultant nanoparticles conform with the size and shape of the reverse micelles.[74,75] The reverse micelles can be used as nanoscale reaction vessels, so-called the nano-reactors.[18,76,77] The reversed micelles solution loaded with ionic nanoparticles can be spin-coated onto any substrate. To expose the nanoparticles, oxygen plasma etching is typically used to destroy the C-C bond of the polymeric micelles shells, which shall be discussed in Chapter 4.[18,78]

Compared to the ligated methods, the RMD technique allows greater control over the size distribution due to controlled nucleation and crystal growth. By separating the precursor solvation and reaction steps, it circumvents the high temperature kinetics of hot injection, bypasses the metastable equilibrium required for ligand assisted re-precipitation, and avoids the reversibility of ion-exchange approaches. Additionally, using micellar nanoreactors rather than the dynamically stabilizing ligands leads to the formation of monodispersed spherical nanoparticles.

Chapter 3

Methods of Nanotransfer printing

As described in Ch. 2.3, there involves the use of oxygen plasma to remove the polymeric shell of micelles to expose the nanoparticles inside. For this reason, the nanoparticles cannot be directly deposited on the organic active layer in the device as the plasma will also destroy the organic layer. Therefore, an extra step is needed for putting these nanoparticles to the target organic layer indirectly.

Nanotransfer printing is one of the latest developments in soft lithography. Soft lithography in general is different from other photolithographic techniques, which typically involve the use of chemical solutions, high vacuum, high cost or long times.[79] The advantages in soft lithography are its low cost, simplicity and reusability of tools such as stamps and molds.[80,81] With device fabrication in mind, these advantages are also important when moving nanoparticles to the target organic layer effectively. Therefore, in this Chapter, several ways of nanotransfer printing will be discussed in depth for its feasibility and compatibility to be implemented to the device.

3.1 Pick-and-Release (PDMS, PMMA, Parylene)

Nanotransfer printing (nTP) was developed from the microcontact printing (μCP) technique that has been widely used for micron scale patterning.[82] Both nTP and μCP share some common components– there is an elastomer stamp, a printing material (thiol ink for μCP; nanoparticles (NP) for nTP), a donor substrate where the printing material is initially located, and the receiver substrate where the stamp finally releases the printing material. Though μCP is an excellent technique, it is only limited to a lateral

resolution of 35 nm as it relies on the conformal contact of a thiol-inked elastomer stamp, typically polydimethylsiloxane (PDMS), to Au or other thiol compatible metal-coated substrates.[83,84] The choice of printing material is strictly restricted to metal-compatible groups. The problem with the ink is that it can smear on the metal-coated substrate once being transferred from the elastomer stamp thus limiting the resolution.[81,85] These restrictions cause precision problem in using μCP for transfer printing.

The major development in nTP which makes it superior to μCP, is its independence from the capillary action of the thiol ink with the elastomer. nTP is based on the surface energy difference of the substrate, NPs and stamp. The NPs to be printed can be picked from one substrate and released to another substrate. For this reason, the nTP approach is referred to as the "pick-and-release" method. It enables a printed nanoscale feature size as low as 20nm.[86,87]

Over the last 20 years, much research has gone into optimizing the nTP pick-and-release efficiency by focusing on some critical parameters. There are the surface energy, stamp mechanical properties, surface roughness, peeling velocity and temperature and pressure control of the system.

3.1.1 Surface energy difference

nTP can transfer films or nanostructures to virtually any desired receiver substrate, governed by the work of adhesion differences of the stamp/particle/substrate system as in Eqn. 3.1[80]

$$W_{sub-np} - W_{stamp-np} = (\gamma_{sub} - \gamma_{stamp}) - (\gamma_{sub-np} - \gamma_{stamp-np}) \tag{3.1}$$

where W is the work of adhesion, γ is the surface energy of the material indicated by the subscript, and sub is the substrate.

The surface energy (γ) of the material is defined as the surface excess energy per unit area, which is an attractive force between materials in contact.[88,89] Table 3.1 shows the surface energies of some common material used in nTP.[90–92]

The ionic or metallic particle γ (see Table 3.1) is usually larger than those of the

Table 3.1: Surface energy of candidates for nanotransfer printing

	Stamp			Particle			Substrate				
Material	PFPE	Parylene-C	PDMS	PMMA	LiF	Au	P3HT:PCBM	P3HT	PCBM	Graphene	Si
γ (mJ/m^2)	15.8	19.6	19.8	41.1	460	1500	19.7	26.9	38.2	46.7	60-90

substrates and stamps. Therefore, in Eqn. 3.1, the work of adhesion is approximately just the γ difference between the substrate and stamp. Low surface energy materials such as the common elastomer stamp used in nTP, PDMS, is hydrophobic (contact angle=105°).[93] The particles on these hydrophobic surfaces can be easily transferred to substrates with higher surface energies such as polymethacrylate (PMMA), which is hydrophilic (contact angle=68°).[94–96] PDMS-PMMA can be used in the release process, as Eqn. 3.1 yields a positive work of adhesion to the substrate. For the pick-up process, as seen from Table 3.1, a donor substrate often used in nTP like Si, has higher γ than the elastomers. Thus, Eqn. 3.1 yields a negative value and the pick-up process cannot occur. In such cases, the pick-up process cannot simply rely on the work of adhesion difference. It takes extra energy to overcome the work difference of the system. This pick-up process is in fact the major challenge for the pick-and-release method. The release process, on the other hand, is relatively easy even for the organic target substrate like the (Poly (3-hexylthiophene): [6,6]-phenyl C61-butyric acid methyl ester) (PCBM)(P3HT:PCBM) blend as the surface energy difference is not immense.

There are a number of ways of introducing extra energy such as increasing the peeling velocity of the stamp to promote the pick-up process but it is also possible to perform the pick-and-release process using the same stamp on a variety of material systems. This can be done by changing the surface energy of the stamp. For example, the stamp and the receiving substrate can be modified by O_2 plasma etching or UV exposure to change the surface functional group.[97,98] By plasma etching the PMMA, it will be made more hydrophilic until it restores its hydrophobicity.[99]

In some cases, a self-release layer can be added to the receiver such that the apparent surface energy of the donor can be increased and the particles can be released by the stamp at ease.[86,100,101]

Peeling velocity of the stamp can also change the effective surface energy for promoting successful transfer. At high peeling velocity, more energy is supplied to the system and it can surpass the pick-up threshold.[102]

A good conformal contact ensures the stamp for a high degree of proximity for the particles to the substrate. Microscopically, a rougher stamp processes more indented sites on the surface than a smoother stamp. The indented sites are less likely to be in contact with the particles during pick-up. Additionally, if particles were picked up, they are trapped in the indented sites as the receiver cannot reach the particles.

Table 3.2: Young's modulus of stamp candidates

Stamp	PDMS	PFPE	PS	Parylene-C	PMMA	Graphene
E /GPa	0.36-0.87	1.05	3	4	4.8	1000

Therefore, a smoother stamp can enhance the yield of the pick-and-release process.[103] Plasma treatment may be used to specific stamps (such as O_2 plasma for PDMS) for smoothing the surface.[104] Poly(monochloro-p-xylylene) (Parylene-C) grown by CVD on Si wafers copies the roughness of Si, therefore, it is guaranteed with its atomic smoothness. It is also a good candidate for nTP not only because of its low surface energy as stated in Table 3.1, but also its chemical inertness to solvents.[105] Parylene-C is also readily removed in oxygen-based plasma so that it can be patterned by plasma etching.[105]

The elastomer stamp mechanical properties are related to the Young's modulus (E) which describes the material stiffness. Stiffer elastomers can be made thinner and maintain patterns while withstanding the external peeling force. Thus, a high E is critical to the replication of fine features and patterns.[84] Table 3.2 shows the stamp candidates E including some common elastomers such as the PDMS, PMMA and perfluropolyether (PFPE) and compared with the world's strongest material, graphene.[91,106–109]

3.2 Use of sacrificial layer (Graphene, Au, TRT, PNIPAAm-coated-PDMS, optical adhesive)

Other approaches which are complementary to nTP, can also be exploited avoiding the pick-up process of nanoparticles entirely. They do not involve the traditional donor-stamp-particles-receiver system, but instead use the idea of a sacrificial layer or a carrier layer for nanoparticles.

The exceptionally high E of graphene from Table 3.2 makes it an excellent transfer layer candidate, even the high surface energy ($46.7 mJ/m^2$) is not a concern now.[91] Many groups have successfully transfer pieces as large as $20 cm^2$ of high quality, crackless chemical vapor deposited (CVD) graphene using elastomer stamps such as PDMS or PMMA.[110–112]

This allows a modification of the pick-and-release method because the stamps

can be cast onto graphene for picking up the ultra-thin graphene. The transferred large-area, crack-free, highly crystalline graphene has been used as transparent and flexible anode for OPVs and OLEDs.[23,24] Using these well-developed graphene transfer mechanisms, one can make use of the graphene layer for carrying the nanoparticles to the target substrate for nanotransfer printing. The technical challenge for depositing nanoparticles on the graphene layer is minimal using the reverse micelles technique.

The graphene-assisted transfer process involves etching of two materials in the stack– the elastomer and the metal substrate graphene is grown on. The elastomer stamp can be etched away using chemicals but that leaves the organic residues to be further rinsed off by deionized water.[112] Unfortunately, the two drawbacks with this etching is organic device degradation has been linked to adsorption of water in the organic layer, making such a graphene-assisted transfer process undesirable and the organic residue that is left behind.[113] PMMA in particular, is notorious in leaving behind a significant amount of residue on graphene very difficult to be getting rid of after etching.[31,112,114–116]

An example of stamp-etching-free graphene transfer technique involves the use of thermal-release tapes (TRT), where the surface energy can be varied by temperature. They are commercially available with various adhesive strengths and thermal-release temperatures. The TRTs are ordinary tapes at room temperature but at the thermal-release temperature, the surface energy reduces so that it loses adhesive contact. These thermal-release tapes have been used to transfer nanostructures in nanowire devices.[117] However, it has been pointed out that the TRT also leave behind residue difficult to be cleaned and affect device performance.[112,118] Other TRT studies have combined the use of a thin Au layer as the assisting transporting layer under the TRT for transporting carbon nanotubes.[119,120] The real benefit of using TRT is its application for scalable roll-to-roll transfer of graphene.[118,121]

To avoid the unwanted polymer residue on graphene, Martins et al. has demonstrated the cold lamination method of CVD graphene (in room temperature) which does not require etching of an elastomer stamp.[115] They simply laminate a stack of PET/protective paper/CVD graphene/ target substrate/PET through the rollers and finish by removing the paper and PET.[115]

Feng et al. also demonstrated another method of using the target substrate (poly(3-hexylthiophene (P3HT)) directly as the graphene holder. Figure3.1 shows the transfer printing procedures involving graphene from reference [31] and [115].

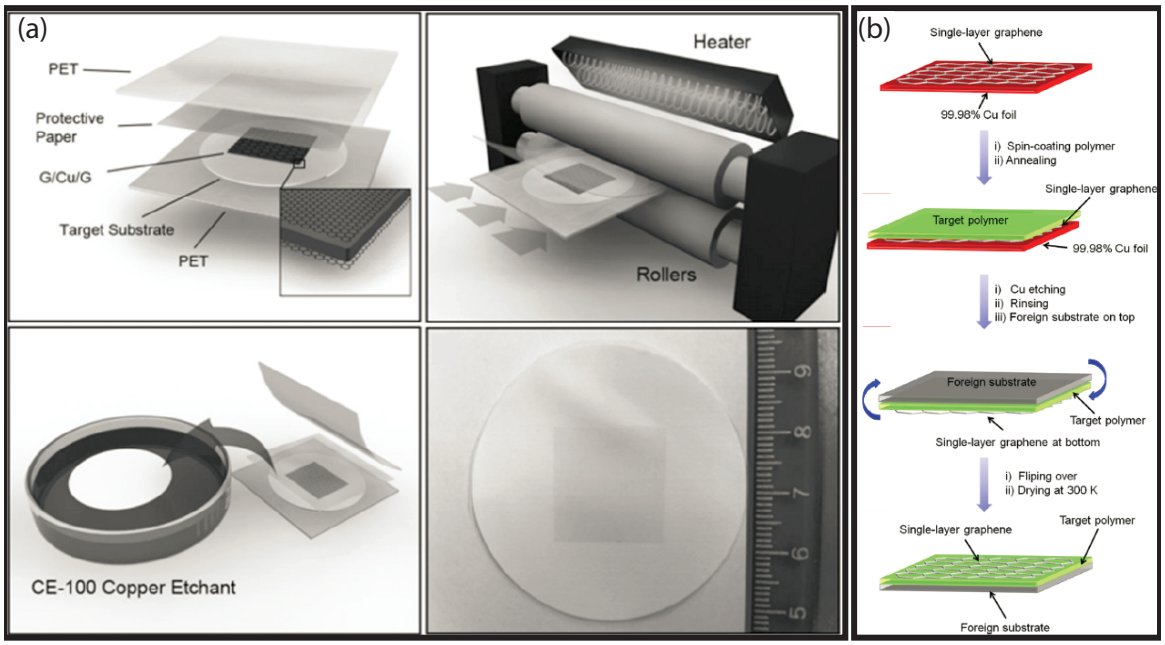

Figure 3.1: (a) Schematic diagram of the direct transfer technique via lamination. Copper foil with CVD graphene grown on both sides (G/Cu/G) is placed in between the target substrate and the protective paper. This stack is then put between two PET films. The PET/substrate/(G/Cu/G)/paper/PET sandwich is inserted into the hot/cold lamination machine. The PET films and the protective paper are then removed and the remaining substrate/graphene/copper stack is floated on a copper etchant solution for 15 min. The graphene/substrate is rinsed in DI water and blow-dried with nitrogen. In this picture, graphene is on a Teflon filter. The ruler is scaled in centimeters. From reference [115]. (b) Schematic of transfer process of the single layer graphene onto target polymer organic materials. Single layer graphene on Cu foil obtained by CVD growth, spincoating target polymer on single layer graphene, after Cu etching, a foreign substrate (i.e. Si wafer) is covered on top of polymer and then the sample is flipped over in ultrapure water. Single layer graphene on top of target polymer. Reprinted from Carbon, 87, Feng et al., "Engineering the metal–organic interface by transferring a high quality single layer graphene on top of organic materials", 78-86, Copyright (2018), with permission from Elsevier.

Since CVD graphene is preferred for the transfer process because it offers the highest quality of graphene.[112] These methods in Figure 3.1, however, still requires the post-transfer etching of Cu substrate from the CVD graphene, which was done with an aqueous base Cu etchant ($FeCl_3$ or ammonium persulfate solution). Therefore, they still have some inevitable drawbacks for organic device fabrication.[115]

As mentioned above, some approaches using TRT involves an extra layer of Au.[119,120]

A thin (100 nm) Au layer was grown on top of the nanocubes on quartz and then the TRT was used to pick up the Au layer with the nanocubes at room temperature. The release action was done by elevating the temperature to 140°C so that the Au layer with the nanocubes can be released from the TRT to the target substrate.[119] A detailed schematic of the TRT-Au transfer process is depicted in Figure 3.2 a.[120] The benefit of this method is that the residue of TRT will not be introduced to the target layer. The potential drawback is the etching of the Au layer, which requires the use of an Au etchant (KI).[119] This brings the problem of compatibility problem or contamination to the target layer by the Au etchant ions.

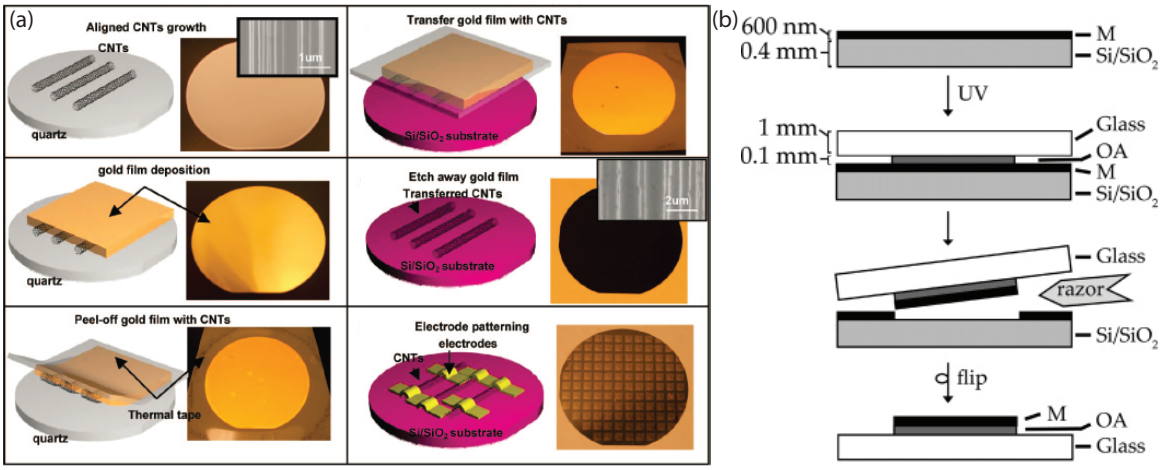

Figure 3.2: (a) Schematic diagram and photograph of full wafer synthesis of aligned nanotubes on a 4 in. quartz wafer. Inset shows SEM image of aligned nanotubes. Schematic diagrams and photographs showing the transfer procedure, i.e., gold film deposition, peeling off the gold film with nanotubes, transfer of the gold film with nanotubes onto a Si/SiO2 substrate, etching away the gold film, and device fabrication on the transferred nanotube arrays. Reprinted (adapted) with permission from [120]. Copyright (2018) American Chemical Society. (b)Schematic diagram of the procedure for template stripping using the composite of glass/OA as a mechanical support: (i) We deposited a metal onto an Si/SiO_2 substrate by evaporation with an e-beam. (ii) OA attached a glass slide to the surface of the metal. (iii) We cured the OA by exposing it to UV light for 1 h. (iv) In the case of mechanical template-stripping, we used a razor to cleave the glass/OA/metal composite manually from the Si/SiO_2 template to expose the smooth surface of the metal that was at the metal/SiO2 interface. Reprinted (adapted) with permission from [122]. Copyright (2018) American Chemical Society.

If the removal of Au is not of importance, here is another method called template stripping (TS) which was first developed to facilitate production of ultraflat metal (Au,

Ag, Pt and Pd) substrates.[122] In this method, Au or other metals are first evaporated on atomically smooth Si. The idea is to lift off the smooth Au from the Si substrate, so in the schematic in Figure 3.2 b, optical adhesive (OA) (Norland, no.61) is used to cure the metallic layer and the glass under UV exposure. Once the OA is cured, the Au/OA/glass stack will be cleaved off by means of a razor blade because the OA sticks prefentially well with the metal.[122] As a result, there leaves a nice smooth Au layer. The inorganic Au layer should not be affected by plasma action, so it will be nice for the RMD and can then be placed on the target organic substrate. Weiss et al. also tried with supporting substrates other than glass, they found that TS also works well with PDMS or even solder.[122] With these soft supporting substrate, TS is not restricted to rigid and flat surfaces. The final step is to remove the OA from the Au. Though the commercially available OA comes in a range of solubility, some can be dissolved in acetone and some can be dissolved in hot water, it is problematic that it would potentially leave behind some organic residue on the Au surface. It is only a matter of how much OA residue is left compared to the TRT method, let alone the Au and KI residue in both transfer methods.

Another method quite similar to the concept of the TRT is recently reported by Khabbaz Abkenar et al. where they used a thermoresponsive polymer called poly-N-isopropylacrylamide (pNIPAAm) as the elastomer stamp.[123] Like TRT, the thermoresponsive pNIPAAm undergoes molecular conformational change at the lower critical solution temperature (LCST), with the exception that it is reversible.[123] The polymer will switch its surface dominant moieties depending on the temperature to either the hydrophilic secondary amine group (below LCST) or the hydrophobic isopropyl group (above LCST) and hence, changing the surface energy.[123] In the hydrophobic state, the polymer is in the "collapsed" state with a local stiffness 100 times more than its hydrophilic state (swollen by water).[123] This change of surface energy is very useful for transfer printing of nanoparticles. Referring back to Eqn. 3.1, pNIPAAm would be preferably at the hydrophilic state (swollen) for the pick-up process and at the hydrophobic state (collapsed) for the release process. It was reported that the pNIPAAm is conveniently at the swollen state at 10 °C and collapsed at 35 °C in ambient humidity.[123]

Khabbaz Abkenar et al. managed to pick-and-release Au nanoparticles from Si (donor substrate) using a pNIPAAm-coated-PDMS stamp and transferred the nanoparticles to another Si substrate (receiver substrate).[123] The PDMS here was

needed for the growth of pNIPAAm by CVD.

However, due to the wrinkles formed during the swollen and collapsed process, only the nanoparticles located at the ridges are transferred. Moreover, some pNIPAAm residue is left on the surfaces of both the donor and receiver Si substrates, which at the end, suffers the same problem as TRT and PMMA.[123]

From all the nTP methods discussed, there is yet a perfect solution as all of them has their drawbacks. It is nevertheless, still worth-trying to look for the one with least damage on the device.

Chapter 4

Plasma reaction with graphene and the organics

Plasma etching is a common tool used to modify surface properties of materials such as the surface energy, morphology and resistivity [124, 125]. Plasma treatment can be used to functionalize polymer surfaces, making them more hydrophilic.[126] It can also be used for polymerizing monomers, cross-linking of polymer chains and remove surface contaminants.[126]

The etching mechanisms of plasma can be from energetic ion bombardment of plasma species directly on the surfaces, the reaction with chemically active plasma species or both simultaneously.[105,127] Oxygen plasma for example, its atomic oxygen ions can form molecular ions and neutral atomic radicals with oxygen molecules.[127] Any impurities in the plasma gas such as nitrogen, hydrogen and carbon dioxide can speed up the oxygen dissociation rate and hence the etching process.[127] The oxygen etching process can also be interfered by the chemical species of the organics. By abstracting hydrogen species from carbon bonds on the polymer surfaces, the species will form a radical to take part in the etching process; whereas the exposed site where the bond was first broken is now reactive to molecular or atomic oxygen absorption and form unstable radicals specials, which can become volatile species and be desorbed.[105,127] Parylene C is an example that can be readily removed by oxygen plasma in the same manner, of which the plasma results in the opening of the benzene rings.[105]

In fact, one of the earliest applications of plasma in industrial device fabrications is for stripping the organic photoresists which is still now a general practice.[127,128] As

discussed earlier in Chapter 2.3, oxygen plasma can be used to remove the diblock copolymer which makes up the micelles and leaves behind the nanostructure formed inside the nanoreactor.[129]

In some special cases, such as the silicone-based elastomer polydimethylsiloxane (PDMS), instead of being destroyed by oxygen plasma, it will be oxidized by the plasma and results in a rapid chemical conversion on the top surface into a stiff glassy silica-like film.[130–132] This is attributed to the formation of silanol groups (Si-OH) at the expense of methyl groups on the PDMS surface and the thickness of the glassy film grows as the oxygen plasma dosage increases.[97,130]

Plasma etching techniques by different gases have also been used to pattern graphene nanostructures, introducing defects and non-conductive regions in a variety of dispersions.[133–137] Studies based on the controllable introduction of disorder with plasma etching provides insights into the optoelectronic properties of functionalized graphenes.[135,138–141] Oxygen plasma is again the most common approach to manipulating surface properties of graphene.[142] In graphene and graphite, oxygen plasma etching is most likely to proceed by a chemical reaction rather than a physical process,[124,143,144] with the mechanisms of oxidation well studied[137,143,144] and widely simulated.[145–147] Briefly, oxygen exposure of graphene and graphite proceeds by the formation of epoxide groups at bridge or top sites on the graphene basal plane by oxygen adsorption.[143] The formation of epoxides induces C-C bond stretching, asymmetry of the hexagonal ring structure, and distortion of the planar geometry. This, along with the attachment of oxygen, modifies the hybridization and disrupts the π-network, opening up a gap in the degenerate states at the K point.[143] The induced semiconducting and photoluminescent properties of such functionalized graphene is related to the degree of oxygen attachment on the surface.[139] However, with these of the distortions of the graphene network, upon further exposure to oxygen, the etching process is enhanced. The C-C bond is under tension with the epoxide groups and hence the C-C bond weakens and eventually breaks upon any slight perturbation, resulting in ring opening.[143] As ring opening propagates through the graphene sheet, the defected graphene converts into sp^2 amorphous carbon, also defined as the "highly-defected regime",[138] where it loses all of its unique mechanical and optoelectronic properties.[148] Pits develop in graphene under intense oxygen plasma at high energy dosage and temperature and grow in size as the treatment increases.[124,135]

In free standing and supported exfoliated graphene, the more technologically useful

"lowly-defected-regime"[124,133,138,149] with interesting semiconducting and photoluminescent properties is usually only accessible within a very small window of oxygen plasma exposure.[138] Seconds or at most minutes of oxygen plasma exposure can send such films through various stages of doping and disorder before being completely removed.[134,135,141,143] This is also the case for graphene on some weakly bonded transitional metal substrate such as Ir and Ru (0001), where oxygen intercalates between the graphene sheet and the metallic substrate.[137] By contrast, CVD graphene on Cu, which has a stronger van der Waals force between the substrate and graphene, shows a considerable resistance to etching, tunable with a low temperature anneal.[150]

Chapter 5

Raman

5.1 Basics

Raman scattering radiation is an inelastic scattering process of photons with phonons. It arises from the electric dipoles oscillating at $\nu_0 \pm \nu_i$ produced when the oscillating dipole at ν_0 is modulated by the molecule oscillating at ν_i. The coupling between the nuclear motions and the electromagnetic radiation is provided by the rearrangement of electrons with respect to the nuclear motion that imposes a harmonic variation on the polarizability.[151] It is therefore governed by the intrinsic properties of the material, such as the atomic bonds, vibrational states, purity, crystallinity and strain. Long et al. used the musical analogy of beat frequencies between the radiation frequency ν_0 and the molecular frequency ν_i to describe the frequencies observed in Raman scattering.[151]

5.1.1 Electromagnetic Radiation Theory

As a phonon interacts with a molecule, it induces a dipole moment P to the electron cloud. The Raman spectrum is a result of radiation frequency shift of the vibrational frequency of a molecule (ν_{i}) from the incident frequency (ν_0) of a phonon. The light scattering phenomenon can be described by the electromagnetic radiation theory classically in Eqn.5.1.

$$P = \alpha E = \alpha E_0 cos\,(2\pi\nu_0 t) \tag{5.1}$$

where E is the time dependent electric field, it is maximum at E_0; α is the polarizability. P is the induced dipole moment and assuming simple harmonic motion for a molecular

vibration (mechanical harmonicity), it can be expanded with higher order terms.

$$\begin{aligned} P &= \alpha E_0 cos\left(2\pi\nu_0 t\right) + \left(\frac{\partial\alpha}{\partial q}\right)_0 q E_0 cos\left(2\pi\nu_0 t\right) \\ &= \alpha E_0 cos\left(2\pi\nu_0 t\right) + \left(\frac{\partial\alpha}{\partial q}\right)_0 q_0 E_0 cos\left(2\pi\nu_0 t\right) cos\left(2\pi\nu_i t\right) \\ &= \alpha E_0 cos\left(2\pi\nu_0 t\right) + \frac{1}{2}\left(\frac{\partial\alpha}{\partial q}\right)_0 q_0 E_0 \left\{cos\left[2\pi\left(\nu_0+\nu_i\right)t\right] + cos\left[2\pi\left(\nu_0-\nu_i\right)t\right]\right\} \end{aligned} \tag{5.2}$$

q is the vibrational amplitude at the normal coordinates of vibration, a scalar quantity that maximizes at q_0 with the molecular vibrational frequency ν_0.[151] The dipole moment therefore consists of three terms. In the classical theory, the first term in Eqn. 5.2 is the Rayleigh scattering of an oscillating dipole that radiates at a frequency of ν_0. The second and third term consists of the Raman scattering components, which are inelastic, with the frequency of ν_0+ν_i for the anti-Stokes and ν_0-ν_i for the Stokes. The term $\left(\frac{\partial\alpha}{\partial q}\right)_0$ determines if the vibration process is Raman active with respect to the normal coordinate of vibration q_0. It describes physically that in order for the vibration process to be Raman active, the rate of change of polarizability cannot be zero. For a vibration to be infrared active, the dipole moment derivative with respect to the normal coordinate at the equilibrium position cannot be zero.[151] The Raman spectra originates from the Stokes and anti-Stokes, which are inelastic scattering processes and they are about $1/10_6$ times weaker than the elastic Rayleigh scattering.[152,153]

This gives the classical representation of the Raman effect. This frequency shift is unique to certain chemical bonds and vibrations of the lattice.[152,153] Fig. 5.1 shows the energy transitions in a Normal Raman scattering process. Typically in a Raman spectrometer, a laser source excites the molecule to a higher energy level in the virtual excited state (dotted line) below the first electronic transition state (E_1).

Here in Fig. 5.1, the Stokes transition happens when the excited molecule is transited from the ν=0 state to ν=1 by scattering a frequency of ν-ν_1, whereas the anti-Stokes process arises when the excited molecule transits from the ν=1 state to the virtual excited state and reverts back to the ν=0 state. According to thermodynamics, the Maxwell-Boltzmann distribution states that the population of molecules at the ν=0 state is higher than at the ν=1 state. As a result, the Stokes line always radiates stronger than the anti-Stokes line.[152,153]

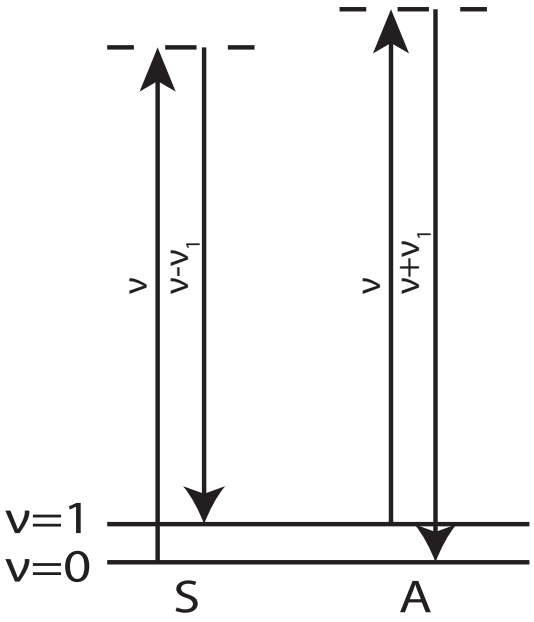

Figure 5.1: Normal Raman scattering mechanism, where S is the Stokes and A is the anti-Stokes scattering

5.1.2 Symmetry Selection rules

The Raman activity is determined by the change of polarizability (α) with respect to normal vibration q_0. A simple way to visualize the changes of polarizability during vibration is from the model of a linear symmetric small molecule such as CO_2, which possesses four modes of vibrations: a symmetric stretching mode Q_1, an antisymmetric stretching mode Q_2 and two bending modes Q_{3a} and Q_{3b} which have the same vibrational frequency and make a degenerate pair.

For Q_1 mode, since non-zero bond dipole derivatives of the C-O bonds always stretch in opposition that cancels out, it is IR inactive. For the Raman activity of CO_2, the P and E relation in Eqn. 5.1 has to be modified to include the vector components in the x, y and z coordinates as written below to fully describe the behavior of an actual molecule. It can be represented in a matrix form in Eqn.5.3 with the polarizability tensor.

$$\begin{bmatrix} P_x \\ P_y \\ P_z \end{bmatrix} = \begin{bmatrix} \alpha_{xx} & \alpha_{xy} & \alpha_{xz} \\ \alpha_{yx} & \alpha_{yy} & \alpha_{yz} \\ \alpha_{zx} & \alpha_{zy} & \alpha_{zz} \end{bmatrix} \begin{bmatrix} E_x \\ E_y \\ E_z \end{bmatrix} \tag{5.3}$$

Normally $\alpha_{ij} = \alpha_{ji}$, so there are six independent components in this tensor. In the

CO_2 example, for the Q_1 mode, the non-zero bond polarizability derivatives in the two C-O bonds are additive, that $\left(\frac{\partial \alpha_{xx}}{\partial Q_1}\right)_0 = \left(\frac{\partial \alpha_{yy}}{\partial Q_1}\right)_0 = \left(\frac{\partial \alpha_{zz}}{\partial Q_1}\right)_0$ and is non-zero. Thus, this mode is Raman active.

For the antisymmetric Q_2 mode, the non-zero bond dipole derivatives add up, making the mode IR active. Whereas, the bond polarizability derivatives cancel each other as $\left(\frac{\partial \alpha_{xx}}{\partial Q_2}\right)_0 = \left(\frac{\partial \alpha_{yy}}{\partial Q_2}\right)_0 = \left(\frac{\partial \alpha_{zz}}{\partial Q_2}\right)_0 = \left(\frac{\partial \alpha_{xy}}{\partial Q_2}\right)_0 = \left(\frac{\partial \alpha_{yz}}{\partial Q_2}\right)_0 = \left(\frac{\partial \alpha_{zx}}{\partial Q_2}\right)_0$. This vibration mode is therefore Raman inactive.

For the two bending modes, first of all, the bond dipole derivatives do not cancel each other, so they are IR active. However, the six polarizability derivatives are all zero, making these two modes Raman inactive.

However, the classical approach has its limitations as for example, it cannot be applied to molecular rotations. On the other hand, in the quantum mechanics treatment, perturbation theory is often used.[154] The ground state molecular wavefunction is perturbed to a new wavefunction describing the vibrational excited state and that the transition from state to state is the summation of perturbations applied.[154] In the quantum mechanical approach, the classical amplitude Q_k for molecular vibrations is replaced by a quantum mechanical amplitude and in contrast to the classical polarizability, the quantum mechanical representation includes the wave functions and energy levels.[151] The following equations shows the quantum mechanical treatment of the induced transition electric dipole moment.

$$\left(\tilde{\mathbf{p}}^{(1)}\right)_{fi} = \left\langle \Psi_f^{(1)} \left| \hat{\mathbf{p}} \right| \Psi_i^{(0)} \right\rangle + \left\langle \Psi_f^{(0)} \left| \hat{\mathbf{p}} \right| \Psi_i^{(i)} \right\rangle \tag{5.4}$$

where i and f defines initial and final state of the wavefunctions Ψ; and the indices of (0) and (1) represent the unperturbed and first-order perturbed time-dependent states of the wavefunctions respectively. The first-order induced transition electric dipole moment is complex in nature that

$$\left(\mathbf{p}^{(1)}\right)_{fi} = \left(\tilde{\mathbf{p}}^{(1)}\right)_{fi} + \left(\tilde{\mathbf{p}}^{(1)}\right)^*_{fi} \tag{5.5}$$

Eqn. 5.4 involves obtaining the relations between the unperturbed and perturbed time-dependent wavefunctions of the system and the interaction Hamiltonian is entirely electric dipole in nature. The assumption used for simplifications of this treatment is that the magnetic dipole and electric quadrupole terms in the Hamiltonian are not in play significantly.[151] For real wave functions, the ρ component (equivalent to the x in

xyz coordinate) of $\left(\mathbf{p}^{(1)}\right)_{fi}$ is expressed as:

$$\left(p_{\rho}^{(1)}\right)_{fi} = \frac{1}{2\hbar} \sum_{r \neq i,f} \left\{ \frac{\langle \psi_f | \hat{p}_\rho | \psi_r \rangle \langle \psi_r | \hat{p}_\sigma | \psi_i \rangle}{\omega_{ri} - \omega_1} + \frac{\langle \psi_f | \hat{p}_\rho | \psi_r \rangle \langle \psi_r | \hat{p}_\sigma | \psi_i \rangle}{\omega_{rf} + \omega_1} \right\} \tilde{E}_{\sigma 0} \exp\left(-i\omega_s t\right) + \text{complex conjugate} \tag{5.6}$$

where there are r states in the system, only the real wavefunctions are considered and ω_s is introduced as the scattered radiation frequency

$$\omega_s = \omega_1 - \omega_{fi} \tag{5.7}$$

Here the general transition polarizability α_{fi} is defined with components $(\alpha_{\rho\sigma})_{fi}$.

$$(\alpha_{\rho\sigma})_{fi} = \frac{1}{\hbar} \sum_{r \neq i,f} \left\{ \frac{\langle \psi_f | \hat{p}_\rho | \psi_r \rangle \langle \psi_r | \hat{p}_\sigma | \psi_i \rangle}{\omega_{ri} - \omega_1} + \frac{\langle \psi_f | \hat{p}_\rho | \psi_r \rangle \langle \psi_r | \hat{p}_\sigma | \psi_i \rangle}{\omega_{rf} + \omega_1} \right\} \tag{5.8}$$

Then using the real transition polarizability, Eqn. 5.6 can be re-written as:

$$\left(p_{\rho}^{(1)}\right)_{fi} = \frac{1}{2} (\alpha_{\rho\sigma})_{fi} \left\{ \tilde{E}_{\sigma 0} \left[\omega_1 \exp\left(-i\omega_s t\right)\right] + \tilde{E}^*_{\sigma 0} \left[\omega_1 \exp\left(i\omega_s t\right)\right] \right\} \tag{5.9}$$

The trigonometric representation (Eqn. 5.10) will be then similar to Eqn. 5.1.

$$\left(p_{\rho}^{(1)}\right)_{fi} = (\alpha_{\rho\sigma})_{fi} \tilde{E}_{\sigma 0} \omega_1 \cos \omega_s t \tag{5.10}$$

The selection rule for the Raman spectrum is determined by the integrals of the polarizability tensor components. For example, Eqn. 5.11 show the energy exchange as a result of the interaction between radiation absorbed or emitted and the molecule.

$$(\alpha_{\rho\rho})_{fi} = \int \Psi_i^* (Q_a) \, \alpha_{\rho\rho} \Psi_f (Q_a) \, dQ_a, \tag{5.11}$$

Q_a is the normal coordinate of the normal vibration, which defines the symmetry of the molecule. Eqn. 5.11 states that the selection rule is governed by the spatial geometric arrangement of the atoms in the molecule (Q_a). Therefore, in order for the the vibration to be Raman active, all the components in the integral in Eqn. 5.11, including the polarizability tensor and the wavefunctions, have to be belong to the

same symmetry species with the normal vibration coordinate of the molecule.

By understanding the symmetry elements of a molecule, one could obtain the symmetry selection rules for its Raman spectrum. It is straight-forward for a simple molecule like CO_2 in the above example. However, for molecules with more complex structure, it is complicated to infer the symmetry properties of the mode of vibrations, let alone the derivatives of bond dipole moment and polarizability. This is where Group theory, a mathematical procedure, become useful for predictions of symmetry properties of vibrational modes, dipole moment and polarizability derivatives of a molecule.

5.1.3 Point symmetry and Group theory

In crystallography, molecules are described in terms of various degrees of symmetry. The molecules can be conveniently classified mathematically into groups based on symmetry operations applied on the molecule. These molecules belong to a certain symmetry point groups if no change is observed after the symmetry operation is applied. There can be more than one symmetry operations applied to a molecule.

The Raman tensor in the quantum mechanical treatment is derived with components R_{ij}. Any changes in the $\alpha_{ij}(R_{ij})$ will result in Raman activity and its components is used to generate the irreducible representations of the molecular point group. These components can only be changed by molecular vibrations that also generate the same irreducible representations, meaning that they possess the same symmetry. The symmetry species of polarizability tensor components for all the point groups are well documented in various literatures.[151]

The following Table 5.1 illustrates a simple example of applying Group theory to obtain the vibrational modes of ammonia (NH_3), which is a member in the C_{3v} point group.[155] The C_{3v} point group has a rotational axis of order three with three vertical planes of symmetry on the rotational axis.[155] There are then six operations for C_{3v}. Each of the operation procedures are specified as a reducible matrix in the table in Cartesian displacement coordinates. Rotation of the molecule in terms of radians are designated by C_3. The superscript "2" is an indication of the number of operations performed and E is simply the rotation of zero degrees, that is the identity operation itself.[155] σ_v indicates the symmetry operation of reflection in the vertical plane at the rotation axis and there are three of them for C_{3v} as shown in the table.

Table 5.1: Table:Reducible and irreducible representations of C_{3v}

Operations		E	C_3	C_3^2	σ_v	σ_v'	σ_v"
Reducible		$\begin{bmatrix}1&0&0\\0&1&0\\0&0&1\end{bmatrix}$	$\begin{bmatrix}-\frac{1}{2}&-\frac{\sqrt{3}}{2}&0\\\frac{\sqrt{3}}{2}&-\frac{1}{2}&0\\0&0&1\end{bmatrix}$	$\begin{bmatrix}-\frac{1}{2}&\frac{\sqrt{3}}{2}&0\\-\frac{\sqrt{3}}{2}&-\frac{1}{2}&0\\0&0&1\end{bmatrix}$	$\begin{bmatrix}\frac{1}{2}&\frac{\sqrt{3}}{2}&0\\\frac{\sqrt{3}}{2}&-\frac{1}{2}&0\\0&0&1\end{bmatrix}$	$\begin{bmatrix}\frac{1}{2}&-\frac{\sqrt{3}}{2}&0\\-\frac{\sqrt{3}}{2}&-\frac{1}{2}&0\\0&0&1\end{bmatrix}$	$\begin{bmatrix}-1&0&0\\0&1&0\\0&0&1\end{bmatrix}$
Irreducible	Γ_1	(1)	(1)	(1)	(1)	(1)	(1)
	Γ_2	$\begin{bmatrix}1&0\\0&1\end{bmatrix}$	$\begin{bmatrix}-\frac{1}{2}&-\frac{\sqrt{3}}{2}\\\frac{\sqrt{3}}{2}&-\frac{1}{2}\end{bmatrix}$	$\begin{bmatrix}-\frac{1}{2}&\frac{\sqrt{3}}{2}\\-\frac{\sqrt{3}}{2}&-\frac{1}{2}\end{bmatrix}$	$\begin{bmatrix}\frac{1}{2}&\frac{\sqrt{3}}{2}\\\frac{\sqrt{3}}{2}&-\frac{1}{2}\end{bmatrix}$	$\begin{bmatrix}\frac{1}{2}&-\frac{\sqrt{3}}{2}\\-\frac{\sqrt{3}}{2}&-\frac{1}{2}\end{bmatrix}$	$\begin{bmatrix}-1&0\\0&1\end{bmatrix}$
Characters	Γ	3	0	0	1	1	1
	Γ_1	1	1	1	1	1	1
	Γ_2	2	-1	-1	0	0	0

The reducible representations are block-factored by similarity transformation to irreducible representations that can no longer be reduced. Γ with the subscripts refer to the vibration types which corresponds to the irreducible representations. Now Γ_1 only affects the z-coordinate and conserves the x and y; whereas the Γ_2 only affects the x and y-coordinates. From the submatrices in the irreducible representations, the characters can be extracted from the traces and an even simpler character table for the point group can be deduced with the basis in Table, where the operation symmetries are grouped to the same class. The last two columns indicate the basis chosen like the one-dimensional translational basis T_x, T_y, T_z and rotational basis R_x,R_y,R_z; and two-dimensional basis xx, yy, zz, xy, yz and xz. The vibration is IR-active if it belongs to a symmetry species that contains T components. It is Raman active if it has symmetry components that contains the α tensor component.

In the table, "1" means there is no change for symmetry class, "-1" means it becomes opposite when the operation is applied and "0" means the basis are moved. It is also commonly found in chemistry and spectroscopy character tables to have Mulliken symbols instead of the Γ. In such a case, Γ_1 will be A_1 (totally symmetric); Γ_2 will be E (double degenerate) and Γ_3 will be A_2 (anti-symmetric to the vertical plane of reflection).[152] From the character table, two A_1 vibrations are Raman-active and two E vibrations modes being Raman-active. Since the E vibrations are double degenerate, there are actually two vibration modes in each. Therefore, all six normal vibrations (degree of freedom for non-linear molecule is 3N-6, where N is the number of atoms) of the ammonia molecule are Raman-active.

Group theory is frequently used by spectroscopists to evaluate the normal modes in a molecule and predict the IR; Raman; and hyper-Raman activity of each mode.[154] There are also crystallographic servers readily available online for Group theory applications

Table 5.2: Character table for C3v

C_{3v}	E	$2C_3$	$3\sigma_v$	IR activity	Raman activity
Γ_1	1	1	1	T_z	$\alpha_{xx}+\alpha_{yy}, \alpha_{zz}$
Γ_2	2	-1	0	(T_x,T_y) (R_x, R_y)	$(\alpha_{xx}-\alpha_{yy}, \alpha_{zz})$ $(\alpha_{yz}, \alpha_{xz})$
Γ_3	1	1	-1	R_z	

on IR, Raman and hyper Raman modes calculations.[156–159]

5.2 Extended Raman techniques and its Effects

Despite the versatility of Raman spectroscopy, due to the low inherent sensitivity of Raman scattering, this method often suffers from low scattering cross sections when applied to ultra-thin films and highly reflective materials.[160–162] Different Raman spectroscopy techniques have been developed to tackle those difficult samples, one of which uses the surface plasmonic resonance (SPR) to give rise to an extraordinary enhancement of Raman scattering when the molecule in question is located near the proximity of a plasmonic moiety.[162] This technique is called the Surface-enhanced Raman spectroscopy (SERS) first developed by Fleischmann et al.[163] As more advanced technique was developed after SERS, rather than using the metal coated substrate to generate SPR, a metal-coated AFM tip is used for an even more localized SPR effect. Figure 5.2 a-d shows the different set-ups of Raman techniques with Figure 5.2 a being the upright normal Raman. SERS in Figure 5.2 b is similar to a normal Raman set up (Figure 5.2 a) with the addition of a metal layer in between the sample and the substrate. For conventional TERS (upright), the set up would be having an AFM probe above the sample in close proximity as in Figure 5.2 c. Additionally, for the set up of IERS (see Figure 5.2 d), it requires a smooth back-coating under the substrate for reflection to achieve interference. All these different arrangements from normal Raman would result in an enhanced Raman spectrum even with the same sample.

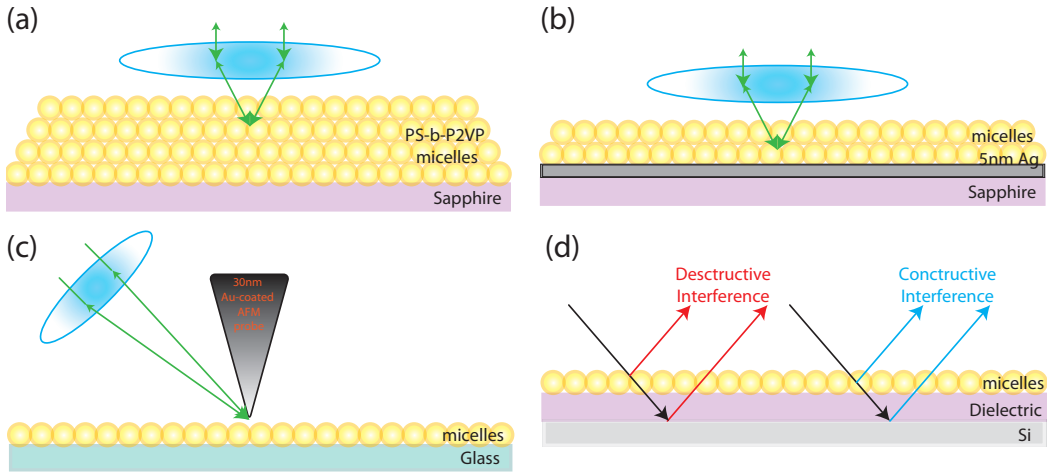

Figure 5.2: Configurations of various Raman set-ups for (a) Inverted TERS of monolayer micelles; (b) Inverted normal Raman of monolayer micelles; (c) SERS of multilayer micelles on 5nm-Ag-coated Sapphire; (d) Normal Raman of drop-casted thick micelles layers on KBr and (e) Normal Raman of bulk PS-b-P2VP flake on Cu tape on glass. (f) Raman spectra of micelles of all techniques in the schematic.

5.2.1 Surface-enhanced Raman scattering (SERS)

SERS is a technique that exploits the surface plasmons generated by the thin metallic coating on the substrate. The plasmonic coating is a prerequisite for the set-up of SERS as seen in Figure 5.2 b.

The enhancement comes from the pronounced local electromagnetic (EM) field at the metal surface with nanostructure features. As the incident radiation hits the metal substrate, the conduction band electrons are excited and generates an SPR, such that the metal nanostructure becomes polarized. The SPR then increases the EM field at the interface with the material of interest significantly from the incident applied field.[152]

Conventionally, noble-metal nanostructures which are free from interferences from interband transitions, such as silver films have been used as the plasmonic layer to provide enhancement.[152,164] Recently, indium tin oxide (ITO) is proved to be possible for SERS.[164,165]

In some case, the polarizability (α) can also be enhanced during the process due to bond formation and charge transfer between the adsorbate species and the metal substrate.[152,163,166] SERS has demonstrated enormous enhancement of (10^5-10^6) on the scattering intensity from the adsorbed species compared to the non-adsorbed

species.[152,167] (See figure 5.3)

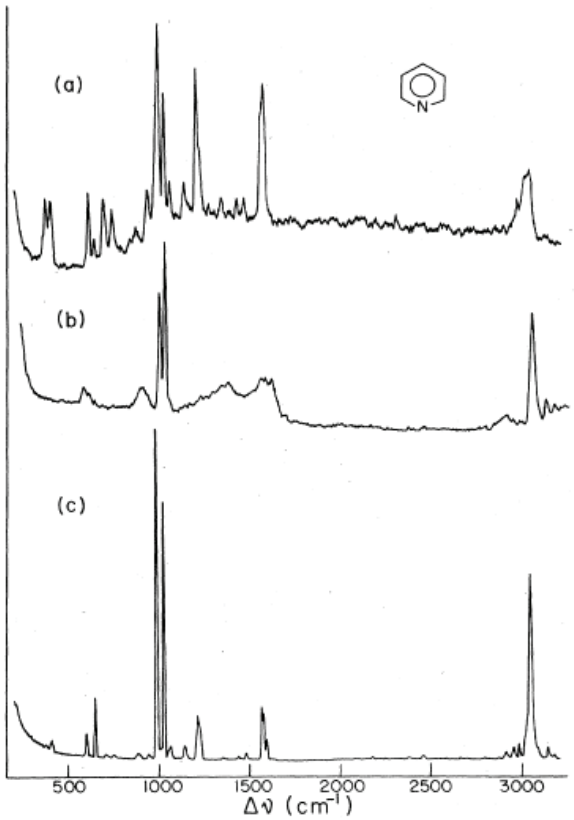

Figure 5.3: Enhanced Raman spectrum of pyridine by SERS of pyridine on (a) Ag film and (b) Ag colloid. (c) Ordinary Raman spectrum of pyridine solution. With permission from reference [167].

The chemical or physical interaction of the plasmonic layer with the sample can be a drawback for characterization as it can be a permanent effect and will be a problem for preserving sample integrity.

5.2.2 Tip-enhanced Raman Scattering (TERS)

Similar to SERS, tip-enhanced raman spectroscopy (TERS) is a variation of SPR exploitation with the only difference that the nanostructured metal substrate is replaced by a sharp metal tip of an atomic force microscopy (AFM) probe.[168,169] It is in fact a hyphenated technique of Raman spectroscopy with the addition of AFM. The AFM tip employed in this TERS study was coated with 30nm of Au. This method is superior to SERS because now there is an exclusive active site from the AFM tip, which is

coated with noble-metal and it ensures a constant field enhancement that is otherwise impossible for SERS.[168] This special instrumentation, therefore, allows a capability of spatially resolved quantitative Raman measurement. Figure 5.4 shows an example of 4,4-bipyridine Raman spectrum enhanced by TERS with Au-tip.[170]

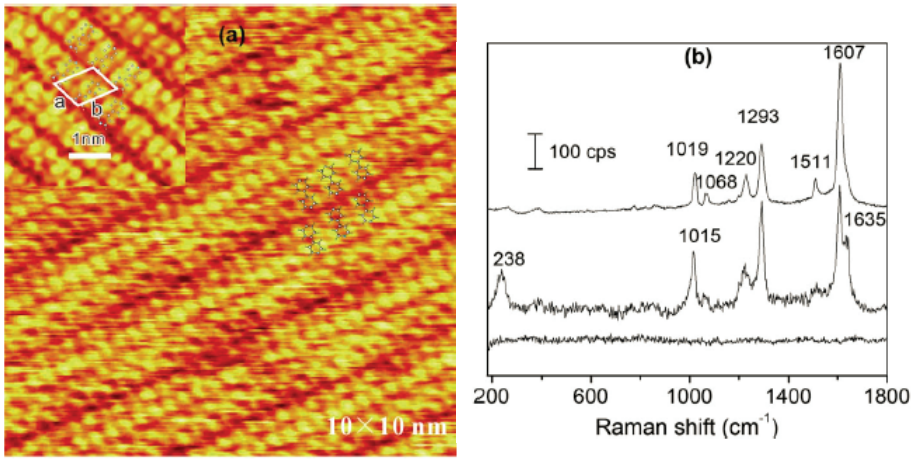

Figure 5.4: 4,4-bipyridine layer on Au (111). (a) STM image and (b) (top) SERS spectrum, TERS spectrum with Au tip engaged(middle) and Au tip retracted (bottom). Reprinted from Appl. Phys. Lett. 91, 101105 (2007) (Reference [170]), with the permission of AIP Publishing.

Several near- and far-field optical effects are in play which result in enhanced Raman response. Firstly, due to the fine tip structure, there is an electrostatic lightning rod effect which results in a highly confined electric field at the apex of AFM tip where the free electrons of the metal probe gathers. The evanescent standing wave from the localized surface plasmons of the metal nanoparticles also intensify the localized electric field at the tip apex. Theoretically, a spatial resolution as high as 2.2nm can be achieved from the near-field effect of this technique, far beyond the diffraction limit of light.[168,171] When light scatter from the non-spherical objects such as the tip apex, it will generally be partially depolarized into in-plane (parallel with respect to sample plane or so-called s-polarization) and out-of-plane (perpendicular to sample plane or so-called p-polarization) polarizations.[172] Guccuardi et al. quantified the degrees and intensity of depolarization of light scattered from different parts of AFM probes.[172] It was found that light scattered from the AFM tip apex depolarizes most when compared to other parts of the probe such as the shaft and cantilever.[172] It is a far-field scattering event of which the depolarization should still be observable even when the AFM tip is retracted from the sample surface as long as the laser is focused

at the tip. In such a case, it is similar to the polarized Raman spectroscopy that some Raman-active vibrational modes would be selectively enhanced.

The near-field depolarization process due to the tip apex is found to be much more complicated than the far-field one which can be understood with a full classical theory.[171] It would be inaccurate to approach the near-field scattering process as a downscaled version of the lightning rod effect; nor would it be enough to take the molecular and tip polarizability, and tip apex electric field gradient into considerations.[171] The nature of the near-field scattering process instead, has to be meticulously treated with a quantum mechanical approach which involves coupling of photons and plasmons. As the metal nanoparticle coating on the AFM tip takes part in the scattering process, it generates surface plasmon polaritons (SPPs) and because of the subnanometer interaction region well-below the excitation wavelength, the electromagnetic excitation can no longer be treated as a wave.[171] Poliani et al. proposed a detailed Feynman diagram describing the energy interaction between the photon-plasmon and polariton of this near-field scattering process of TERS. Consequently, there is a breakdown of the selection rules for TERS compared to the classical normal Raman scattering.

Generally for TERS, a number of light-scattering phenomena due to the tip are involved, which some can be non-linear optical effect such as the second-harmonic generation (SHG), the Hyper Raman effect and the stimulated Raman Effect.[151,152,168] In such cases, the conventional selection rules can be lifted under the influence of strong field from the tip. This is also due to the polarizability gradient attributed to the varying applied electric field along the vibrational mode. In such a case, non-active Raman modes can be observed.[151,168]

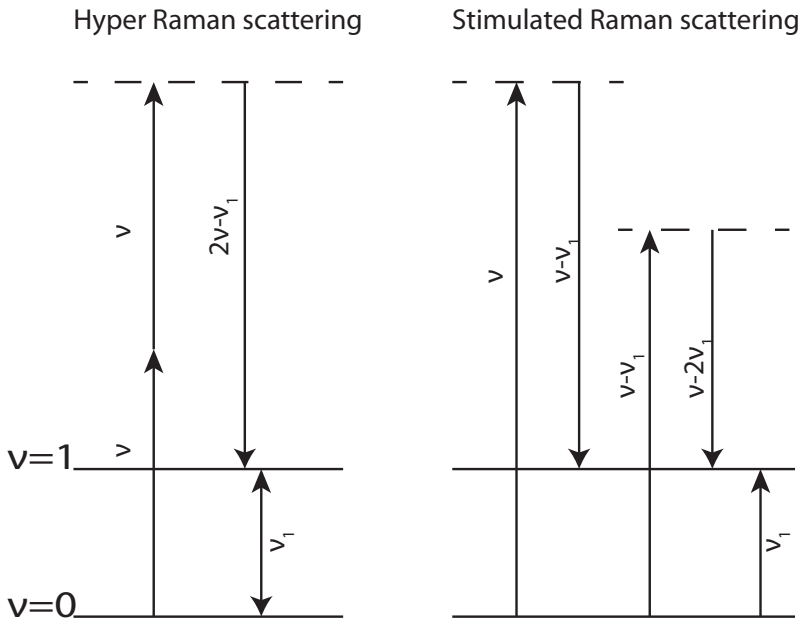

Figure 5.5: Non-linear Raman scattering mechanisms of Hyper Raman scattering and stimulated Raman scattering

Consider an irradiance deflected from the TERS tip apex being scattered on a sample. When a sample is illuminated with a large irradiance radiation of frequency ν and the scattered radiation consists of frequencies doubling the original excitation frequency to 2ν, it is called the hyper Rayleigh scattering effect.[151,152] If this scattering process is inelastic such that the radiation becomes $2\nu \pm \nu_{\mathrm{i}}$, it is considered as a hyper Raman scattering effect.[151,152] Figure 5.5 describes the energy transfer of a hyper Raman scattering process. Using a photon description of electromagnetic radiation, before the interaction, there are n photons of energy $\hbar\nu$. During the interaction of the molecule with the radiation, a successive annihilation of two photons was created with the energy of $2\hbar\nu$. The radiation then involves (n-2) photons with $\hbar\nu$ and one photon of $2\hbar\nu$. This phenomenon is experimentally difficult to observe as only a factor of 10^{-12} of radiation is converted to $2\nu \pm \nu_{\mathrm{i}}$.[152] The intensity of the hyper Raman scattering is proportional to the square of the incident irradiance, however, over a certain limit of irradiance, the stimulated Raman effect will take over.[151,152] Similarly, SHG is a process when a signal of twice the frequency of the excitation source is emitted from the oscillating dipole of the tip; it is initiated by the strong parallel E-field component depolarized at the apex. The sequential scattering process would be the same as the hyper Raman scattering.[168]

A distinct advantage of SHG and hyper Raman effect over normal Raman is that they have different selection rules because of the non-linear scattering process. In fact, a fuller expression for the induced dipole in Eqn. 5.1 should be written as a sum of a series of time-dependent induced electric dipole moment vectors as follows:[151]

$$P = p^{(1)} + p^{(2)} + p^{(3)} + \cdots = \alpha E + \frac{1}{2}\beta E^2 + \frac{1}{6}\gamma E^3 + \cdots \tag{5.12}$$

where β is the 1st-hyper-polarizability and γ is the 2nd-hyper-polarizability. P is the induced dipole moment, $p^{(1)}$ is linear in E, and $p^{(2)}$ and $p^{(3)}$ are non-linear in E. The 2nd and 3rd terms in Eqn. 5.12 are usually ignored in normal Raman with lower incident electric field because $\alpha >> \beta >> \gamma$. The typical orders of magnitude for α is $10^{-40}CV^{-1}m^2$; β is $10^{-50}CV^{-2}m^3$ and γ is $10^{-61}CV^{-3}m^4$.[151] As a result, some vibrations that are not IR or Raman-active become hyper Raman-active. It is noted that the hyper Raman spectrum contains all the modes in an IR spectrum.[152]

Stimulated Raman effect can also be resulted in TERS if the resultant laser electric field on the sample exceeds 10^9 Vcm^{-1}.[152] Under the strong irradiance, the hyper Raman effect will be superseded by the stimulated Raman effect. The energy transfer of the stimulated Raman scattering effect is illustrated in Figure 5.5. During the energy exchange between the photon and phonons, 50% of the incident radiation is converted to the first Stokes line ($\nu - \nu_1$) as only one Raman-active normal mode (ν_1) is strongly enhanced.[152] This intense first Stokes line then acts as a source for the second Stokes line ($\nu - 2\nu_1$), and this "energy recycling" process can keep going for more Stokes lines as long as it exceeds the threshold.[152,173] Therefore, more higher-order stimulated Stokes lines will be found in the Raman spectrum with frequency shifts of exactly twice, thrice, four and so forth more times of the first line. The intensities of these higher-order stimulated Stokes lines fall off progressively. However, this effect provides little value to characterizing the sample as it only provides one most intense vibrational frequency together with its multiples.[173] The practical importance of this effect lies in the intense coherent light of shifted frequency obtained.

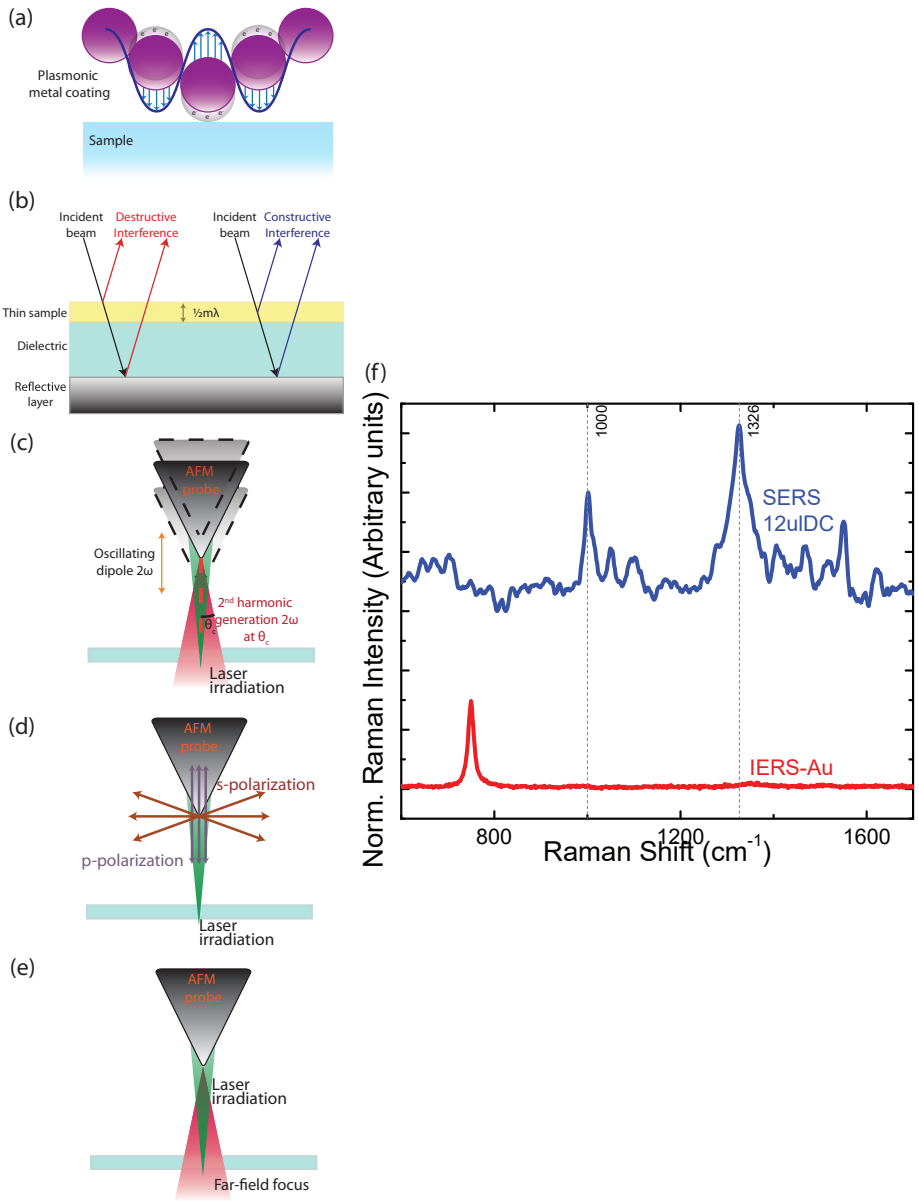

Figure 5.6: Possible Raman enhancing mechanisms of TERS. (a) Enhancement of localized electric field due to surface plasmon generation from metal tip coating. (b) Interference-enhanced Raman scattering due to the reflective back coating of sample substrate. (c) 2nd harmonic generation effect or hyper Raman effect. (d) Depolarization of laser due to the tip. (e) Far-field Focusing enhancement due to tip. (f) Raman spectra of micelles by SERS (blue), polarized Raman, and IERS (red).

5.2.3 Interference enhanced Raman scattering (IERS)

Substrates also play a heavy role in enhancing the Raman signals with its intrinsic optical properties. IERS employs a simple optical phenomenon and yet demonstrates a powerful signal enhancement of up to theoretically 30 times.[165] It was found that if the sample thickness is comparable to the incident excitation wavelength, the incident and scattered ray will exhibit self-interference effects. The set-up of IERS is illustrated in Figure 5.6 b, where a thin dielectric is used as the substrate for the sample and the bottom of the substrate should be reflective. In this case, it can be coated with reflective metal or the dielectric can be simply supported by a smooth reflective substrate such as a Si wafer.[165] Theoretically, the combined thickness of the sample and the dielectric substrate should be around $\frac{(2m+1)\lambda}{4}$.[165] For n 514nm excitation laser, the combined thickness for IERS purpose would then be 400nm. The thickness of the dielectric layer will result in π-phase shifts as the incident ray is reflected from the bottom with higher refractive index, where destructive interference occurs on the reflected component of the incident ray while constructive interference occurs for the scattered ray.[174,175] The total modification factor (F(d,λ_1, λ_2))of IERS is the combination of the modification (f_1(d,λ_1)) due to the self-interference of the incident light (λ_1) and modification (f_2(d,λ_2)) from the self-interference of scattered and emitted light (λ_2).[165]

$$F(d,\lambda_1,\lambda_2) = f_1(d,\lambda_1)\cdot f_2(d,\lambda_2) \tag{5.13}$$

$$f_1(d,\lambda_1) = 1 - R = 1 - |r_{123}|^2 = 1 - \left|\frac{r_{12}+r_{23}e^{2i\beta}}{1+r_{12}r_{23}e^{2i\beta}}\right|^2 \tag{5.14}$$

$$f_2(d,\lambda_2) = \frac{1}{1+a}\left|1+\sqrt{a}\left(\frac{2\sqrt{N_1N_2}}{N_1+N_2}\cdot\frac{r_{23}e^{2i\beta}}{r_{12}r_{23}e^{2i\beta}}\right)\right|^2 \tag{5.15}$$

where d is the thickness of the dielectric in Figure 5.6 b; a is the intensity ratio of the forward to the backward scattering; $\beta = 2\pi\frac{d}{\lambda}N_2 cos\theta_2$, where N_2 is the refractive index of the dielectric medium and θ_2 is the reflected angle at the interface of dielectric and reflector; r_{jk} is the reflectance at interface of phase j and k, $r_{jk} = \frac{N_j cos\theta_j - N_k cos\theta_k}{N_j cos\theta_j + N_k cos\theta_k}$.

Yang et al. evaluated this effect with aqueous rhodamine 6G (R6 G) solution on thin sputtered ITO on Si and showed the thickness-dependence of the enhancement.[165] Moreover, as the top layer of noble-metal is thin enough to be optically transparent, the clever optical design of IERS can be paired with the benefits from SERS for co-enhancement effect.[164]

5.3 Raman details of various materials

5.3.1 Graphene

Raman spectroscopy is widely used to determine the quality, number of layers, edge disorder, doping and strain effect of graphene.[135,176–182] The Raman spectrum of a graphene with defects is shown in Figure 5.7 a. To understand the Raman spectrum of graphene, one has to start with the atomic structure of the sp^2 hybridized carbon network.

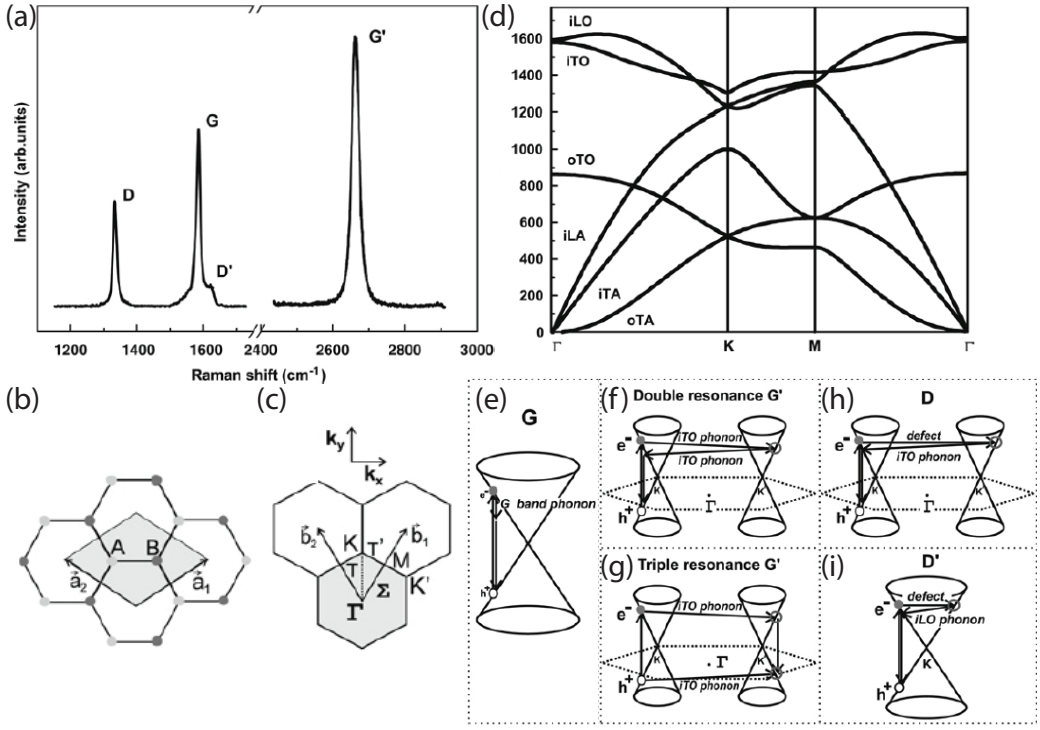

Figure 5.7: (a) Raman spectrum of a graphene with defect. (b) Unit cell of the monolayer graphene in real space from top view, showing inequivalent atoms A and B and unit vectors $\mathbf{a}_1$ and $\mathbf{a}_2$. (c) Reciprocal lattice of the 1st Brillouin zone with symmetry points of the monolayer graphene. (d) The phonon dispersion relation of graphene. Raman scattering process of (e) 1st-order G-band phonon; (f) double resonance G' (or 2D)-band and (g) triple resonance G'-band. Resonance points are indicated as open circles. (h) One phonon 2nd-order double resonant of intervalley D-band phonon in the Brillouin zone and (i) intravalley D'-band phonon. Reprinted from Physics Reports,473, L.M. Malard et al., Raman spectroscopy in graphene, 51-87, Copyright 2018, with permission from Elsevier."

There are two carbon atoms in the unit cell of graphene as illustrated in Figure 5.7 b and the reciprocal lattice of a unit cell is shown in Figure 5.7 c. As there are two atoms in the unit cell, there are six phonon dispersion bands in k-space in Figure 5.7 d. Three of the bands are optical modes (O) and the other three are acoustic modes (A).

The branches in each set of O and A modes, have different phonon vibration directions to the adjacent carbon atoms A and B. The longitudinal vibrating (L) modes are those where the carbon atoms are vibrating in line with each other in the same plane (i), so two of the bands are assigned to iLA and iLO. For atoms vibrating perpendicular to each other in the transverse mode (T), they can go in-plane or out-of plane (o). Therefore, the remaining four modes are designated as oTA, iTA, oTO and iTO. The in-plane optical modes iLO and iTO are degenerate at the zone centre (Γ) and they are Raman active modes, determined by group theory analysis of the E_{2g} symmetry.[183] They represent the A and B sub-lattices pressing against each other, which contribute to the G band at 1576cm^{-1} in the Raman spectrum (Figure 5.7 a).[182,184,185] This band is a 1st-order Raman scattering progress that involves only the phonon at Γ.[186] The process is illustrated in Figure 5.7 e where there is a strong electron-hole coupling upon photon excitation near the Γ circle.[183]

The other Raman active mode in graphene comes from a double resonance (DR) process of two iTO phonons near **K** points at the corner of the reciprocal lattice. It is named as the 2D or G' band centered at around 2680cm^{-1}.[183,187] For the ease of discussion, 2D is used for naming this band in the chapter. As seen in Figure 5.7 f, upon excitation of a photon, an electron with **k** is scattered inelastically to an iTO phonon by q wave-vector, interacts with another iTO phonon at the proximity of **K**' Dirac circle and finally scattered back to the **k** to recombine with a hole. This is an intervalley process between the Dirac circles at **K** and **K**' points in the first Brillouin zone.[183] This band can also be produced by a triple resonance (TR) process in Figure 5.7 g, such that the hole will also be scattered to an iTO phonon, similar to the DR process and finally recombine with the electron at **k**. The TR process is one possible explanation for the observed larger intensity of 2D compared to the G band in pristine monolayer graphene.[183] The 2D band can evolve into multiple peaks as the number of graphene layers increases but for the case of monolayer graphene, it remains as a single peak as seen in Figure 5.7 a.[188] The intensity ratio of G to 2D band can be used to determine the number of layers of graphene.[177,189]

It is inevitable for defects to be present in the monolayer graphene. One kind

of defects is from the graphene edges; another kind of defect is the structural defect such that there is a vacancy of C atom in the Brillouin zone.[141,180,190] The D band located at 1340cm^{-1} in Figure 5.7 a results from a one phonon DR process where one of the iTO phonons involved for the 2D band is now replaced by an elastic scattering effect with a defect (See Figure 5.7 h).[141,180,191] This defect band can be used to reveal the crystallinity of graphene by comparing the band intensities, ID/IG , which varies inversely to the size of the crystalline graphene grain.[188,192]

As seen in Figure 5.7 a, there is one more band located at 1620cm^{-1} at the shoulder of the G band, namely the D' band. It is also a defect-activated band. It has a different scattering mechanism from the DR process in the D band mainly due to the fact that it is an intra-valley scattering process inside the same **K** Dirac cone as seen in Figure 5.7 i.[177] The D' band, however, is less likely to be observed in general because it is a weak band. For a pure pristine monolayer graphene, only the G and 2D bands will be present.

5.3.2 Ionic compounds

5.3.2.1 Fe_xO_y

The crystal structure of iron oxide nanoparticles has a strong impact on their magnetic properties as the arrangement of Fe and O atoms controls the arrangement of magnetic dipoles. Each of the polymorphs of iron oxide has a different structure and thus diverse magnetic properties.[193] For iron(III) oxide, the α-Fe_2O_3 with corundum structure ($R\bar{3}c$) and the γ-Fe_2O_3 with an inverse spinel structure ($P4_132$) are present in nature, while other polymorphs: β-Fe_2O_3 with bixbyite structure ($Ia\bar{3}$) and ϵ-Fe_2O_3 with orthorhombic structure ($Pna2_1$) are rare phases only produced in the laboratory.[193,194] The other naturally occurring phase, iron(II,III) oxide (Fe_3O_4), also possesses a similar inverse spinel structure as γ-Fe_2O_3. Among these phases, only γ-Fe_2O_3 and Fe_3O_4 possess ferrimagnetism with relatively high accessibility at room temperature.[195]

As γ-Fe_2O_3 and Fe_3O_4 share a similar inverse spinel structure with only around 1% difference in lattice constant,[195] it is hard to distinguish the exact phase between the γ-Fe_2O_3 and Fe_3O_4 with electron diffraction or x-ray diffraction methods. In addition, both γ-Fe_2O_3 and Fe_3O_4 are ferrimagneitc in nature which could yield a similar saturation magnetization (M_s) and magnetization applied magnetic field (M-H) curve.[196] As a consequence, superconducting quantum interference device (SQUID)

measurements are not sufficient to distinguish between them either.

Given the different crystal structures of the Fe_xO_y polymorphs, the vibrational modes and Raman spectra of α , β , ϵ and γ of Fe_2O_3, Fe_3O_4 and $FeCl_3$ have been observed to be distinct from each other.[197–203] Using group theory, the active Raman modes of a system can be predicted. The γ-Fe_2O_3 with the $P4_132$ space group has five (A_{1g}, E_{1g} and 3 T_{2g}), mathematically describing their atomic vibrations against their rotational principle axis and inverse structures. Though γ-Fe_2O_3 and Fe_3O_4 belong to the same space group, the observed Raman phonons at similar wavenumber have a different atomic origin, making them easily distinguishable.[196,198] This provides a convenient way to differentiate between γ-Fe_2O_3 and Fe_3O_4.

Raman can as well readily determine the purity of the crystallographic phase in the particles under various conditions, as α-Fe_2O_3 with $R\bar{3}c$ space symmetry possesses seven Raman active modes ($2A_{1g}$, $5E_g$). Raman is also capable of differentiating the hydrogenated $FeCl_3$ species[202,203] and peaks shifting induced by laser illumination for α-Fe_2O_3.[193] Table 5.3 summarized the characteristic peaks for several phases of iron oxide and $FeCl_3$.

Table 5.3: Table of expected Raman peaks and assignments for $FeCl_3$ and several phases of iron oxide

$FeCl_3$[203–206]		α-Fe_2O_3[207]		γ-Fe_2O_3[208]		Fe_3O_4[209]	
Peak (cm^{-1})	Assignment	Peak (cm^{-1})	Assignment	peak (cm^{-1})	Assignment	Peak (cm^{-1})	Assignment
282	A_{1g}	225	A_{1g}	365	T_{2g}	301	T_{2g}
330	A_{1g}	247	E_g	511	E_g	533	T_{2g}
		293	E_g	700	A_{1g}	663	A_{1g}
		412	E_g				
		498	A_{1g}				
		613	E_g				

5.3.3 Polymer

5.3.3.1 Micelles

Polymeric reverse micelles are formed by poly(styrene-b-2-vinyl pyridine) (PS-b-P2VP) diblock copolymer dissolved in non-polar solvent such as toluene and o-xylene above the critical micelles concentration.[74] Figure 5.8 c shows the molecular structure of a PS-b-P2VP and the structure of a reverse micelle.

The diblock copolymer consists of a polystyrene (PS) backbone, a phenyl group and a pyridine (VP) group. When it comes to complex molecules like PS and P2VP

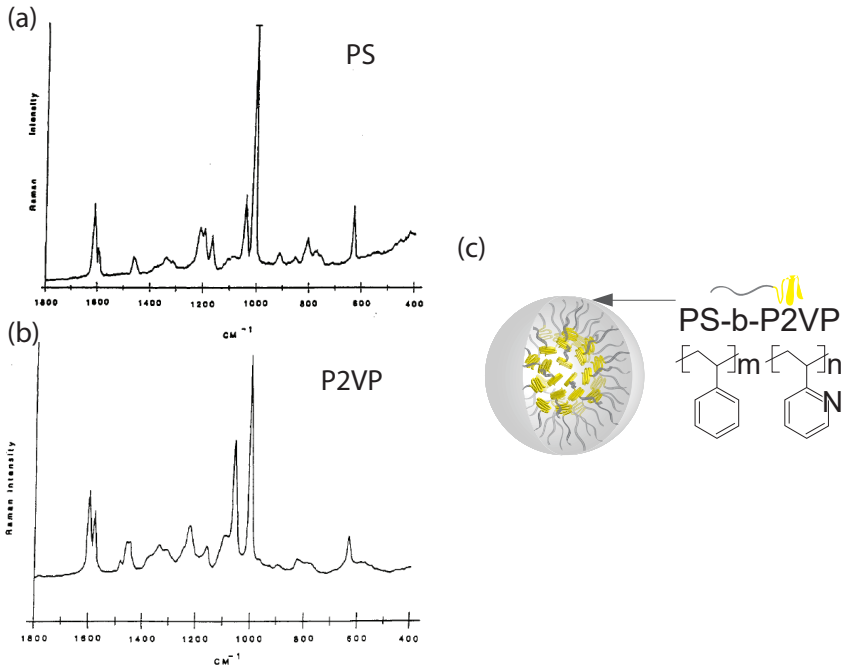

Figure 5.8: Normal Raman spectra of (a) polystyrene only and (b) poly(2-vinyl pyridine). Reprinted (adapted) with permission from Macromolecules 1993, 26, 15, 3953-3959. Copyright (2018) American Chemical Society. (c) Schematic of a poly(styrene-b-2-vinyl pyridine) diblock copolymer micelle.

components in the diblock copolymer micelle, numerous scattering mechanisms are possible, making the use of Group theory inevitable to compute the Raman-active modes. For instance, the point group of the isotactic polystyrene is R3c, with a= 21.9 Å and c= 6.65Å.[210–212] One could input the crystallographic information to the Bilbao Server and generate the expected Raman, IR and hyper-Raman modes of it. The experimental Raman spectra of PS and poly(2-vinyl pyridine) (P2VP) is presented separately in Fig. 5.8 a and b, showing all the normal Raman active modes.

As the molecules possess structural similarities, the Raman spectra of PS and P2VP share some very common features. As the polymer backbone is common in both group, modes such as the stretching mode at 900cm^{-1} for PS and 912cm^{-1} for P2VP is present in both cases.[166,213] Twisting modes of the backbone at 1330cm^{-1} and the methylene deformation at 1456cm^{-1} are also observed in both cases.[166,213] Some more prominent bands are shifted slightly between the two spectra due to the ring structure difference between benzene and VP. For instance, the 1012cm^{-1} totally symmetric ring breathing mode $\nu(1)$ (assigned with the Wilson's numbering system) in PS is shifted

to 1005cm^{-1} in P2VP;[166,213] another ring stretching mode $\nu(8a)$ at 1612cm^{-1} in PS is shifted to 1602cm^{-1} in P2VP.[166,213] A more obvious band difference is the mode $\nu(18a)$ at 1040cm^{-1} in PS and mode $\nu(18b)$ at 1064cm^{-1} in P2VP, they are both in-plane CH bending modes.[166,213] The $\nu(1)$ mode for is the strongest mode, so it is in general very distinctive in a pure micelles spectrum. However, in some cases, when the micelle is loaded with salts of transitional metal such as Fe, Pb, Zn and etc., the 2VP in the inner core of the micelle will be coordinated with the metal ion and cause suppression of the symmetric breathing mode.[153,214,215] The relatively weak pyridine ring stretching mode of $\nu(8b)$ will be enhanced because of the complexation of 2VP to the metal ions (See Chapter 10).[153,215]

One of the polymers in the study reported by Hong et al. has the polymer ratio of PS: P2VP as 152:15.[213] The Raman spectrum of this diblock copolymer reported is much more dominated by the PS feature (See Figure 5.9 b).[213] The reason for the Raman spectrum to have a higher PS character is explained by Boerio et al. as due to the extremely low chain length ratio of P2VP compared to that of PS.[166] Therefore, considering the likelihood of Raman scattering events in the polymer, the PS Raman spectrum should have a much larger component in the resultant spectrum. This also implies that for diblock copolymer with less PS ratio may have a P2VP feature as a function of the chain length ratio but in reality, the ratio has to be contrasting enough for it to be significant in the spectrum.

Although the diblock copolymers selected for the RMD of different nanoparticles have different polymer ratio of PS: P2VP, they are not as extreme as the case in Hong's study. As can be seen in Fig. 5.9 a, which is the Raman spectra of a PS-b-P2VP diblock copolymer of equal block length ratio, the Raman spectrum does not look substantially different than the spectrum in Fig. 5.9 b. Therefore, the reference spectrum from Hong's study is general applicable to the diblock copolymers in the RMD study.

Fig. 5.9 c shows the spectrum the same diblock copolymer in Fig. 5.9 a from an extended Raman technique called the Surface-enhanced Raman Spectroscopy (SERS) which theory is covered in Chapter 5.2.1.

Essentially, due to the adsorption of polymer onto the silver surface, the extended Raman technique SERS yields a different spectrum of micelles from the normal Raman. Some of the modes are shifted and some are enhanced. For example, since P2VP interacts with the silver surface through the pyridine nitrogen, the symmetric

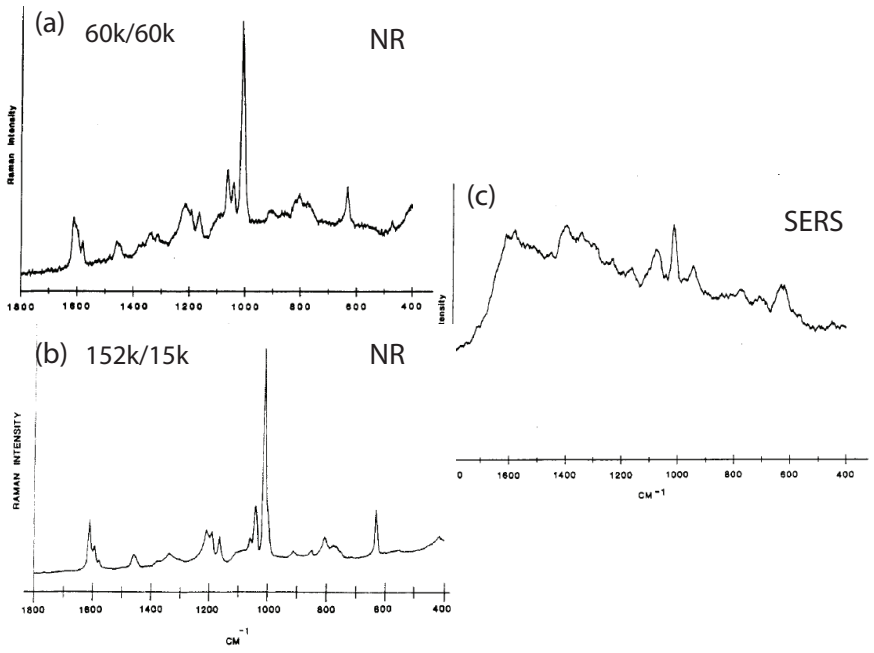

Figure 5.9: Comparison of Raman spectra of poly(styrene-b-2-vinyl pyridine) diblock copolymer with (a) Normal Raman (NR) on 60K/60K molecular weight of each block, (b) NR on 152K/15K molecular weight of each block and (c) Surface-enhanced Raman Spectroscopy (SERS) on 60K/60K molecular weight of each block. Reprinted (adapted) with permission from Macromolecules 1991, 24, 9, 2538-2545. Copyright (2018) American Chemical Society.

breathing mode normally observed at 1005 cm^{-1} in normal Raman of P2VP was shifted significantly to 1015 cm^{-1} in SERS and the CH bending mode of P2VP was shifted from 1064 cm^{-1} to 1073 cm^{-1} in SERS.

The modes of the PS-b-P2VP diblock copolymer from both normal Raman and SERS and assignments are summarized Table 5.4.[166,213]

Table 5.4: Expected Raman modes of PS, P2VP and PS-b-P2VP diblock copolymer[166,213]

PS, cm^{-1}		P2VP, cm^{-1}		PS-b-P2VP, cm^{-1}		Assignment	Mode description
NR	SERS	NR	SERS	NR	SERS		
633	636	631	629	633		$\nu(6b)$	In-plane bending of the ring
806		828	829	806		$\nu(12)$	CC Stretching between ring and backbone
852				852		$\nu(10a)$	CH out-of-plane bending
		900		900		$\nu(CC)$	Backbone stretching
912				912		$\nu(17b)$	CH out-of-plane bending
1012	1015	1005	1015	1005; 1012	1015	$\nu(1)$	Symmetric ring breathing
1040	1041			1040	1041	$\nu(18a)$	CH in-plane bending
		1064	1073	1064	1073	$\nu(18b)$	CH in-plane bending
1170	1172	1160	1161	1160; 1170	1161	$\nu(15)$	CH in-plane bending
1196				1196		$\nu(9a)$	CH in-bending
1210		1224	1227	1224		$\nu(13)$	CC Stretching between ring and backbone
1330		1335	1336	1330; 1335	1336	$\gamma(CH_2)$	Methylene twisting
		1443				$\nu(19b)$	Pyridine ring stretching
1458	1461	1456	1458	1456		$\sigma(CH_2)$	Methylene deformation
1596		1583	1585	1583	1585	$\nu(8b)$	Pyridine ring stretching
1612	1615	1602	1603	1602		$\nu(8a)$	Ring stretching

5.3.3.2 Useful substrates

Substrates play an important role in obtaining reliable Raman spectrum. Substrates with heavy background Raman spectrum should be avoided as much as possible. For example Si, one that is particularly used for calibration purpose of Raman, has an immense peak at 520 cm^{-1} from the zone centre phonons.[216] Any sample on Si that has any features near the Si peak would be shielded and become unresolvable.

Another problematic case is the Cu substrate which the CVD graphene grows on. Cu fluoresces under the 514 nm excitation laser and forms a wide broad band that sometimes some weaker modes of the sample will be impeded.[217] The only way to avoid the intrinsic fluorescent background in this case would be to pick a wavelength that does not satisfy the resonant conditions. For Cu, a 488 nm laser would suffice to eliminate the fluorescence.

Careful selection of substrates should also be considered to avoid chemisorption of sample with substrates.

The following substrates are some nice candidates with little background or influence to the sample for Raman measurements.

KBr

Potassium bromide (KBr) are commonly used for infrared (IR) spectroscopy for its complete optical transmittance in the mid-IR region.[218] Also owing to the inversion

symmetry, the pure cubic crystal of KBr possesses no first-order Raman modes.[219] Only second- or higher-order Raman modes can be observed with the strongest mode at 126 cm^{-1} from the TA+LA(X) phonon scattering and another prominent one at 216 cm^{-1} from TA+LO(L) phonon scattering.[220] As long as the sample is hydrophobic, since the second-order and higher-order Raman modes are all gathered in the low Raman shift region, KBr will be useful for organic samples which have modes at high Raman shift region.

Sapphire

Polycrystalline sapphire (Al_2O_3) are also frequently used for IR applications due to its good transmission in IR region.[221] For Raman measurement, though not as clean as the KBr Raman spectrum, sapphire has still a rather clean spectrum as reported by Porto et al. for the corundum phase and the polycrystalline structure by Wan et al.[222,223] The following Figure 5.10 shows the Raman spectrum of a polycrystalline sapphire measured by Wan et al. Unlike KBr, sapphire is not hygroscopic, so it can be applied for hydrophilic samples.

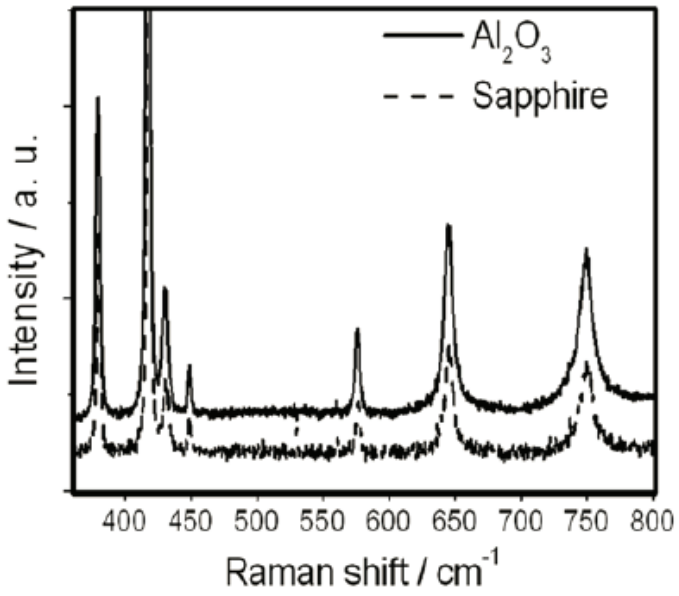

Figure 5.10: Typical Raman spectra of the c-plane sapphire (dotted line) and polycrystalline Al_2O_3 (solid line). Reproduced with permission from reference [223].

PMMA, P3HT and Parylene-C

Sacrificial polymeric substrates are used for the transfer printing process described in Ch. 3.2.

Polymethyl methacrylate (PMMA) is employed particular for graphene transfer purpose. As the presence of D, G and possibly other modes like 2D depending on the defectiveness of graphene after transfer, determine the degree of success of the transfer printing process. It is important to select a substrate that has little to no overlapping Raman modes with the graphene modes. The Raman spectrum of PMMA is shown in Figure 5.11 a, which the modes assignments are described in detail by Thomas et al.[224] The Raman spectrum of PMMA is quite busy on its own, but when PMMA is covered with graphene as demonstrated by Feng et al., the Raman spectrum are dominated by the graphene Raman modes.[31] Therefore, PMMA is a good candidate for the transfer printing purpose.

On the other hand, for poly(3-hexylthiophene (P3HT) the organic active material in OPVs, even though it has Raman modes (see Figure 5.11 b (red curve)), it is not suitable for Raman to gauge the transfer printing process. P3HT has a strong luminescence background, which is thousands of times stronger than the Raman response of graphene, the graphene peaks would be shielded by P3HT Raman modes as demonstrated by Feng et al. in Figure 5.11b (black curve).[31]

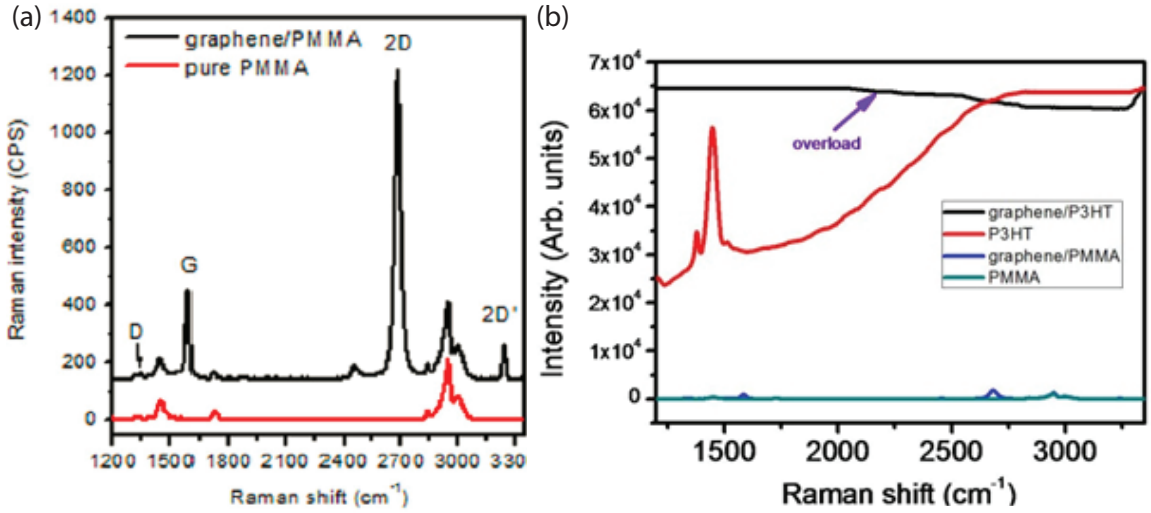

Figure 5.11: (a) Raman spectra of graphene/PMMA and pure PMMA obtained with 532 nm excitation. (b) Raman spectra of graphene/P3HT (black), pure P3HT (red), graphene/PMMA (blue) and pure PMMA (dark cyan). Both figures reprinted from Carbon, 87, Feng et al., "Engineering the metal–organic interface by transferring a high quality single layer graphene on top of organic materials", 78-86, Copyright (2018), with permission from Elsevier.

Owing to the difficulty of removing PMMA residue from transferred graphene, there are also alternative substrates to substitute PMMA for transfer printing as previously mentioned in Ch. 5.3.3.2.[116] Parylene-C is one of the examples and has been demonstrated by Kim et al. to transfer monolayer wafer size CVD graphene to parylene-C.[116] As can be seen in Figure 5.12, there are strong modes at 1609 cm^{-1} in the parylene-C Raman spectrum and at 1342 cm^{-1}, which are very close to the G and D bands of graphene.[116] This is due to the benzene ring structure also common in parylene-C, which then limits the Raman analysis in certain degree.[116] However, as can be seen from the inset in Figure 5.12, there is no Raman modes of parylene-C near the 2D region (2690 cm^{-1}) of graphene. Although one can still rely on this 2D mode to gauge the transfer process, note that the 2D mode in graphene is sensitive to defect and doping level of graphene, i.e. graphene oxide.[225] Therefore, depending on the graphene treatment prior to the graphene transfer, parylene-C may not be the best candidate for gauging the graphene transfer printing process.

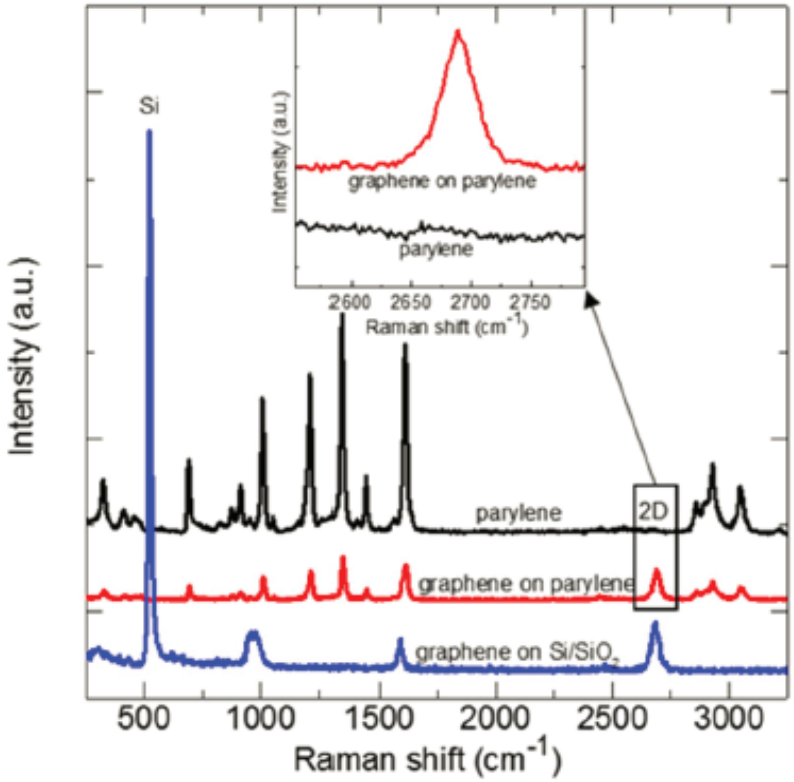

Figure 5.12: Raman spectra of graphene/parylene film, parylene only and graphene on Si/SiO2. Figure adapted from Ref. [116] under the Creative Commons Attribution 3.0 licence. The inset shows the spectrum around graphene 2D peak for parylene and graphene on parylene in detail.

5.3.4 Perovskites

Raman is a great candidate to provide comprehensive information to understand the components in the hybrid organic-inorganic perovskite material. Not only does Raman provide the vibrational modes such that the composition variations as well as the phases of the perovskites crystals can be identified,[226,227] it can serve as a major quality control characterization technique for perovskite PV devices.

5.3.4.1 $MAPbI_3$

Methylammonium (MA) Lead Iodide ($MAPbI_3$) is the prototype of perovskite photovoltaic devices. Depending on the temperature, $MAPbI_3$ possesses three different crystallographic phases, the orthorhombic phase at low temperature; tetragonal phase

at 165K;and the cubic phase at room temperature.[228,229] Quarti et al. published first-principles density functional theory (DFT) simulations and compared experimental Raman measurements of the $MAPbI_3$ with three crystal structures.[228] Although the simulated Raman spectra are differentiable from each structure, the experimental measurement showed very similar spectra, likely because of the anharmonicity and torsional and librational modes of the MA cations.[228]

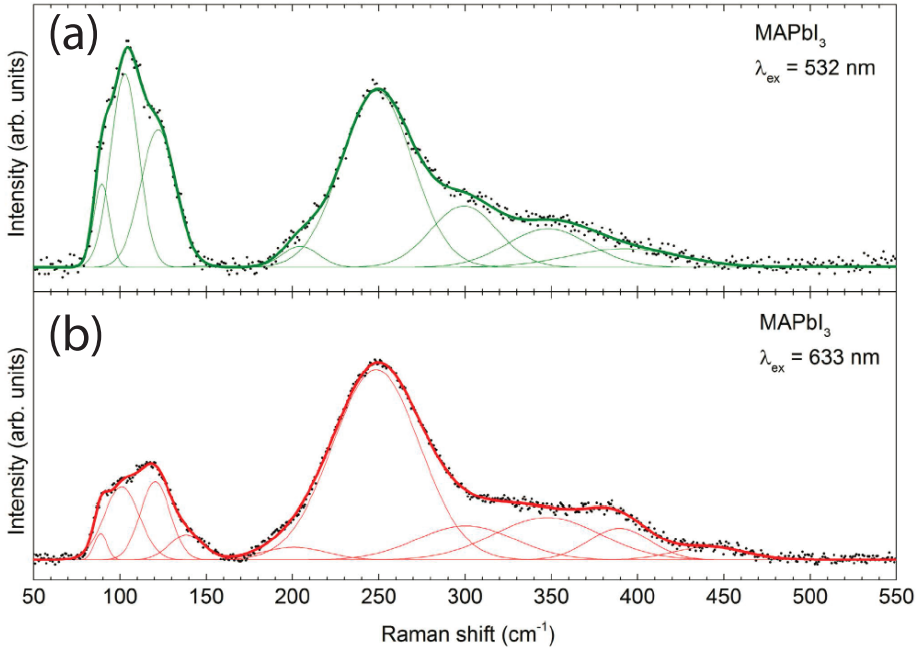

Figure 5.13: Raman spectra of Methylammonium Lead Iodide measured at (a) 532nm and (b) 633nm excitation lasers. Figure reproduced from reference[230] under the Creative Commons Attribution 4.0 International License.

Figure 5.13 shows the Raman spectra of $MAPbI_3$ obtained by Pistor et al. at 532nm (Figure 5.13 a) and 633nm (Figure 5.13 b) excitation wavelength. Although the vibrational modes in the low wavenumber region in Figure 5.13 a are more pronounced for the 532 nm excitation than the 633 nm, it is not preferable to use 532nm for Raman measurement. This is because 532nm is close to the resonant excitation of $MAPbI_3$, using low photon energy of 632nm laser excitation would result in less damage and potential sample bleaching.[228,230]

The first order Raman spectrum of $MAPbI_3$ comprises of two broad bands located mostly at the low wavenumber region and can be deconvoluted into vibrational modes from the ionic cage of Pb-I and the librational and torsional modes of the organic

Table 5.5: Raman modes and assignments for $MAPI_3$[228,230]

Raman peak, cm^{-1}	Assignment
62	I-Pb-I bending
94	Pb-I stretching and librational
119=141	MA librational
154	MA cation librational
200-390	MA cation torsional

cation (MA^+). Quarti et al. assigned the broad band at 200-340 cm^{-1} as the torsional mode of the MA^+ which presents the orientational order of the whole crystal.[228] They also predicted the modes from 100-200 cm^{-1} as the librational modes of MA^+.[228,230] In a more recent study, Pistor et al. noted the higher full wave half maximum (FWHM) (50 cm^{-1}) of the resolved peaks in the 175-450 cm^{-1} region, that it agrees with the random-character of the molecular origin and are important to be fitted with Gaussian peaks for deconvolution.[230]

On the other hand, while the modes at the lower wavenumber region (50-150 cm^{-1}) possess a lower FWHM of only 20 cm^{-1}, they are in fact contributions from the Pb-I cage which are also near the proximity of the PbI_2 modes.[230] Therefore, they have to be fitted using Lorentzian curves for highly ordered crystal structures.[230] The nature of the modes also explains the Raman intensity ratio difference measured at the two excitation wavelengths in Figure 5.13 a. The excitation energy of 532 nm is equivalent to 2.3eV of photons energy and is close to the energetic band at 2.4eV of $MAPbI_3$ contributed by the Pb and I atoms.[230] The Raman cross section efficiency of the inorganic component is then higher at 532nm for the selective enhancement it has on the inorganic modes. Table 5.5 highlights some of the important Raman modes assigned to the components of $MAPbI_3$ as reported.

As $MAPbI_3$ is known to be prone to degradation from moisture, heat and even laser exposure, one can identify the stages of the degraded $MAPbI_3$ from the Raman spectrum of a degraded product.[228–230] For example, $MAPbI_3$ tends to degrade into PbI_2 upon heating and illumination, and further degradation will result in the formation of polyiodide compounds (I_x).[230] This process should be traceable by first the disappearance of MA^+ modes and then the emergence of I_x modes at near 170 cm^{-1}.[230]

5.3.4.2 $FAPbI_3$

Formamidinium (FA) Lead Iodide ($FAPbI_3$) is considered more advantageous than $MAPbI_3$ for Perovskites PVs recently, for its lower hysteresis in I-V measurement, longer carrier lifetime, better photo and thermal stability and hence better power conversion efficiency.[226,227,231–233] $FAPbI_3$ has two main polymorphs: the α and δ-phase.[226] Figure 5.14 a shows the diffraction pattern of the α-phase (black line) and δ-phase (yellow line). While the α-phase black trigonal crystal is stable at high temperature, its δ-phase yellow hexagonal counterpart is not. Most importantly, the δ-phase crystal is nonperovskite, making it not useful for perovskite PVs (see Figure 5.14 c for photoluminescent of both phases excited at 532nm).[226]

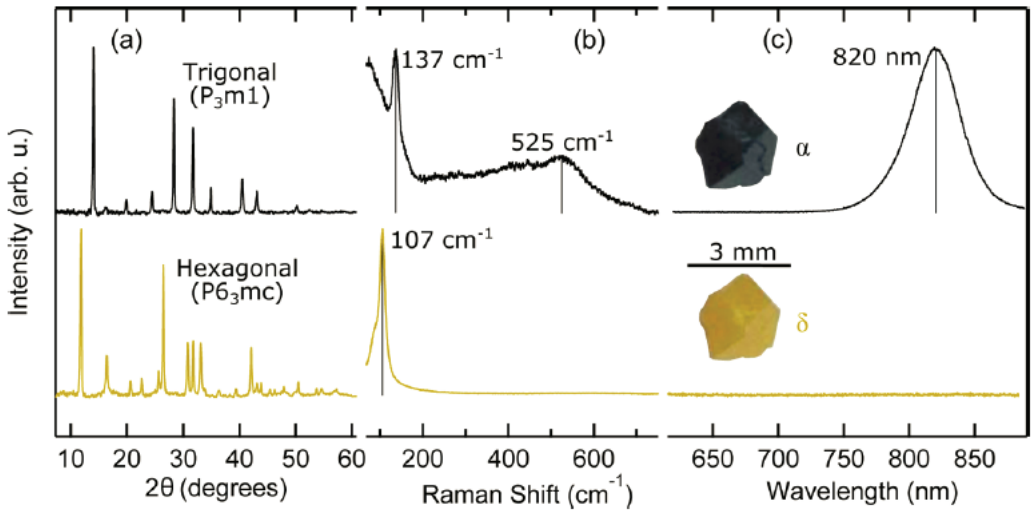

Figure 5.14: Physical properties of polymorphic Formamidinium Lead Iodide Characterization of the pure α-phase (top traces) and δ-phase (bottom traces) by means of (a) powdered XRD, (b) Raman scattering, and (c) PL at 532nm excitation wavelength. Figure reproduced from reference [226] under the ACS AuthorChoice License.

The two phases of $FAPbI_3$ show a similar yet shifted Raman spectrum as shown in Figure 5.14 b, where the black curve is for α-phase and yellow curve for δ-phase. The mode of δ-phase at 107cm^{-1} is originated from the I-Pb-I bending and stretching mode, very much like the Pb-I mode at 94 cm^{-1} of $MAPbI_3$.[226,228] The blue-shift of this peak is a result of lattice constant difference between the cubic structure of $MAPbI_3$ at room temperature and hexagonal structure of δ-$FAPbI_3$ as the same mode is further blue-shifted to 137 cm^{-1} for the trigonal structure of α-$FAPbI_3$.[226] There is also a weak broad band at 525 cm^{-1} related to the in-plane bending of FA cation for the δ-phase.[226]

5.3.4.3 $MAPbBr_3$

Methylammonium Lead Bromide ($MAPbBr_3$) is another perovskite material that is like $MAPbI_3$, it possesses a cubic structure at room temperature, a tetragonal structure from 145 to 237 K and orthorhombic structure at low temperature.[45]

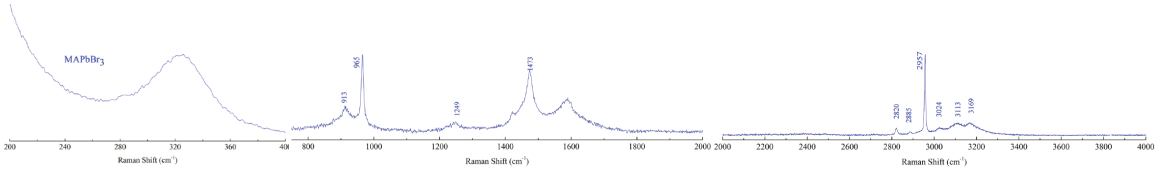

Figure 5.15: Raman spectra of Methylammonium Lead Bromide measured at 632nm excitation laser. Figure reproduced from reference [234] under the Creative Commons Attribution 4.0 International License.

Most literature only report on the Raman spectrum of the cubic form $MAPBr_3$ from above 200 cm^{-1} wavenumber. The lower wavenumber region which contains typically the inorganic cation is only presented in one case at cryogenic temperature where a peak of 127 cm^{-1} is located.[45] This mode corresponds to a longitudinal phonon of the Pb-Br chemical bound.[45] The rest of the Raman spectrum of $MAPBr_3$ can be referred to Figure 5.15 from reference.[234]

Like $MAPbI_3$, there is a broad band at 200-340 cm^{-1} that centers at 325 cm^{-1} for $MAPbBr_3$. It also represents the rotational mode of the MA cation.[234] The rest of the Raman-active modes due to the organic cation in Figure 5.15 are located at the high wavenumber region as tabulated with mode assignments in Table 5.6. They are all vibrational modes well-predicted by Glaser et al. and in fact, are only slightly shifted from each other in the MA lead halide ($MAPbX_3$) family, where X can be I, Br or Cl.[41]

The reason behind the shifting of modes between the $MAPbX_3$ is due to the interaction between the MA cation and the halide anion.[234] Depending on the electronegativity of the halide anion, the rotational motion of MA cation can be restricted.[41] For example, the 325 cm^{-1} is entirely suppressed for the case of $MAPbCl_3$ as Cl^{-1} has a higher electronegativity than Br^{-1}.[167] There is in general a blue shift of Raman-active modes for halide with higher electronegativity ($Cl^{-1} > Br^{-1} > I^{-1}$).[41,234] This means that due to the change of the microenvironment of the inorganic PbX_3^{-1} framework, more energy is required for the MA cation to move freely.[234]

Table 5.6: Raman modes and assignments for $MAPBr_3$[41,234]

Raman peak, cm^{-1}	Assignment
325	MA cation rotational
913	MA cation rocking
965	C-N stretching
1249	Rocking between CH_3 and NH_3 cation
1473	Asym. NH_3 cation bending
1590	NH_3 cation twisting
2820	Stretching between N^+-H
2885	Asym. CH_3 stretching
2957	Sym. CH_3 stretching
3024	Sym. NH_3 cation stretching
3113	
3169	

Part III

Experimental Details

5.4 General experimental

5.4.1 AFM, PL, and Normal Raman analysis

Atomic force microscopy (AFM) characterization were carried out by an Asylum MFP-3D instrument in the alternating current mode under ambient environment on spin coated samples on Si wafers. The AFM images were processed by WSxM[235], where the representative height of the nanoparticles was extracted by averaging the height profiles from 100 randomly selected nanoparticles.[236, 237].

Photoluminescence (PL) measurements carried out at McMaster were done using a 488nm Argon laser with laser power in the range of 10 mW (spot diameter 1-2mm). The samples for PL measurements are identical to the ones for SEM. The sample was focused with a 60x objective and the laser power was adjusted to 33% to avoid laser bleaching, with an exposure time of 5s and a slit opening of 0.02mm. The detection range is from 650 to 960nm. Both the corners and the center of the spin-coated sample on sample were examined as more material tend to be flushed to the corners during the process of spin-coating. The measurement was taken in a darkened environment to prevent stray light.

Normal Raman spectroscopy was performed with a Renishaw inVia spectrometer. All measurements were illuminated with 633nm laser excitation. The laser power was set to 10mW and an objective of 20x and 1800 l per mm grating was used.

5.5 Tip-enhanced Raman Spectroscopy

Tip-enhanced Raman Spectroscopy (TERS) was performed with the Atomic Force Microscopy and Raman Spectroscopy (NT-MDT Ntegra Spectra) at the University of Toronto (Scarborough) with bottom illumination for both the inverted TERS and inverted normal Raman. Atomic Force Microscopy Probes (MMHQ. NSC15/Al BS-15) for tapping mode 325kHz purchased from NanoAndMore USA were mounted as the tips for TERS. The AFM probes were coated with 30nm Au by the e-Beam Evaporator (UHV Instruments) at the Centre for Emerging Device Technologies at McMaster University beforehand and stored in vacuum until usage. Normal Raman spectroscopy, IERS and SERS were performed by a Renishaw inVia spectrometer at McMaster University. All measurements were illuminated with 514nm laser excitation. The

laser power was set to 10mW and an objective of 20x and 1800 l per mm grating was used. The bulk sample for polystyrene-*block*-poly(2vinyl pyridine) (PS-b-P2VP) was taken as is from the vial shipped from Polymer Source Inc., using the P1330 with M_n: 48500-b-70000. Cu tape was used to hold the polymer flake for measurement and it was affixed to a microscope glass piece. For the rest of the micelles samples, they are prepared by dissolving P1330 PS-b-P2VP into o-xylene above the critical micelles concentration of 3g/l and kept being stirred with a magnet bar at room temperature to maintain micelles formation and integrity. The micelles sample for normal Raman measurement was prepared by drop casting 5 times of 1ul micelles solution on freshly cleaved KBr substrate. In order to ensure adequate signals for the drop-casted micelles spectra acquisition, the laser was focused at regions with visible residue ("coffee stain" area as the drop-cast sample solution) where more materials were aggregated. The thinner sample for SERS was prepared by spin-coating 12ul of micelles solution on a Sapphire substrate which was pre-sputtered with 5nm of Ag with the DC Sputterer (Torr). The sample for the inverted TERS and inverted normal Raman measurements is the same and it was prepared by spin-coating 4ul of solution to a Sapphire disc. The schematic of set-ups for the Raman techniques were depicted in Figure 8.2 a-e. The baseline of the spectra was created and then subtracted to highlight the peaks of interest. In addition, the spectra were smoothed using the Savitzky-Golay function in Origin. The smooth spectra were normalized to 0-1 in the region from 600cm^{-1} to 1700cm^{-1}.

5.6 Nanoparticle synthesis

Preparing empty reverse micelles The polystyrene-*block*-poly(2vinyl pyridine) powders(PS-*b*-P2VP, M_n: 75000-b-66500, labelled as P4824; Polymer Source) were dissolved in o-xylene to yield solutions above the critical micelle concentration, typically between 3.00-3.75mg/ml.[238] The solutions were kept under magnetic stirring to facilitate the reverse micelles formation at least 24 hr.

5.6.1 Synthesizing γ-Fe_2O_3 nanoparticles and its characterization

The iron precursor ($FeCl_3$, sublimed grade, > 99.9%; Sigma-Aldrich) was added to the reverse micelles solution with various loading ratios (the ratio between the Fe^{3+} and the total amount of 2-vinyl pyridine(2VP) units of the copolymer). The solutions were kept under magnetic stirring for at least 24h to ensure adequate precursor loading. To produce the iron oxide nanoparticles, the above $FeCl_3$ loaded reverse micelles solution was spin coated or drop cast onto clean substrates. Oxygen plasma treatment (29.6W, 950mtorr, Harrick Plasma cleaner) was employed to convert the $FeCl_3$ precursor into iron oxide and remove the carbon-based micelles ($\sim$ 25mins). Annealing was conducted at 600°C or 350°C under N_2 or air environment using a flow gas, tube furnace. Homopolymers of poly(2-vinyl pyridine) (HP2VP, M_n: 77000g/mol, Polymer Source) and polystyrene (HPS, M_n: 41000g/mol, Sigma Aldrich) were used to study the interaction between $FeCl_3$ and poly(2-vinyl pyridine). In this case, 6mg of HP2VP or HPS was added to 1ml o-xylene with $FeCl_3$ to yield a 0.3 loading ratio mixture and then kept stirring for at least 24h before drop-casting on KBr substrates. Control tests were carried out by dissolving $FeCl_3$ in o-xylene to prevent immediate oxidation of the hygroscopic salt. The copolymer, HP2VP and HPS were also mixed with o-xylene individually for comparison.

The magnetic properties of the nanoparticles spin coated on Si wafers were investigated at 300K by a liquid Helium cooled superconducting quantum interference device (SQUID) magnetometer (Quantum Design, Inc.).

Raman spectroscopy was performed by a Renishaw inVia spectrometer at 514nm laser excitation on drop cast (2μl twice) samples on freshly cleaved KBr substrates. The laser power was set to 10mW and an objective of 20x and 1800 l per mm grating was used. In order to generate adequate signals for the spectra acquisition, the laser was focused at regions with visible residue ("coffee stain" area as the drop-cast sample solution) where more materials were aggregated. $FeCl_3$ precursors without micelles were measured in its solution form in o-xylene due to its hygroscopic nature. The measurement was performed before evaporation of the solvent after the solution was drop-cast on the KBr substrate. The solvent prevents the $FeCl_3$ from absorbing moisture from the environment for a short period while the solvent slowly vaporizes during the measurement. The baseline of the spectra was created and then subtracted

to highlight the peaks of interest (see supporting information Figure SI1). In addition, the spectra were smoothed using the Savitzky-Golay function in Origin. The smooth spectra were normalized to 0-1 in the region from 150cm^{-1} to 2000cm^{-1} or from 150cm^{-1} to 900cm^{-1} for further discussion. The processed spectrum features from 150cm^{-1} to 900cm^{-1} were deconvoluted using Lorentzian line shape profiles to highlight the iron oxide characteristic peaks.

Transmission electron microscopy (TEM) samples were spin-coated by on Si_3N_4 membrane window TEM grid (Norcada) inside the glovebox at 2000rpm for 45s (Specialty Coating Inc. G3P spin coater). JEOL 2010F TEM imaging was operated at 200kV accelerating voltage with the field emission gun (FEG) source. Energy-dispersive X-ray (EDX) line scan and mapping were collected under the same conditions in the scanning transmission electron microscopy (STEM) mode. The STEM data collected was analysed with Gatan Microscopy Suite 3 software and the EDX data was processed by INCA Microanalysis Suite.

5.6.2 Synthesizing Perovskite and its characterization

Perovskites precursor solution preparation: 0.5M precursor solutions were made by adding organic salts (Methylammonium iodide (MAI), Methylammonium bromide (MABr) and Formamidinium iodide (FAI) purchased from Greatcell Solar Ltd.) to isopropanol (IPA) (Caledon, reagent grade) and the inorganic salts (Lead(II) iodide (PbI_2)(Alfa Aesar, 99.9985%) and Lead(II) bromide ($PbBr_2$)(Alfa Aesar, 98%)) to N,N-Dimethylformamide (DMF) (Sigma Aldrich, 99.8%).

Perovskites nanoparticles synthesis by the reverse micelles technique: Reverse micelles were prepared by dissolving various poly(styrene-b-2-vinyl pyridine) di-block copolymer purchased from Polymer Source Inc. i.e. P4824-S2VP (75.0-b-66.5), P1330-S2VP (48.5-b-70.0), P9861-S2VP (28.0-b-36.0), in reagent grade non-polar solvents such as toluene and o-xylene, with the concentration of 3g/l under continuous stirring. After confirmation of reverse micelles formation by AFM, equal parts of perovskites precursor solution were pipetted sequentially by adding the organic salt first to the reverse micelles solutions with a time interval of 24 hrs to allow thorough infiltration of each precursor salts. Methylammonium Lead Iodide ($MAPbI_3$) was formed by mixing MAI and PbI_2; Methylammonium Lead Bromide ($MAPbBr_3$) was formed by mixing MABr and $PbBr_2$; Formamidinium Lead Iodide ($FAPbI_3$) was formed by mixing FAI and PbI_2. The final perovskite salt loaded reverse micelles solution was centrifuged to

remove excess, non-infiltrated salt and stirred further to prevent coagulation.

Perovskites nanoparticles synthesis by injection method: The nanoparticles were made by injecting a 0.5M solution of $MAPbI_3$ (MAI and PbI_3 equimolar in DMF) into toluene in a 50:1 volumetric ratio and stirred vigorously at 80^{o}C. As a ligand of octylamine, in the ratio of 1:100, with respect to the $MAPbI_3$ solution were added (can be added to toluene before injection or afterwards). The particles were washed 4 times with toluene to remove the DMF by use of a centrifuge.

I_2 staining of micelles for TEM Thin layer of micelles was deposited to the porous carbon thin film TEM grids by using dip-coating, which allowed direct TEM/STEM characterization of the individual micelles. In order to selectively stain the P2VP cores, the micelles coated TEM grids were then exposed to I_2 vapor (Iodine, > 99.8%, Sigma-Aldrich) for 3 hours at room temperature, by placing iodine crystals and TEM grids in a sealed glass container [239–241]

SEM measurements Scanning electron microscope (SEM) measurements were performed with a FEI VERSA 3D. SEM images of $MAPbI_3$ reverse micelles samples were obtained using the with accelerating voltage of 5kV and a probe current of 12pA. All SEM samples was prepared by dynamically spin-coating 4ul of perovskite solution to a 1x1 cm ^{2} p-doped Si substrate inside the glovebox at 2000rpm for 45s (Specialty Coating Inc. G3P spin coater).

QNM mapping Quantitative nanomechanical property mapping (QNM) AFM was done using a Bruker Bioscope Catalyst with an RTESPA probe. To confirm the formation of the perovskite nanoparticles within the reverse micelles, hardness maps were generated using the QNM AFM mode provided by the Bruker Nanoscope software. The hardness maps were created by calculating the elastic modulus at each AFM interaction point using the Derjaguin-Müller-Toporov (DMT) model. For each round of measurements, the probe was calibrated using a relative method of calibration with a sample of known modulus. The average elastic modulus for the sample was determined by taking a line profile through 100 micelles by matching the coordinates in the topography channel to the elastic modulus channel in WSxM. The elastic modulus for each micelle was determined by taking the average modulus of 10 points were taken for each micelle. The histogram of 100 modulus measurements were fit using a Gaussian approximation to calculate the average modulus value and error for the unloaded and loaded micelles. The QNM sample preparation is similar to the AFM sample preparation procedures, with the exception for the spin speed being 8000

rpm to promote sparse dispersion.

Polydispersity index analysis: SEM or AFM images were first imported into ImageJ and the image was processed to extract quality sufficient for further analysis, where outlines of micelles can clearly be displayed.

To find the sizes of the micelles/ particles, depending on the quality of the image, one of the following two processing options are chosen: the first is to binarize the image, and use ImageJ to calculate the location and radius of each of the particles. If the noise level of the image is too high, or the binary image does not accurately represent the sizes of the cells, the size of the micelles has to be found manually, by drawing an ellipse around the micelle. The major and minor radius measurements from either approach are used to find the approximate radius and area of the micelle. This was converted into an effective radius of a circular micelle for each particle. In general, a hundred measurements on different particles within a 2x2um area were sampled for determine the average radius and PDI from a histogram of the radii distribution. The PDI was calculated by dividing the standard deviation by the mean of the data set.

Dispersion analysis:

The dispersion analysis of the SEM image can be performed after extracting the x-y coordinates using the same procedures for PDI extraction. The analysis is run by the in-house developed tool called the DisLocate package in Mathematica. The pair correlation function (PCF) quantifies the positional order of intermolecular morphology. It describes the probability g(r) to find other particles at varying distances away from the centre of each particle, which is chosen as the origin to measure the distance from. A circular shell of width δr expands from the centre to a radius distance r. Any particles inside a circular shell of width Δr are counted over the radial spatial dimension. $g(r)$ is normalized by the density of the configuration, which then describes its the deviation from of a hexatic lattice. An entropic force map shows the planar probability map of first neighbour in relation to the centre particle by translating the particles to a common origin, which shows the degree of rotational symmetry of the system. A detailed description of the package and its other capabilities is described elsewhere.[242]

5.7 CVD Graphene, post-annealing and plasma treatment

Graphene was synthesized by chemical vapour deposition (CVD) on commercially available 25 μm copper foils (Alfa Aesar). The foils were first chemically treated with acetic acid and annealed for 4 hours at 1078°C under a flow of 8 sccm hydrogen gas in order to prepare the copper surface. The temperature was maintained at 1078°C during a 4 min CVD growth phase where gas flows of 1.2 sccm methane was introduced. Long annealing time and short growth period were chosen in order to limit the size and density of the graphene domains. To observe the graphene flakes, oxidation of the Cu surface is necessary to provide contrast between the graphene coated and uncoated portions of the Cu surface.

Samples were annealed in a batch on a hot plate (Thermo Scientific) in air at 180°C with different annealing times (AT) indicated in minutes. The groups of samples with different annealing times were then separated into batches for air (unfiltered laboratory air), nitrogen (Alphagaz, 99.999%) and oxygen (Alphagaz, 99.999%) plasma etching.

The plasma etching was performed in a Harrick Plasma PDC-001 plasma cleaner system with 13.56MHz R.F. generator at 29.6W. The plasma chamber was held at a base pressure of 70mTorr prior to target gas filling. During etching, a gas flow rate of 30 sccm was maintained. The samples were progressively etched one at a time. The partial graphene patches were observed under microscope (Leica DMR microscope) to detect the first disappearance of the contrast. For the case of N_2 plasma etching, post-annealing of the etched samples was needed to show contrast of Cu-graphene after treatment. The time intervals are then accumulated as the minimum time required for etching away graphene, designated as the critical etching time (CET) in minutes.

The XPS spectra were collected and generated by a monochromated Al K source with a photon energy of 1486.6 eV at a pass energy of 25.00 eV (Thermo K-Alpha). The spot size was 400 μm^2. The XPS measurements were not charge corrected, given the samples were highly conductive and peak charging were insignificant. The XPS spectra was analyzed with the Thermo Avantage software tool with the Smart background correction option, which is based on the Shirley background correction method. The peaks were then fitted with the Gaussian-Lorentzian function. The fitting of the $Cu\,2p_{3/2}$ was also compared against the fitting of the $Cu\,2p_{1/2}$ peak for

fitting reliability.

ATR-FTIR was collected on a Bruker Vertex 70 FTIR equipped with the Platinum Diamond ATR apparatus, using the standard mid-IR laser (Globar). The measurements were accumulated for 152 scans with a $4cm^{-1}$ resolution and collected with a RT DLaTGS detector. The output spectrum was subtracted against the background environment spectrum.

Contact angle measurements were performed with the Kruss Drop Shape Analyzer-DSA100, using a 26s gauge (0.474mm outer diameter) flat needle for 10ul water droplet dispensing. Samples of full graphene aged for the same amount of time were annealed in air for 0, 4, 15, 30, 60 mins at 180°C on a hotplate. The samples after annealing were immediately kept in a glass Petri dish and stored under vacuum prior to measurement, to avoid airborne contamination. Each sample was recorded for 50s with 1s intervals. The contact angle is measured from the sessile drop image at the points of intersection between the drop contour and the baseline which is the sample surface. The final contact angle of each sample is an average of the 100 measurements from both left and right sides of the droplet images.

Part IV

Transfer Printing

Chapter 6

Substrate-assisted Transfer of Nanoparticles by Graphene Oxide on Metal-organic Interface

6.1 Introduction

Incorporation of nanostructures into devices have been applied to a variety of advanced technological fields, including organic photovoltaics, display industry, sensing technology, photonics, micromechanical systems, microfluidics and microelectronics.[18,75,243–248] These nanostructures for nanopatterning ranges from all sorts of materials, such as the noble metals, metal alloys, magnetic metal oxides, dielectric salt and more to allow better device performance.[18,75,86,101,243]

Size and order of dispersion are important aspects when incorporating nanoparticles in devices as they affect device electrical properties such as the charge transport behaviour and work function at interfaces.[18,86,243] Reverse micelles formed by diblock copolymer offers a high degree of nanoparticle size control depending on the copolymer block lengths and the spherical reverse micelles tend to close pack spontaneously in a hexagonal order.[242,249] It is also feasible to produce a wide variety of nanoparticles with the reverse micelles.[76,249] Therefore, the reverse micelles deposition (RMD) method is chosen to fabricate nanoparticles for the device fabrication purpose here. The drawback of using RMD to synthesize nanoparticles is that the polymeric shell of the micelles has to be destroyed at the end by plasma etching or UV in order to expose the

nanoparticles. This makes direct deposition of RMD nanoparticles on organic devices impossible as it will also lead to destruction of organic materials in the devices.

Nanotransfer printing methods using elastomer stamps is one way to move the nanoparticles from a donor substrate to the organic target substrate. However, it does not always work as it can be hindered by the intrinsic surface energy differences between the stamp and the donor substrates depending on the materials. A more universal way of transferring the nanoparticles is under scrutiny, we propose using graphene as the carrier layer to transport the nanoparticles directly onto the organic layer. Large area graphene grown by Chemical Vapour Deposition (CVD) on metals, have been transferred to devices to fabricated graphene-based organic photovoltaics (OPVs), field-effect transistors and resonators.[14,115,136,250–253]

The usual concerns with graphene transfer is the polymer residue contamination from the stamp, tears and wrinkles.[253] Feng et al. reported a direct transfer method for CVD graphene on Cu using the target organic layer as a holder substrate, which avoids the process of having unnecessary organic contaminants.[31] The quality of the transferred graphene remains defect free and it could be applied to wafer size.[253] To adapt this graphene transfer process developed by Feng et al., a slight modification has to take place because now the graphene would be carrying a layer of nanoparticles produced by RMD which then involves plasma etching. In-depth studies on the dynamics between graphene and plasma has been conducted, which provided valuable insights on pre-conditioning the graphene by annealing to attain a good quality for transfer purpose.[150,254] A generic type of Fe_2O_3 nanoparticles are selected for this transfer printing by using $FeCl_3$ as the salt precursor in the poly(styrene-b-2-vinyl pyridine) (PS-b-P2VP) diblock copolymer reverse micelles. The whole process of graphene transfer with nanoparticles can be monitored by Raman spectroscopy and optical microscopy, to determine the level of success of transfer.

6.2 Results and Discussion

The RMD process must go through an extra oxygen plasma treatment in order to get rid of the polymeric shell of micelles. The same amount of plasma dosage that is adequate to destroy the reverse micelles would be applied on the graphene. A pristine free-standing monolayer graphene would not be able to resist the violent etching action of plasma in seconds, whereas a CVD monolayer graphene on Cu is

slightly better.[138,191,254] This is due to the synergistic oxidation effect from the Cu substrate on the graphene, which after the plasma treatment becomes the reduced graphene oxide (rGO). A full description on the synergistic oxidation mechanism is provided in an earlier study.[254] In fact, even the CVD graphene on Cu would not be able to withstand the plasma dosage for micelles, it requires the special treatment of low temperature (180 °C) pre-annealing in order to eliminate the surface contaminants which are the volatile organic compounds adsorbed almost immediately to the surface after the CVD growth of graphene (see Chapter 12.3).

This step of annealing proves to be quintessential to preserve the rGO structural integrity which can be determined by the Raman spectrum of the annealed rGO after plasma etching. A minimal of 4 min annealing time is enough for a monolayer CVD graphene on Cu to undergo 25 min of plasma etching (ET25).[150] That is for the case of pure oxygen plasma etching on "blank" graphene. When micelles is deposited on the graphene, the plasma etching dynamics could be elevated. Since prolong low-temperature annealing does not cause more defects on the graphene, an annealing time (ATX) of 60 min (AT60) is employed (see Chapter 12.2 and 12.3). The Raman spectrum of the resultant CVD graphene on Cu with monolayer micelles underwent 60 min of low-temperature annealing and 25 min of oxygen plasma etching (AT60ET25) is obtained in SI Figure 13.10.

A broadened G mode with peak maxima at 1603 cm^{-1} (also known as the G_{app} mode which is resulted by the merging of G mode at 1590 cm^{-1} and D' mode, deconvoluted as a Lorentzian curve at 1606cm^{-1}), D mode (at 1354 cm^{-1}) and 2D mode (at 2790 cm^{-1}) can be identified. The peak position difference of 3cm^{-1} between G_{app} and D' mode indicates that the CVD graphene is oxygen-doped by the plasma which becomes an rGO and the fact that the 2D mode is still strong implies a good degree of sp^2 hybridization (see Chapter 12.3).[255] Therefore, the rGO is still quite intact and should be strong enough for transferring the $FeCl_3$ nanoparticles onto the target organic layer.

A schematic flow of the modified procedure from Feng's study is shown in Figure 6.1. After the CVD graphene on Cu is annealed at 180°C for 60 min, the reverse micelles loaded with $FeCl_3$ is spin-coated onto the graphene. The micelles together with the CVD graphene is plasma etched in oxygen to destroy the polymeric shell. The $FeCl_3$ will be converted to Fe_2O_3 during the process and the graphene will be doped to become rGO. At this point, the target organic layer can be introduced by spin-coating onto the rGO which holds the Fe_2O_3 nanoparticles and the thickness can

be willingly controlled by the spin-coating speed and volume of polymer casted. After the target organic layer is cured according to the manufacturer instructions, the whole stack of material will be floated onto a Cu etchant solution to dissolve the Cu from the rGO. Since there are graphene on both sides of the Cu for CVD grown graphene, graphene at the bottom side of the Cu, which is not in contact with the nanoparticles, will also detach as Cu dissolves into the etchant. Therefore, towards the end of the Cu wet etching process, only the rGO should be in contact with the Cu etchant. The process is followed by displacing the Cu etching with deionized water so that any Cu etchant residue can be washed away, leaving a clean back side of rGO. The final step is to fetch the stack from the water. It can be done by lowering a substrate like glass or ITO-coated-glass on top of the stack and let the organic layer attach to the substrate. Finally, the stack is flipped with the configuration of rGO/nanoparticles/organic layer/ITO and let dry in the N_2 filled glovebox environment.

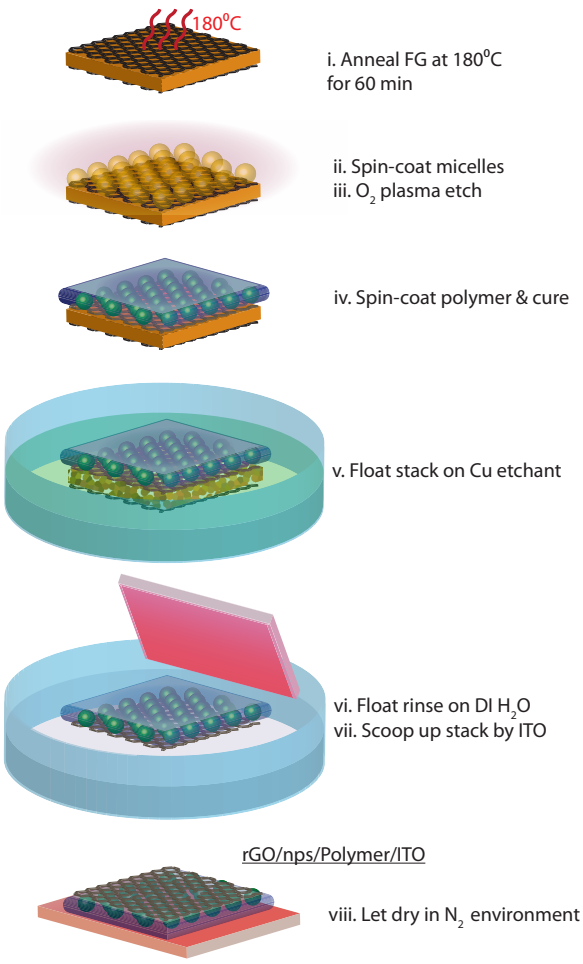

Figure 6.1: Schematic flow of transfer printing process– direct graphene transfer with nanoparticles using polymer holder. (i) Anneal CVD full graphene on Cu in air at 180°C for 60 min. (ii) Spin-coat nanoparticles-loaded-micelles solutions on the annealed CVD full graphene on Cu. (iii) Plasma etch the whole stack in oxygen for 25 min to expose the nanoparticles from the micelles. (iv) Spin-coat polymer (P3HT or PMMA) on the stack and cure. (v) Float the stack on Cu etchant solution to etch away the Cu layer. (vi) Float the stack on DI water for three times to rinse off any Cu etchant residue. Displace water carefully with syringe to avoid tearing of the stack from water surface tension. (vii) Scoop up the stack from the solution by lowering the substrate (ITO) on top of the stack. (viii) Flip the stack up-side-down and let dry in N_2 environment overnight. Final configuration of stack: Reduced graphene oxide/nanoparticles/polymer/ITO.

As a proof of concept, the actual transfer process was first performed with poly (methyl methacrylate)(PMMA) as the target polymer substrate and partially grown CVD graphene on Cu (PG). PG (n=2) is conveniently used for its differences in

refractive index from the background PMMA (n= 1.49) which can provide an optical contrast.[256,257] In such a way, one can optically identify spots where PG is transferred.

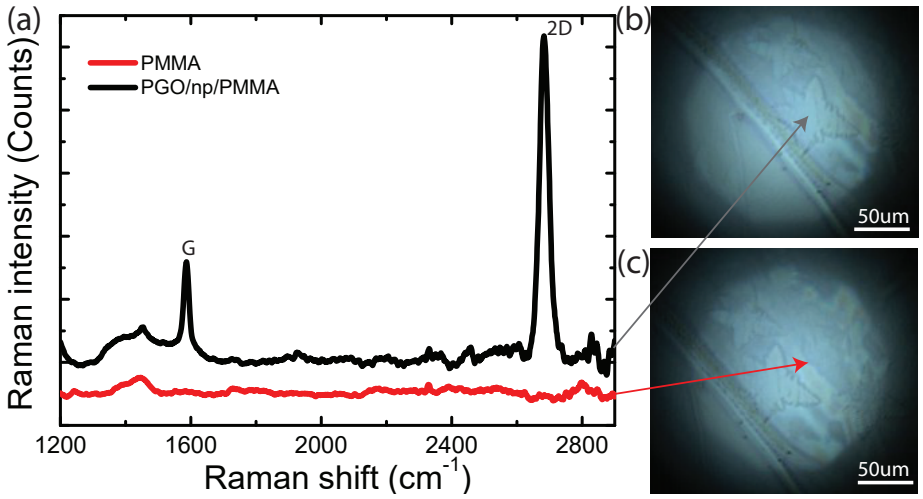

Figure 6.2: (a) Comparison of Raman spectra of PMMA (red line) and partial graphene oxide with nanoparticles transferred to PMMA (black line). Optical images of exact spots taken for Raman measurements, indicated by arrows in (b) for partial graphene oxide where a flake a visible, and (c) for PMMA right next to the empty space of the flake.

Figure 6.2 a shows the Raman spectra of a successfully transferred reduced partial graphene oxide (rPGO) with Fe_2O_3 nanoparticles on PMMA. Figure 6.2 b and c are the optical images indicating where the Raman laser was focused at for Raman measurements, with Figure 6.2 b at the rPGO spot and Figure 6.2 c at the blank spot immediately next to the identical rPGO spot. The rPGO flake can be clearly outlined from the optical images against the PMMA background. The blank spots are locations where no PG was grown on the Cu.

Presumably, no nanoparticles are left at the blank spot because without the barrier of rPGO, as the Cu etchant etches away the Cu, the nanoparticles attached to the Cu will go with the Cu to the etchant. For the parts where PGO flakes are found, there should be a layer of nanoparticles sandwiched in between the rPGO and the PMMA. However, since it is only a monolayer of Fe_2O_3 nanoparticles, there is not enough material to be detected by the Raman in Figure 6.2 a. The Raman spectrum shows a clear G_{app} mode, a strong 2D mode and maybe a D mode hidden in the broad peak for the rPGO (black curve). The Raman spectrum of the blank spot is only PMMA (red curve), matches with the background of the black curve. The broad band

at the 1460 cm^{-1} Raman shift region is attributed to the asymmetric C-H stretching mode in the methyl group and methoxy group.[224,258,259]

Lin et al. recently did a measurement on water permeability of rGO. With 17% of oxygen concentration, rGO would be impermeable to water because of the small pore size for any water to pass through.[146] rGO with 25% oxygen content would be permeable to water at high reduction temperature of 2500K.[146] The rGO produced through annealing and plasma etching from our earlier study has an oxygen content of 23.1%, so it is essentially impermeable to water in ambient glovebox environment.[254] This is important for the organic active layer poly (3-hexylthiophene):(6,6)-phenyl C61-butyric acid methyl ester (P3HT:PCBM) in organic devices. Moisture is one of the key degradation factors for P3HT,[16,260] but the rGO layer can theoretically block the direct contact of P3HT:PCBM from water during the Cu etching process in the glovebox.

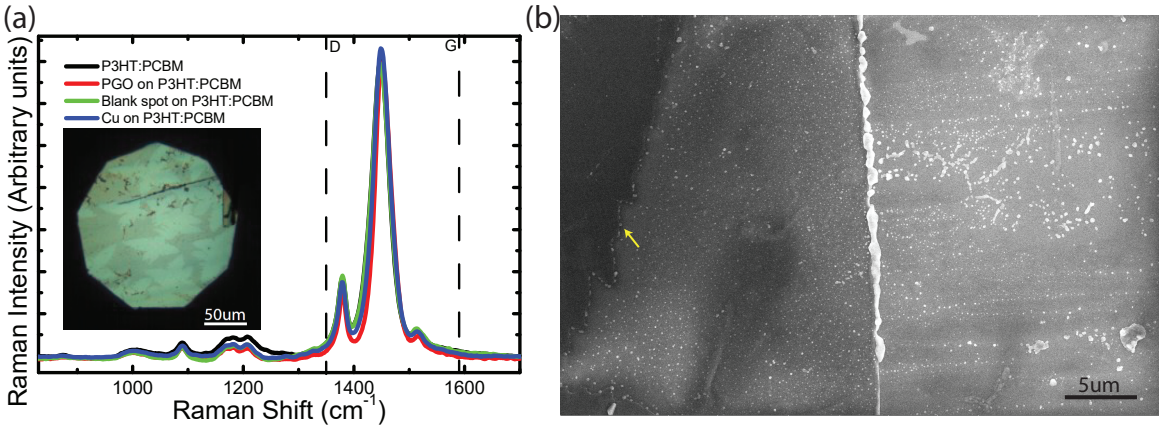

Figure 6.3: (a) Comparison of Raman spectra of PMMA (black line); partial graphene with nanoparticles transferred to P3HT:PCBM (red line); blank spot next to the reduced partial graphene oxide on P3HT:PCBM (green line), and Cu on P3HT:PCBM (blue line). Dotted vertical lines indicate the expected peak positions of the G and D mode of graphene. Inset shows the optical image of the transferred partial graphene oxide flakes with nanoparticles on P3HT:PCBM for Raman measurements.(b) SEM image of the partial graphene oxide with nanoparticles on P3HT:PCBM where the graphene boundary is indicated by the yellow arrow.

Figure6.3 a shows the Raman spectra of rPGO transferred on P3HT:PCBM, the dotted vertical lines indicate the expected positions for the D and G modes of graphene. A reference spectrum of P3HT:PCBM is shown as the black curve. The blue curve in Figure 6.3 a is the control sample where only the Cu substrate and nanoparticles

are used to transferred to the P3HT:PCBM. Measurements taken at the rPGO flake (red curve) and the blank spot next to the flake (green curve) are also plotted. Unfortunately, the high luminescence background from P3HT:PCBM measured by the resonant condition of 514 nm is too strong that it overwhelmed any signals coming from the rPGO.[261] The strong mode at 1445 cm^{-1} comes from the symmetric C=C stretching mode of thiophene ring in P3HT and the peak at 1381 cm^{-1} belongs to the C-C skeletal stretching mode of P3HT.[261,262] The strong signal from the P3HT:PCBM also oversaturated the detector at the high Raman Shift region, so no 2D peak can be detected (not shown here). As a result, the Raman spectra is all identical to the P3HT:PCBM spectrum in Figure 6.3 a. However, one can still clearly outline the rPGO flakes from the optical inset in Figure 6.3 a, meaning that the rPGO and possibly the nanoparticles sandwiched underneath are transferred. Again, due to the monolayer coverage of Fe_2O_3 nanoparticles, it remains undetectable in the Raman spectrum.

Figure 6.3 b shows the SEM image of the rPGO transferred with nanoparticles to P3HT:PCBM, where the boundary of the rPGO can be seen as indicated by a yellow pointer. The darker region (to the left of the yellow pointer) is the rPGO and the remaining lighter part is the blank region, which is the P3HT:PCBM. The white particles all over the blank region are unlikely to be the Fe_2O_3 nanoparticles, because the size of these white particles are around 50nm, whereas the Fe_2O_3 nanoparticles should be less than 10nm in diameter. Theoretically, the Fe_2O_3 nanoparticles under the atomically thin rPGO should be visible as well, but no nanostructure can be seen from the dark region in Figure 6.3 b.

Although ideally the nanoparticles should be trapped under the graphene oxide layer using this transfer method, it would be necessary to gauge the post-transferred condition of the nanoparticles optically or chemically. To prove that Fe_2O_3 nanoparticles are in fact transferred, one would suggest using a higher coverage of Fe_2O_3 nanoparticles that is above the Raman detection limit. However, as the amount of $FeCl_3$ reverse micelles are increased, the plasma etching action is also escalated that the reduced graphene oxide is severely damaged. The Raman spectra of multiplayer Fe_2O_3 nanoparticles on FG before transfer (blue curve) is shown in SI Figure 13.10, only the G_{app} mode and a broad D peak can be seen, they may as well be only adventitious carbon left on the surface. Therefore, one needs to use a direct characterization method such as the atomic probe spectroscopy to look for the transferred Fe_2O_3 nanoparticles.

6.3 Conclusion

Successful transfer of reduced graphene oxide with nanoparticles are transferred to organic layer. The transfer results of the reduced graphene oxide are supported by the post-transfer optical images and Raman spectrum. The reduced graphene oxide transferred onto PMMA still shows high level of intactness, which highlights the importance of pre-conditioning of graphene by low-temperature annealing. Direct evidence of nanoparticles transfer can be further obtained from atomic probe tomography, but presumably the nanoparticles are sandwiched between the reduced graphene oxide and organic layer.

6.4 List of failed transfer

Numerous attempts of failed transfer printing is documented in the table below.

Table 6.1: List of failed transfer printing techniques of different donor substrates (DS) and receiver substrates (RS).

Method	DS	Stamp	RS	Condition	Result
Pick-and-Release	Si	PNIPAAm -PDMS	Si	Pick-up: Temp= 5°C, mg=2kg, t= 2.5hr; release: Temp= 50°C, mg=2kg, t=2hr	nothing removed (AFM), a lot of residue
	Si_3N_4	Parylene -C(3g)	Double-sided tape on glass	Parylene-C deposited on DS with nps. Create notch on surface by razor for peel off	nothing removed (AFM
	Si_3N_4	Lotrafilcon	nil	Lotrafilcon cleaned by sonication in DI H_2O. Laminated 6 times, peeled off by tweezers	nothing picked up (AFM)
	Au-Si	Parylene -C(3g)	nil	Wooden pressor (finger-tight)	nothing picked up (AFM)
Direct stamping	Lotrafilcon	NA	Si	ET 5min lotrafilcon creates a glassy surface	nothing removed (AFM), lotrafilcon got stiff
FG Wet etching with Ammonium Persulfate	Float etch	NA	glass	t=133min	FG disintegrated in etchant
	Drip etch	NA	glass	Used filter paper and funnel for dripping. Used 150ml, t=54min	FG disintegrated while floating on etchant droplets
	Pipette drip etch	NA	glass	Glass pipette filled with glass wool, fritter used to hold FG and glass. Pump-assisted drainage. t=45min	FG disintegrated, sample moved
	Glad pouch Float etch	NA	NA	Glad pouch pierced with inlet and outlet holes. Laminated with FG. t=overnight	No visible FG contrast, no FG Raman signals
	On PDMS Float etch	NA	Parylene-C	Conformal contact of FG and parylene-C by cold lamination. Can separate FG easily from PDMS. Float parylene face up	Parylene-C permeability is too low, no etching
	On PDMS Float etch	NA	Parafilm	Conformal contact of FG and parafilm by cold lamination. Can separate FG easily from PDMS. Float parafilm face up	Parafilm permeability is too low, no etching
	FG	NA	Lotrafilcon	Laminate FG to lotrafilcon, sticks too well. Float etch face down. t= overnight	No visible FG contrast, no FG Raman signals
	FG	PDMS	Si	PDMS pressed on FG. Float etch face down. Pressed to Si.	No visible FG contrast, no FG Raman signals
	FG	NA	PDMS	PDMS cured on FG. Float etch face down	FG Raman signal present

Part V

Why Raman

Chapter 7

Characterization techniques attempted but failed

In order to detect the transfer printed system all together, several characterization techniques were attempted such as the Atomic Force Microscopy (AFM), Secondary Electron Microscopy (SEM), Transmission electron microscopy (TEM) for imaging purposes; the X-ray photoelectron spectroscopy (XPS), X-ray Diffraction (XRD), Raman Spectroscopy, Fourier Transform Infrared (FTIR) Spectroscopy and its hyphenated techniques, the Diffused Reflectance Infrared Fourier Transform Spectroscopy (DRIFTS) for chemical analysis.

The imaging techniques can provide topography information on the micelles and nanoparticles. Despite that SEM sometimes suffers from the charging effect, it can also provide a cross-sectional view of the sample which can be achieved by Focused Ion beam (FIB) or simply cleaving the sample. In fact, the Energy Dispersive X-Ray Spectroscopy (EDX) feature in both the SEM and TEM are also very useful for chemical identification. However, the EDX line scans manage to provide details on the perovskite nanoparticles (see Chapter 13), but failed to detect light elements of LiF. Moreover, graphene is transparent under SEM, so these imaging techniques has to be compensated with other methods.

Out of these chemical detection methods, the most sensitive characterization for thin micelles is the FTIR in Reflection mode. It is capable of detecting even the thinnest layer of micelles on Si. However, when considering also for the graphene system, since pristine graphene has no IR active modes, FTIR is not ideal for the

transfer printed system that involves graphene (see Chapter 6).

XPS and XRD usually requires high volume of material. For instance, the minimum thickness of iron oxide to be detectable by XRD is at least 200 um, which would be multi-layer thick for the nanoparticles made by RMD. Therefore, it is not suitable for the purpose of detecting thin interlayer nanoparticles. XPS can provide important compositional information (see Chapter 12.1), whereas XRD can provide structural information of the material.

It was found that out of all the techniques, Raman spectroscopy is the best for characterizing the micelles (with or without the nanoparticles), organic layer and graphene. Using the 455nm LASER source, the heavy fluorescent from the Cu background where graphene is synthesized on will not overwhelm the relatively weak signals from the polymeric micelles. The excellent capabilities of Raman will be discussed in the chapters to follow.

Chapter 8

Advanced Unconventional Tip-enhanced Raman Spectroscopy on Ultra-thin Reverse Micelles

8.1 Introduction

Tip-enhanced Raman spectroscopy (TERS) is a powerful technique that utilizes the incorporation of a fine scanning probe for obtaining both chemical and morphological information of a sample down to the nano-regime. Due to the many mechanisms proposed and confirmed by various groups, the Raman spectrum from TERS are enhanced in terms of signal strength for orders of magnitude (10^4) and also modes which do not exist in normal Raman scattering conditions.[167] It is particular useful when it comes to a thin sample that is beyond the detection limit of a normal Raman set-up. Some extended Raman techniques are available, such as the Interference-enhanced Raman spectroscopy (IERS) and Surface-enhanced Raman spectroscopy provide also a better enhancement than normal Raman, where IERS relies on pure optics effect of interference and SERS makes use of surface plasmons (SPR) generated by the metallic layer on the substrate to enhanced local electric field.[160,161,165,166,174,175,213] However, these techniques are not suitable for device characterization as SERS requires the substrate to be coated with thin plasmonic metallic layer and IERS has a strict thickness threshold for it to work.[160,161,165,166,174,175,213]

SPR is one of the enhancement mechanisms that SERS has in common with TERS

and it was first studied with poly(styrene-b-2-vinyl pyridine) (PS-b-P2VP) diblock copolymer by Hong, Tsai and et al.[166,213] The normal vibrational Raman-active modes and SERS-active modes of PS-b-P2VP has been well-documented.[166,213] The sensitivity of the PS-b-P2VP to substrate due to the pyridine group is also well-reported.[263] It is also practically feasible to be manipulated into different thickness which makes it ideal for gauging the detection limit of TERS. Practically, this diblock copolymer has been used in various occasions to synthesize nanoparticles, which can be implemented into devices.[18,74,243,264]

The superior detectability of TERS over normal Raman is then crucial for organic device making as it makes detection of nano-structured materials and thin organic layers possible. Moreover, unlike SERS, TERS is considered more non-destructive because the tapping motion of the tip never alters the structure of the material while the SERS substrate needs to be coated with plasmonic material that could in turn react the material of interest permanently.[166,213]

The scanning probe material can be a selection of scanning tunnelling microscopy (STM) probe or atomic force microscopy (AFM) probe, which is employed in this specific study. There are two modes of TERS in terms of tip preparation, the conventional mode and here in the study, the gap-mode, of which the AFM probe is coated with nobel metal for its plasmonic property.[167] Due to the geometry of the AFM probe, a bottom illumination optical design of TERS was used. The limitation of this approach is that it requires the sample and the substrate to be completely transparent as the laser comes from the bottom side (Figure 8.2 a), which is not a concern for PS-b-P2VP. This bottom illuminated TERS is denoted as inverted-TERS for discussion purpose.

It was found possible for inverted-TERS to detect a monolayer of micelles produced by the PS-b-P2VP diblock copolymer with an exceptionally informative Raman spectrum. The Raman spectra of PS-b-P2VP of inverted-TERS, inverted normal Raman, SERS and normal Raman (upright) are investigated and the far-field enhancement mechanisms of TERS due solely to the tip will be highlighted.

8.2 Results and discussion

The Raman-active spectra of a PS-b-P2VP diblock copolymer should consist of components from both the the PS and the VP part. Figure 8.1 a shows a hexagonal dispersion of a monolayer micelles spin-coated on Si and an inset of a schematic of each

micelle, displaying the PS and P2VP blocks. It is true that theoretically, due to the differences between molecular weight of the PS and P2VP blocks, the Raman modes of the final PS-b-P2VP may show dominance of either blocks.[166] In our study, in spite of the molecular weight difference, the Raman spectra of reverse micelles synthesized with various types of di-block copolymer are very similar (see Figure 8.1 b).

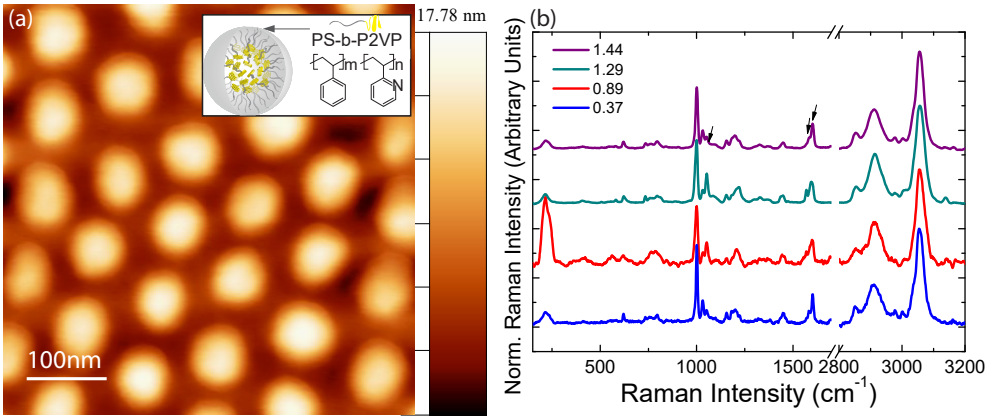

Figure 8.1: (a) AFM topography of a monolayer P1330 micelles spin-coated on Si. Inset: schematic of a PS-b-P2VP reverse micelle. (b) Offset normalized Raman spectra of various diblock copolymer, showing P1330 (purple curve), P9861 (green curve), P4824 (red curve) and P10492 (blue curve) drop-casted on KBr measured by normal upright Raman.

Therefore, the thick micelle layers drop-casted on KBr (red curve) and the normal Raman measurements of the bulk PS-b-P2VP flake (black curve) are served as the reference spectra in Figure 8.2 f. The normal Raman spectra of the bulk flake and thick micelles layer agrees with the literature spectrum of PS-b-P2VP.[166,213] Although the spectra has been background subtracted, they do not show any peak shifting or enhancement due to substrate, hence there is no interaction with their substrates. The normal Raman modes are described in detail in Ch. 5.3.3.1 with table 5.4 for all the Wilson's numbering assignments listed.

Since the sample thickness is reasonably thick in both cases of the bulk flake and thick micelles layer, spectra of good signal to noise ratio could be obtained. On the other hand, when the sample gets thinner that the interaction volume for the laser with the sample becomes less, the signal to noise ratio will be higher until only the signal from the substrate background can be obtained, that is when the detection limit of the normal Raman system is reached. The optical set-up upright normal Raman system (Renishaw) is capable of detecting a minimum of six layers of spin-coated

micelles, which is estimated to be near 200nm thick.

Any layers of micelles thinner than 200nm remains undetectable by the upright normal Raman, unless the sample substrate is specially coated with a plasmonic metal layer for SERS. The SERS spectrum (blue curve) of a thinner micelle layer is shown in Figure 8.2 e. The SERS spectrum of micelles appears to be different from the normal Raman spectra (blue and black). The micelle layer for the SERS is estimated to be 100nm thick and because of the surface plasmons from Ag sputtered on the Sapphire substrate, the Raman signals were enhanced. For example, the broad peak at 1324cm^{-1} is greatly enhanced and is comprised of two P2VP modes of $\gamma(CH_2)$, the methylene twisting mode and $\nu(13)$, the C-C stretching mode between the pyridine ring and the backbone.[166] The pyridine ring stretching mode (ν(8b)) at 1585cm^{-1} is also greatly enhanced.[166] As discussed in Ch. 5.3.3.1, some modes were shifted due to adsorption of VP block on Ag. Pyridine is a strong adsorbate to silver.[152] The 2VP can be adsorbed to the silver substrate through the nitrogen atoms, which caused the micellar structure of the diblock copolymer to unravel and the bands related to the 2VP increased significantly over time.[166,213] All these modes enhancements were due to the SPR near field effects of SERS and were elaborated in Ch. 5.2.1. However, this SERS spectrum appears to be noisier again due to the detection limit of the upright Raman. Therefore, it is impossible to obtain a Raman signals from a monolayer thick micelles. It is important to emphasize that the plasmonic layer may cause permanent changes to the sample and SERS is practically difficult to be applied on actual device characterization for its substrate requirement.

A monolayer thick micelles spin-coated on Sapphire is estimated to be 30nm by AFM. Although it was undetectable by the upright normal Raman set-up, it was resolvable by the inverted normal Raman. The monolayer thick micelles inverted normal Raman spectrum is plotted as the green curve in Figure 8.2 e. It resembles the reference normal Raman spectra (black and blue) obtained by the upright normal Raman, though not all modes are visible that some weaker modes in the 1100-1200cm^{-1} are hidden in the noise level. The better detectability of the inverted normal Raman set up can be due to the slightly different optical arrangement. Since the set-up involves bottom illumination geometry, an inverted microscope configuration was integrated. An oil-immersion objective with short working distance that the lens and the glass in Figure 8.2 b were actually touching with the oil and a high numerical aperture could be used, which helps with the focusing of laser to the sample and collection of the

scattered laser to the detector.[167] This is a pure far-field optics enhancement effect that mildly improved the detectability of the normal Raman while keeping the laser excitation power the same.

As an AFM probe is mounted to the inverted normal Raman, the set-up becomes a quasi-inverted-TERS configuration in Figure 8.2 a. It is quasi because the AFM probe will never tap on the micelles sample as it is separated by a Sapphire substrate and a glass cover slide, which would be too thick for any near-field optical effect due to the tip to take place as opposed to the tapping proximity of conventional inverted-TERS. Therefore, the SPR effect (see Figure 5.6 a) is not found in the inverted-TERS spectrum (purple curve) in Figure 8.2 e. In fact, the SPR mechanism from plasmonic tip is found to be much more complicated than that in SERS (Ch. 5.2.2). Note that the micelles sample used for inverted normal Raman and inverted-TERS is the same, yet, the effect of the tip is still in play as compared to an inverted normal Raman set up (Figure 8.2 b). The inverted-TERS spectrum is much more resolved and similar to the reference samples. In other words, there is an exceptional detectability by inverted-TERS that is capable of detecting Raman signals from a 30nm-monolayer thick micelles.

Figure 5.6 a-e shows the possible enhancement mechanisms of TERS in general, which is discussed in Ch. 5.2.2. Apart from the near-field effect of SPR in Figure 5.6 a, enhancement from IERS in Figure 5.6 b is also excluded not only for the inverted-TERS but in all other Raman techniques applied in Figure 8.2. Details of the IERS mechanism can be found in Ch. 5.2.3 but the main reason for the exclusion is that the combined thickness of the micelles sample and the substrate for all cases is more than 400nm, which exceeds the IERS condition of $\frac{(2m+1)\lambda}{4}$ for a 514nm excitation laser.[165] Figure 5.6f shows an IERS spectrum of micelles (red curve) under optimized conditions.

The AFM probe in inverted-TERS is possibly providing the following effects in Figure 5.6 c-e. Figure 5.6 c shows the 2nd harmonic generation and the hyper Raman effect, which is achievable when the electric field at the sample is strong as discussed in Ch. 5.2.2. However, it is challenging to verify if the hyper Raman effect alone by the tip as the tip will introduce other optical effects. When the tip is oscillating, the electric field from the tip is changing and hence results in a polarizability gradient of the samples. Some non-active Raman modes can be activated during these non-linear scattering processes. However, since the inverted-TERS spectrum resembles the reference normal Raman spectra, this effect of varying electric field from oscillating

AFM probe is insignificant.

The depolarization of laser due to AFM tip is a possible explanation for the enhanced invert-TERS spectrum. The mechanism is described in detail in Ch. 5.2.2. Some polarization active modes with strong depolarization ratio will be enhanced as compared to its normal vibrational Raman-active modes. The mode at 1454 cm^{-1} due to methylene deformation and 1613 cm^{-1} due to the ring stretching mode of P2VP could be greatly enhanced due to the polarization.[265] To verify this effect, a polarized Raman control measurement was conducted on thick micelles layers with the upright Raman set-up and the spectrum is shown in Figure 5.6 f (green curve). In fact, the existence of the AFM probe helps further with the far-field focusing such that more scattered light is harvested at the detector.

The final enhancement effect of inverted-TERS can be a combination of all the far-field effects due to the tip for 2nd harmonic generation, hyper Raman, depolarization and improved focusing ability of the set-up.

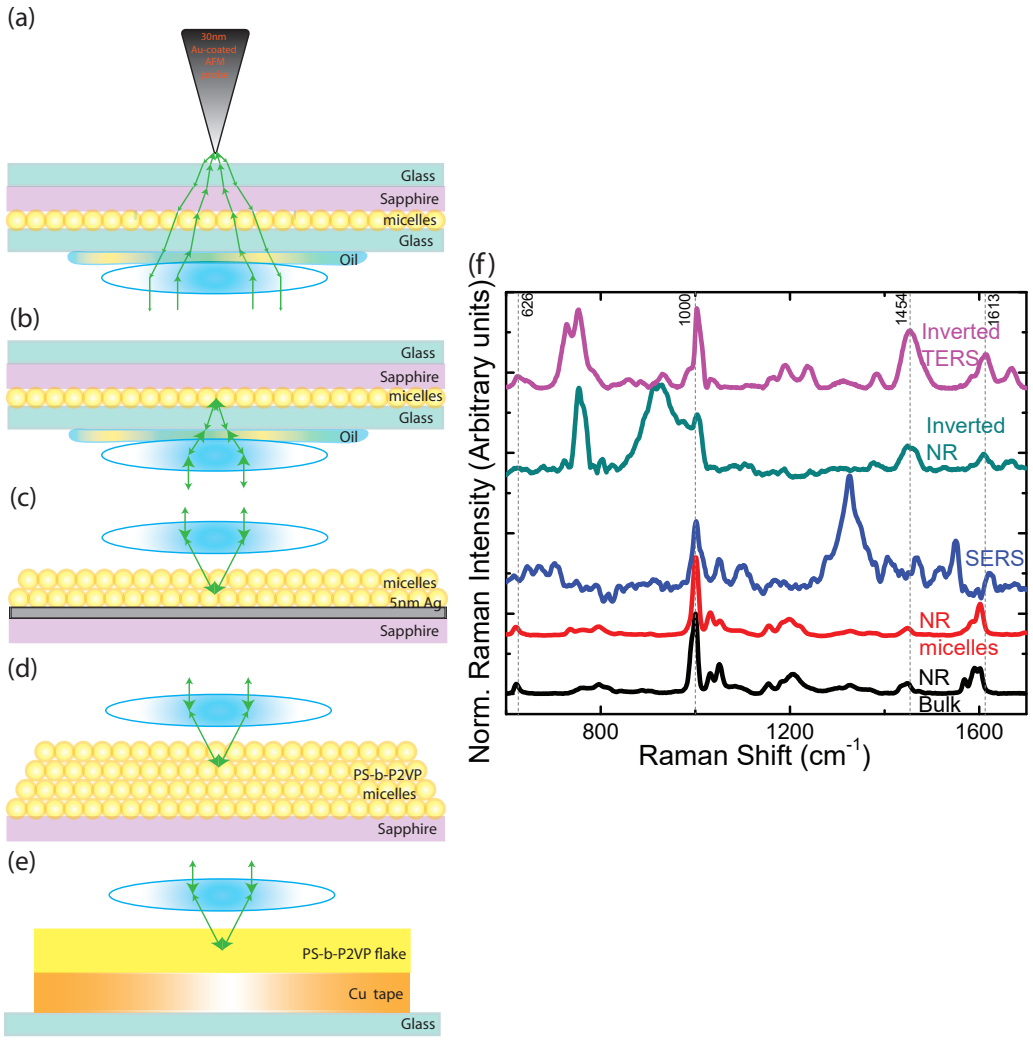

Figure 8.2: Configurations of various Raman set-ups for (a) Inverted TERS of monolayer micelles; (b) Inverted normal Raman of monolayer micelles; (c) SERS of multilayer micelles on 5nm-Ag-coated Sapphire; (d) Normal Raman of drop-casted thick micelles layers on KBr and (e) Normal Raman of bulk PS-b-P2VP flake on Cu tape on glass. (f) Raman spectra of micelles of all techniques in the schematic.

8.3 Conclusion

Detection of monolayer thick polystyrene-*block*-poly(2vinyl pyridine) is found possible by invert-TERS, which is unachievable by normal upright Raman measurements. Though the configuration of inverted-TERS is different compared to conventional inverted-TERS, the presence of the AFM probe is substantial to promote signal enhancement from far-field optical effects. Tip depolarization of laser, strengthened electric field from focusing that results in 2nd harmonic generation and hyper-Raman effect are investigated and proposed to be the contributing factors of the signal enhancement. Unlike SERS, this unconventional inverted-TERS technique provides a highly resolved characterization method for ultra-thin samples without disrupting the sample structure during measurement. It will be extremely helpful for characterization of organic devices, where the interlayers are covered by layers of organic matter that the near-field enhancement of TERS will not be applicable and in turn, will have to rely on the far-field enhancement effects of from the AFM tip of inverted-TERS.

Chapter 9

Structure tunability from manipulation of reverse micelle deposition: single crystalline maghemite (γ-Fe_2O_3) nanoparticles with tunable coercivity

9.1 Introduction

Magnetic iron oxide nanoparticles are of widespread interest due to their abundance, stability, and biocompatibility.[253,266–268] Aside from their use in fundamental research on the mechanisms of magnetization, they have a wide variety of applications,[268,269] including high-density data storage disks,[270] Li-ion batteries,[271] gas sensors,[272] solar cells,[273–275] drug delivery systems,[276] catalysis,[277] and magnetic resonance imaging..[278,279] It is generally difficult to synthesize iron oxide nanoparticles with controlled size, narrow size distribution and a target crystal structure through thermal synthesis routes due to the complexity in the control of nucleation and particle growth.[280] Understanding the evolution of the synthesis process for a versatile low cost approach for monodisperse single phase nanoparticles is critical to tuning nanoparticle properties for widespread application.

The crystal structure of iron oxide nanoparticles has a strong impact on their

magnetic properties as the arrangement of Fe and O atoms controls the arrangement of magnetic dipoles. Numerous phases of iron oxide are possible with different crystallographic structures and/or variable oxidation states of the Fe ions but not all show significant magnetic properties. Each of the polymorphs of iron oxide has a different structure and thus diverse magnetic properties..[193] For iron(III) oxide, the α-Fe_2O_3 with corundum structure ($R\bar{3}\bar{c}$) and the γ-Fe_2O_3 with an inverse spinel structure ($P4_132$) are present in nature, while other polymorphs: β-Fe_2O_3 with bixbyite structure ($Ia\bar{3}$) and ϵ-Fe_2O_3 with orthorhombic structure ($Pna2_1$) are rare phases only produced in the laboratory.[193,194] The other naturally occurring phase, iron(II,III) oxide (Fe_3O_4), also possesses a similar inverse spinel structure as γ-Fe_2O_3. Among these phases, only γ-Fe_2O_3 and Fe_3O_4 possess ferrimagnetism with relatively high accessibility at room temperature.[195] γ-Fe_2O_3 is of particular interest in practical applications owing to its high Curie temperature (T_c = 928K) and stability against oxidation.[195,266,281] However, as the α-Fe_2O_3 phase is more thermodynamically stable, it is possible to convert γ-form iron oxide to the α-form with annealing.[193,196,197,208,266]

The saturation magnetization, M_s, and thus the response to an external magnetic field, of γ-Fe_2O_3 is strongly affected by particle size, especially in the nanometer regime.[282,283] 35 nm average diameter was reported as an upper bound for γ-Fe_2O_3 nanoparticles where the M_s is almost as high as that observed in bulk films.[196] As the ratio of surface to bulk atoms increases with smaller particle size, incomplete coordinations and broken exchange bonds on the surface can lead to surface magnetic anisotropy, and a decay of the M_s..[284] The surface spin-canting effect can, therefore, be used to tune the magnetic response of iron oxide particles through control of the particle size. Additionally, nanoparticles can lie below the single domain and superparamagnetic limits, heavily affecting the magnetic response. Hence, control of the size and phase of iron oxide is essential for their application.

Due to the capabilities in controlling size and dispersion, diblock copolymers reverse micelles have been applied extensively to synthesize nanoparticles.[74,285,286] Using proper metal precursors, which typically combine with the hydrophilic block, reverse micelles have been adopted to produce nanoparticles of metals, metals oxides and metal alloys.[237,249,286,287] Typically, iron oxide nanoparticles that have been synthesized successfully using polystyrene-*block*-poly(4vinyl pyridine) (PS-*b*-P4VP),[288] polystyrene-*block*-poly(2vinyl pyridine) (PS-*b*-P2VP)[289] and polystyrene-*block*-poly(acrylic acid) (PS-*b*-PAA),[290] are thought to have a γ phase; however, the similar structure of the

two ferrimagnetic phases, γ-Fe_2O_3 and Fe_3O_4, makes it difficult to confirm the exact phase of the system. Additionally, the magnetic properties for resultant nanoparticles are seen to vary significantly based on post processing steps. The detailed evolutions of the phase and structure of the iron oxide nanoparticles produced by reverse micelle deposition have seldom been addressed.

In this contribution, PS-*b*-P2VP was employed to synthesize iron oxide nanoparticles from $FeCl_3$ using oxygen plasma oxidation and post annealing. We examine each step in the reverse micelle synthesis process with Raman spectroscopy to track the formation and transformations of iron oxide nanoparticles. Characterization techniques such as energy-dispersive X-ray spectroscopy (EDX) and electron/X-ray diffraction can provide atomic compositions and crystal structures that only partially differentiate the various phases of iron oxide, while giving limited information on the precursors or the polymeric micelles. On the other hand, Raman spectroscopy relies on an inelastic scattering process of photons with phonons, which can provide detailed information of the material based on the vibrational modes of the phonons. Hence, it is a versatile tool that has been widely used to characterize iron oxides, as different phases exhibit distinctive Raman peaks.[198–201,207] It has also been used to investigate $FeCl_3$[202–204] and PS-*b*-P2VP.[166,213] Therefore Raman spectroscopy was employed to confirm the exact form of the iron oxide nanoparticles and to monitor the processes of the reverse micelles method, to investigate the evolution of iron oxide nanoparticles in different stages. Using Raman, we can clearly identify the interaction between $FeCl_3$ and the hydrophillic P2VP core, proposing two new Raman modes, and monitor the effect of annealing in the transformation of the desirable γ-Fe_2O_3 into weakly ferrimagnetic α-Fe_2O_3. Using insights from examining the entire synthesis process, we have adjusted the processing parameters to achieve coercivity and saturation magnetization values for small nanoparticles ($\sim$6nm) that are usually only obtainable from larger particles (>25 nm). This detailed information can direct the tuning of the magnetic properties of iron oxide nanoparticles for eventual use in a variety of applications.

9.2 Results and Discussions

9.2.1 Iron oxide nanoparticles synthesized by the reverse micelles method

The typical array of iron oxide nanoparticles spin coated on a silicon substrate can be seen in Figure 9.1(a). Produced with a $FeCl_3$ loading ratio of 0.3, these nanoparticles have an average height of 5.5 nm with 1.1 nm standard deviation. SQUID measurements were carried out to investigate the magnetic properties of such iron oxide nanoparticles after oxygen plasma treatment and with two different annealing treatments, high temperature annealing at 600°C in N_2 for 2h, and low temperature annealing at 350°C for 12 hr in N_2 and air. Figure 9.1(b) shows the magnetization-applied magnetic field curves (M-H curve) of the sample with iron oxide nanoparticles array, normalized by the total sample weight including the substrate. Since the area density of iron oxide nanoparticles on the substrate and the volume of each iron oxide nanoparticle can be estimated from Figure 9.1(a), saturation magnetizations can be normalized by the total weight of iron oxide nanoparticles themselves without the substrate, assuming bulk iron oxide density for each nanoparticle. For high temperature annealing, the magnetization saturates at around 2000Oe applied magnetic field, showing a similar saturation magnetization as reported by Yun et al.[288] for similar sized particles, approximately 30 emu/g. Such small nanoparticles are expected to be below the single domain limit of ∼50nm (see supporting information), such that each particle is defined by a single magnetic dipole. As magnetization reversal can only happen with magnetic moment rotation without the domain wall motion, single domain nanoparticles could have large coercivity (H_c) compared to the larger multidomain particles.[196,291] In our systems, there is a relatively small coercivity (∼ 50 Oe), which is larger than that observed by Yun et al. for similar particles. Additionally, we were able to improve both the coercivity and the saturation magnetization by annealing the particles at a lower temperature, achieving ∼100 emu/g and ∼100 Oe. Though tuning of the magnetic response has been observed with changing particle size,[193,253,288,292] we observed no significant change in the particle size as a function of annealing. It is possible that this response is related to the purity of the crystal structure of the final particles, resulting from differences in annealing conditions.

To verify the composition and structure of the nanoparticles, STEM equipped with EELS was employed, where compositional information was collected by the electron energy loss signal (change in kinetic energy) from the inelastic scattering of electrons that interacted with the samples. High magnification STEM images and the EELS elemental maps were acquired to directly compare the position of the nanoparticles with the intensity of the elemental components in a selected area as shown in Figure 9.1(c). As the iron(Fe) and oxygen(O) signals were concentrated in the areas corresponding to the nanoparticles in the STEM image, we confirmed that the nanoparticles were composed of Fe and O. In addition, the lack of Cl and C characteristic energy loss peaks in the EELS spectrum (see supporting information Fig. SI2) indicates that the oxygen plasma and annealing treatments are adequate to oxidize the $FeCl_3$ precursor and remove the polymeric micelles of the single layer spin-coated sample. Moreover, the high resolution TEM image in Figure 9.1(d) reveals single crystal nanoparticles with clear lattice fringes. The inset Fast Fourier Transform of this nanoparticle generates a pattern with 4 different d spacings of 4.8 Å, 2.9 Å, 2.5 Å and 2.1 Å (labelled as 1, 2, 3 and 4 respectively), which can be assigned to the (111), (220), (311) and (400) lattice planes of γ-Fe_2O_3(JCPDS number 39-1346) or Fe_3O_4 (JCPDS number 19-629). The selected area electron diffraction pattern from a large number of nanoparticles also provides a similar result (see supporting information Fig. SI2). As they share the similar inverse spinel structure with only around 1% difference in lattice constant.,[195,268,293] it is hard to distinguish the exact phase between the γ-Fe_2O_3 and Fe_3O_4 with electron diffraction or x-ray diffraction methods. In addition, both γ-Fe_2O_3 and Fe_3O_4 are ferrimagneitc in nature which could yield a similar M_s and M-H curve.[196] As a consequence, SQUID measurements are not sufficient to distinguish between them either. Based on the TEM measurements, no significant differences between low and high temperature annealing was observed.

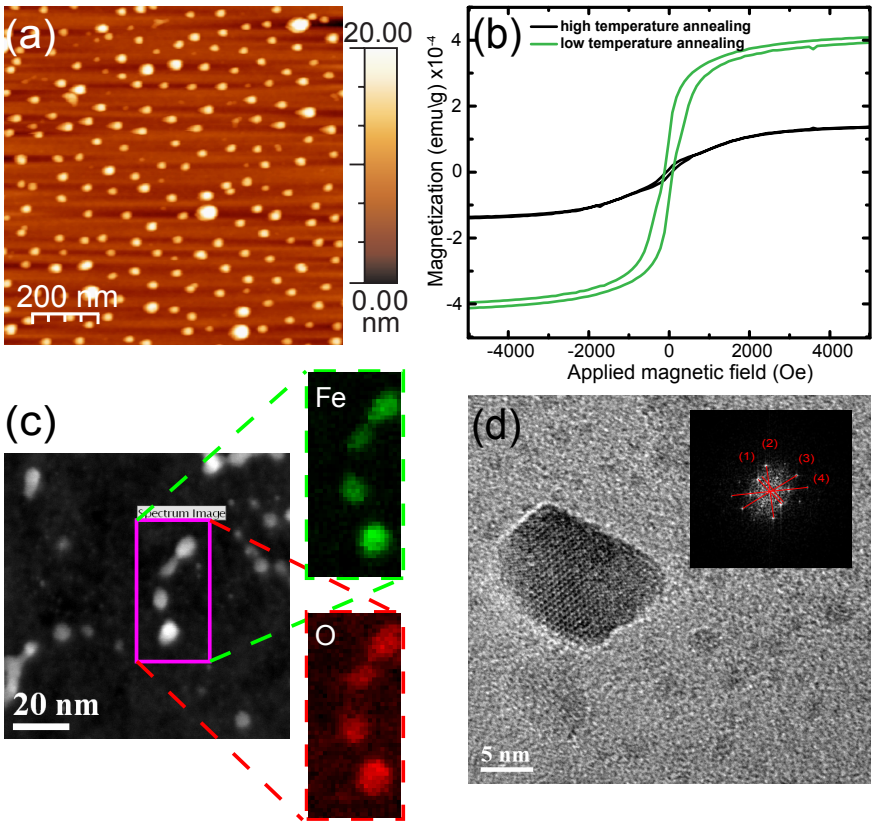

Figure 9.1: Confirmation ofs iron oxide nanoparticle formation after reverse micelle deposition. (a) AFM topography image of mono-layer spin-coated nanoparticles on Si; (b) Magnetization-applied magnetic field curves at 300 K of monolayer spin-coated nanoparticles on Si with different annealing conditions; high temperature corresponds to 600°C, N_2 for 2h while low temperature to 350°C N_2 and air for 12h; magnetization was normalized by total sample weight including the substrate (c) STEM of the nanoparticles with EELS Fe and O elemental mapping; (d) High resolution TEM (HRTEM) of a single nanoparticle annealed at 600°C (inset show the fast Fourier transform pattern the HRTEM image).

9.2.2 Raman spectroscopy for phase identification of the iron oxide nanoparticles

Raman scattering radiation is an inelastic scattering process of photons with phonons, which can provide detailed information of the material based on the vibrational modes of the phonons. The Raman spectra originates from the Stokes and anti-Stokes components in the dipole moment, from which the polarizbility can be expanded as a linear function of oscillation frequency and its availability is governed by selection rules.[152] As an incident phonon interacts with a molecule, it induces a dipole moment P to the electron cloud. The Raman spectrum can be induced by the frequency shift from the incident frequency (μ_0) of the phonon as a result of the vibrational frequency of the molecule (μ_{m}). It is therefore, capable of revealing the material properties, such as the atomic bonds, vibrational states, purity, crystallinity and strain.

Raman spectroscopy has been applied to identify the phase of iron oxide thin films,[208] particle aggregations[196] and bulk solids.[294] Given the different crystal structures of the Fe_xO_y polymorphs, the vibrational modes and Raman spectra of α , β , ϵ and γ of Fe_2O_3, Fe_3O_4 and $FeCl_3$ have been observed to be distinct from each other.[197–203] Using group theory, the active Raman modes of a system can be predicted. The γ-Fe_2O_3 with the $P4_132$ space group has five (A_{1g}, E_{1g} and 3 T_{2g}), mathematically describing their atomic vibrations against their rotational principle axis and inverse structures. Though γ-Fe_2O_3 and Fe_3O_4 belong to the same space group, the observed Raman phonons at similar wavenumber have a different atomic origin, making them easily distinguishable.[196,198] This provides a convenient way to differentiate between γ-Fe_2O_3 and Fe_3O_4. Raman can as well readily determine the purity of the crystallographic phase in the particles under various conditions, as α-Fe_2O_3 with $R\bar{3}c$ space symmetry possesses seven Raman active modes ($2A_{1g}$, $5E_g$). Raman is also capable of differentiating the hydrogenated $FeCl_3$ species[202,203] and peaks shifting induced by laser illumination for α-Fe_2O_3.[193] Table 9.1 summarized the characteristic peaks for several phases of iron oxide and $FeCl_3$.

The Raman spectra of the diblock copolymer and its components have been well-reported in literature[166,213] with modes mostly in the higher wavenumber regime, which do not interfere with the iron oxide modes. When $FeCl_3$ infiltrates inside the reverse micelles, it is expected that the Raman modes of the polymer will be shifted due to the steric hinderance of Fe-2VP complexation, as had been observed previously for the IR

Table 9.1: Table of expected Raman peaks (cm^{-1}) for $FeCl_3$ and several phases of iron oxide

$FeCl_3$[203–206]	α-Fe_2O_3[207]	γ-Fe_2O_3[208]	Fe_3O_4[209]
	225 (A_{1g})		
	247 (E_g)		
282 (A_{1g})	293 (E_g)		
			301 (T_{2g})
330* (A_{1g})			
		365 (T_{2g})	*hydrated $[FeCl_4]^-$
	412 (E_g)		
	498 (A_{1g})	511 (E_g)	
			533 (T_{2g})
	613 (E_g)		
			663 (A_{1g})
		700 (A_{1g})	

spectrum,[215] though this has not been previously reported. As Raman can be used to monitor the precursors, the micelles and the resultant particles simultaneously under various processing steps, it is an excellent candidate for studying the polymorphous transition of the iron oxide nanoparticles from the very beginning of the synthesis process.

The Raman spectra from each step of the reverse micelle process can be seen in Figure 9.2 from (a) to (f), with assignments for visible features summarized in Table 9.2. Starting from the spectrum of the empty micelles in Figure 9.2(a), two significant peaks at 1000cm^{-1} and 1591cm^{-1} were visible, which can be assigned to $\nu(1)$ symmetric ring breathing mode and $\nu(8b)$ ring stretching mode of 2-vinyl pyridine (2VP) (complete assignment of the other visible peaks are given in Table SItable1).[166,213]

After the loading of the $FeCl_3$ (See Figure 9.2(c)), a new peak appeared at 294cm^{-1}, which could be related to $FeCl_3$ A_{1g} mode.[204,206] Although the expected A_{1g} mode of a pristine $FeCl_3$ should be at 282cm^{-1},[204] the upshift was probably caused by the configuration change with the $FeCl_3$ coordinated with 2VP.[215] Similar behaviour was observed when $FeCl_3$ intercalated with graphite.[204,206]

Additionally, after loading, the strong symmetric ring mode at 1000cm^{-1} was suppressed, the modes at 1591cm^{-1} were enhanced and new peaks emerged at 1306cm^{-1}, and 1475cm^{-1} which was not observed in the empty micelles.

Table 9.2: Table of observed Raman peaks

Observed Raman shift (cm^{-1})	Related spectra in Figure 9.2	Assignment	References
213	(d)(e)	A_{1g} of α-Fe_2O_3	207,294
223	(f)	A_{1g} of α-Fe_2O_3	207,294
243	(f)	E_g of α-Fe_2O_3	207,294
292	(f)	E_g of α-Fe_2O_3	207,294
294	(c)(d)	A_{1g} of $FeCl_3$	204,206
330	(b)	A_1 of hydrated $FeCl_3$	203,205
345	(e)	T_{2g} of γ-Fe_2O_3	208
385	(e)	T_{2g} of γ-Fe_2O_3	208
409	(f)	E_g of α-Fe_2O_3	207,208
497	(f)	A_{1g} of α-Fe_2O_3	207,208
507	(e)	E_g of γ-Fe_2O_3	208
610	(f)	E_g of α-Fe_2O_3	207,208
663	(f)	LO E_u of α-Fe_2O_3	208
677	(e)	A_{1g} of γ-Fe_2O_3	200,294,295
725	(e)	A_{1g} of γ-Fe_2O_3	200,294,295
1000	(a)(b)(c)(d)	Symmetric ring breathing of 2VP	166,213
1155	(b)(c)(d)	P4824 CH in-plane bending	166,213
1306	(b)(c)(d)	*$FeCl_3$-P2VP complex	this work
1446	(b)(c)(d)	P4824 ring stretching	166,213
1475	(b)(c)	*$FeCl_3$-P2VP complex	this work
1591	(a)(b)(c)(d)	Ring stretching of 2VP	166,213

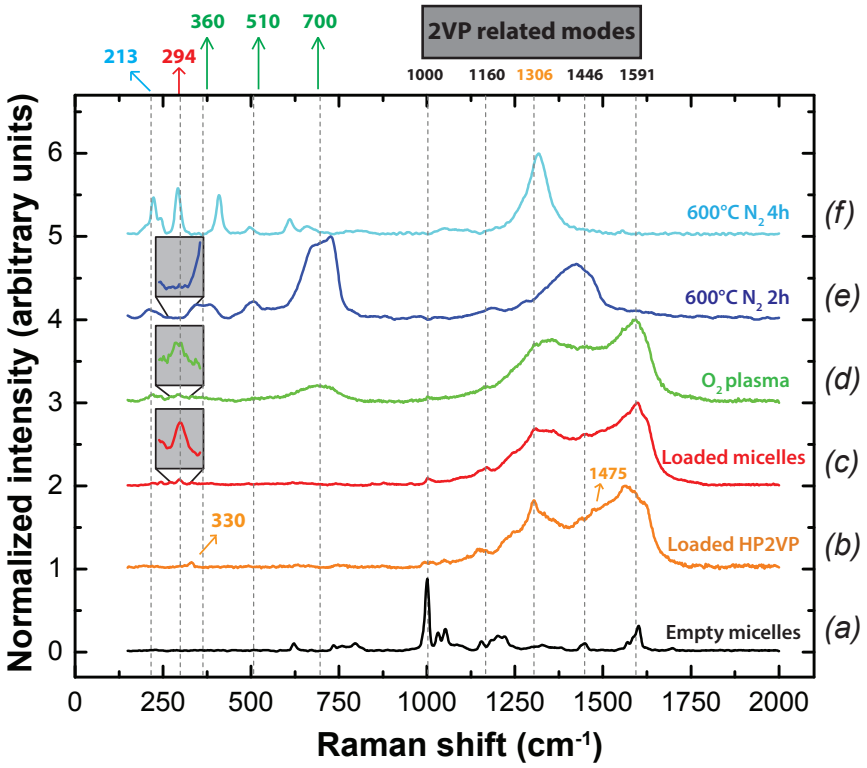

Figure 9.2: The Raman spectra of the evolution of the iron oxide nanoparticles synthesized by the reverse micelles method. Note that the intensity of magnified insets for spectra labeled (c) Loaded micelles, (d) O_2 plasma and (e) 600°C N_2 2h are amplified by 5x in the region from 270 to 320cm^{-1} to highlight the peak.

To confirm that this is due to the interaction of $FeCl_3$ and the hydrophilic interior of the micelle, a homopolymer HP2VP/$FeCl_3$ mixture was examined, as shown in Figure 9.2(b). The peaks above 1000cm^{-1} were very similar to that of the loaded micelles, reinforcing that the new peaks could be attributed to the interaction between $FeCl_3$ and 2VP. Similar emergence of shifted IR modes was observed by Sageshima et al.,[215] assigned to the complexation of the Fe^+ ions with the lone pair electrons on N at the pyridine ring. As can be seen in supporting information Figure SIcontrol and Table SItable1, these features were not observed for the homopolymer HPS/$FeCl_3$/o-xylene mixture sample (which only showed PS features) nor for $FeCl_3$/o-xylene sample (which only show the hydrated $FeCl_3$ and o-xylene features), reinforcing that they originated from the interaction between $FeCl_3$ and 2VP groups.

The activation of those peaks likely arise from the $FeCl_3$-2VP complexation when the system was brought into resonance by the incident frequency of the laser at

514nm.[153,215] It has been reported that Fe-complexes of bipyridine (bipy) exhibit strong absorption near 520nm due to the allowed electronic dipole Fe(3d)-ligand (π) charge-transfer transition, such that the active vibrational modes of this electronic transition, which are also totally symmetric, are strongly enhanced.[153,296] It is therefore expected that these same features would be visible for the FeCl-2VP complex inside the micelles, which mimics closely the structure of a Fe-bipy complex (see Figure 9.4). Under such resonance, the strong symmetric ring mode at 1000cm^{-1} has also been observed to be suppressed for bipyridine-$FeCl_3$ complexes.[153,296] For this reason, the strong mode at 1000cm^{-1}, clearly visible in the empty micelles spectrum in Figure 9.2(a) became barely detectable in both the loaded micelles and loaded HP2VP spectra of Figure 9.2(b) and (c), effectively caused by the role of Fe complexating with the pyridine group.

The HP2VP/$FeCl_3$ mixture solution, Figure 9.2(b), also shows a low wave number peak related to $FeCl_3$ similar to the micelle loaded spectrum in Figure 9.2(c); however, in this case, the peak is extremely red shifted to 330cm^{-1}. This can be assigned to the hydrated $FeCl_3$-P2VP complex A_1 mode[203,205] due to hygroscopic nature of the $FeCl_3$ and the affinity of Fe ion with the VP group as proven by the presence of the 1306cm^{-1} $FeCl_3$-P2VP complex mode in the spectrum. Unlike in the micelles, which provide a shielded environment for salts infiltrated inside due to the hydrophobic PS groups in the shell, the $FeCl_3$ salts are upon deposition exposed to water adsorbed on the KBr substrate when complexating on the homopolymer HP2VP chain. This effect is also observed for $FeCl_3$ salts dissolved in o-xylene deposited directly on the KBr substrates (see supporting information Figure SIcontrol), accompanied by a peak at $\approx$ 1550 cm^{-1}, not observed for the micelle loaded mixture.

In the reverse micelle deposition process, oxygen plasma is used to simultaneously convert the precursor into iron oxide and remove the polymeric micelle shell surrounding the nanoparticles. The spectrum of loaded micelles after 25mins O_2 plasma treatment appears in Figure 9.2(d). A broad peak emerged at around 700cm^{-1}, which could be assigned to the A_{1g} mode of γ-Fe_2O_3; this provides evidence of the iron oxide formation after plasma treatment. This was further supported by the appearance of a new peak at 213cm^{-1} which could be attributed to A_{1g} mode of the laser induced α-Fe_2O_3 due to local heating.[207,297] Chourpa et al.[294] found that using laser power higher than 1.6mW could lead to the instantaneous transformation of Fe_2O_3 from the γ

phase to the α one, with an accompanying blue shift of the Raman peaks. Though 25 mins plasma etching is sufficient to completely remove the di-block copolymer shell for a spin coated monolayer of nanoparticles (see Figure 9.1), the features consistent with the $FeCl_3$-2VP complexation, both above 1000cm^{-1} and at 294cm^{-1}, persisted without significant change of intensity. This suggests that the majority of the loaded micelles were unaffected by the O_2 plasma. One possible explanation is that only the surface regions reacted with O_2 plasma due to the thick layer of loaded micelles from drop-casting.

To promote formation of γ-Fe2O3, the O_2 plasma treated sample was annealed at 600°C in N_2 for 2h (Raman spectrum in Figure 9.2(e)). The 2VP related peaks at above 1000cm^{-1} disappeared while the second order scattering broad peak of γ-Fe_2O_3 at around 1420cm^{-1}[208] emerged, demonstrating the complete removal of all the carbon-based micelles by annealing. As shown in the insets, the $FeCl_3$ A_{1g} peak at 294cm^{-1} also vanished, compared with that of the loaded micelles (Figure 9.2(c)) and post-O_2 plasma treatment (Figure 9.2(d)) spectra. The disappearance of the FeCl_2VP complexation related peaks suggests the complete removal of micelles and complete conversion of the $FeCl_3$ for the drop-cast sample. To clearly identify the crystallographic phase, the characteristic peaks of iron oxide below 900cm^{-1} were fitted with Lorentzian functions to aid in the assignment of the vibrational modes (See Figure 9.3(a)).

The center positions of the fitted Lorentzian peaks from Figure 9.3 were listed in the first column of Table 9.2 along with the peak assignments and references. After the first annealing step (600°C, N_2, 2h) (Figure 9.3(a)), the broad peak at around 700cm^{-1} could be fitted with two Lorenztian components at 677cm^{-1} and 725cm^{-1}, representing the A_{1g} stretching mode of tetrahedral units in γ-Fe_2O_3.[198,200,294,295] The peak at 507cm^{-1} could be assigned to the symmetric E_g mode (vibration of O with respect to Fe) of γ-Fe_2O_3 while the broad peak at around 360cm^{-1} related to the translatory three dimensional T_{2g} mode of γ-Fe_2O_3 had two Lorenztian component at 345cm^{-1} and 385cm^{-1}.[198,208,294] These characteristic peaks indicate that the iron oxides nanoparticles were in the γ form after annealing at 600°C in N_2 for 2h, with no evidence of Fe_3O_4, referencing Table 9.1. However, a peak observed at 213cm^{-1} is likely the A_{1g} mode of α-Fe_2O_3. Though this might result from the laser heating effect,[207,297] it is also possible that the sample is a mixture of γ and α phases. As 600°C is sufficient to convert γ form iron oxide to the thermally stable α form,[196,208] further annealing

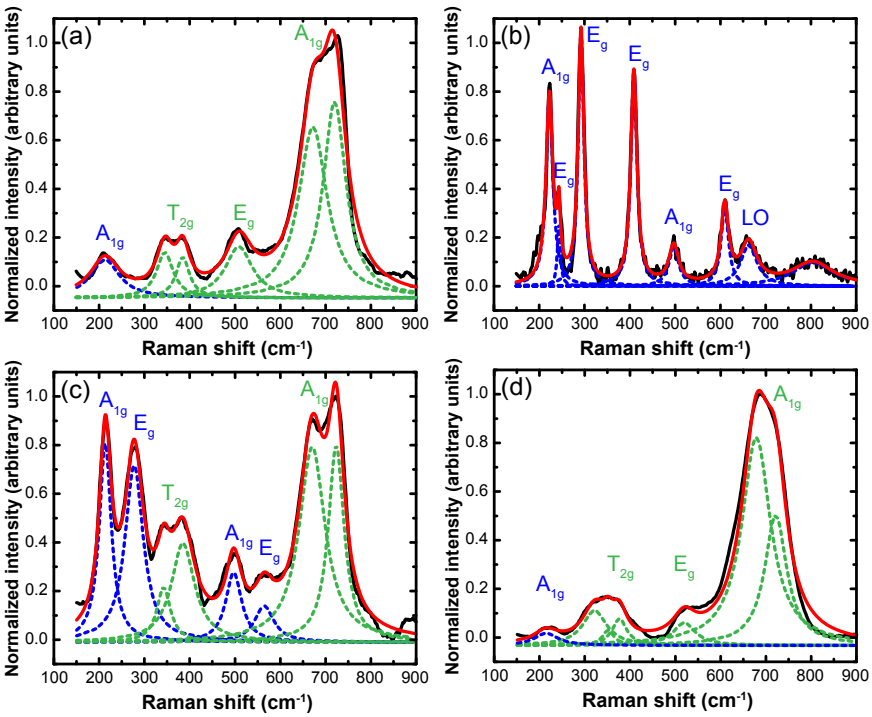

Figure 9.3: Raman spectra of the iron oxide nanoparticles under various annealing conditions with peaks fitting. (a) Annealing at 600°C under N_2 environment for 2h; (b) Annealing at 600°C in N_2 environment for 4h. (c) Annealing at 600°C in N_2 and air environment for 6h (d) Annealing at 350°C in N_2 and air environment for 12h. Note that the spectra were fitted with Lorentzian line profiles.

treatments were performed to study the evolution of the nanoparticles (See Figure 9.2 f)) and (Figure 9.3(b)-(d).

Figure 9.3 (b) shows the Lorentzian-fitted spectrum after a second annealing step (600°C, N_2, 2h) for a total annealing of 4h at high temperature. This second annealing step yield a Raman spectrum which is distinct from Figure 9.3(a). The spectrum features can be considered as mostly characteristic of α-Fe_2O_3. Five E_g modes should be expected for α-Fe_2O_3 but two of them (293cm^{-1} and 299cm^{-1}) are typically resolvable only below 100K.[207] As our Raman spectra were collected at room temperature, four symmetric double-degenerate E_g modes[207,208,298] – 243cm^{-1} and 292cm^{-1} (vibrations due to Fe atoms), 409cm^{-1} (vibrations of O ions with respect to the Fe ions in the plane perpendicular to the c-axis of the hexagonal unit cell) and 610cm^{-1} – of α-Fe_2O_3 were observed.The other two peaks of α-Fe_2O_3 at 223cm^{-1} and 497cm^{-1} could be assigned to the A_{1g} stretching modes due to the vibrations of Fe ions moving along the c-axis of

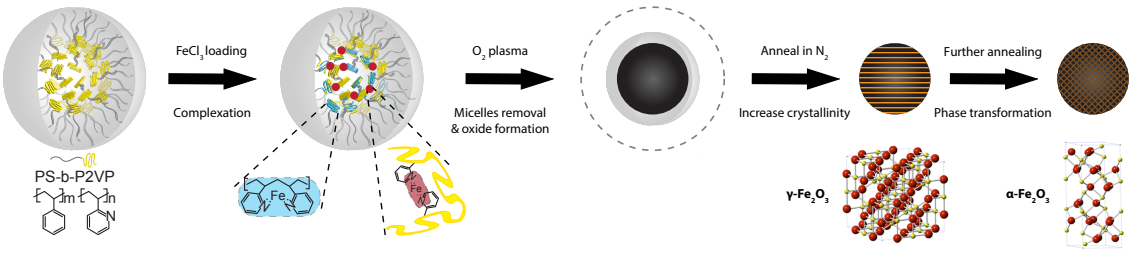

Figure 9.4: Schematic of the evolution of iron oxide nanoparticles synthesized by the reverse micelles method.

the hexagonal unit cell and O ions moving along the c-axis of the hexagonal unit cell respectively.[207,298] In addition, the peak at around 660cm^{-1} can be considered as the IR active longitudinal optical E_u mode activated by disorder..[197,208,299] The transformation from γ-Fe_2O_3 to α-Fe_2O_3 is further supported by the shift of second order scattering peak from 1420cm^{-1} to 1320cm^{-1}.[197,208] Consequently, the characteristic peaks of Figure 9.3(b) confirm the complete conversion to α form after the second annealing.

To examine the effect on the magnetization, the same sample used for the SQUID measurement in Figure 9.1 (b) was annealed a second time at 600°C in N_2 for 2h, which should covert the γ-Fe_2O_3 to the α-Fe_2O_3 as indicated in the above Raman results. The weak ferromagnetic nature of α-Fe_2O_3[193] and the small amount of the nanoparticles on the Si substrate resulted in a very weak M-H response that was below the detection limit of the SQUID, further confirming that the ferrimagnetic γ-Fe_2O_3 nanoparticles was responsible for the magnetic response as shown in Figure 9.1(b).

As the environment during annealing can also affect the phase transformation of iron oxide nanoparticles,[193] nanoparticle arrays were also annealed at 600°C in air for 6h. Figure 9.3(c) shows the Lorentzian-fitted spectrum, where features of both α and γ-Fe_2O_3 could be observed. Using a ratio of the peak areas for the A_{1g} mode for the α-Fe_2O_3 and γ-Fe_2O_3 modes, sample shows that around 52% γ phase is present in the samples. SQUID measurements of monolayer arrays with similar annealing conditions again resulted in a very weak M-H response below the detection limit of the SQUID.

Both Raman and SQUID measurement indicate that high temperature annealing can lead to the complete or partial transformation from γ phase to α phase, which reduces the magnetic response. However, with low temperature annealing procedures,

it is possible to minimize the formation of α-Fe_2O_3. As shown in Figure 9.3(d), annealing for 12hr at 350°C significantly decreases the A_g mode from α-Fe_2O_3 and allows all three T_{2g} modes from γ-Fe_2O_3 to be resolved. As this sample showed an increased magnetic response with the H_c ∼100Oe and M_s around 100 emu/g without any increase in the size of the nanoparticles, it is likely that the nanoparticle array produced under these conditions is mono-phase γ-Fe_2O_3. As SQUID is more sensitive to the crystallographic structure of the nanoparticle array, it is likely that the initial high temperature annealing process at 600°C for 2h for a monolayer of nanoparticles already resulted in a mixed phase (only 89% γ-Fe_2O_3), reducing the magnetic properties, even though diffraction indicated predominately γ phase formation. Partial conversion of the structure to α form may also account for the discrepancy in the coercive field an magnetic response as reported by Yun et al. for particles of similar size prepared in a similar manner.[288] Slightly different annealing conditions may have lead to a different mixed phase configurations with different magnetic responses.

Combining the results from the TEM, SQUID and Raman analyses, we can summarizes the complete iron oxide nanoparticles synthesis processes in Figure 9.4: In the beginning, the PS-*b*-P2VP reverse micelles are formed in a PS selective non-polar solvent. When $FeCl_3$ is added, it complexates with P2VP through the interaction of the Fe+ ion with two pyridine rings, resulting in loaded micelles. Oxygen plasma treatment removes the carbon-based micelles and forms iron oxide in the γ form. Annealing the nanoparticles results in γ-Fe_2O_3 with a high degree of crystallinity. It is also possible to control the partial or complete transformation of the particles into α-Fe_2O_3, particularly by annealing at high temperatures.

9.3 Conclusion

In this study, the iron oxide nanoparticles synthesized by PS-*b*-P2VP reverse micelles was evaluated by TEM, SQUID and Raman spectroscopy. This approach can yield pure γ-Fe_2O_3 nanoparticles with controlled size and a narrow size distribution, if the conditions are carefully controlled. The Raman spectra for each stage of the synthesis also contained some unique features that helped to reveal the evolution of the nanoparticles. We were able to identify characteristic spectral features related to the complexation of $FeCl_3$ with the P2VP component of the di-block copolymer micelles, including two new Raman modes, by comparing the spectra of empty micelles, loaded

micelles, precursors and loaded homopolymers for P2VP and PS. Infiltration of the iron salt into the micelle was shown to protect it from hydration. Due to the sensitivity of Raman to the different vibrational modes of iron oxide polymorphs, Raman analysis of the low wave number region allowed for clear phase identification between γ-Fe_2O_3, Fe_3O_4 and α-Fe_2O_3 as the resultant crystallographic phases with plasma etching and annealing treatments. High temperature annealing was observed to produce mostly γ phase, with some conversion to the more thermally stable α phase. Mixed phase formation can be eliminated by extending the annealing time at high temperature or by lower temperature annealing to produce crystallographically pure nanoparticles, tuning the properties without changing the particle size. Understanding the evolution of the synthesis process allows for the tuning of the nanoparticle properties, which can be lead to targeted synthesis for particular applications.

Chapter 10

Raman study of Methylammonium Lead Bromide Nanoparticles Complexation with Reverse Micelles Nanoreactor

10.1 Introduction

Organic-inorganic halide perovskites is the next most promising material for cost-effective and high power conversion efficiency solar cells.[43,300] There are examples of perovskite materials being used for improving solar cells both as bulk thin films for light absorbing and nanomaterials in nanoporous materials for transporter of charge carriers.[43] While it is relatively well-developed to make bulk thin perovskite films, making a controlled zero-dimensional perovskite nanomaterial remains a challenge as the resultant particles come in ranges of size and high poly dispersity index (PDI).[43,56]

One of the advantages of using reverse micelles as nanoreactor is its feasibility in controlling the salt sizes formed inside the core with low poly dispersity. This approach of making controlled size of nanoparticles with reverse micelles have been reported in detailed elsewhere, and perovskites materials such as formamidinium (FA) lead iodide ($FAPbI_3$) and methylammonium (MA) lead iodide ($MAPbI_3$) were also attempted recently with a PDI of 0.0999 and average size of 6.8 nm.[18,242,301] Herein, we report the first methylammonium lead bromide ($MAPbBr_3$) nanoparticles synthesized by

the reverse micelles techniques. $MAPbBr_3$ is an excellent perovskite candidate as light emitting diodes (LEDs) for its exceptional luminescent property.[43] Nano-sized $MAPbBr_3$ platelets have shown quantum-confinement effect useful for tuning optical properties for applications in LEDs.[52,56,60,302]

Careful selection of diblock copolymer block lengths for micelles proves to be crucial for size controlling and more importantly, successful $MAPbBr_3$ synthesis. The subsequent characterizations of $MAPbBr_3$ formed by reverse micelles are essential as to ensure $MAPbBr_3$ are constrained inside the micellar shell. Therefore, we use photoluminescence (PL) measurement to look for $MAPbBr_3$ signature in the non-fluorescent micelles and Raman spectroscopy to study chemically the infiltration process of $MAPbBr_3$ in the micelles.

10.2 Results and discussion

Using the reverse micelles as nanoreactor, $MAPbBr_3$ was loaded in the micelles solution. Three types of diblock copolymers (namely P4824, P9861 and P10492 from manufacturer) with different block lengths were chosen initially in attempt for size control of $MAPbBr_3$ nanoparticles. Typical single crystal bulk $MAPbBr_3$ would show a PL peak centre at 540 nm, which can be further deconvoluted into two peaks at 545nm and 560nm.[234] In order to test whether the reverse micelles approach yields any working $MAPbBr_3$, PL measurements on the micelles were conducted and presented in Figure 10.1 a.

PL signals were checked on multiple spots for the micelles samples spin-coated on Si substrates. Only the $MAPbBr_3$ in P9861 micelles (black curve) displays a PL signal centre at 540 nm while the other two, P4824 (red curve) and P10492 (green curve) micelles do not. The peak at 540 nm can be resolved into two Gaussian peaks at 533nm (Peak 1) with linewidth 14.7 nm (FWHM) originated from band-to-band transition and Peak 2 at 547 nm with a broad linewidth of 21 nm, originated from trap states recombination on the crystal surface below the optical gap.[234] The fitted PL emissions are blue-shifted likely due to the size confinement of the $MAPbBr_3$ micelles. Hintermayr et al. has also reported on being able to tune the PL emission of $MAPbBr_3$ nanocrystals to as low as 439 nm, which is equivalent to one unit cell thick of 2D $MAPbBr_3$ nanoplatelets synthesized by the Sichert group.[56,302] The PL results are one of the indications that the $MAPbBr_3$ salt failed to infiltrate P4824 and P10492

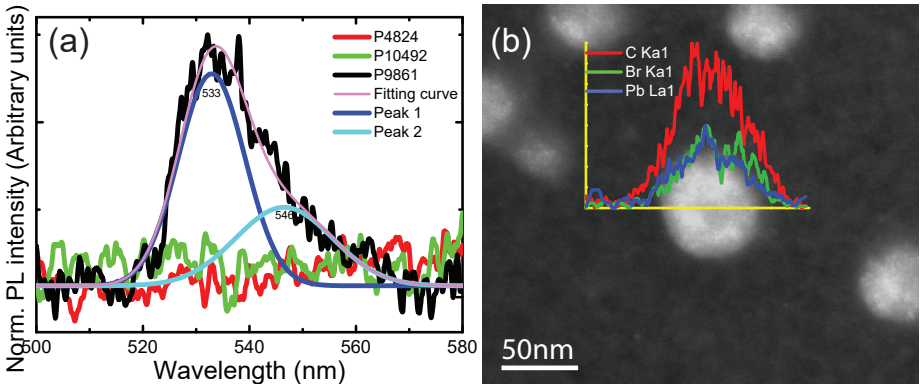

Figure 10.1: Synthesis of $MAPbBr_3$ by reverse micelles. (a) Photoluminescence spectra of $MAPbBr_3$ P9861 micelles (black curve) compared with failed $MAPbBr_3$ formed by P4824 (red curve) and P10492 (green curve), all spin-coated as monolayer on Si substrate, measured with 488nm laser excitation. PL spectra all taken from the centre spot of the substrate. The PL peak of P9861 was deconvoluted to two Gaussian peaks shown as blue (peak one at 533 nm) and light blue (peak 2 at 547 nm) curves. The light purple curve is the final fitted PL peak of P9861. (b)TEM image with EDX line scan showing evidence of salt infiltratio, displaying composition of carbon (red line), lead (blue line) and bromine (green line) along the P9861 micelle diameter.

polymeric shell and form nanoparticles inside the micelles.

At the corners of the substrate, however, all three $MAPbBr_3$ loaded micelles samples show strong PL signal at 540nm in this case. Typically, materials dispersed by spin-coating are fairly uniform across the substrate with the exception of the corners where thick dried solvent and materials tend to gather at. It is therefore suspected that there were $MAPbBr_3$ formed outside of the P4824 and P10492 micelles in the solvent.

To prove the successful infiltration of $MAPbBr_3$ in the P9861 micelles, a TEM EDX line scan of $MAPbBr_3$ loaded P9861 is shown in Figure 10.1 b. The atomic distribution of carbon (red line), lead (blue) and bromine (green) is overlayed on the P9861 micelle. Evidently, the Pb and Br content of $MAPbBr_3$ is contained inside the carbon-rich micelle environment. Though $MAPbBr_3$ is relatively stabler than $MAPbI_3$ in air,[43,300,303] it is still susceptible for degradation in air. The P9861 micelle can effectively protect the $MAPbBr_3$ inside from moisture and air and hence, the photoluminescence property of the $MAPbBr_3$ is preserved.

While $MAPbBr_3$ is formed nicely in the P9861 micelles, as can be seen in the AFM image in Figure 10.2 a, the P9861 $MAPbBr_3$ loaded micelles remain intact

with an average diameter of 35nm. The topography of P4824 and P10492 were also examined with AFM in Figure 10.2 b and c respectively. Unlike P9861, the $MAPbBr_3$ loaded P4824 and P10492 look non-spherical, somewhat deformed and appear to be abnormally flat.

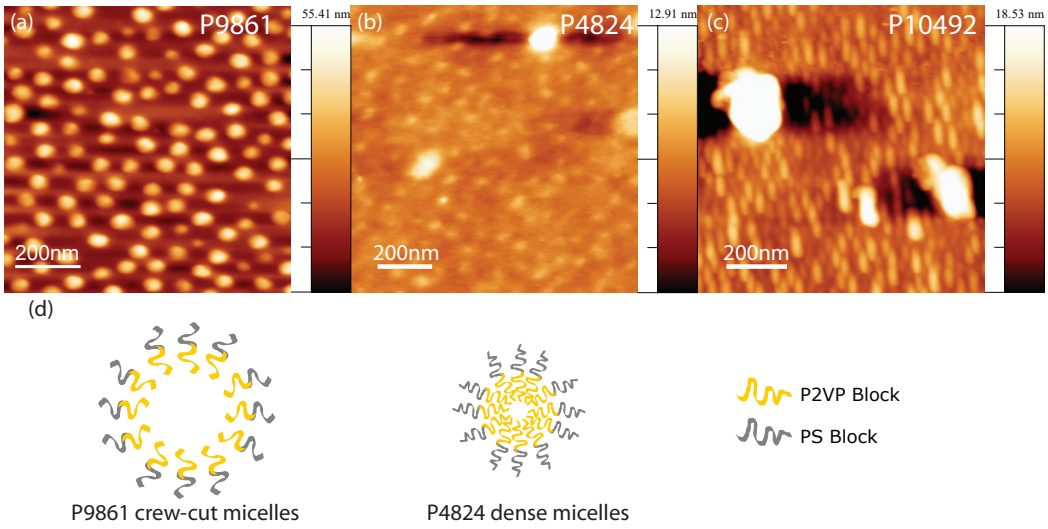

Figure 10.2: AFM images of $MAPbBr_3$ loaded to (a) P9861, (b) P4824 and (c) P10492 reverse micelles. (d) Schematic comparison of micelles made up of P2VP and PS blocks with different block lengths, resulting in different micellization to form crew-cut micelles (P9861) and dense core micelles (P4824).

The infiltration process of salt to micelles is naturally driven by osmotic pressure.[304] The two-step loading process of $MAPbBr_3$ starts with the loading of MABr, followed by the addition of $PbBr_2$. This sequence of salt loading is very critical because of the possible complexation of Pb with the pyridine group which will cause disintegration of micelles as reported in detailed in Ch. 13. However, it will be problematic if the loading process is already hindered at the first step for the osmotic force is not enough for materials like MABr with a large organic cage of 5.93 Å lattice parameter.[43]

It was found that these perovskite materials have different degrees of dissolution behaviour in polar solvents.[29] The MA group dissolves very well in polar protic solvent while the metal halide group does the opposite.[29] This selective dissolution behaviour makes it problematic for MA halide to leave the non-polar solvent to go into the hydrophilic micelle core. $MAPbI_3$ on the other hand, because of a stronger charge-transfer (CT) interaction between the iodide anion and pyridine group, the infiltration process was found to be actively assisted regardless of the selective dissolution behaviour.[305]

Aloisi et al. showed the formation constants of the halogen-pyridine complex and because the electron affinity of the bromide in MABr to the halogen-pyridine complex is less, the complex is less stable than the iodide-pyridine complex,[305] making infiltration more difficult.

From the micelle structure perspective, it would be easier for the salt to enter the core if the polymer strands are not densely intertwined. The PS and P2VP block lengths of P9861 are both short compared to P4824 and P10492. Since the loading process involves two steps, this may explain how MABr manage enter the P9861 without much difficulty as P9861 can be pictured as a crew-cut micelle, with a large peripheral. Whereas for both P4824 and P10492, their PS blocks are longer than the P2VP blocks, which then creates resistance for MABr infiltration. Figure 10.2 d shows a schematic cross section of a crew-cut P9861 empty micelle and a dense P4824 empty micelle. As a consequence, the MABr loaded P9861 micelles are stabilized before the $PbBr_2$ are further infiltrated. In the contrary, MABr never entered the P4824 and P10492 dense micelles, and when the $PbBr_2$ is added, the Pb ions immediately complexate with the pyridine groups and cause destruction of the micelles as can be seen in the AFM images. The remaining excess $PbBr_2$ can still react with the MABr in the solvent outside of the micelles, but they are never formed inside the micelles.

Typical $MAPbBr_3$ shows yellowish green fluorescence under UV illumination.[234] As speculated from the AFM images, the non-infiltrated MABr reacts with the excess $PbBr_2$ in the solvent to form $MAPbBr_3$ and suspend in the o-xylene. Therefore, it is reasonable for both P4824 and P10492 micelles exhibit fluorescent behaviour under UV illumination with slight variance of green tone and intensity (see Figure 10.3 a). The P9861 $MAPbBr_3$ loaded micelles however, shows little fluorescent behaviour under UV illumination, possibly because the $MAPbBr_3$ all entered the micelles. Therefore, the PL results and the AFM measurements both points to the verdict of no infiltration for P4824 and P10492 micelles, which contradict with the luminescent results of the $MAPbBr_3$ loaded micelles solutions.

$MAPbBr_3$ formed outside of the micelles would degrade once it is exposed in ambient environment. In particular, upon exposure to moisture, metallic Pb will first segregate from $MAPbBr_3$ on the surface and the MABr will further degrade to volatile gaseous products of methylammine (CH_3NH_2) and HBr.[300] It was speculated from the PL results that without the micelles protection, the $MAPbBr_3$ suspension would degrade as the solvent dries in air. We attempted to study the process of degradation

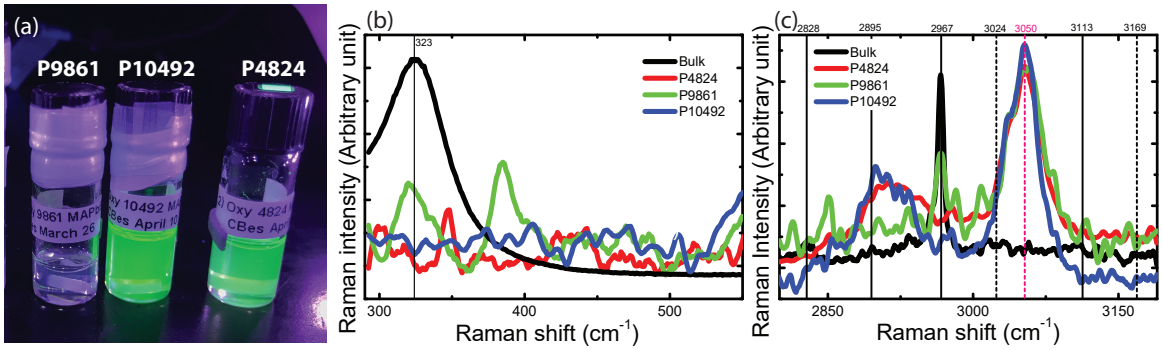

Figure 10.3: Comparison of $MAPbBr_3$ synthesized by reverse micelles of different block lengths. (a) Vials of $MAPbBr_3$ micelles solutions under UV illumination. Raman measurements of $MAPbBr_3$ in micelles of P4824 (red curve), P9861 (green curve), P10492 (blue curve) and in solution only (black curve) with Raman shift in ranges of (b)290-870 cm^{-1} and (c) 2800-3190 cm^{-1}.

chemically with Raman spectrometry.

Raman spectra were collected from these three $MAPbBr_3$ loaded micelles of P4824 (red curve), P9861 (green curve) and P10492 (blue curve) as shown in Figure 10.3 b-c. A control sample of bulk $MAPbBr_3$ (black curve) was also taken for comparison. The black vertical lines are indications of expected Raman modes for $MAPbBr_3$ as discussed in Ch. 5.3.4.3 and the Raman modes expected for micelles are indicated as blue dotted lines as discussed in Ch. 5.3.3.1. As the samples for Raman were all thickly drop-casted samples, there is a rich signature of micelles from all the spectrum (see SI Figure 13.8 for full Raman spectrum of $MAPbBr_3$ loaded P4824 and P9861 micelles). Unfortunately, the modes of micelles overlap quite a lot with those in $MAPbBr_3$ in the Raman shift region from 900-1600 cm^{-1}, the Raman modes due to $MAPbBr_3$ are overshadowed by the micelles modes. For instance, a peak at 970 cm^{-1} is expected for $MAPbBr_3$ (C-N stretching mode), but because it is located so close to the intense symmetric ring breathing mode of micelles at 1000 cm^{-1}, it could easily be hidden in the shoulder of this micelle Raman mode.[166,306] On top of the peaks from the micelles, there is also a strong peak at 3050 cm^{-1} (indicated by the pink dotted line in Figure 10.3 c) present in all the micelles samples but does not belong to any modes of the micelles. It is indeed an out-of-phase methyl umbrella mode from the residue of o-xylene, which is likely trapped under the micelle layers.[307] The low and high Raman shift region are more informative. For instance, the strong MA cation rotational mode at 323 cm^{-1}[1234] of $MAPbBr_3$ (Figure 10.3 b) can be found in both the

bulk and P9861 $MAPbBr_3$ loaded samples. The other mode and perhaps the most significant one, is the strong asymmetric CH_3 mode at 2967 cm $^{-1}$[306] (Figure 10.3 c) found both in the bulk and P9861 sample but the P4824 and P10492.

Although there should be more excess MABr left in the micelles solution of P4824 and P10492, that more modes of pure MABr are anticipated, only one of the MABr modes can be found in their Raman spectra. This is due to degradation of $MAPbBr_3$ without the protection of micelles. In Figure 10.3 c, the broad mode at 2895 cm $^{-1}$ is present in both the P4824 and P10492 micelles. This mode can be both from o-xylene (in plane out-of-phase stretching CH_3) or the symmetric CH_3 mode that appears to be stronger in MABr than $MAbPBr_3$ as reported by the Xie group.[306,307]

From the Raman measurements, it is confident to say there is no signs of $MAPbBr_3$ forming CT complex with pyridine in all cases, as some of the pyridine modes in the micelles would be shifted according to Maes et al.[308] In those cases, some major peak shifts would be observed (see Figure SI 13.9)such as the mode at 1570 cm^{-1} would be blue-shifted to 1579 cm^{-1}; and 1005 cm^{-1} would be blue-shifted to 1020 cm^{-1}.[308] Therefore, it supports the fact that the infiltration of $MAPbBr_3$ into micelles is purely an osmotic process and hence the diblock copolymer micelles block lengths play an important factor for successful salt loading.

Based on the Raman results, although they are limited by the micelles signals in this case, Raman still provides a more than complementary insight to the PL results. It concludes that $MAPbBr_3$ is only formed successfully in the P9861 micelles and it provides insights to how failure infiltration cases arise.

10.3 Conclusion

We demonstrated the first successful $MAPbBr_3$ nanoparticles synthesized using reverse micelles technique. Although all the $MAPbBr_3$ loaded micelle solutions glow yellow-green under UV illumination, it does not necessary imply $MAPbBr_3$ is formed inside the micelles. Having verified by photoluminescent measurement, Raman spectroscopy and TEM EDX line scans, only the P9861 crew-cut micelles allow $MAPbBr_3$ infiltration. Due to the lack of Br complexation with the pyridine group in the micelles, denser micelles with longer PS block length (P4824 and P10492) failed to function as nanoreactors for $MAPbBr_3$. Consequently, the $MAPbBr_3$ in these dense micelles solutions undergo degradation in air, while the P9861 micelles encapsulated $MAPbBr_3$

still show PL signals and the $MAPbBr_3$ Raman signature.

Chapter 11

Facile Synthesis of Monodispersed Thermal-Stable α-phased Formamidinium Lead Iodide Nanoparticles by Reverse Micelles Nanoreactor

11.1 Introduction

Formamidinium (FA) Lead Iodide ($FAPbI_3$) is the rising star among perovskite materials its lower hysteresis in I-V measurement, longer carrier lifetime, better photo and thermal stability and hence better power conversion efficiency.[226,227,231–233]

While there are plethora examples of perovskite materials being used for improving solar cells both as bulk thin films for light absorbing and nanomaterials in nanoporous materials for transporter of charge carriers.[43] It remains very challenging to make zero-dimensional perovskite nanomaterial and manipulated to a desired size with low poly dispersity index (PDI).[43,56]

Reverse micelles made of diblock copolymer has been applied vastly as nanoreactor in making nanoparticles for its high level of controlling the salt sizes formed inside the core with low poly dispersity. Herein, we report the first ever $FAPbI_3$ nanoparticles synthesized by the reverse micelles technique. In particular, since $FAPbI_3$ has two

main polymorphs: the α- and δ-phases,[226] it is significant to differentiate the phases of the polymorph synthesized inside the micelle. The desired phase to be formed in the micelles would be the α-phase $FAPbI_3$ because the δ-phase crystal is nonperovskite, which it not useful for applications of perovskite PVs.[226] Moreover, it was found more challenging to have thermal stabilized α-phase $FAPbI_3$ at room temperature that phase transition is common.[226] Therefore, both Raman spectroscopy and Photoluminescence measurements are used for characterizing these $FAPbI_3$ micelles.

11.2 Results and discussion

The $FAPbI_3$ micelles solutions was spin-coated onto a Si substrate for verification of PL properties. Typical α-$FAPbI_3$ single crystal have a PL peak at 820 nm, though Steele et al. also reported having α-$FAPbI_3$ PL peak at near infrared emission of 780 nm.[226] The PL measurement of $FAPbI_3$ synthesized in reverse micelles solution is plotted in Figure 11.1 a, the signal appears to be noisy but definitely showing the signature peak of perovskite α-$FAPbI_3$ at 780 nm. The signal could be limited to the thin layer of material which results in less scattering with the incident laser.

Nevertheless, the Raman spectrum of these $FAPbI_3$ micelles also echoes with the PL results that α-$FAPbI_3$ is yielded from the reverse micelles. Figure 11.1 b shows three spectra of $FAPbI_3$ formed in three conditions: in o-xylene solvent alone (black curve); in P4824 micelles (green curve) and in P9861 micelles (red curve). The $FAPbI_3$ in solution serves as the reference spectrum in this case, it has the strong 137 cm^{-1} mode for α-$FAPbI_3$ originated from the I-Pb-I bending and stretching mode.[226,228] There should also be a weak broad band at 525 cm^{-1} related to the in-plane bending of FA cation but it is not observed in the reference spectrum. The $FAPbI_3$ formed by the two types of micelles, which only differ from each other with the block lengths, also show a similar spectrum with the reference spectrum. On top of having the 137 cm^{-1} mode, which indicates the α-phase property, there is also a peak at 220 cm^{-1} which is the background peak from the KBr substrate. The $FAPbI_3$ formed in solution was chunk like such that it was thick enough to block the laser from reaching the KBr substrate, so there is no KBr peak in its spectrum. Though is a 30 cm^{-1} of Raman shift difference between the α and δ-phase and it is close to the detection limit of the sensor at such a low wavenumber region, it cannot be ruled out the possibility to have a mixture of both phases formed in the micelles. However, the preliminary results

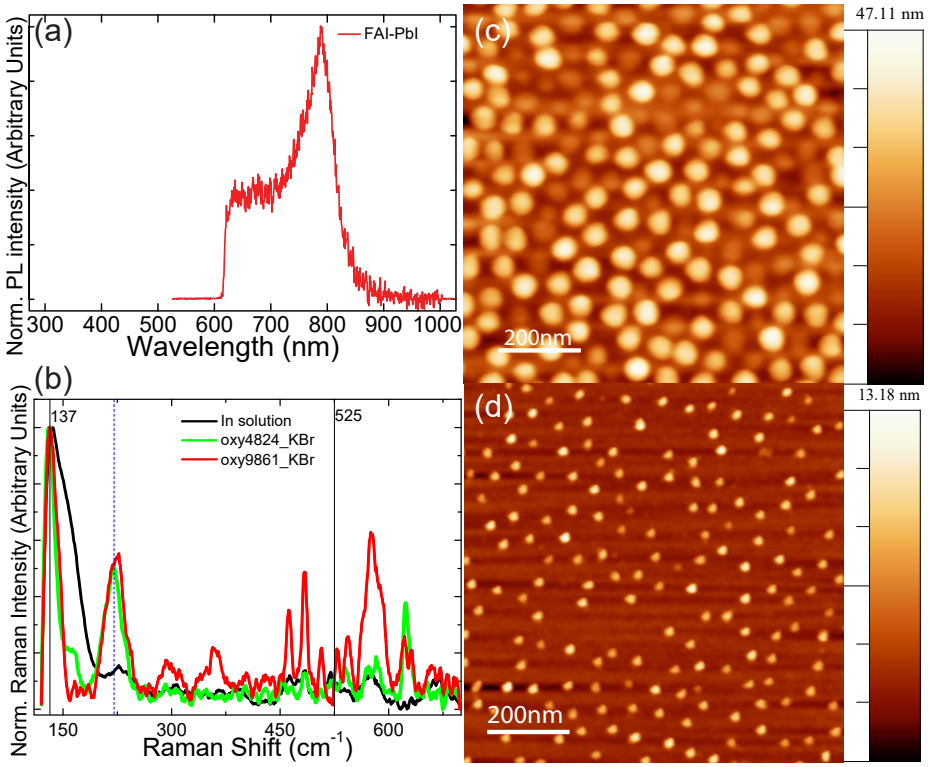

Figure 11.1: Successful synthesis of $FAPbI_3$ by reverse micelles. (a) PL measurement of micelles loaded with $FAPbI_3$ drop-casted on Si substrate. (b) Raman spectra of $FAPbI_3$ formed by micelles solutions of P9861 (red curve), P4824 (green curve), and in solution only (black curve), drop-casted on KBr substrates. AFM topography images of $FAPbI_3$ loaded P4824 micelles spin-coated on Si substrate (c) before plasma etching and (d) after plasma etching, revealing nanoparticles of size 8 nm in diameter.

from Raman shows a promising formation of α-$FAPbI_3$, one can perform XRD for further verification.

The α-$FAPbI_3$ micelles were further examined under the AFM for two purposes. One is to verify that the infiltration of $FAPbI_3$ salt in the micelles that the $FAPbI_3$ are not decoration outside the micelle or only suspended in the solvent. Given that the Raman results has already shown a non-degraded spectrum of α-$FAPbI_3$, formation of α-$FAPbI_3$ outside the micelles are unlikely. The micelles can effectively protect the α-$FAPbI_3$ from moisture and air. The second insight AFM can provide is the size and PDI of the α-$FAPbI_3$ micelles and nanoparticles.

The AFM topography of the α-phase $FAPbI_3$ micelles are presented in Figure 11.1 c. It has a self-assembled monolayer dispersion with an averaged micelle size of 30nm in diameter as measured from the AFM. Using the reverse micelles techniques, the

PDI obtained for the α-$FAPbI_3$ loaded micelles is incredibly low of only 0.12.

Furthermore, the α-$FAPbI_3$ nanoparticles inside the micelles are revealed after the polymeric micelles are stripped by plasma etching and is shown in Figure 11.1 d. The final size of the α-$FAPbI_3$ nanoparticles is 8 nm as measured from the AFM, while retaining a good PDI value of 0.16.

The reverse micelles technique proved to be a feasible way to synthesize thermal stable α-phase $FAPbI_3$ nanoparticles.

11.3 Conclusion

Synthesis of Formamidinium Lead Iodide by reverse micelles is demonstrated for the first time. The photoluminescence and Raman measurements support the phase formed inside the micelles are indeed α-phase, which is the desired perovskite phase. The reverse micelles technique allows high degree of manipulation for size and low poly dispersity of the α-phase Formamidinium Lead Iodide.

Chapter 12

Raman study of CVD Graphene and its interaction with oxygen plasma and annealing

12.1 Synergistic oxidation of CVD graphene on Cu by Oxygen Plasma Etching

Reproduced from Ref. [254] with permission from Elsevier.

12.1.1 Introduction

Due to its unique properties, graphene, and its oxygen functionalized varieties – reduced graphene oxide (rGO) and graphene oxide (GO) – are all technologically interesting two dimensional materials which can be tuned and exploited for a variety of applications. With the addition of oxygen species on the basal-plane of graphene, the sp^2 hybridized, 2-D honeycomb network of carbon is perturbed and the zero band-gap semi-metallic graphene turns into GO as the band gap opens, becoming an insulator under high oxygen concentrations.[139,309,310] GO itself can be manipulated to rGO, a form structurally similar to graphene with low oxygen concentration, in numerous ways by thermal, chemical and electrochemical processes.[19,311–313] Due to the differences in the chemical structures of these graphitic materials, they exhibit different mechanical, electrical and optical properties, which can be incorporated into a great variety of

graphene-based devices including photovoltaics, ballistic-like transistors, transparent electrodes, and chemical sensors.[19,102,133–136,138,140,143,149,191,309,310,312–314]

As discussed in Chapter 4, plasma can modify surface properties of materials and can be used to pattern graphene nanostructures, introducing defects and non-conductive regions in a variety of dispersions.[133–137] Studies based on the controllable introduction of disorder with plasma etching provides insights into the optoelectronic properties of functionalized graphenes.[135,138–141] Details of the graphene interaction and etching mechanism studies with oxygen are discussed in Chapter 4.

Since in free standing and supported exfoliated graphene, the "lowly-defected-regime"[124,133,138,149] with interesting semiconducting and photoluminescent properties is usually only accessible within a very small window of oxygen plasma exposure up to seconds or at most minutes.[138] This is also the case for graphene on some weakly bonded transitional metal substrate such as Ir and Ru (0001).[137] On the other hand, CVD graphene on Cu has a stronger van der Waals force between the substrate and graphene, which shows a considerable resistance to etching and tunable with a low temperature annealing.[150]

This provides an opportunity to examine in greater detail the lowly-defected regime of graphene with oxygen functionalization, to understand the evolution of the structure using Raman spectroscopy and x-ray photoelectron spectroscopy. In the current study, we examine the evolution of CVD graphene on Cu foil under oxygen plasma treatment, showing that the synergistic oxidation of graphene and copper is responsible for the increased resistance to etching. Recent classification of the GO Raman spectra[255] has allowed us to trace the evolution of graphene in great detail. The longer window of plasma induced damage on CVD graphene, tunable with annealing, suggests new avenues for patterning nanostructures in graphene based devices.

12.1.2 Results and Discussions

As shall be discussed in the next Chapter 12.2,[150] we observed considerable increased robustness of CVD graphene with low temperature annealing. Fig. 12.1a shows the Raman spectra for full coverage (FG) graphene on Cu foil annealed for various times, and exposed to oxygen plasma for 30 mins, normalized at the G_{app} mode at 1590cm^{-1}. All Raman spectra have features from CuO (620cm^{-1}),[315] and graphene features: G_{app}, D (1340cm^{-1}), and a 2D mode (2790cm^{-1}).[176,177,192] The G peak corresponds to the first order degenerate phonon energy, E_{2g} mode at the G point of graphene;[177] the sharp

2D peak is a result of the second order phonon intervalley scattering, from the $\pi - \pi^*$ transition.[176,182,316] The 2D mode comes from D mode overtone and is indicative of sp^2 hybridization of graphene.[317] After plasma etching, the presence of 2D mode suggests intact graphene, with a higher ratio of 2D to G suggestive of greater resistance to etching. Fig. 12.1b shows the 2D to G mode area ratio of the FG samples, with increasing robustness with annealing as expected. The two red data points for 15min and 30min anneal correspond to etching times that resulted in the complete loss of signal from the D and G modes, suggesting complete destruction of the graphene layer. For an unannealed sample, 30 min etching is sufficient to completely remove all mode peaks associated with the graphene layer.

However, unexpectedly, the D to G_{app} peak area ratio appears unchanged as annealing time increases. The D mode is the signature of sp^3 defects.[176,177] If the ratio of D to G is taken as an indication of the defectiveness of the graphene layer, as it has been traditionally,[138,141,191,318] one would expect to see the D mode and the ratio to decrease as the annealing time increases, to support the hypothesis of increased amounts of intact graphene. Recently, there has been some suggestion that this interpretation of the G and D modes may not be directly applicable to functionalized graphenes, and particularly to oxidized graphene systems.[255] Particularly the observed peak at the G position may actually be a convolution of defect modes. To understand this phenomenon further, we examined the effect of oxygen plasma exposure on a mildly annealed (4 min) CVD FG system.

Fig. 12.2 shows the Raman spectra of the 4 min annealed FG on Cu (AT4) with various oxygen plasma etching times. In all spectra, the D mode (at 1340 cm^{-1}) activated by defects is prominent and a broadband near the G mode (at 1590 cm^{-1}). For a highly defected graphene, previous studies have observed the emergence of a second defect peak D', blue-shifted relative to G, associated with the C–H sp^3 hybridization defect and the overtone of the D mode.[319,320] The evolution of the G mode to the D' mode with plasma etching of free standing and supported exfoliated graphene has been demonstrated,[141] and described as the evolution of the pristine graphene to a highly defected vacancy regime. However, as seen from Fig. 12.2, for the CVD graphene, there is no obvious splitting of the G mode in any of the spectra. As the plasma power in our study is lower compared to the study of Zandiatashbar et al,[141] to compare the results, we need to establish an equivalent plasma dosage metric, $E = P \times t$ where E is the applied plasma energy in Joules, P is the power of plasma in Watts and t is

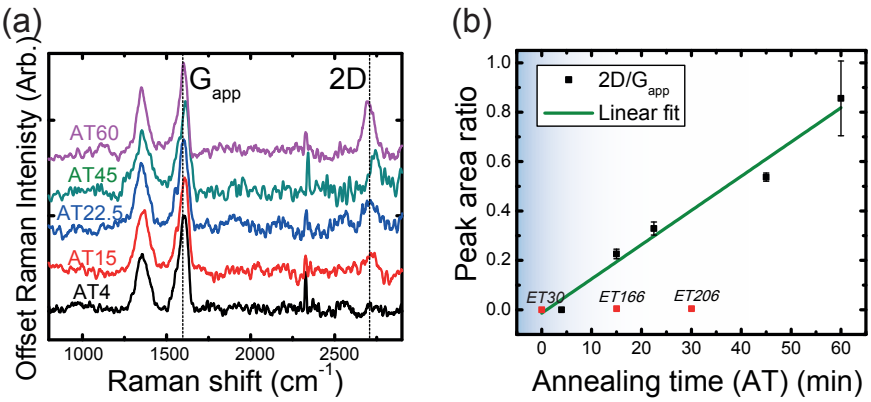

Figure 12.1: (a) Offset normalized Raman spectra of fully grown CVD graphene on Cu with different annealing times, plasma etched for 30 min. Spectra normalized to G_{app}. (b) Peak area ratio of 2D to G mode. Red points indicate the etching time to full disappearance of D and G modes, suggesting complete destruction of the graphene layer.

the etching time in seconds. With as little as 5.4 kW (54s) of etching for exfoliated graphene, the D and G modes can no longer be resolved, while these modes persist up to 162 kW (90 min of etching) in the CVD FG samples.

The clear splitting of the G and D' modes is visible for plasma dosages ranging between 1.2 kW and 2.4 kW (12-24 s) for free standing films, and between 2.1 kW and 3.6 kW (21-36 s) for supported films on SiO_2. Within these ranges for our CVD system (0.75-2.25 min), we observed no splitting of the peaks.

However, the shape of the G mode differs from that of pristine graphene even after 30 s of etching ($ET0.5$) for the CVD graphene as shown in Fig. 12.2a. This suggests that the D' mode overlaps strongly with the G mode, which has also been observed under higher etching doses for exfoliated films.[141] This G_{app} peak, which can be assumed to be the convolution of the real G and D' modes, is initially centered at 1595 cm^{-1} at $ET0.5$ min and undergoes a blue shift to 1604 cm^{-1} at $ET90$ min. These peaks may, therefore, correspond to some oxidized form of graphene such as reduced graphene oxide (rGO), graphene oxide (GO) or even amorphous carbon rather than defected graphene. Taking the position of the G mode as fixed, at 1590 cm^{-1}, the G_{app} peak can be deconvoluted as shown in Fig. 12.2. Although it has been suggested that one could use the 2D' mode near 3246 cm^{-1} to infer the D' mode by just halving the position,[255] the 2D' mode was never observed in any of the FG samples in this study. This is very likely due to the strong fluorescent of Cu in the background stimulated

by the green laser that shielded the relatively weak 2D' mode. In our approach, we instead fixed the G mode position and used a least square fitting to extract the relative intensities and peak centres of gravity.

As the plasma etching time increases, the D' component of the G_{app} mode dominates while the G component decreases (Fig. 12.2e), as would be expected. As the D' mode is also defect activated, this can still be used to assess the quality of the graphene layer. It is worth noting, however, that the D' mode undergoes three phases. Initially, below the dose where the splitting was activated in exfoliated graphenes ($ET0.5 = 0.8kW$), the G mode dominates; under the highest dose ($ET90$), the defect mode dominates (highlighted in blue in Fig. 12.2e). In between these two extremes, starting with as little at $ET1$, the ratio of the G and D' modes is almost unchanged. This is also true for the samples annealed at various times and exposed to a 30 min oxygen plasma etch– in all cases, the D' mode corresponds to approximately 30% of the G_{app} peak.

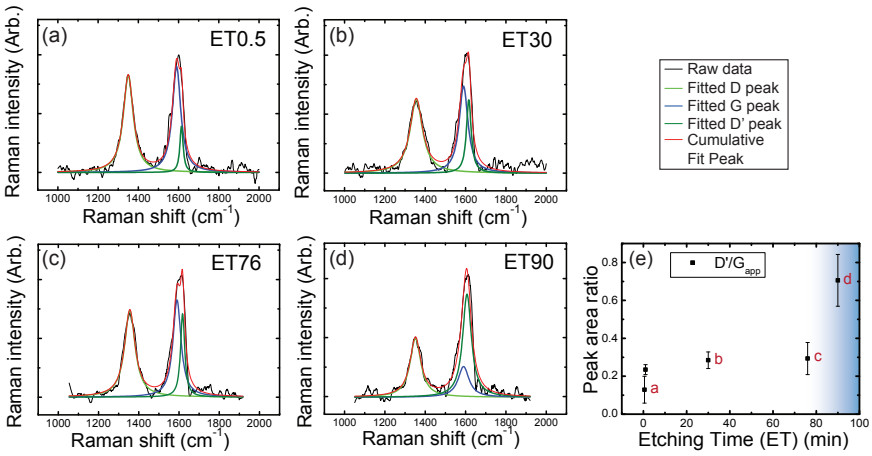

Figure 12.2: Raman spectra of 4-min-annealed fully grown CVD graphene on Cu, plasma etched at different time in oxygen: (a) 30 s (b) 30 min (c) 76 min (d) 90 min. The black line is the raw spectrum after background correction, fitted into single Lorentzian peaks, with G mode fixed at the 1590 $cm^{-1}$the typical position (blue) and the D' mode near 1620 cm^{-1}(dark green) was obtained. The D mode (green) and the resultant fitted spectrum (red) are indicated. (e) The G_{app} peak are normalized and the D' to G_{app} peak area ratio of the fitted spectra are shown, the blue area indicates the phase II rGO regime.

King et al. recently suggested that using the ratios of mode peak intensities for functionalized graphitic material as a measure of their defect density could be misleading as it is not as universally applicable, especially for GO.[255] They also observed that the

ratio of peak intensities were not correlated to the extent of oxygen integration in the graphene layer. They proposed a new metric using the Raman spectra using instead the peak position difference of the G_{app} mode and D' mode, to differentiate between graphene, GO and rGO.[255] If there is obvious peak splitting with a difference more than 25 cm^{-1}, as seen for exfoliated graphene under plasma treatment, the material can be considered as graphene. If there is a negative difference, the system is likely heavily doped with oxygen to a graphene oxide state. If the peak position difference (D'-G_{app}) ranges between 0 cm^{-1} to 25 cm^{-1}, the material is only lightly doped with oxygen, falling into a region analogous with rGO.[255] Using this metric, we examined the evolution of the D' and G_{app} modes. According to the newly developed metrics, the etched FG falls into the rGO regime with light oxygen doping as the peak position difference of D' to G_{app} ranges from 19 cm^{-1} at $ET0.5$ to 2.8 cm^{-1} at $ET90$ (Fig. 12.3c). There appears to be a major transition in the system after 76 min of etching, where the rGO goes from a lightly oxygen doped system (phase I GO) to a heavily oxygen doped graphene system, closer to GO (phase II GO highlighted in blue in Fig. 12.3c)). Note that the evolution of the modes would not have been clearly observed for free standing or supported exfoliated graphene on other substrates as the modes would have been removed under the same etching conditions.

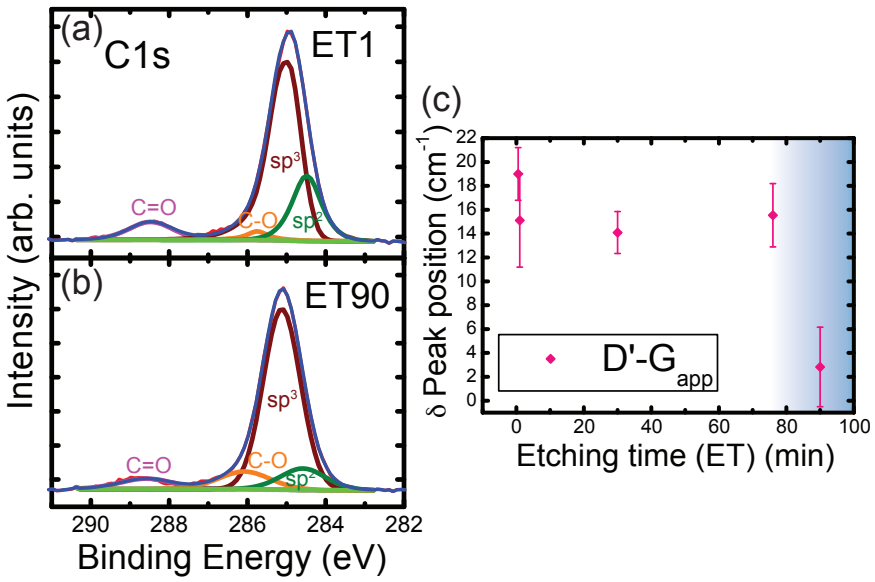

Figure 12.3: *C* 1*s* XPS result of fully grown CVD graphene on Cu annealed for 4 mins and oxygen plasma etched for (a) 1 min and (b) 90 mins (c) Raman peak position difference between D' to G_{app} mode of the 4-min-annealed fully grown CVD graphene on Cu, oxygen plasma etched for different times, with blue area indicating the phase II rGO regime.

XPS was performed on 4-min-annealed FG under low and high etching, showing the presence of graphitic oxide, as implied by the Raman results. Fig. 12.3 shows the *C* 1*s* spectra of the 4min-annealed FG etched in oxygen plasma. Both spectra have a main peak at 285.1eV, which can be deconvoluted into three component peaks at 286.08 eV, 285.12 eV and 284.58 eV, assigned to the phenol C-O, sp^3 and sp^2 carbon bonds respectively.[321–328] An additional C=O peak was observed at 288.58eV. Pure graphene is generally dominated by sp^2 hybridized carbon, GO is dominated by sp^3 hybridized carbon, and rGO is generally seen as a mixture of the two.[328] After plasma etching for 90 mins in oxygen, the area ratio of sp^3 to sp^2 increased from 3.02 (Fig. 12.3a) to 7.08 (Fig. 12.3b). This suggests that early in the etching process, rGO forms immediately which becomes more heavily doped, almost GO like, in phase II GO after long etching.

The ratio of the C=O peak intensity to the main *C* 1*s* peak at 285.1eV can be used to estimate the amount of oxygen in the graphene oxides, using Nishina et al.'s study, in which a continuum of oxygen content in GO was differentiated with XPS.[324] In this case, the *ET*1 *C* 1*s* corresponds to 27.8 wt% oxygen content rGO and *ET*90 to

23.1 wt% oxygen content rGO.[324] Interestingly, while Raman indicates that the CVD graphene on Cu system after ET90 became highly defected, implying high oxygen doping, the XPS results appear to indicate a lower amount of oxygen attachment to the carbon network than in the very early stages of oxidation. One possible explanation could be the desorption of carbon dioxide. During the etching process, various forms of graphene oxide, such as the epoxy and lactone groups, nucleate on the graphene; eventually these epoxide groups may break and form CO and CO_2 that can desorb into the plasma gas.[143] However, though this route is possible, it is energetically unfavorable with an energy barrier of more than 600 kJ/mol.[143] Another possible route that is more energetically favourable is the reaction of the dangling oxygen groups with the Cu substrate.

In fact, simulations of CVD graphene exposure to oxygen suggest that there is preferential formation of a specific negative epoxide group, enolate, rather than the more stable epoxy.[145] This was found to occur only in strongly bound epitaxial graphene on Cu and Ni due to the metallic n-doping the graphene layer leading to a stabilized graphene oxide. The strong intermixing of the Cu $3d$ electron states with the the C $2p$ electron states[145] opens up reactive pathways for Cu to scavenge the oxygen. As the activation energy for forming cuprous oxides can be as low as 37.5 kJ/mol,[329] whereas the energy barrier for oxidation of graphene is 184 kJ/mol,[143] the preferential formation of copper oxides at defect sites is expected.[330,331]

This preferential oxidation is the behaviour that we observed from the Cu XPS spectra for the etched films. The Cu $2p_{3/2}$ XPS spectra in Fig. 12.4 demonstrate a broad feature at 934 eV representing a mixture of various cuprous oxides present in the annealed FG samples after plasma etching treatment. This main peak at 934 eV can be resolved into 3 features: metallic Cu at 932.5 eV (green curve), CuO at 933.6 eV (pink curve) and $Cu(OH)_2$ or $CuCO_3$ at 934.7eV (orange curve).[325,332,333] In both spectra, there is also a strong CuO satellite feature ranging from 941-944 eV, unique to CuO.[332] As we also observed a CuO mode in the Raman spectra before etching and the intensity of the CuO features in the satellite and Cu $2p_{3/2}$ were unchanged under plasma etching (see Fig. 12.4c, this suggests the polycrystalline Cu foils have some intrinsic oxidation unrelated to the etching process. To examine the effect of the oxygen exposure then we focus on the metallic Cu and copper hydroxide/carbonate signals. Initially, under a very mild plasma exposure, the sample has a strong signal from metallic Cu. The initial $Cu(OH)_2$ or $CuCO_3$ formation could result from oxygen

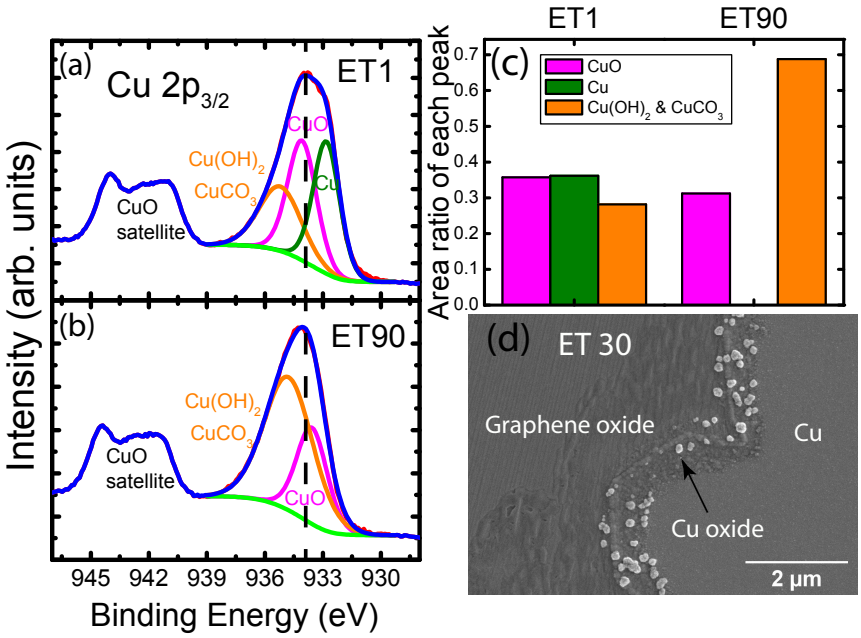

Figure 12.4: $Cu\ 2p_{3/2}$ XPS result of fully grown CVD graphene on Cu annealed for 4 mins and oxygen plasma etched for (a) 1 min and (b) 90 mins (c) Area ratio of peaks (d) SEM image of partially grown CVD graphene on Cu etched in oxygen for 30mins. The left side is the graphene side, the partially grown CVD graphene on Cu boundary is in the middle, separating the graphene and Cu substrate.

atoms attacking the defect sites at the random grain boundaries on the relatively intact FG, oxidizing the Cu underneath. As the plasma etching progresses, and the samples enter phase II rGO (plasma etched for 90 min), the Cu metal peak disappears. (Fig. 12.4b). The main 934eV centred feature is now dominated by the $Cu(OH)_2$ /$CuCO_3$ peaks, with the initial CuO feature relatively unchanged. Fig. 12.4c shows the area ratio of each feature under the two etching conditions. The $Cu(OH)_2$ and $CuCO_3$ peaks doubled after 90 mins of etching, the metallic Cu disappears, while the CuO peak remains nearly constant. There is also slight increase in the area ratio of the $O1s$ core level at 533eV to the higher binding energy feature, which consists of the superposition of cuprous hydroxide and C=O and C-O peaks.[333] As the graphene and copper oxidation features are indistinguishable, and we propose a net transfer of the graphene oxides to copper hydroxides, the O $1s$ core level looks very similar under all etching conditions.

This assisted formation of cuprous oxides due to the enolate group can also be observed in SEM for a partially covered graphene (PG) layer on Cu (Fig. 12.4d). The pellet-like cuprous oxides are visible at the graphene flake boundary, formed due to the defect-rich edge region where enolate groups can easily attach to, then transfer to the adjacent exposed Cu, forming cuprous oxides. Upon exposure to oxygen plasma, there is a competition between creating more defect sites on the graphene and forming more cuprous oxides anchoring points below defects. This oxidation mechanism is then a synergistic effect between graphene and its CVD substrate, Cu, where the graphene acts as an oxygen barrier for Cu at the initial stage and Cu on the other hand, prevents the graphene from being more oxidized in the later stage. This could also explain the behaviour observed by Schriver et al.[334] that graphene, though initially providing a protective barrier, actually enhances the oxidation of Cu over long time periods.

This mechanism also helps to explain the behaviour previously observed for the PG under plasma exposure. In our other study in the next chapter 12.2,[150] contrast between oxidized and unoxidized Cu allowed the visualization of the size and shape of the graphene flakes on the Cu surface under an optical microscope, as shown in Fig. 12.5a. The complete destruction of the graphene flakes was previously assumed when the contrast disappeared, as in Fig. 12.5b. However, throughout the etching process, the size of the PG flakes did not shrink nor change shape, as would be expected for removal of the graphene around the boundary. Instead, the contrast diminished as etching progressed until the graphene flakes were no longer visible (see Fig. 2 in

Chapter 12.2.[150]).

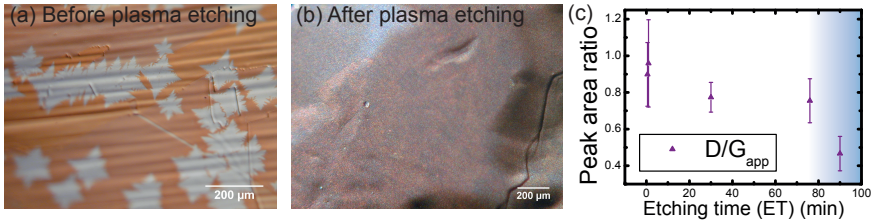

Figure 12.5: Optical image of 2-min-annealed partially grown CVD graphene on Cu for (a) non-etched (b) 71 min etched in oxygen plasma. Raman peak area ratio the annealed fully grown CVD graphene plasma etched at different times in oxygen of (c) D/G_{app} modes, the blue areas indicate the phase II rGO regime.

This disappearance of contrast can now be explained using the synergistic oxidation mechanism between graphene and copper. With long plasma exposure, the refractive index of phase I GO would shift to a higher refractive index of phase II GO, which can range from n=2 to n=2.5.[256] At the same time, metallic Cu (n=1.12) would be transforming into cuprous oxides (Cu_2O: n= 2.26 and CuO: n=2.4),[335,336] at defect sites inside the graphene flake. With plasma etching, therefore, the refractive indices for both species converge and the contrast disappears. This supports the mechanism of the synergistic transformation of graphene from phase I to phase II rGO after plasma etching for some time accompanied by the conversion of Cu to cuprous oxides.

Finally, the mechanism helps to explain the observed decrease of the area ratio of D mode to G_{app} (Fig. 12.5c). Seo et al.[337] recently correlated the adhesion strength with this ratio for CVD graphene treated with UV ozone.[337] In their analysis, lower ratios suggested less adhesion strength. In the synergistic oxidation, as etching time increases, the Cu underlying defect sites becomes oxidized. These defected areas are still oxygen rich, and an oxygen can bridge a dangling defect C-C bond, forming a C-O-C bond.[143] When this happens at defect sites which is cuprous oxide rich, it can result in a local lift-off of the GO platelet section to the Cu substrate. The interfacial distance increases, hence, the van der Waals force between the interfaces weakens and the adhesion energy decreases.

The complete mechanism is summarized in Fig. 12.6. Initially, the graphene is converted into a functionalized graphene layer with ~25% oxygen doping, analogous to a reduced graphene oxide (phase I GO). Due to the stabilization between the carbon and the Cu, the ionic enolate form of graphene oxide is preferentially formed from metallic n-doping of the graphene layer. These enolate groups formed near defect sites

at random grain boundaries on the relatively intact FG will have access to the metallic copper, leading to the formation of copper hydroxides, and the removal of the oxygen doping of the graphene. These oxides act as pinning states at defects, stabilizing those sites against further attack. As etching continues, more and more sp^3 defect sites are opened up over the graphene layer, oxygen ions proceed to synergistically oxidize both the graphene and copper. Eventually, there are so many sp^3 defect sites that the metallic copper is completely oxidized, and the oxygen can bridge dangling defects, causing a lift-off of the whole graphene layer. This phase II GO has more GO-like sp^3 hybridization, though the amount of oxygen attachment is lower due to the scavenging nature of the copper layer. The onset of the phase II GO is accompanied by a significant decrease in the inter-defect distance,[148,176,177,192] as shown by the decreased area ratio of the D phonon scattering defect to the real G mode from the sp^2 carbon network (Fig. 12.6d). These defect sites likely correspond to the exact sites where the cuprous oxides can be formed. Until the layer lift-off was observed, the defect scattering modes were pinned and inaccessible by the copper oxides. By annealing the FG for different times, the Cu underneath the FG is also oxidized in a different degree. The formation of cuprous oxide acts as anchoring points which secure the FG to the Cu substrate. Those pinning sites are not as susceptible to the synergistic oxidation.

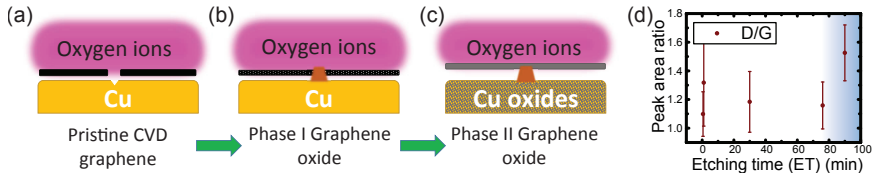

Figure 12.6: Schematic diagram of graphene oxide formation from fully grown CVD graphene on Cu by oxygen plasma etching (a) initial stage before etching occurs (b) etching begins with oxygen plasma preferably oxidizing the graphene defect sites, forming enolates that in turn form cuprous oxide with the Cu substrate exposed at the defect sites (c) final stage when bridging of graphene oxide at the cuprous oxide sites occur, resulting in a lift-off of graphene oxide from the Cu substrate. (d) Raman peak area ratio of D/G modes for the annealed fully grown CVD graphene plasma etched at different times in oxygen. The blue areas indicate the phase II GO regime.

The different behaviour for exfoliated graphene sheets, as well as graphene weakly bonded on Ir and Ru, is as a result of this synergistic oxidation. Without the supporting Cu substrate, the free standing graphene is destroyed by oxygen ions breaking bonds; with weakly bonded systems, the oxygen intercalates between the graphene and the

substrate, again attacking the graphene; with the Cu substrate, the oxygen ions not only destroy the carbon bonds, but also oxidize the Cu underneath the defect sites. The competition between creating more defect sites on the graphene and forming more cuprous oxides anchoring points in CVD graphene prolongs the resistance of the CVD graphene layer.

12.1.3 Conclusion

A detailed study of the impact of oxygen plasma treatment on CVD graphene was undertaken to explain its increased robustness compared to other forms of graphene. The destruction mechanism of the CVD full graphene and free standing graphene by oxygen plasma etching are found to be different due to the multiple roles that the oxygen ions have in each case. In free standing and weakly bonded graphene, the oxygen ions only attack the carbon bonds, whereas in CVD full graphene, the oxygen ions also oxidize the Cu substrate in a way that anchors the graphene with the cuprous oxide sites. Both XPS and Raman analysis show that the full graphene was initially lightly doped with oxygen, analogous to reduced graphene oxide upon oxygen plasma etching (phase I GO). With increasing oxygen exposure, the Cu underneath the defect sites begin to oxidize, stabilizing the graphene layer. Eventually, the reduced graphene oxide undergoes a transformation into a graphene oxide-like reduced graphene oxide (phase II GO), accompanied by the complete oxidation of the Cu foil underneath. At that point, the adhesion energy of the reduced graphene oxide to the Cu substrate decreases as the cuprous oxide lifts the heavily defected graphene sheet, due to the bridging oxygens. The synergistic effect of Cu and graphene oxidation by oxygen plasma means that both are stabilized, with the graphene acting as an oxygen barrier for Cu at the initial stages and the Cu preventing the graphene from being further oxidized until significant plasma dosages are reached. The longer window of plasma induced damage on CVD graphene, tunable with annealing, suggests new avenues for patterning nanostructures in graphene based devices.

12.2 Effect of post-annealing on Plasma etching of graphene-coated-copper

Reproduced from Ref. [150] with permission from The Royal Society of Chemistry.

12.2.1 Introduction

Due to its chemical inertness, excellent mechanical strength, and high electrical conductivity, graphene has been a widely studied material since its discovery in 2004.[338–340] Potential applications include its use as electrodes,[25,341,342] charge carrier transport layers,[343–345] lubricants,[346] impermeable barriers,[332,347] and nanoelectromechanical systems (NEMS).[348]

Though much research has focused on understanding the electronic and thermal properties of graphene,[338–340] less has been done on its mechanical properties. Recent work, however, suggests that the mechanical and friction properties of graphene are just as impressive as the electronic.[338,349,350] Despite the recent excellent work, there is still some controversy on the strength of adhesion of chemical vapor deposition (CVD) graphene, especially on Cu surfaces.[351–353] CVD is an excellent low cost method of producing large area graphene with controlled thickness and high quality.[354,355]

Though the film quality is high, CVD graphene grown on Cu foil at high deposition temperatures (>1000°C) tends to have a non-equilibrium structure,[356] characterized by wrinkles and folds.[319,351,356,357] Deposition at high temperatures leads to rapid contraction of the graphene upon cooling due to the mismatch in the thermal expansion coefficients between Cu and graphene.[356–360] The Chen group have recently used high temperature post-deposition annealing to recover the crystallinity of the Cu surface, recovering the equilibrium structure of graphene on Cu.[319,320,361] The equilibrium structure has been found to have much higher adhesion energies 18 than that found on as-deposited samples.[351] In this study, post-deposition annealing (post-annealing) was examined in order to investigate the possible influence on the graphene layer under plasma treatment. Post-deposition annealing, even at modest temperatures (<200°C), appears to be the key in manipulating the adhesion strength of graphene on Cu, reflected by the increase etching times to completely remove CVD graphene from the Cu surface.

12.2.2 Results and Discussions

Though exposure to plasma is often used to modify the electronic properties of graphene layers,[141,185,362–364] under sufficient high doses, bombardment with the energetic particles can also completely etch away the graphene layer. Therefore, plasma interactions are a potential method of probing the mechanical strength of graphene-copper interfaces.

As our interest concerns the robustness of the graphene to plasma etching, partially covered substrates were desired. The CVD process was tuned to produce square graphene flakes on the Cu foil with 30-100 μm widths.

Impact of etching times

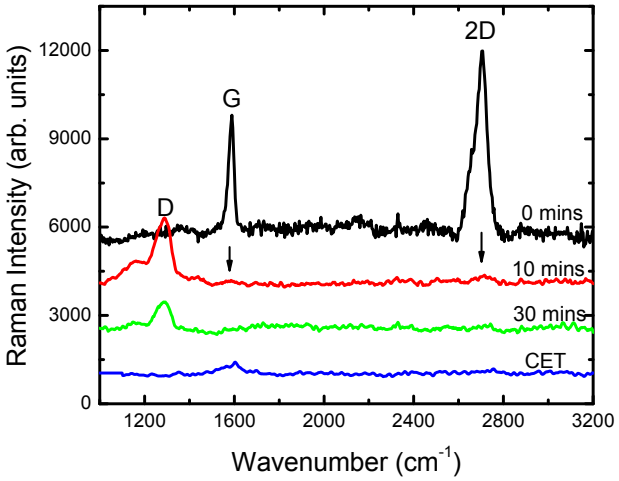

Figure 12.7: Raman spectra for CVD graphene on Cu foil at etching times of 0, 10, 20 and 201 (CET) min, showing the evolution of the etching process for O_2 plasmas. The critical etching time is defined as the complete removal of graphene, as determined by optical methods.

Figure 12.7 shows the Raman spectra for as-grown graphene, and the resultant spectra after etching in O_2 for various times. The pristine samples show both the characteristic features for graphene, the G and 2D peaks at 1587 cm^{-1} and 2705 cm^{-1} respectively. The G peak corresponds to the first order of degenerate phonon energy, E_{2g} mode at the Γ point of graphene;[177] the sharp 2D peak is a result of the second order phonon intervalley scattering, from the π-π^* transition.[177,182,316] The absence of a peak between 1280-1350 cm^{-1} suggests that the graphene islands are mostly defect free.[177,365] The I_G/I_{2D} (peak height) ratio of 0.4 indicates that the graphene flakes on the Cu surface are single layer.[177,189] The 2D peak can be fit by a single Lorentzian (not shown), further supporting the idea that the CVD grown graphene films are mostly single layer, defect free patches on the Cu surface.[177] Some multilayer islands were also observed, however, with slightly higher I_G/I_{2D} ratios and a shoulder on the 2D peak.[177]

After a short etch in O_2 plasma, significant sp^3 defects are introduced with a

strong D band appearing at 1290 cm^{-1}.[177,366] Though much reduced, both the G and 2D bands are still barely visible as shown by the arrows in Figure 12.7. There may also be a merging of G and D' broad band at 1590 cm^{-1}, which is attributed to the C-H sp^3 hybridization defect and the overtone of D mode activated after plasma treatment.[319,320] These changes suggest that the plasma has initially introduces defects into the graphene rather than removing it, as is often seen in plasma processing used to tune the electronic configuration of graphene flakes.[362] Another option is the formation of graphene oxide.[367] Further etching eliminates the G, D' and 2D signals and reduces the scattering intensity of the D band, indicating that graphene/graphene oxide is being removed from the surface. Finally, after the critical etching time (CET), there is no more evidence of graphene in the Raman spectrum. This fully etched condition of the graphene was determined with optical microscopy.

As received, the graphene on Cu foil is without any contrast in the forward scattering condition. Cu, however, is prone to oxidation in air even at low temperatures. Graphene has been widely reported as an excellent passivation layer11,[347] protecting the surface from chemical oxidation as the densely packed benzene-ring structure makes graphene impermeable to most gases, including helium.[368,369] Mild oxidation, from short post-annealing treatments in air or even exposure to oxidizing plasmas, can therefore be used to visualize the graphene islands (see Figure 12.8(a)). The contrast results from the different light scattering intensity and refractive indices of cuprous oxide and the unoxidized Cu protected under the graphene. The oxidation contrast therefore can be used as a method of tracking the progress of the etching procedure. Figure 12.8 shows the effect of the etching procedure on the graphene islands, supporting the findings suggested by the Raman analysis. After short etching times, the graphene is still visible, then becomes progressively less and less visible as etching progresses. Finally, the critical etching time (CET) is determined as the point where no contrast is visible after etching, suggesting complete removal of the graphene layer. (Figure 12.8(d)).

After CET, there is still a Raman feature visible at the G/D' location of 1580 cm^{-1} (Figure 12.7). However, the eigenvector of the G mode involves the in-plane bond-stretching motion of pairs of C sp^2 atoms, and does not require the presence of six-fold rings.[192]

Without the accompanying 2D peak, which needs six-fold rings to be excited,[192] this cannot be taken as a feature of graphene, and is most likely due to C=C residue on the surface. As can be seen in Figure 12.9, after the CET as determined from optical

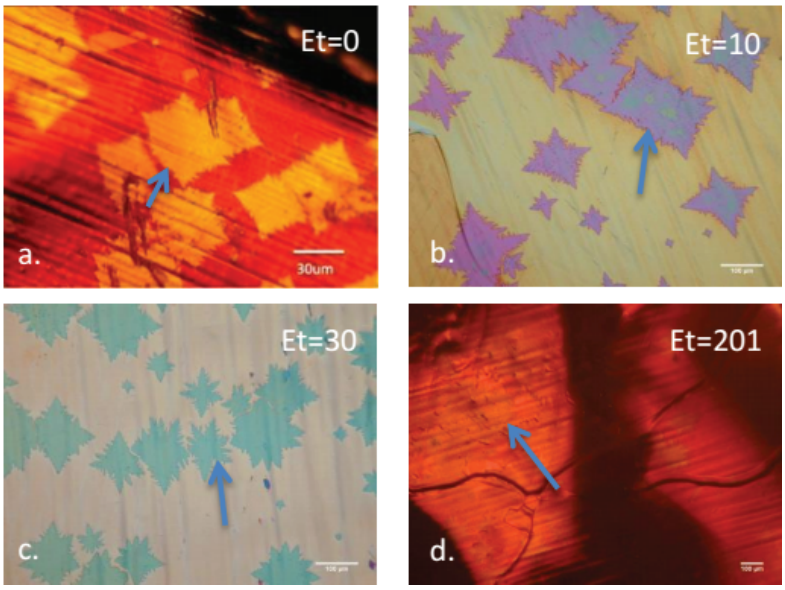

Figure 12.8: Optical micrographs of CVD graphene on Cu foils. (a) As-grown samples, annealed to show contrast between bare and graphene covered regions (b-d) same sample after etching in O_2 plasma for 10, 30 and 201 min. Etching time is denoted as "Et" in the figures. Blue arrows indicate the contrast showing the graphene islands. The final panel was used to determine the critical etching time (CET).

observations, Raman measurements show no indication of graphene on the surface for pure N_2, O_2 and unfiltered laboratory air etching plasmas. This suggests that the optical method is adequate to determine the CET for complete removal of graphene from the Cu surface, and the CET can be considered to be roughly proportional to the strength of the interaction between graphene and the Cu surface. Optical determination of CET is straight-forward for O_2 and air plasmas, as exposure to the plasma also oxidized the Cu surface; however, identification of N_2 CET required a post-etching annealing of the etched samples to show contrast of Cu-graphene after treatment. It is likely therefore that the visual method leads to an over estimation of the real CET for N_2 plasmas. This was confirmed with Raman measurements where graphene patches were visible optically, but there was no signature of graphene (see next section).

Effect of post-deposition annealing

CVD graphene grown on Cu foil, at high deposition temperatures, such as those in this study, tend to have a non-equilibrium structure.[356] Egberts et al recently showed that the work of adhesion for graphene on Cu is low for such systems.[351] The Chen

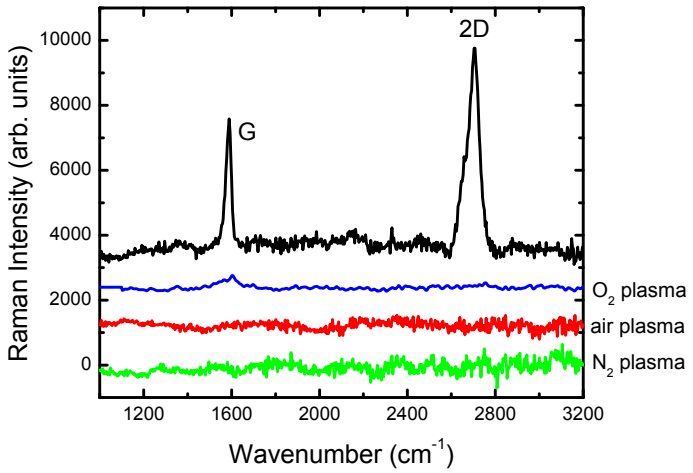

Figure 12.9: Raman spectra of as-grown CVD graphene on Cu and after etching with different gases.

group have been able to use high temperature post deposition annealing to recover the crystallinity of the Cu surface,[320,361] approaching the equilibrium structure of graphene on Cu,[319] which has been reported to have much higher adhesion strengths.[352] This suggests that post-deposition annealing might increase the interaction strength between graphene and Cu.

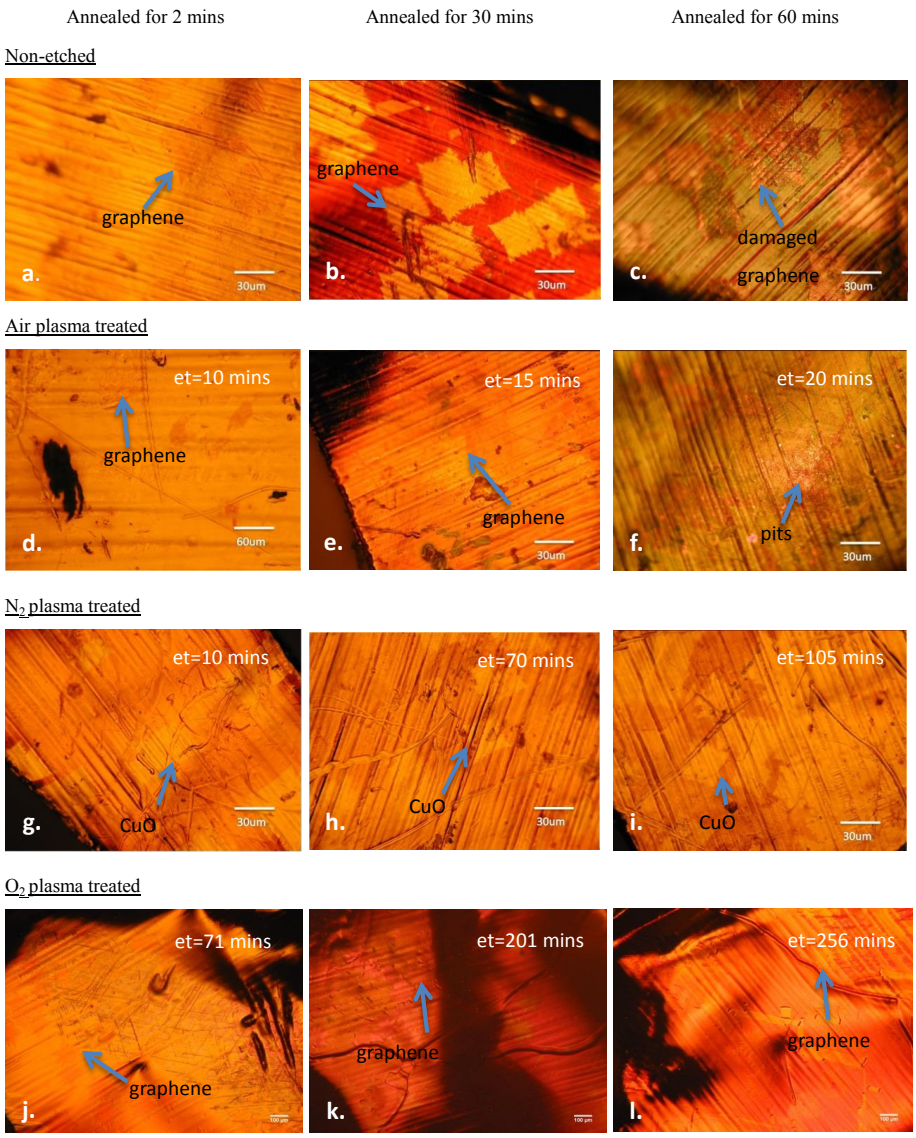

Figure 12.10: (a-l) Optical micrographs of CVD graphene on Cu foil annealed and etched for various times. (a, d & g) samples post-annealed for 2 min ; (b, e & h) for 30 min and (c,f & i) for 60 min. (a-c) Samples have not been plasma treated; (d-f) treated with air plasma, (g-i) N_2 plasma treated and (h-l) O_2 plasma treated with the etching time denoted as "et" in the figures. Blue arrows indicate the contrast showing the graphene islands.

To examine this effect, we performed low temperature (180°C) post-deposition annealing on our graphene-Cu samples for various annealing times. As described above, short annealing times can make visible the graphene islands. Under further annealing (Figure 12.10(b)) the contrast increases, likely due to the enhanced oxidation of unprotected Cu in the presence of graphene, recently described by Zhou et al.[346] Eventually, under long term annealing, in some areas of the sample, the graphene islands edges are no longer clear. This is a likely result of graphene exfoliating from the surface, due to a mismatch in the thermal expansion coefficient of graphene ((-8.0 ± 0.7)x 10^{-6} K^{-1}) and the Cu crystals (14x10^{-6} K^{-1}).[359,360] With longer annealing time, more material is allowed to expand and the rigid graphene structure is not fully bonded to the surface, exposing some of the Cu underneath the surface, resulting in a more "messy" oxidation of Cu foil.[326]

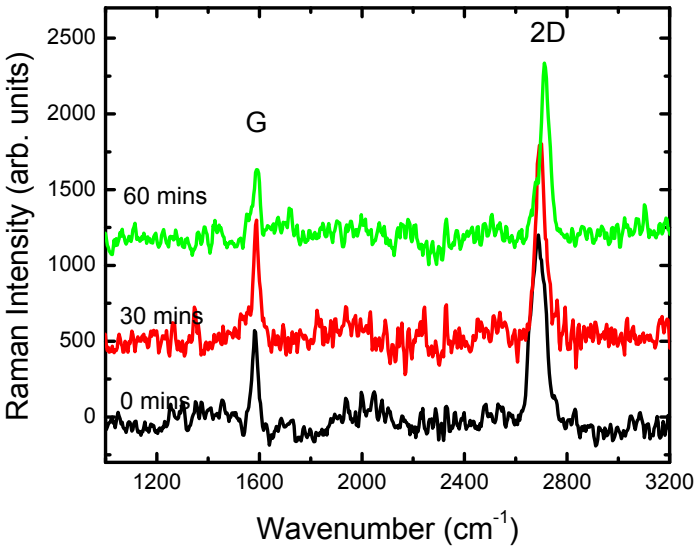

Figure 12.11: The Raman spectra of CVD graphene on Cu samples with different post-annealing times at 180°C (0,3 & 60 min). The spectra were normalized to the 2D peak at 2700 cm^{-1} intensity for comparison.

Figure 12.11 shows the Raman spectra for the post-deposition annealed films. In all cases, the G and 2D bands are both visible, without D band development. This suggests that there was neither significant defect nor graphene oxide formation.[179,367] Post-deposition annealing in fact seems to have very little impact on the graphene islands, even when optically significant damage appears to have occurred. The only

notable change is a slight blue shift of the 2D band observed to occur systematically with annealing time. Though this is characteristic of multilayer graphene,[183] no peak broadening or change in I_G/I_{2D} ratio (varies between 0.36-0.46 depending on graphene flake) was observed. The observed features can be well fitted with a single Lorentzian peak shape with similar full width at half maximum (FWHM), pointing to defect free, monolayer graphene in all cases.

Upon exposure to plasma, however, significant differences were observed with the post-annealing time. Optically, as can be seen in Figure 12.10, systematically longer etching times were necessary to fully remove the graphene from the substrate with post-annealing, for all etching gases. The observed CET for all the process gases are summarized in Figure 12.12. In all cases, increased annealing time protects the system against etching. The visually different etching times as a function of annealing, as shown in Figure 4(d,e & f), (g,h& i) and (j,k& l) support the premise that annealing can be used to control the removal of graphene, by making the structure more robust. It takes much longer in all cases to see complete removal of the graphene from the surface. Figure 12.13 shows the Raman spectra for the optically determined CET for O_2 plasma with various post-annealing times. Though there is no evidence of graphene or even C residue on the as-grown samples, even short post-deposition annealing changed the resultant spectra. With only 2 min of annealing, the defect or graphene oxide D band observed previously with only 10 min etching, was still visible after 75 min of etching. Further annealing shows increasing signal from the G/D' band, which may be due to C=C residues that are not removed even with extremely long etch times (250 min etching for 60 min post-annealing time). The extremely long etching times, and the inability of the plasma to remove carbon residues indicates a strong interaction between the Cu and the graphene.

Effect of plasma gas

Though Figure 12.12 shows that the trend of increasing CET with annealing holds for all process gases, there are significant differences in the measured CET times for the different etch gases. These effects are visible even with normalization to remove sample variations. Using the CET estimations, air is the most aggressive etchant, with O_2 and N_2 plasmas having decreasing aggressiveness. The effect of post-annealing in protecting the graphene from etch removal is greatly enhanced the less aggressive the etchant. However, the optical measurements are slightly misleading. Raman measurements for the same etching time, shown in Figure 12.14, support the order of

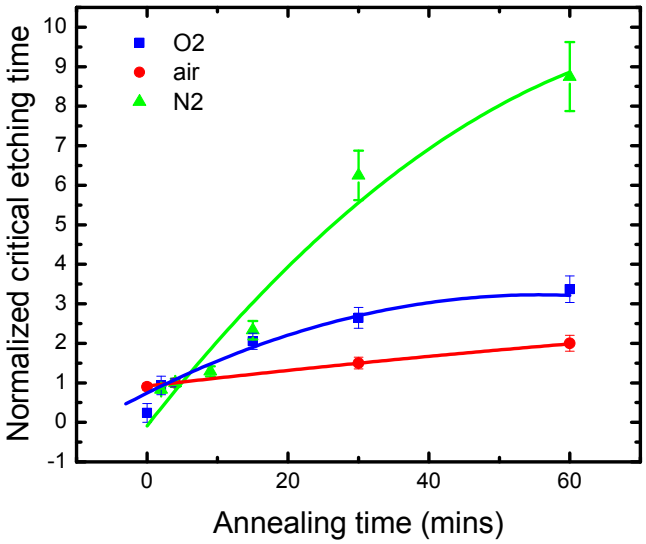

Figure 12.12: Normalized CET for graphene with different post-annealing treatment for various plasmas. Lines are least squares fit on data. The CET have been normalized using to the value of annealing time at 4 min, where contrast is visible, to eliminate possible sample discrepancies and emphasize the common trend for all process gases.

the O_2 and air plasmas, but completely contradict the behaviour with N_2 etching.

Figure12.14 does confirm that the different process gases have different impacts on the graphene for the same etching time. In this case, N_2 plasmas appear to be the most aggressive, with no Raman signal visible for graphene nor are there any C-O, C=O bands after only 10 min etching, suggesting a total destruction of graphene and carbon residues. N_2 plasma etching is a physical sputtering process, that has previously been used for nitrogen doping of graphene and is thought to lead to unsaturated dangling carbon bonds at the graphene edges.[370] The dangling carbon bonds can react with oxygen atoms once it is exposed in air. (see Figure 12.10f). However, in this study, no evidence of graphene or graphene oxide was observed, only complete sputter removal of the graphene.

It appears that, while the optical detection for determining the CET works well for air and oxygen plasmas, values of the CET as determined optically are highly overestimated for N_2. Optically, Figure 12.10h shows that the contrast initially assigned to graphene is still visible for a sample that has been etched for 75 min, under the same annealing conditions as the 10 min etching in Figure 12.14. As N_2 plasma

cannot oxidize the Cu during etching, this contrast is more likely to result from the varying degree of Cu oxidation rather than a signature of graphene on the surface. The first annealing step oxidizes the regions without graphene. After interaction with the plasma, the graphene is removed, leaving behind regions with different levels of oxidation. During low temperature oxidation, metastable Cu_3O_2 forms first followed by CuO, the thermodynamic stable phase of cuprous oxide.[315] Possibly, the regions covered with graphene form the metastable oxide during the second annealing step (i.e. after plasma etching to expose the graphene), while the previously oxidized regions continue to oxidize further. Eventually, what appears to be "fully-etched", without contrast, indicates uniform oxidation or complete removal of the initially formed oxide by the vigorous physical sputtering action of the plasma. The trend in the observed CET for N_2 plasma may suggest that it takes longer for the cuprous oxide to be sputtered away at longer annealing times.

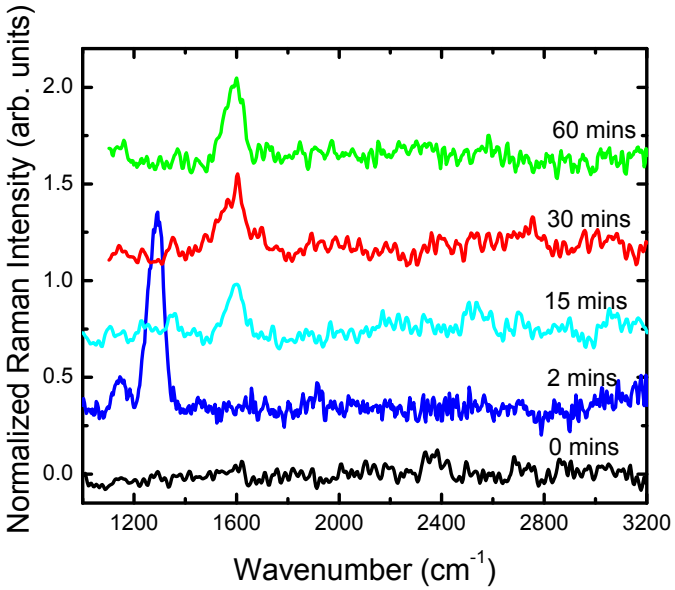

Figure 12.13: Raman spectra for CET on CVD graphene on Cu foils with O_2 plasma for various post-annealing times (0-60 min) at 180°C.

The Raman data also indicates that air plasma is also very aggressive, leaving only the C=C residue/G band at 1590 cm^{-1}. Air plasma etching is a very vigorous process, with CET reached quickly with visible pitting observed on the Cu/graphene surface. The pitting effect is likely due to the effect of hydrogen plasma in air as Diankov et al. has observed the high selectivity of hydrogen gas on graphene.[371] Pits are not present

on samples etched by N_2 (Figure 12.10i) or O_2 plasma (Figure 12.10l) for the same annealing time and even for much longer etching times. It is likely that there is true etching occurring with the air plasma, due to the highly reactive O- and H- radicals, as well as the sputtering observed with nitrogen.

O_2 plasmas were the least aggressive, showing the defect structure, D band, with some G and 2D peaks barely visible. As described previously, there could also be a D' broad band, merging with the G. The presence of both D' and D peaks suggesting significant doping and defects are introduced but likely little removal of graphene. The gas with the slowest etching rate is thus the oxygen plasma, where only chemical etching takes place of only O- species.

The rates observed for the various plasmas can be attributed to the mechanisms of plasma etching for the different gases. Different plasma gases can have varied interaction mechanisms and diverse ions in the plasma.[128,371,372] Plasma is ignited by the large voltage applied across the electrodes outside the plasma chamber, which causes the free electrons to accelerate rapidly towards the anode. When the electrons collide inelastically with the gas molecules, an electron will be removed from the gas molecule and thus the gas will then be dissociated or ionized. The electron removed continues to be accelerated to the anode and collides with other gas molecules, resulting in a cascading effect. The process of etching is due only to radicals which actively break the chemical bonding and react with the surface of the substrate.[142]

Ions can also cause energetic bombardment or ejection of atoms, that is, sputtering on the surface. For the three plasma gases, O_2 will form highly reactive radicals by molecule dissociation, while N_2 can be ionized and form ions.[373–375] The gas discharge causes excitation and relaxation of gas molecules that releases energy in the form of photons and thus causes the glow inside the expected to be etched and sputtered by O_2, H_2, N_2, carbon and other atoms of trace gases present in air.[372] As there is high concentration of 78% of N_2 in air, one might expect the air plasma etching process to be dominated by N_2. However, pure N_2 plasma showed a much faster etching rate to air and O_2 plasma.

Possible mechanisms for increased adhesion strength with annealing

The etching time for complete removal of any residue is correlated to the strength of the adhesion of the coating on the surface.[376] The observed increase in the CET with annealing for Cu-graphene systems therefore suggests significant improvement in the interaction between graphene and Cu, and an improvement in the mechanical

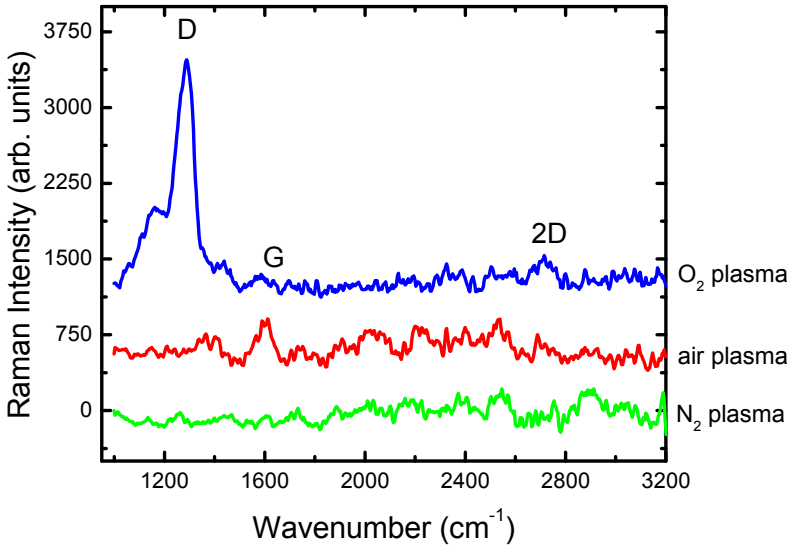

Figure 12.14: Raman spectra for CVD graphene on Cu foils with the same post-annealing (30 min) and etching times (10 min) with different gases.

properties of the interface. There is some controversy in the literature on the value of the adhesion strength between graphene and Cu,[351–353] and about the nature of the interaction leading to this value.

There are two main mechanisms that might describe the observed behavior with plasma etching of the graphene-Cu interface: the process of Cu oxidation itself, or the reconstruction of the Cu surface with annealing.

The CET as determined for N_2 etching seems to be due to the removal of Cu oxides rather than the graphene layer. Yet, the trend of increasing resistance to etch removal with annealing is observed. As Cu is highly susceptible to oxidation, even at low temperatures, it may be that the oxidation process itself leads to the increased strength of the interaction between Cu and graphene.

Fundamentally, the oxidation of Cu can be described by the Cabrera-Mott theory.[377] Cu ions and electrons migrate to form the oxide layer on the surface, leaving cationic Cu sites behind.[378] The strong electric field that results promotes further diffusion of Cu ions to continue oxidation.[378]

In the composite Cu-graphene system, prolonged annealing may provide more kinetic energy for Cu ion migration to areas where graphene is absent (Figure 12.15). As the vacant Cu cation sites draw Cu ions to the oxide-metal interface, they may pile

up under the graphene flake. This could result in a stronger coupling of C-π orbitals and Cu d-orbitals hybridization of the graphene-Cu interface.

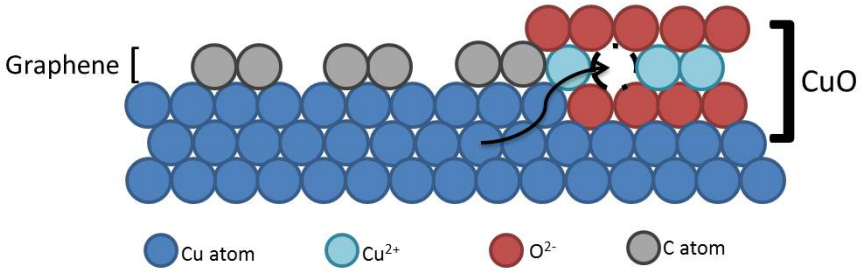

Figure 12.15: Schematic of graphene-Cu interface oxidation

Another possibility influencing the etch resistance of the post-annealed system is the surface reconstruction of the Cu due to annealing. High temperature deposition (>1000°C) leads to rapid contraction of the graphene upon cooling[356–358] due to the mismatch in the thermal expansion coefficients.[359,360] This is one of the possible mechanisms for the formation of wrinkles widely observed in graphene-Cu systems.[319,351,356,357] Cho et al and Tian et al. have seen that high temperature post-annealing is able to partially heal the non-equilibrium structure that results from high temperature growth.[320,361] Zhang et al.,[356] saw that the existence of steps in Cu under the graphene lowers the adhesion. With annealing induced reconstruction recovering the steps within a Cu grain the graphene wrinkles could relax,[320] recovering the Moire reconstruction pattern.[319] In the equilibrium structure, graphene is unwrinkled, and flat graphene flakes have higher adhesion to the surface than the wrinkled ones.[352,379] Though we use lower temperatures for our post-annealing study, it is possible that a similar, though incomplete, reconstruction is occurring in our samples. The increase in interaction strength, as suggested by the robustness to etching, with annealing time therefore could be correlated to the amount of reconstruction.

12.2.3 Conclusion

The graphene grown on Cu foil by high temperature CVD was annealed after deposition, and exposed to various plasmas. The post-annealing treatment alters the mechanical strength of graphene adhering on the Cu foil, as shown by the resistance to plasma

etching. Raman spectroscopy confirms that the graphene is damaged after the annealing and plasma treatments, but typically not oxidized during these treatments. The samples were etched and sputtered by air, oxygen, and nitrogen plasmas, yielding different etch rates and appearance and uniformity of the graphene. Nitrogen plasma has a much faster etch rate than air and oxygen due to the mechanism of physical sputtering. For any given plasma however, with post-annealing before plasma exposure, the graphene is harder to remove due to the interactions of surface bonding between the graphene and Cu substrate. Our results imply that etching of graphene on Cu can be controlled by proper annealing and the right choice of plasma gas. Plasma etching appears to be an effective method of estimating the impact of post-processing effects on the mechanical properties of CVD graphene.

12.3 Tuning Reduced graphene oxide by low temperature annealing

A version of this section is submitted to Thin Solid Films.

12.3.1 Introduction

In rGO and GO, oxygen is adsorbed by exposing graphene (Gr) and graphite to oxygen which causes the formation of epoxide groups at the bridges or top sites of the Gr basal plane.[137,143,309] With the addition of oxygen species on the 2D-basal plane of Gr, the sp^2-hybridized honeycomb carbon network is perturbed.[309,310] Depending on the degree of attachments of oxygen functional groups, the optoelectronic properties of the functionalized Gr can be effectively controlled.[139,380] Increasing the proportion of carbonyl and hydroxyl groups, which alters the projected density of states of the carbon atoms in rGO,[381] can increase the work-function, decrease the conductivity over many orders of magnitude and shift the photoluminescent (PL) emission peak into the red.[380–382] The versatility of rGO as a semiconductor material is therefore of great interest if one can effectively tune and functionalize the material in a controlled manner, which is technically challenging.[381]

In Chapter 12.1, we have shown that Gr on Cu produced by chemical vapour deposition (CVD) method behaves very differently compared to free standing Gr and Gr supported on other substrates,[254] forming rGO-like structures under direct

oxygen plasma bombardment, in a manner similar to that observed with downstream plasma treatments.[383] Due to the synergistic oxidation mechanism between Gr and the underlying Cu, the degree of oxygen functionalization of rGO can be effectively tuned with the oxygen plasma dose.[254]

Controlled oxidation generally requires a relatively clean surface, free of contaminants. Gr and graphite, however, are easily doped by adsorption of oxygen in ambient environments which modify the wettability, carrier mobility, adhesion, and charge doping.[165,384–386] As little as 20 min exposure to ambient environments is sufficient to make freshly grown CVD Gr on Cu significantly more hydrophobic.[384] Due to this strong affinity of Gr, contaminant sources are ubiquitous, even in high end nanofabrication facilities,[387] from the volatile organic compounds (VOC) emitted by common plastic-ware such as plastic petri dishes[388] or sample boxes,[387] to organic solvents and plasticizers[389] to even the quality of the quartz tube during fabrication.[390]

In this chapter, we show that the presence of oxygen compromises the tunability of functionalizing rGO using a plasma. Using Raman and Attenuated Total Reflection-Fourier Transform Infrared (ATR-FTIR) spectroscopy, we examined the surface composition of as-received, plasma-oxidized, plasma-etched and annealed samples. The Raman analysis confirms that similar rGO like structures are formed on the surface during plasma oxidation, and that low temperature annealing, through decontamination of the surface, allows tunability of plasma induced rGO formation on Gr, paving new avenues for patterning nanostructures in functionalized Gr based devices.

12.3.2 Results and Discussions

We have demonstrated in Chapter 12.1 that Gr on Cu produced by chemical vapour deposition (CVD) method behaves very differently compared to free standing Gr and Gr supported on other substrates,[254] forming rGO-like structures under direct oxygen plasma bombardment, in a manner similar to that observed with downstream plasma treatments.[383] Tuning the oxygen content of such surfaces by oxygen plasma etching is reflected in the high resolution $C\,1s$ XPS spectra in Fig. 12.16b and c, where a CVD Gr on Cu annealed for 4 mins ($AT4$) was etched briefly in oxygen plasma for 1 min ($ET1$). The $C\,1s$ signal at 285.1 eV can be deconvoluted into sp^3-hybridized C-H bonds and sp^2 carbon bonds can be as expected for Gr, rGO and possibly graphane.[321–328,391] For the pristine and annealed unetched Gr sample (AT4 ET0 solid red line in Fig. 12.16a), sp^2 hybridized carbon at 284.58 eV dominates, with the sp^3 at 284.97 eV resulting

from a combination of defects and adventitious carbon,[325] with a slight addition of C-O phenol group at 285.75 eV.[321] After only 1 min of etching, the C 1s at 285.1 eV (open circles) after deconvolution is dominated by the C-H bonds, while the phenol group C-O remains. There is also an increase in the C=O group after etching in Fig. 12.16b with the peak height ratio of the C=O to the main peak for the non-etched (Fig. 12.16a) and 1-min-etched sample (Fig. 12.16b) doubling from 0.04 to 0.08. This ratio can be used to estimate the amount of oxygen incorporated if the graphene is converted to GO, based on Nishina et al.'s study, in which a continuum of oxygen content in GO was differentiated using XPS.[324] Under such estimation, one minute of etching resulted in an rGO with 27.8 wt% surface oxygen content.[324] This was supported by Raman analysis in the last Chapter 12.1, establishing the presence of rGO using the relative difference in the D and G' peak positions.[254] The high level of C-H bonds may spark speculations for the presence of regional graphane, the hydrogenated-graphene, after the oxygen plasma etching, which may have resulted from the little presence of moisture and hydrogen content in the oxygen plasma chamber. Unfortunately, both the XPS and Raman results of graphane and rGO are not distinctive to conclude.[391] The abundance of oxygen in the plasma species would more likely result in oxidation rather than reduction that causes hydrogenation of graphene, thus, rGO is still the more dominating product of the plasma treatment.

As ATR-FTIR is more sensitive to carbon functionalization, it was performed to identify the oxygen species with various processing steps. In Fig. 12.16e, the peaks in the 3100-2800 cm^{-1} region in belong to the CH_2 or CH_3 groups[333] whereas the peaks in the 800-1800 cm^{-1} region in Fig. 12.16f belong to the oxygen functional groups.[333] As pristine Gr should have no significant FTIR features,[392] the various functional groups identified with dotted lines show evidence of significant oxygen doping on Gr by plasma etching. Slight oxygen doping is also visible for the annealed Gr sample, but significantly less than that for the pristine sample (ET0 AT0), as would be expected for Gr on Cu with exposure to ambient air.[384] In keeping with our XPS findings that the oxygen content in the Gr increased with short etching, the ATR-FTIR results show significantly increased oxygen functionalization for the $ET1$ sample compared to the $ET0$ sample, where there was clear hydroxyl and epoxy formation with slight plasma interaction. The increase in the C-H bond species after the plasma etching of the $ET1$ sample in Fig. 12.16e may again be due to the presence of regional graphane. As the pristine samples also show similar features, this supports our conclusion above

that the sp^3 hybridized C-H bonds mostly originates from defects on the graphene surface. Further adjustment of this oxygen doping is possible with controlled plasma oxidation,[139,254] shown by the modification of the rGO surface energy, decreasing the water contact angle from 82° to 51° after 1 min, to below 20° with longer oxidation (Fig. 12.16). Using an oxygen plasma, therefore, it is possible to tune the rGO properties.

However, this level of control over the rGO oxygen doping is not possible without a mild annealing step. We believe that this is due to surface contamination. Ambient air and other volatile organic compounds are known to contaminate Gr and graphite with radical modification of surface properties.[165,384–386,393] Li et al. showed that as little as 20 min exposure to ambient air was enough to saturate the surface of a freshly grown CVD Gr on Cu with airborne hydrocarbons.[384] We similarly observed an increase in the contact angle with 20 mins aging in air of the etched sample, as shown in Fig. 12.16.

To explain this mechanism, it is helpful to consider the process by which carbon based systems oxidize. Oxidation typically proceeds by the dissociation of C-H bonds to produce radical polymer species. An oxygen molecule can react at this site to form a peroxide radical which can then form a hyperoxide with reaction of adjacent carbons.[394] If there is sufficient energy, and a steady supply of oxygen, as in an oxygen plasma, these volatile fragments can instead cleave off, removing the hydrocarbon, through a chemical etching process.[395] The critical etching time (CET) for CVD Gr on Cu established in Chapter 12.2 and 12.1 as the time in minutes required for the total disappearance of all the Raman modes of Gr,[150,254] indicating complete etching removal and cleaning of the Cu surface.

As shown in Fig. 12.17c, and observed in Chapter 12.2,[150] a dramatic increase in the CET is achieved with low temperature annealing from less than 20mins to over 2 hours. Without annealing, the CET for as-received Gr is found to be roughly 17 mins.[150,254] As little as 4 mins of annealing dramatically increases the CET from 17 to 190 mins; however, subsequent annealing does not dramatically affect the CET. This plateau of enhancement suggests some a mechanism that occurs at the very early stage of annealing, such as decontamination.

In a plasma, the highly energetic ions bombard the surface, displacing surface bonded species within the collision cascade and creating dangling bonds where incident radicals may then chemisorb or chemically etch the carbon network.[396] In plasma surface modifications, RF power is used to create chemically active species from a

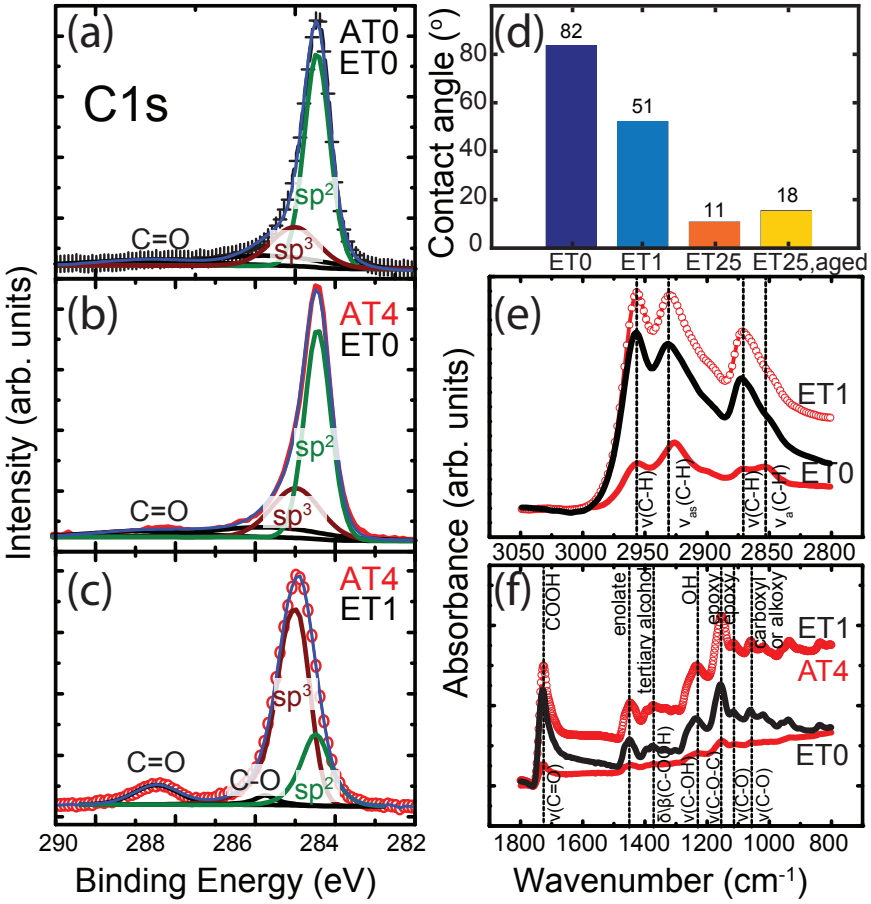

Figure 12.16: High resolution $C\ 1s$ XPS spectra comparison of CVD full graphene on Cu (a) as-received (AT0, ET0), (b) annealed for 4 mins at 180°C (AT4) and (c) annealed AT4 then etched for 1 min (ET1). (d) Contact angle measurements for samples annealed for 4 mins at 180°C (AT4), under various conditions of etching and aging. Background subtracted ATR-FTIR spectra CVD full graphene annealed for AT4 mins at 180°C and etched for 1 min, highlighting (e) the stretching modes of CH_2 or CH_3 groups between 2800 and 3100 cm^{-1} (f) the stretch modes of oxygen functional groups between 800 and 1800 cm^{-1} at indicated by the dotted lines. Note that red lines correspond to samples that have been annealed

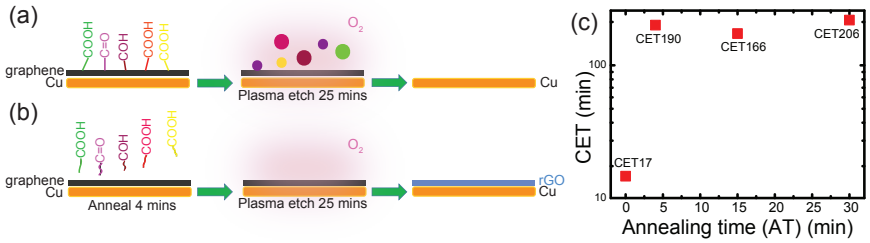

Figure 12.17: Schematic of oxygen plasma etching process of hydrocarbon contaminated CVD graphene on Cu for (a) untreated surface and (b) low-temperature annealed surface. (c) Critical etching time required to complete removal of all Raman features related to graphene for annealing times up to 30 mins.

relatively inert molecular gas such as oxygen or argon. These reactive ions interact with surface species to form the volatile compounds.[397] Typically, the combination of ion bombardment to dissociate the bond with an inert gas, coupled with reactive chemical etching with volatile oxygen species, results in faster etching than either alone.[398] Therefore, either increased bond dissociation or more abundant oxygen species will accelerate oxidation and trigger etching. If oxygen or surface species are already present at the surface, weakening the C-H bond though chemi- or physi-sorption, the initial bombardment to create dangling surface bonds does not need to occur, and the etching rate can be dramatically increased.

This contamination-assisted plasma etching action of CVD Gr on Cu is shown schematically in Fig. 12.17. The as-received sample initially has many hydrocarbon contaminants attached to the Gr surface (see Fig. 12.16). With the presence of these contaminants, exposure to the plasma rapidly over-etches the whole Gr sheet and it is completely cleaned off from the Cu substrate. However, when low temperature annealing is performed on the Gr, hydrocarbon contaminant species are desorbed by the annealing, leaving a cleaner Gr surface. In such a case, exposure to the plasma for the same length of time instead oxidizes the film, producing an rGO film of controlled oxygen doping.

Ultraviolet-ozone (UV-O_3) treatment and high temperature (550°C) thermal annealing in inert gases have been used to eliminate residues on CVD Gr on Cu.[384] However, these methods have been known to alter the intrinsic properties of the Gr surface, such as introducing interlayer strain between the Gr and Cu by high temperature annealing[182] and uncontrolled oxygen doping during the UV-O_3 treatment.[337,384] The mild annealing on the other hand desorbs the absorbed oxygen, without significantly

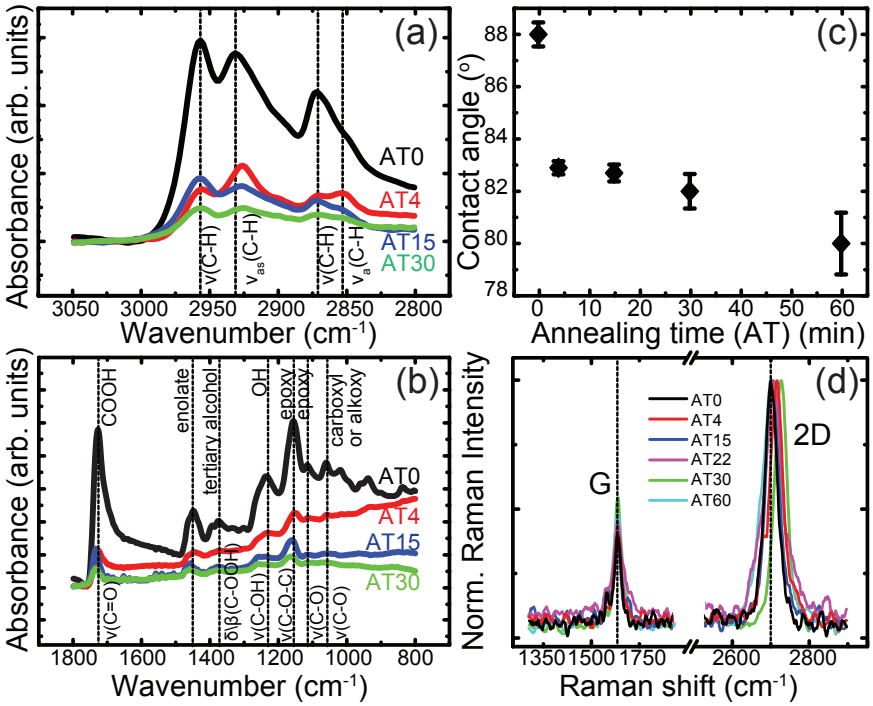

Figure 12.18: Background subtracted ATR-FTIR spectra CVD full graphene annealed for ATX mins at 180°C and non-etched, highlighting (a) the stretching modes of CH_2 or CH_3 groups between 2800 and 3100 cm^{-1} (b) the stretch modes of oxygen functional groups between 800 and 1800 cm^{-1} at indicated by the dotted lines (c) contact angle measurements from sessile drop water droplets. (d)Raman spectra comparison of CVD full graphene on Cu annealed for ATX mins at 180°C and non-etched, normalized using the peak height of the 2D mode.

affecting other properties of the system, as shown in Fig. 12.18.

ATR-FTIR was performed on Gr annealed for various times, showing the degree of decontamination systematically increases with annealing time. Fig. 12.18a and b shows the ATR-FTIR absorbance spectra of the Gr during annealing up to 30 mins, with oxygen functional groups identified with dotted lines. All the Gr samples have the same aging conditions, having been synthesized at the same time and stored in a low humidity vacuum desiccator for the same period of time. In all cases, there is evidence of some degree of oxygen doping on Gr, as pristine Gr should have no significant FTIR features.[392] The unannealed Gr *AT*0 (black solid line) shows the most significant signs of hydrocarbon contamination. The low temperature annealing treatment desorbed the contaminants as depicted in the schematic in Fig. 12.17b and hence the absorbance intensity of these oxygen functional groups dropped most

significantly from $AT0$ (black solid line) to $AT4$ (red solid line) and continue to drop relatively less as annealing time progresses to $AT15$ (blue solid line) and $AT30$ (green solid line).

In particular, there is a peak around 1450 cm^{-1}, which was not identified previously and we assign it to the enolate group.[254,325,399] This metal enolate peak in particular diminishes with increased annealing time. This group is thought to be the driving force for the synergistic oxidation in our previous Chapter 12.1, ([254]) where the strong intermixing of the Cu $3d$ electron states with the the C $2p$ electron states opens up reactive pathways for Cu to scavenge the oxygen, leaving behind the carbon network. This simple process of low temperature annealing, therefore,[145] is effective in desorbing the oxygen from the Gr and eliminate the contaminants, such that when these "clean" Gr are put upon oxidation by plasma etching, they can persist much longer than untreated Gr, as seen by the dramatic increase in CET.

The water contact angle measurements also support this interpretation, showing initially water contact angles reflective of Gr exposed to ambient for extended periods (see Fig. 12.18c).[393] Even with temperatures as low as 180°C, we see the large initial drop of contact angle after 4 mins annealing, followed by a slight but steady decrease with annealing time.

Most importantly, this low temperature annealing treatment does not have major effect on the quality of Gr. Fig. 12.18d shows the Raman spectra for the unetched Gr samples with various annealing times, showing high quality defect free monolayer Gr, without any defect modes. The G peak at 1580 cm^{-1} corresponds to the first order degenerate phonon energy, E_{2g} mode at the G point of Gr.[177] The 2D mode at 2690cm^{-1} comes from the G mode overtone and is indicative of sp^2 hybridization of Gr.[317] The 2D modes of all the annealed Gr samples can be well fitted with a single Lorentzian peak shape with a similar full width at half maximum (FWHM), indicating that they are indeed defect free, monolayer Gr in most cases.[148] Traditionally, the peak area ratio of the 2D and G modes indicates the number of layers of Gr.[148,177,355] The 2D/G ratio, varying between 3-4 except for AT15, shows no systematic effect from annealing. Measurements at various locations on the surface of each sample indicate a non-uniform surface with 2G/D ratios varying by roughly 10%; therefore, all values can be considered consistent with monolayer Gr. This is also supported by the XPS spectra, which show little change in the sp^2 hybridized fraction of carbon on the surface with annealing (Fig. 12.16), as also reported by others.[380] This suggests

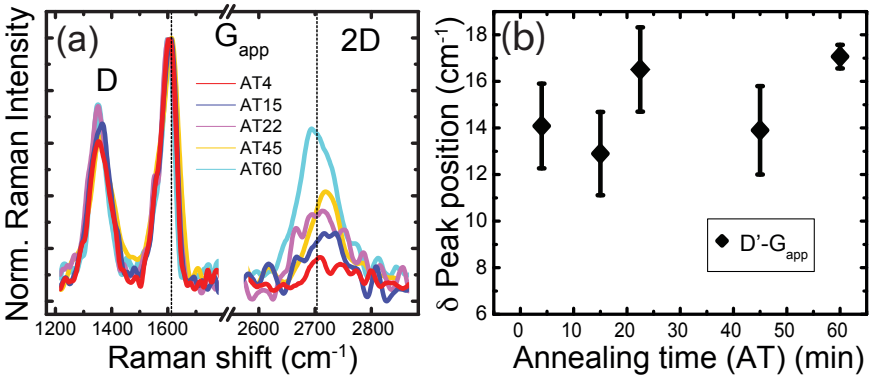

Figure 12.19: Raman spectra comparison of CVD full graphene on Cu annealed for ATX mins at 180°C and etched for 30 mins. (a) Spectra normalized at the peak height of G_{app} mode. (b) Peak position difference of D' to G_{app}.

that the Gr is not modified by annealing at 180°C.

Though all spectra have a consistent peak position difference between G and 2D with Gr suggesting rGO formation,[254,255] there is a slight blue shift of the 2D band observed for all annealing times. Though this is could be a characteristic of multi-layered Gr,[183] the expected accompanying peak broadening was not observed. Another possible explanation for the observed shift is a change of strain at the interface.[182,400,401] All annealed samples are slightly blue-shifted from the original pristine Gr 2D mode. There is no systematic trend with annealing time, with the maximum strain relief around 0.38% (+25cm^{-1}), calculated using the values reported for $\delta\omega_{2D}/\delta\epsilon$ of $\sim 66cm^{-1}/\%$ strain for deposition induced tensile strain[182] and $\sim 64cm^{-1}/\%$ for applied tensile strain.[400] As even 4 mins of annealing show some strain relief, it is possible that surface reconstruction from strain relief plays a role in the oxidation of the Gr, as strain is known to enhance diffusion (see for example Spjut et al.[402]). Even unstrained, Cu is known to be highly mobile at room temperature, especially in the presence of carbon based molecules[403] or with oxygen.[404] A strained Cu surface from high temperature CVD growth would have even more mobile surface atoms at room temperature; with enhanced diffusion, the Cu may be able to scavenge the oxygen from the carbon surface more quickly and rapidly oxidize at defects. Annealing, therefore, could relax some of this strain, slowing down the synergistic oxidation of Cu and Gr[254] under extended plasma exposure. As the CET is maximized at AT30 (30 mins annealing), this strain effect could also be an additional small factor of the resistance of the annealed Gr to complete etching.

With decontamination of the surface without affecting the monolayer Gr film, it is now even possible to control the oxygen doping more effectively during plasma oxidation. The Raman spectra for Gr samples annealed for various times and etched in oxygen plasma for 30 mins ($ET30$) are shown in Fig. 12.19a, normalized at the "apparent" G mode (G_{app}) located at 1590cm^{-1}. This G_{app} is a broadened mode which constitutes of both G and D' (near 1620cm^{-1}) modes.[176,179,225,255,405] The D' is a defect activated intravalley one-phonon mode associated with the C–H sp^3 hybridization defect and the overtone of the D mode.[319,320,405] All Raman spectra of the etched Gr samples also shows peaks from D at 1350 cm^{-1}, which is the defect-activated intervalley two-phonon mode for sp^3 defects[176,177,405] and 2D.[176] Though this ratio is often used to quantify the degree of defectiveness for Gr,[138,141,191,318] it is not meaningful quantitative guide for the degree of defectiveness for GO.[179,225,254,255,321,323] As rGO and GO surfaces are quite inhomogeneous, most forms of rGO and GO show essentially the same D to G ratio, irrespective of oxygen doping levels,[179,225,254,255,321,323] as was also observed in Fig. 12.19a

The peak position difference of D' to G_{app} were compared in Fig. 12.19b to determine which type of Gr was formed for the annealed Gr with same ET, following the metric established by King et al.,[255] as described in detail in Chapter 12.1.[254] We made various attempts at deconvoluting the G_{app} mode by fixing various parameters; however, as the modes are all subject to natural shifting due to strain or sample variations, as mentioned above, without a reference standard it is difficult to justify fixing a particular mode. If 2D' modes (overtone of D'[176]) are present in the Raman spectrum, it may be possible to infer the D' mode position, as was done by King et al;[255] this mode, however, was not observed for any samples in this study. This is not uncommon for GO.[225] Kaniyoor et al[225] failed to see any 2D' modes but were still able to assign a D' within the broad G envelop, aided by a tunable excitation wavelength. For convenience, we fixed the G mode at 1590 cm $^{-1}$. The peak position difference of annealed Gr varies from 12.8 to 17 cm^{-1}, all sitting within the rGO regime,[255] indicating that plasma treated Gr are all functionalized to become rGO, in keeping with our results in Chapter 12.1.[254]

As seen in Fig. 12.19a, the 2D mode intensity becomes stronger as annealing time increases, while the D mode remains almost the same, suggesting a greater degree of intact sp^2 Gr with longer annealing. It is worth noting that the 2D modes experience some degree of red shifting as the ATX increases and the peak shape becomes more

well-defined. The non-annealed Gr sample (AT0) (not shown here) has no Raman modes visible between 1000 and 3000 cm^{-1} as complete destruction of the Gr layer happened after only 17 min as previously shown in Fig. 12.17c. The combination of exposure to plasma and annealing gives two vectors for controlling the oxygen doping profile in the rGO films on Cu.

12.3.3 Conclusion

Low temperature annealing in air of CVD graphene on Cu is found to be effective in removing hydrocarbon contaminants accumulated on the surface, without changing the initial graphene characteristics as observed in other decontamination approaches. Only a brief annealing treatment can provide enough energy to desorb the contaminants on the surface, as seen by ATR-FTIR and water contact angle measurements, without changing the sp^2 hybridization of graphene as shown by XPS and Raman measurements. When low temperature annealing is performed on the Gr, hydrocarbon contaminant species are desorbed by the annealing, leaving a cleaner Gr surface. In such a case, exposure to the plasma oxidizes the film rather than etching it, producing an rGO film of controlled oxygen doping. The addition of an annealing steps allows tuning of rGO oxygen doping and properties by plasma oxidation, suggesting new avenues for patterning nanostructures in graphene based devices.

Part VI

Understanding the Reverse Micelles Approach

Chapter 13

Synthesizing Monodispersed Methylammonium Lead Iodide Perovskite Nanoparticles by Reverse Micelles Templating

13.1 Introduction

Hybrid organic-inorganic and all-inorganic metal halide perovskites have emerged as a disruptive technology in a number of fields, with record breaking developments in photovoltaics,[34,37,406,407] light-emitting diodes,[51,52,408,409] scintillators,[410] visible light communications,[411] and lasers,[50,66,68] among many others. Though these materials have been known for over a century, with their first description appeared in 1884, their current prominence is due to the introduction of highly efficient light emitting diodes and solar cell devices in 2012,[292,412] based on their high optical coefficients, tunable bandgaps, and long charge carrier lifetimes.

The desirable optical and electronic properties of these materials arise from their ABX_3 structure which was described in detail in Chapter 1.4. 'B' is a bivalent cation such as lead, tin or germanium. This is surrounded by six halide ions, usually chlorine, bromine, or iodine ('X'). Lastly, 'A' is a monovalent inorganic or organic cation such as cesium, methylammonium ($CH_3NH_3^+$) or formamidinium ($HC(NH_2)_2^+$).[232] In order to tune the optical and electrical properties, it is possible to use defect engineering,[20,413]

perovskite composition mixing (i.e. I/Br/Cl or organic-inorganic cation mixtures)[59,414] or nanoparticle size control for quantum confinement.[47,56,415]

Recently, there has been increased interest in developing nanostructured perovskite materials, particularly in light emitting diodes, due to their extremely high photoluminescence quantum yields at room temperature compared to bulk perovskites.[408,416] Due to the reciprocity between PL and absorption,[417] this suggests an increased absorption that also makes them attractive for photovoltaics. This feature was taken advantage of in the first use of perovskites in solar cells, as nanoscale sensitizers in dye sensitized solar cells.[34,418] Unlike many quantum dot materials, most defects in perovskites do not act as non-radiative defect centres; rather, there is a tendency for Frenkel defects to form shallow trap states near the band edge.[419] These shallow traps allow for longer PL lifetime due to trap mediated fluorescence.[420] As these defects are controlled by growth conditions,[20] this provides excellent opportunities for performance tuning using various approaches for nanoparticle formation. The high defect tolerance and low density of detrimental midgap states[50,52] makes perovskite nanoparticles ideal materials for high performance devices. Additionally, they allow better infiltration into mesoporous scaffolds for use in so called "meso-superstructured" solar cells,[34] improving efficiencies in exotic PV device architectures.

Despite recent advances, an accurate understanding of thickness and dimensionality dependent optical properties of perovskite nanocrystals has been elusive due to difficulties in the controlled synthesis for highly uniform nanoparticle films.[47] One of the benefits of perovskite based devices is their ease of manufacture. Due to their high effective homologous temperature (i.e. they decompose before melting),[421] their ability to align the inorganic planes parallel to substrates,[422] and their crystallographic flexibility allowing deformation and misorientation much more effectively than more rigid lattices,[421] perovskites do not typically require complicated processing. Due to their high defect tolerance, it is possible to make pervoskite based devices with high efficiency from a variety of approaches. However, as the reaction kinetics are extremely rapid in many metal organic lead halide perovskites, most synthesis approaches result in wide size distributions. Heterogeneity is currently one of the key roadblocks in the development of nanoparticle based applications,[423] and most losses in perovskite devices result from inhomogeneous films and interfaces.[421,424] The current record breaking photovoltaic devices are all based on solution approaches that use spin coating.[407] Particularly over large areas, spin coating tends to produce non-uniform layers, making

it less suitable for industrial scale-up.

Most synthesis approaches for perovskite nanoparticles use ligands, often oleic and octylamine acids, long enough that they cannot be integrated into the perovskite structure.[46] As mentioned in Chapter 1.4, the surface defects are generally not electronically quenching, these ligands are not required for surface passivation as in most quantum dot nanocrystals, and are required mainly to prevent agglomeration[47] and aid in salt solubility.[167] These ligand mediated approaches include hot injection;[43,49–51] ligand assisted recrystallization or re-precipitation;[52–56,167] emulsion-demulsion;[57,58] or ion-exchange.[58–60]

Such approaches have some limitations that restrict their large scale application due to the extremely fast reaction kinetics,[46,54,61,62] which typically require inert environments for iodide based synthesis.[52,425] Such fast kinetics typically will induce random nucleation, leading to inhomogeneous structures with large variations in particle size. Through temperature,[426] precursor concentration,[167] and ligand mixtures,[55] it has been possible to manipulate particle size, with monodisperse nanoparticles observed for some inorganic perovskites.[51] Synthesis of $CH_3NH_3PbI_3$ ($MAPbI_3$) nanoparticles with controlled size dispersion has proven to be more challenging, due to their lower stability and sensitivity to moisture.[52,63–65] Additionally, ligand assisted synthesis has a tendency to form 1D nanowire structures[66–68] or 2D nanoplatelets[54,56,167] rather than true 0D nanoparticles.

Here, we present a facile, room temperature micelle template approach using precursors and non-polar solvents under atmospheric conditions that takes advantage of diblock copolymer reverse micelles to prepare monodisperse metal-organic perovskite nanoparticles. Compared to ligated methods, diblock copolymer micelle templating allows greater control over the size distribution due to controlled nucleation and crystal growth. By separating the precursor solvation and reaction steps, it is possible to circumvent the high temperature kinetics of hot injection, bypass the metastable equilibrium required for ligand assisted re-precipitation, and avoid the reversibility of ion-exchange approaches. Additionally, using micellar nanoreactors rather than the dynamically stabilizing ligands leads to the formation of monodisperse spherical nanoparticles for a wide variety of organic precursors, including methylammonium lead iodide ($MAPbI_3$), formamidinium lead iodide ($FAPbI_3$) and methylammonium lead bromide ($MAPbBr_3$) based perovskites.

13.2 Results and Discussions

The SEM image in Fig. 13.1(a) shows a high density, highly ordered array of $MAPbI_3$ loaded poly(styrene-b-2-vinyl pyridine) (PS-P2VP) di-block copolymer micelles formed using a two step approach, where the two precursors solvated in polar solvents without ligands are sequentially introduced into a solution with pre-formed micellar nanoreactors in a non-polar solvent. By separating the solvation and reaction steps, we are able to achieve spherical $MAPbI_3$ nanoparticles with a polydispersity index (PDI) of the particle diameters of 0.0999. The PDI is a convenient method of expressing the distribution of particle sizes to compare polydispersity for particles of varying average diameter, as it is the relative standard deviation in the particle size, i.e. normalized by the particle diameter.[237] The particle size distributions were determined by randomly selecting over 100 particles in the micrograph images to obtain a statistical representation of the entire population. To confirm the reproducibility of these results, multiple batches of particles with the same loading ratios were produced and examined. Though there have been reports of similar highly uniform films for inorganic or bromide based perovskites from other ligated approaches (see Appendix Information Table 13.3), other reported $MAPbI_3$ nanocrystal systems have diameter PDIs of 0.2-0.3 (see Table 13.1 and Appendix Information Table 13.3). The reverse micelle templated method results in much lower PDI, over a variety of particle sizes. The inset in Fig. 13.1(a) shows the entropic force map[242] (the planar probability map of first neighbour distances) that indicates an arrangement of particles, nearly hexagonally close-packed (Fig. 13.15 shows other spatial statistic parameters). The pair correlation function of this system in Fig. 13.1(c) also confirms a hexatic lattice organization, with a lattice disorder parameter[242] of 13 from a perfect hexagonal organization. Such uniformity, and the ability to produce quasi-hexagonal arrays of nanoparticles, is achieved through the self-assembly of close-packed non-interacting spherical micelles[242] during spin coating on prepared substrates. Unlike with other spin coating approaches, which tend to produce non-uniformity over large areas, the entropic force leading to the close packing of such spheres allows micelle templated films to have long range uniform packing of nanoparticles.

By contrast, with octylamine-assisted synthesis of $MAPbI_3$ nanoparticles, relatively few rod like particles are formed, with little control of distribution on the surface or the PDI. As Fig.13.1(b) shows, sparsely dispersed nanoparticles with a PDI of

Method	Average ϕ (nm)	PDI	Source
Micelle Templated	**6.82**	**0.0999**	**This Work**
Ligand-assisted	**59.42**	**0.2440**	**This Work**
Ligand-assisted	2.60	0.1538	Wang et al., 2017[167]
Ligand-assisted	8.10	0.3161	Li et al., 2017[427]
Ligand-assisted	10.10	0.2874	Aharon et al., 2016[67]
Ligand-assisted	12.65	0.2549	Levchuk et al., 2017[54]
Nanocrystal-in-matrix	5.37	0.2250	Zhao et al., 2017[428]

Table 13.1: Comparison of methylammonium lead iodide nanomaterial average diameter and polydispersity index (PDI).

0.244 are formed under similar deposition conditions. The size of the micelles and the ligand-assisted nanoparticles are comparable, with an average of 54nm for the micelles and 59nm for the ligand-assisted nanoparticles. However, the shapes and PDI are dramatically different due to the differences in the growth mechanisms for ligand assisted and micelle templated deposition. Ligands in solution tend to dynamically stabilize perovskite nanocrystals leading to a rapid exchange between bound and free states.[49] Any unreacted MA cation that is in excess in the solution will dynamically replace ligands and lead to uncontrolled growth,[167] often in one dimension resulting in nanoplatelets and nanorods. In the micelle templated approach, however, due to the two step loading process, any precursor salts that have not immediately infiltrated into the micelles reacts in the non-polar solvents and precipitates out of solution, making it essentially self-limiting. Any excess precursors and precipitates can be easily removed via centrifugation, resulting in only stable loaded micelles which can then be deposited.

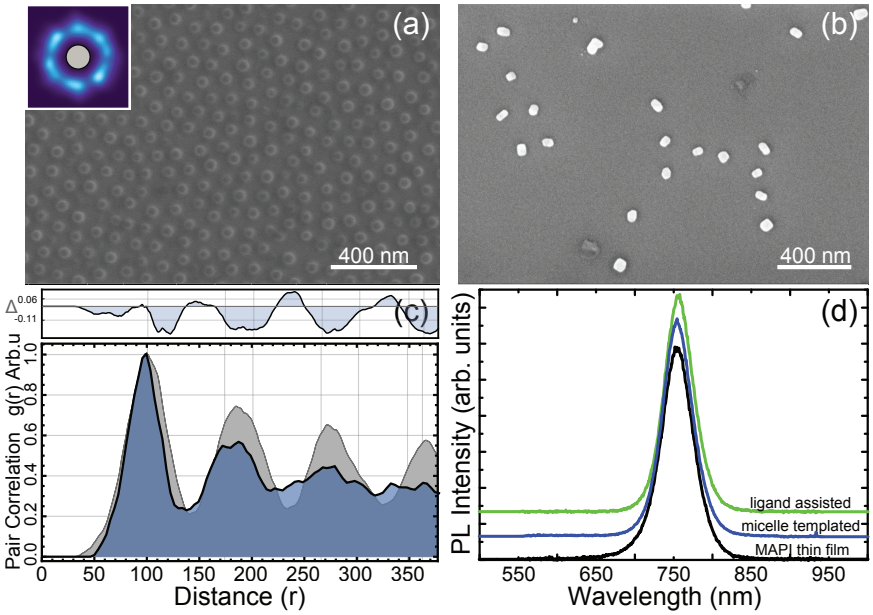

Figure 13.1: SEM micrographs of $MAPbI_3$ nanoparticles synthesized by (a) micelle-templated with inset of entropic force map of first neighbour and (b) octylamine ligand-assisted. (c) Pair correlation function of micelle-templated $MAPbI_3$. (d) Comparison of Photoluminescence measurement of $MAPbI_3$ thin film, micelles-templated $MAPbI_3$ and ligand-assisted $MAPbI_3$.

For $MAPbI_3$ samples from both ligand-assisted synthesis and micelle templated deposition, the photoluminescence (PL) spectra, shown in Fig. 13.1(d), exhibit PL response at near 750nm upon excitation at 532 nm, which is identical with a bulk $MAPbI_3$ thin film formed though anti-solvent washing, after normalization of the peak intensities. Due to the large sizes of the nanoparticles, quantum confinement is not expected.[56] To our knowledge, this is the first $MAPbI_3$ nanoparticles successfully synthesized by the reverse micelles technique, though inorganic perovskites have been successfully produced previously.[429,430]

The main advantage of forming nanoparticles using the reverse micelle method is the ability to control the nanoparticle size and dispersion on various substrates. By modifying the stirring time, the amount of precursor loading per P2VP unit, the solvent, the co-polymer molecular weights, or the ratio of polystyrene to 2-vinyl pyridine blocks, it is possible to modify the size of the micelles and nanoparticles, from nearly 70 nm down to around 7 nm in diameter as shown in Fig. 13.2. Unlike ligand stabilized approaches to $MAPbI_3$,[54] these micelle structures are relatively stable. Though dimethylformamide (DMF) is known to poison ligated colloids,[425,431,432] it is

used with the reverse micelles without any negative effects. The deposited micelles are also not prone to agglomeration; rather, once deposited they maintain their separation and dispersion (average interparticle distance of 100 nm) indefinitely. In all cases, spin coated monolayer films on Si showed PL spectra consistent with $MAPbI_3$ centred around 760 nm.

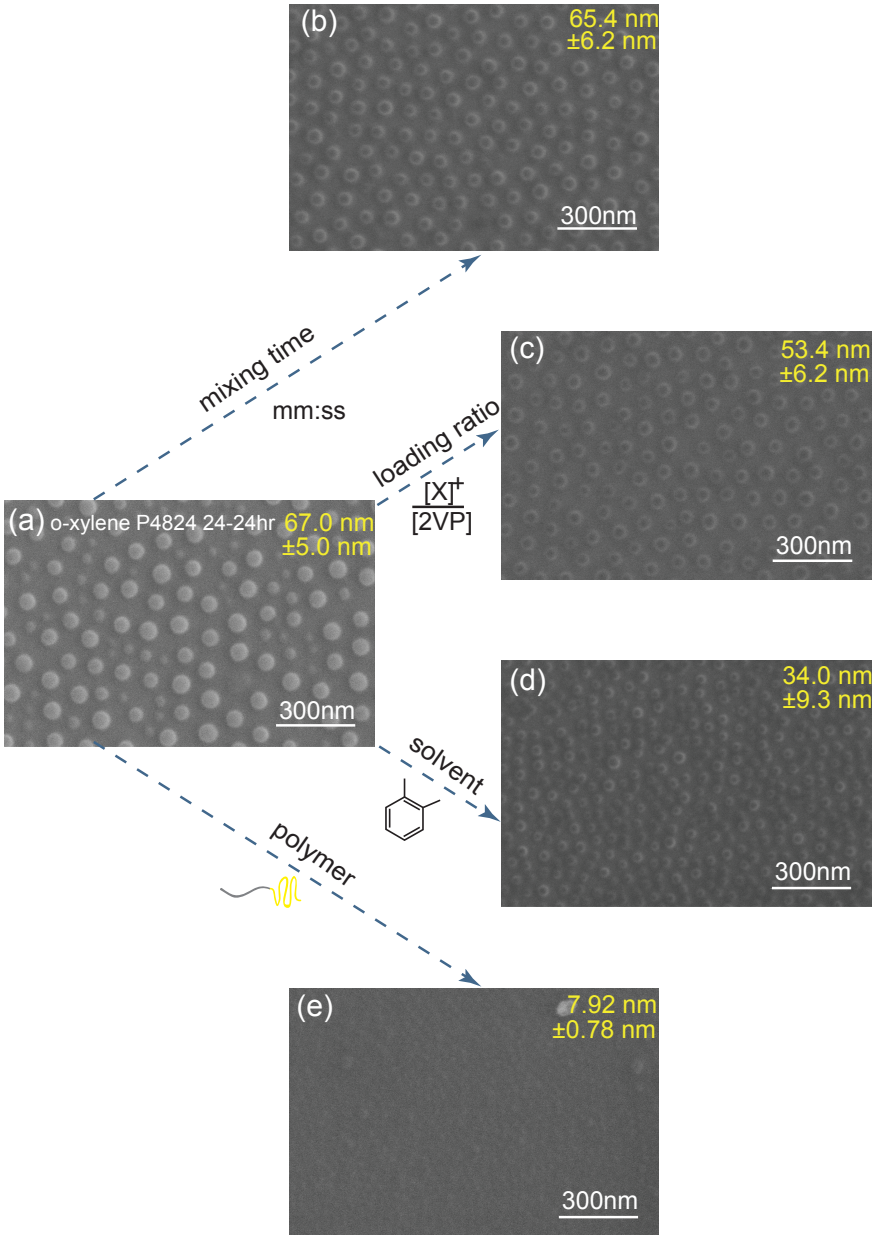

Figure 13.2: SEM micrographs of $MAPbI_3$ nanoparticles in micelles originally formed in (a) P4824 diblock copolymer in o-xylene stirred for 24-24hrs with 2:2 MAI/PbI_2 ratio. Different processing conditions result in various sizes of micelles as indicated in yellow text (b) change of stirring time to 18-30hrs, (c) change of loading ratio to 0.5:0.5 MAI/PbI_2, (d) change of solvent to toluene and (e) change of polymer molecular weight and di-block ratio to P1330 (polystyrene(48.5k)-b-poly(2-vinyl pyridine)(70k)) diblock copolymer.

This level of control relies on an understanding of how such nanoparticles are

formed within the nanoscale reactors.

We were able to confirm that the nanoparticles were formed inside the micelle using two basic approaches. Fig. 13.3 shows an EDX line scan performed in STEM using high magnification to obtain the precise composition information of the loaded micelles. Fig. 13.3(a) shows the STEM image of the loaded micelles with the yellow line highlighting the position from which the characteristic X-ray signals were collected. The corresponding EDX line intensity profiles can be seen in Fig. 13.3(b), displaying I $L_{\alpha 1}$, Pb $L_{\alpha 1}$ and C $K_{\alpha 1}$ signals in blue, green and red respectively. Comparing Fig. 13.3(a) and (b), it can be seen that the I and Pb signals were concentrated in the micelles region with the maximum coming from the centers of two micelles, whereas these signals decreased rapidly when the electron beam scanned to the edge of the micelles. On the other hand, the C $K_{\alpha 1}$ signal was consistent across the two adjacent micelles, indicating a similar amount of the C throughout two micelles area. This is true in the region with low contrast between the adjacent micelles, indicating that they are touching in the PS corona. Consequently, we were able to confirm the successful I and Pb precursor infiltration into the micelles. Additionally, we used quantitative nanomechanical property mapping (QNM) using the AFM in tapping mode to examine the properties of the loaded and micelles, as shown in Fig. 13.3. QNM allows measurement of the Young's modulus variation on a surface, and has been successfully applied to examining the properties of soft materials.[106,433] As shown schematically in Fig. 13.3(c) and (f), the AFM tip interacts with the surface differently when the micelles are empty or loaded with the perovskite nanoparticles. As seen in Fig. 13.3(e), the line profile through the empty micelle indicates that the core of the micelle is softer than the corona region. This lowering of the modulus through the core likely results from anisotropic nature of polystyrene in the diblock copolymer.[434] The diplock copolymers are aligned horizontally when the tip first interacts with the micelle and vertically as the tip interacts with the core; as the polystyrene has a higher Young's modulus when aligned lamellar than vertically, the modulus is reduced through the core. Similar to previous results found using phase contrast AFM for ZnO,[435] the Young's modulus of the micelle core was seen increases when the perovskite precursors infiltrate the micelle core and react to form the perovskite (Fig. 13.3(h)). Nanoparticles have been known to enhance the mechanical properties of copolymer/nanoparticle composites.[436] Therefore, the increase in Young's modulus through the micelle core is most likely due to the stiffening effect of nanoparticles inside the copolymer micelle.

From both techniques, it is possible to observe the perovskite formation occurring inside the micelles, rather than forming in the solvent and coating the micelle structures.

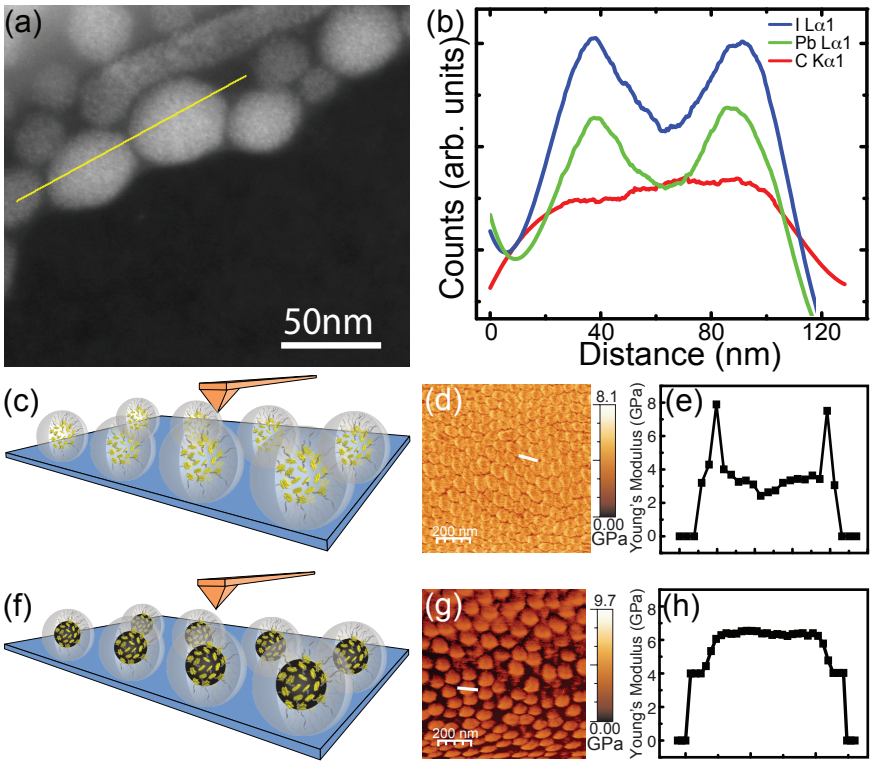

Figure 13.3: (a) STEM micrograph of $MAPbI_3$ -loaded micelles and (b) EDX line profile of Pb (blue line), I (green line) and C (red line) across two loaded micelles (yellow line). Schematic of AFM tip tapping during QNM measurement on (c) empty micelles and (f) loaded micelles. Young's Modulus map measured by QNM of (d) empty micelles and (g) loaded micelles; and the Young's Modulus line profile of one single (e) empty micelle and (h) loaded micelle.

The typical process of nanoparticle formation using micellar templates relies on the spontaneous formation of micelles in selective solvents from diblock copolymer unimers with one hydrophobic and hydrophilic end. With non-polar solvents such as o-xylene or toluene which selectively dissolves polystyrene, PS-P2VP forms reverse micelles as shown in Fig. 13.4, where the hydrophilic poly-2-vinyl pyridine block forms the micelle core surrounded by a corona of polystyrene. The dynamic spherical structure of the loosely associated unimers allows ionic precursor salts to penetrate through the corona due to the osmotic pressure of the non-polar solvent. Driven by the incompatible polarity between nonpolar solvent and the polar metal salt, the precursor ions diffuse into the micellar cores. The ionic salts tend to stabilize the polar core

of the reverse micelles once they are infiltrated either through coordination bonds with several pyridine sites[249] or through intercalation. When a second salt or reactant is loaded, it follows the same infiltration process into the now more ionic core and can react with the first salt as they encounter each other inside the hydrophilic core. The schematic in Fig. 13.4(a) describes the $MAPbI_3$ perovskite formation process where the reverse micelles act as nanoreactors for the salts of MAI and PbI_2. TEM image at the bottom shows a layer of spin-coated reverse micelles loaded with $MAPbI_3$ nanoparticles where MAI was added as the first salt followed by PbI_2 as the second salt.

However, complexation with the P2VP can result in an instability of the micelle structure. This is observed if, for example, the salt loading sequence is reversed. As seen in Fig. 13.4(b), adding the PbI_2 first does not produce nanoparticles and in fact appears to destroy the micelles. Due to the interaction of Pb with P2VP, all that is visible in the TEM image when PbI_2 was added to the reverse micelles solution and stirred for 24 hrs are the remnants of coagulated polymer strands as a result of demicellisation.

It has been reported widely that the nitrogen atom in the pyridine group complexates with transition metal ions such as Cu, Zn, Fe, Cd, In, Hg in metal halide salts.[214,215,289,437,438] If the interaction is strong, the steric hindrance brought about by the coordination of the metal salt with the nitrogen in the ortho position of the vinyl group can result in a loss of resonance stabilization[214] and the polymerization rate of the 2-VP complex becomes very small.[214]

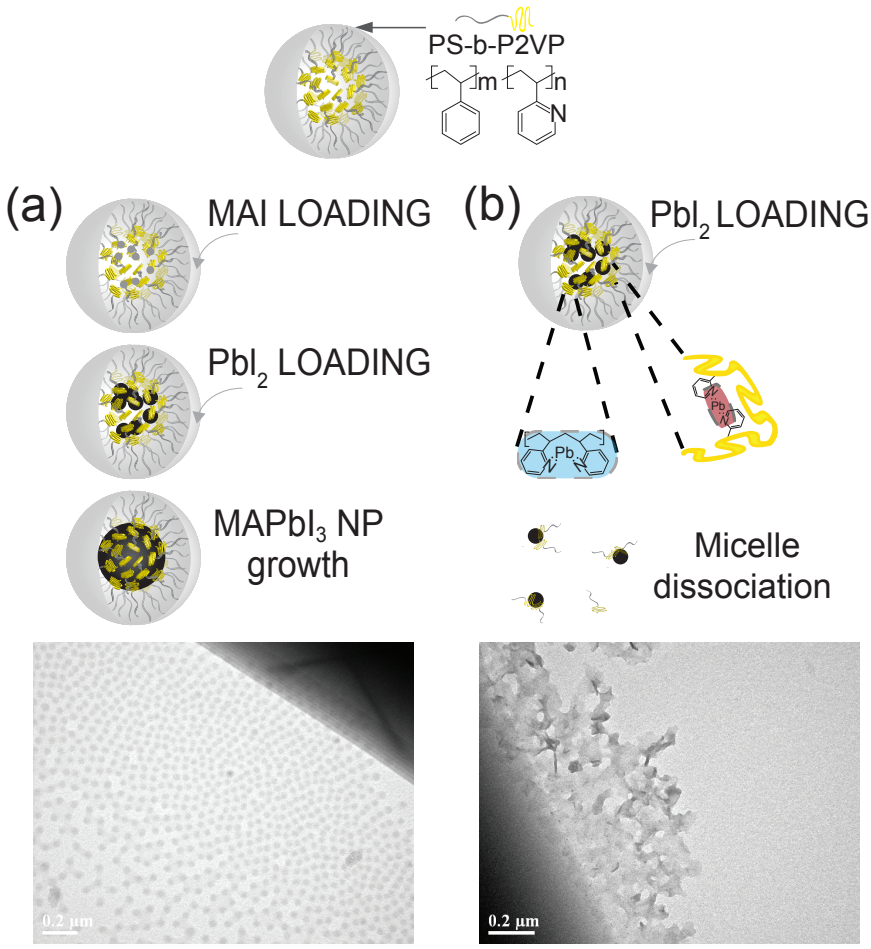

Figure 13.4: Schematic of micelles loading process with route (a) addition of MAI salt followed with PbI_2 salt to form $MAPbI_3$ nanoparticles as the end product as shown in the bright field TEM;(b) addition of PbI_2 salt first, leading to micelles destruction as shown in the bright field TEM.

Using density functional theory (DFT), Hou et al. reported a binding energy of 0.17 eV between the N-Pb bond in the 2VP unit.[430] Therefore, prolonged stirring would result in an unravelling of the micellar structure, with the ionic PbI_2 attach to the polar 2VP end of the di-block copolymer. P2VP once coordinated with the metal would favour intramolecular rather than intermolecular coordination.[215] Therefore, the PS-b-P2VP micelles are dissociated to individual monomer complex strands as seen in the TEM in Fig.13.4(b).

For the MAI salt, segregation into the micelle core may result from either osmotic pressure encouraging segregation of the polar salt into the hydrophilic core or the interaction of pyridine with iodine. Iodine is known to preferentially stain pyridine over

polystyrene, and has been used to enhance contrast in electron microscopy of diblock copolymers.[439,440] Typically in SEM/TEM, empty micelles have very low contrast due to the weak elastic interactions of carbon and nitrogen with energetic electrons, without a significant difference for PS and P2VP blocks. By exposing the empty micelles to an iodine vapor (see Supporting Information Fig. 13.16), the P2VP cores can be made visible due to the preferential complexation of iodine and pyridine, with a binding energy of 0.39 eV.[441] Unlike transition metal interactions, iodine complexation does not appear to destabilize the micelle structure. MAI loaded micelles show similarly strong contrast in high resolution TEM (Fig. 13.16). EDX line scans show the high concentration of iodine, concentrated at the centre of the micelle structure after 24hrs stirring.

When the MAI is present inside the micelle, the micelle is prevented from undergoing demicellisation. MAI is known to readily form adducts with PbI_2 and enhance the solubility of PbI_2 in polar solvents.[442] The presence of MAI appears to stabilize the micelle core, and possibly facilitates the PbI_2 salt infiltration into the micelle. Additionally, the strong interaction between MAI and PbI_2 (Gibbs free energy of formation 1.33 eV[63,443]) suggests that the PbI_2 will preferentially bond with the MAI rather than P2VP when they are both present inside the micelle, leaving the micelle structure intact during nanoparticle formation. However, the infiltration process is not instantaneous.

If both PbI_2 and MAI salts are added to the solution simultaneously, the micelles are visibly intact after 48 hrs mixing time (see Appendix Fig. 13.16). However, in this case, significant black residue of $MAPbI_3$ can be centrifuged from the micelle solution, leaving behind unloaded micelles, much more than the normal residue that results from the self-limiting nature of perovskite nanoparticle formation in the micelles. Such behaviour suggests the formation of large $MAPbI_3$ particles outside the micelles are unable to infiltrate the micelles due to their large size, but do not destroy them. In the simultaneous loading case, the MAI salt does not have enough time to infiltrate the micelles and instead bind immediately with the more readily accessible PbI_2 salt in the non-polar solvent surroundings and precipitate out of solution.

We have recently developed an approach to track the loading of precursors into micelles using QNM of the micelles. QNM allows measurement of the Young's modulus variation on a surface, and has been successfully applied to examining the properties of soft materials.[106,433] In these micellar systems, it is possible to correlate the change

in modulus of the centre of the micelle with the amount of salt that has successfully infiltrated the micelle. For MAI salt loading, QNM shows that the longer MAI is allowed to stir with the micelles prior to adding PbI_2, the harder the micelle core becomes relative to an empty micelle (see Appendix Information Fig. 13.17). This suggests that greater infiltration of MAI with time. It is not possible to track the effect of PbI_2 loading in a similar fashion as the hardness does not change with loading if nanoparticles are formed.

If MAI salts are given enough time to infiltrate into the micelle, and PbI_2 is introduced, organic-inorganic halide perovskites nanoparticles are formed within the micelle. Without the stabilization from MAI, introduction of PbI_2 disturbs the micellar environment and prevents the formation of nanoparticles.

Fig. 13.5 shows the transient PL curve recorded under ambient conditions at an excitation wavelength of 488nm for ligand-assisted and optimal micelle templated nanoparticles. The data for both can be fit with two exponentials with χ^2 confidence of at least 0.995. Though three component and stretched exponential fitting was attempted, the fitting was seen not to converge for either case. The two exponential decay times for both approaches measured under ambient conditions showed an initially fast component with a lifetime of 4.15 ns and 4.65 ns, respectively, and was followed by a slower component with lifetimes of 22.34 ns and 30.10 ns, for ligand-assisted and micelle templated nanoparticles respectively. As radiative recombination time in nanocrystals is predicted by the Stickler-Berg formula to be no longer than a few nanoseconds,[417,420] it is likely that the fast component for both cases might be attributable to radiative recombination, with the longer components due to delayed luminescence by multiple trapping and detrapping of band-tail trap states.[420] Such delayed PL seems to be an intrinsic feature of colloidal nanocrystals.[444,445]

The longer lived PL lifetime for the two approaches are quite similar, with the micelle templated approach yielding slightly longer lifetimes; yet as shown by Fig. 13.5(b) and (d), the micelle templated nanoparticles are much smaller than the ligand assisted particles (6.8 nm vs 59 nm, see Table 13.1). Typically, the PL lifetime tends to decrease with decreasing particle size[415] due to the dominance of surface trapping as the crystal size decreases. Passivating ligands have been used successfully to increase the PL lifetime for small particles.[446] This suggests that the micelle surrounding the nanoparticle is providing increased protection for the small particles, significantly improving the PL lifetimes. In fact, to determine the true size of the nanoparticles inside

the micelle, the micelle sheath was removed by O_2 plasma etching. As the PL intensity after etching was greatly diminished, etching ultimately poisoned the luminescence due to the inherent instability of perovskites with oxygen[443] and subsequent exposure to the ambient environment of the unpassivated nanoparticles.

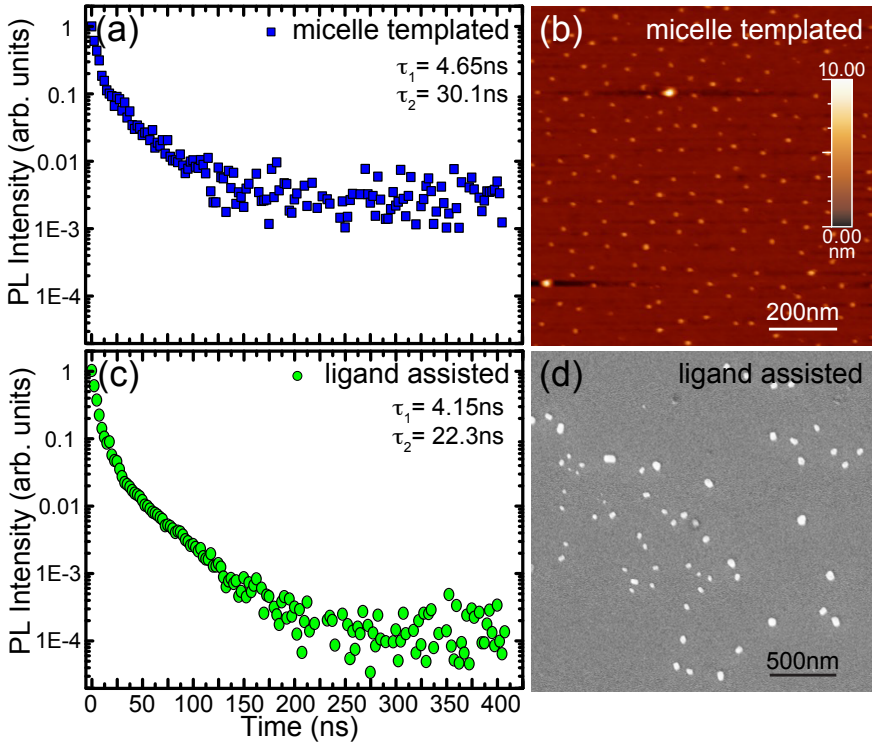

Figure 13.5: Time-resolved photoluminescence decay of $MAPbI_3$ synthesized by (a) micelle-template method and (c) octylamine ligand-assisted method. $MAPbI_3$ SEM images of (b) nanoparticles by micelle-templated after oxygen-plasma etching and (d) nanoparticles by the octylamine ligand-assisted method.

The other major benefit of using a micelle templated approach is its versatile application to a wide variety of material systems – we have used the same basic micellar diblock copolymer nanoreactor to produce oxide,[237] dielectric[75] and metal nanoparticles.[123] In addition to methylammonium iodide, we have also been successful in producing monodisperse nanoparticles of $FAPbI_3$ (PDI=0.16) based perovskites, as shown in Fig. 13.6. Though $MAPbBr_3$ nanoparticles were also successfully formed, they were not monodispersed; instead, they form a bimodal distribution with two mean particle sizes. We see some quantum confinement effects in the case of $MAPbBr_3$ nanoparticles successfully produced inside the micelles, as shown in Fig. 13.6(a) for

solutions under UV illumination. In the vial on the left, which glow with a strong green colour (∼540nm), large bulk-like $MAPbBr_3$ particles were formed outside the micelles; whereas the vial on the right glows closer to cyan, corresponding to ∼510nm, similar to those seen for quantum confined nanoplatelets[54,447] and nanoparticles.[415] As the $MAPbI_3$ and $FAPbI_3$ nanoparticles were produced in sizes around 5-7nm, these are above the Bohr radius ($\sim 2.2nm$[448]) and do not show any quantum confinement effects.

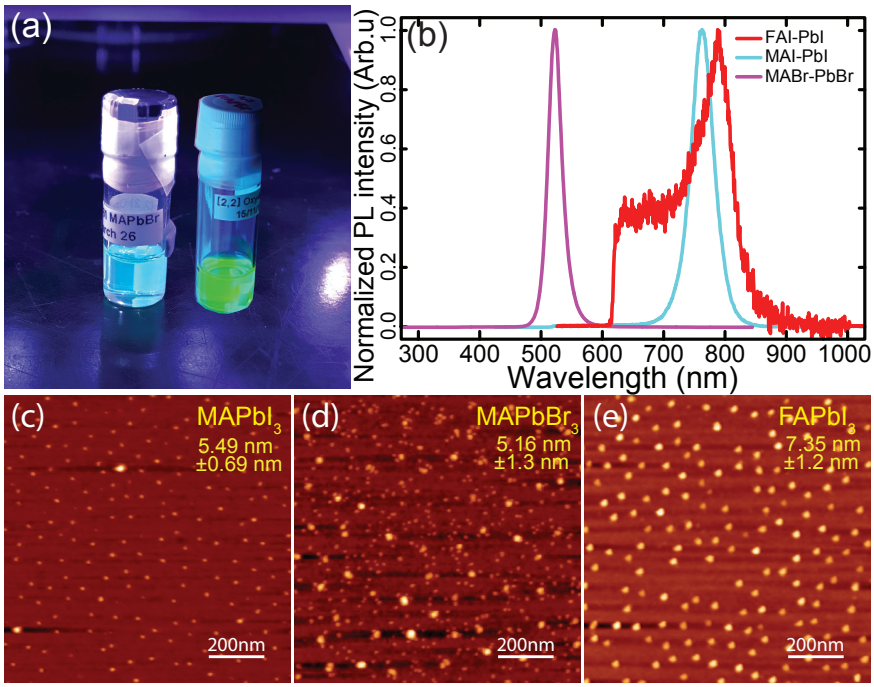

Figure 13.6: (a)P9861 diblock copolymer micelles solution loaded with $MAPbBr_3$ nanoparticles and P4824 diblock copolymer micelles solution with large $MAPbBr_3$ particles under UV illumination. (b) Photoluminescence measurements of $MAPbBr_3$ (violet), $MAPbI_3$ (pale blue) and $FAPbI_3$ (red) colloidal solutions, all synthesized with diblock copolymer micelles. AFM images of perovskite nanoparticles synthesized by the micelles templating method. (c) $MAPbI_3$ nanoparticles in micelles formed in P4824 diblock copolymer in o-xylene stirred for 24-24hrs with 2:2 MAI/PbI_2 ratio. (d) $MAPbBr_3$ nanoparticles in micelles formed in P9861 diblock copolymer in o-xylene stirred for 24-24hrs with 2:2 $MABr/PbBr_2$ ratio. (e) $FAPbI_3$ nanoparticles in micelles formed in P4824 diblock copolymer in o-xylene stirred for 24-24hrs with 2:2 FAI/PbI_2 ratio.

13.3 Conclusion

In this Chapter, we outline a facile room temperature under atmospheric conditions to prepare monodisperse metal-organic perovskite nanoparticles, using the reverse micelle deposition approach. Compared to traditional ligated methods, diblock copolymer micelle templating allows greater control over the size distribution due to controlled nucleation and crystal growth. Using the reverse micelle deposition approach, we have been able to produce monodisperse nanoparticles for a variety of organic precursors, including methylammonium lead iodide ($MAPbI_3$), methylammonium lead bromide ($MAPbBr_3$) and formamidinium lead iodide ($FAPbI_3$) based perovskites. Clearly, the order and time of salt loading are highly significant in forming the perovskite nanoparticles inside the reverse micelles. If organic salts are given enough time to infiltrate into the micelle, organic-inorganic halide perovskites nanoparticles are formed. If the metal halide is added first, or the salts are added simultaneously rather than sequentially, nanoparticle formation does not proceed and large uncontrolled perovskite particles are formed instead. As reaction kinetics between organic and inorganic halide precursors for perovskite are extremely rapid, most synthesis approaches result in wide particle size distributions. Heterogeneity is a key roadblock in the development of nanoparticle based applications, and most losses in perovskite devices result from inhomogeneous films and interfaces. RMD of organic-inorganic halide perovskites is perfectly suited to overcoming these challenges. Compared to traditional ligated methods, RMD minimizes size fluctuations due to controlled nucleation and growth. By separating the precursor solvation and reaction steps, it is possible to circumvent the high temperature kinetics of hot injection, bypass the metastable equilibrium required for ligand-assisted re-precipitation, and avoid the reversibility possible in ion-exchange approaches. Additionally, using micellar nanoreactors leads to the formation of monodisperse spherical QD NPs rather than nanoplatelets for a wide variety of organic precursors, including methylammonium lead iodide ($MAPbI_3$), methylammonium lead bromide ($MAPbBr_3$) and formamidinium lead iodide ($FAPbI_3$) based perovskites.

Part VII

Future Work

13.4 LiF

As discussed in Chapter 1.2, LiF is an extremely useful interlayer often found in organic devices. It is however doomed to be impractically challenging to characterize LiF especially when it is nono-sized because of its light weight nature. Taner et al. had to use the grazing incidence X-ray diffraction at a synchrotron facility to detect the LiF in reverse micelles.[301]

Theoretically, there should be no first-order Raman active modes because of the inversion symmetry of the LiF crystal.[449,450] There is only one LiF bond in a unit cell of LiF, so there are four phonon dispersion curves, the LO, TO, LA and TA. The dispersion relation for LiF is as shown in Fig. 13.7 a. The solid lines are computed results from the deformation dipole model and the dotted lines are experimental results from neutron scattering.[451]

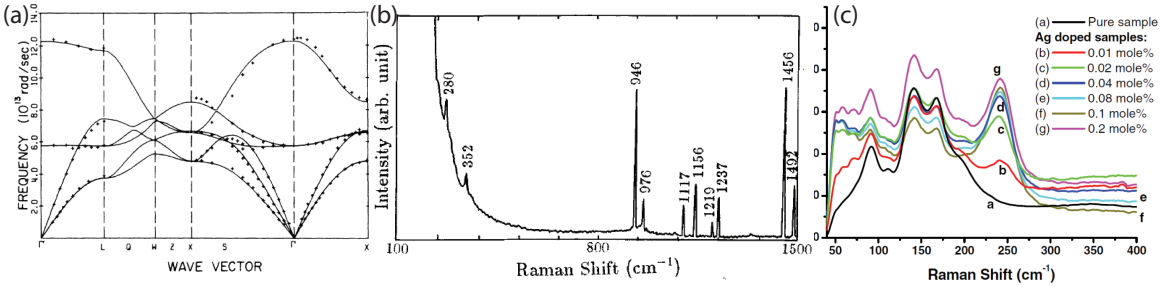

Figure 13.7: (a)Phonon dispersion relation of LiF at room temperature from reference [451]. (b) Raman spectrum measured for LiF cluster with average size of about 10nm from reference.[450] (c) Raman spectrum of pure LiF nanocubes (black curve) with size in the range of 50nm-10um. Reproduced with permission from reference [449].

However, the Raman selection rule can be relaxed when the actual size of the crystal is comparable to the laser wavelength in the nano regime.[449,450] This is because some symmetry rules in the space group might be broken. As a result, the selection rule will be relaxed and this give rise to extra modes, so-called the surface assisted (SO) modes.[449,450] This lifting of selection rules allows nanoparticles of LiF to be observed under Raman as predicted and reported by few groups.[449–451]

Liu et al. published the experimental Raman spectrum of LiF clusters with size 10nm in Figure 13.7 b.[450] These modes somewhat match with the predicted modes in Table 13.2.

Table 13.2 shows the list of Raman active mode that are the optical modes (SO)

predicted by the lattice dynamic theory of Lucas.[450] The SO modes are surface-assisted modes made active for nanocrystals which would otherwise be forbidden in the bulk. However, these size-dependent SO Raman modes cannot be observed directly on their own but only with the overtones or combinations with the acoustic and optical modes.

Table 13.2: Theoretical second-order Raman active phonon modes of LiF[450]

Raman shift, cm^{-1}	Combinations
107	LO(X)-LA(X)
112	LO(X)-TO(X)
121	SO(1)-LO(X)
133	SO(3)-LO(X)
180	LA(L)-TA(L)
207	TA(L)
228	SO(1)-LA(X)
278	SO(1)-TO(L)
286	SO(2)-TO(L)
290	SO(3)-TO(L)
300	TO(L)
387	LA(L)
404	SO_-LO(X)+LA(X)
618	SO_+LO(X)-LA(X)
687	TO(L)+LA(L)
965	SO(1)+LA(L)
968	SO_+LO(X)
973	SO(2)+LA(L)
977	SO(3)+LA(L)

As seen in Fig. 13.7 c, the pure sample of LiF nanocubes (black curve) has three peaks located at 88, 142, 168cm^{-1}. (Note that the other peaks shown in the doped samples of LiF are irrelevant to this discussion.) These modes however, do not correspond to the modes predicted by Lucas in Table 13.2. Liu et al. suggested that phonon scattering from the combination of LO(X)-LA(X) observed at 104cm^{-1} and the combination of SO(3)-LO(X) at 136cm^{-1} are size dependent, suggesting that a shift might occur as a function of size.[450] The nanocluster size in their study was in the range of 4.7-10nm, whereras, the nanocubes in Alharbi's study were 10um-50nm.[449,450] This makes the size-dependence interpretation of Raman spectra for LiF nanoparticles difficult. However, this shows the possibility for the LiF nanoparticles of interest for incorporation into the devices are of the range of 20-60nm, where Raman active modes

could be observed in this regime.

13.5 Optical adhesive transfer process

Although the graphene transfer process works well, there are other potential transfer methods yet to be discovered and utilized. One of the methods is by using optical adhesive which does not require the use of graphene.

The method has been used for template stripping as described in Chapter 3.2, where a Au layer grown on Si can be stripped off from the Si using the optical adhesive. The smooth side can be used for depositing RMD nanoparticles and be etched in plasma without having much to worry about the plasma dynamics. Some preliminary work has been tried with this method by laminating the Au layer with nanoparticles on an organic layer, while the back side of the Au is supported by the optical adhesive to a glass piece. However, there is still challenges of etching the Au layer away after transferring the nanoparticles on the organic substrate. Previous trials of etching the Au layer with gold etchant standard 20% (potassium iodide) ended up being very messy because the set up was not optimized. It was difficult to etch the Au in between the layers. There is also an extra step of dissolving the organic optical adhesive which is cured to the Au layer.

For this method, perhaps the same method used in graphene transfer can be employed again, which is by casting the target polymer on top of the nanoparticles to secure the nanoparticles. However, float etching of Au will be impossible in this case because of the glass at the back side, which makes it too heavy to float on the etchant. Therefore, more work has to be done to optimize or re-design the set-up, but this is a method also worth-trying.

13.6 Micelles thickness dependence of plasma etching dynamics

In Chapter 4, we discussed the plasma interaction with organic materials and that the dynamics would be changed with more plasma species taking part. The graphene etching parameters established in Chapter 12.2, 12.1 and 12.3 would be changed as when micelles are involved in the system. Therefore the graphene used in Chapter 6

with a micelle layer on top used for transfer printing, would have been more etched than just a graphene alone under the same etching circumstances.

The focus of Chapter 6 was not on the degree of graphene oxidation with the micelles, the authors were only concerned with the intactness of graphene oxide after etching that allows the transfer process to take place. The plasma etching action with a monolayer micelles was not too drastic for the graphene. However, it is expected that as more organic materials (micelle thickness) is on the the graphene, the plasma etching action would elevate, which echoes with the idea of desorbing the VOCs on the graphene surface by annealing to have a better control of plasma etching in Chapter 12.3.

At one point, there should be a saturation limit of micelle thickness where the plasma action cannot further increase and because of the thick layer of micelles on top of the graphene, the plasma would not be able to reach the graphene during the etching. In such a case, the micelles maybe able to protect the graphene from the plasma action.

This would require a systemic study on the micelles-graphene system. Having a good idea on the micelles-graphene system under plasma treatment would be beneficial for the optimize the transfer printing process and the degree of functionalization of graphene to grahene oxide for devices.

13.7 Device Optimization

13.7.1 Graphene oxide patterning for devices

On top of the micelles interaction discussed in last section (Chapter 13.6, graphene oxide that results from oxygen plasma etching of graphene is an important aspect for device in terms of the change of work function and band alignment. Moreover, since it is a plasma action, the graphene can be masked to produce patterned graphene oxide for device making purpose. This requires further investigation on the plasma etching time with Raman and XPS to find out the degree of oxidation, and contact angle and Kelvin probe analysis for the surface energy and work function respectively.

13.7.2 Nanoparticles interlayer in devices

Having established the transfer printing method of nanoparticles using graphene in Chapter 6, the method should be applicable to any other types of nanoparticles "synthesizable" by RMD. Testing out various types of nanoparticles in the device would help further understanding the roles of these interlayers.

The most important aspect of using RMD is the great degree of control for dispersion. Having a good control of nanoparticle dispersion allows one to study the effect due to density (coverage), polar moment of the material and roughness. This can be tuned by the spin-coating parameters such as the micelle volume, spin-coating speed and even the approach of spin-coating (dynamic or static) technique. The interspacing of nanoparticles can also be tuned by the size of the micelles, which was discussed in Chapter 13 and solvent used in making micelles. All these can be characterized on the graphene prior to the transfer process using imaging techniques such as the AFM topography and SEM.

13.8 Perovskite nanoparticles compositional tuning

As discussed in Chapter 5.3.4, current state-of-the-art perovskite devices use mixed stoichiometry of halide for stability, enhanced absorption and emission and efficiency. Therefore, it would be worth investigating to use RMD to synthesis perovskites with mixed composition.

Chapter 13 and Chapter 10 serve as the stepping stone of knowing the possible interactions and complexation of various components with the pyridine group in the RMD perovskite system. However, the sequence of salt loading in the micelles may be critical for tuning the composition of perovskites. Much work has to be done on Raman, PL and TEM EDX analysis to understand the mixed stoichoimetry.

Part VIII

Conclusion

The goal of this thesis is to establish a transfer printing method to introduce a thin layer of interlayer nanoparticle material in the organic device, specifically for the interface between the metal cathode and organic layer and be able to detect the transfer of nanoparticles in the whole system with characterization means.

The limitation of putting the nanoparticles directly onto the organic layer comes from the fact that these nanoparticles were synthesized in reverse micelles which offers incredible controllability for both size and dispersion. Since the step of removing the polymeric shell of the micelles would result in also the damage of the organic layer where the reverse micelles sit, a transfer printing method is needed to overcome the inevitable destruction of organic layer.

Therefore, a universal transfer printing method using graphene was presented, which makes use of graphene as a transporting means of nanoparticles. It was made possible by understanding the oxidation behavior and interaction of CVD graphene on Cu with oxygen plasma and mild annealing monitored closely by a detailed Raman trilogy studies. It was found that after proper treatment with the graphene using only mild annealing, the graphene could be tuned to withstand the plasma conditions used to etch away the polymeric micelles for exposing the nanoparticles. Raman shows that the resultant graphene becomes oxidized to graphene oxide. The preliminary Raman results also show that the graphene oxide was transferred to the organic layer.

Raman spectroscopy was further explored because the transfer process requires a well-understanding on all material in the system including the micelles, type of nanoparticles, the transfer substrate–graphene and the organic layer. Raman spectroscopy proves to be such a powerful technique as it provides valuable insights to the evolution of the different phases iron oxides formed from the reverse micelles technique. Raman was also used to study the formation of the hot-topic perovskites materials in reverse micelles which has not been achieved before. Using the extended Raman techniques, the unconventional inverted-TERS, a monolayer of micelles could be detected while it is impossible for a normal Raman setting. The underlying mechanisms of this technique with high-resolution were proposed.

Finally, a micelle study with the pervovskite material was performed in order to understand and explore the tunability of reverse micelles on nanoparticle synthesis. Knowing how the precursors could interact and complexate with the pyridine group in the micelles; how the size of nanoparticles can be tuned by using micelles of different block lengths; and how the solvent of plays a role in the reverse micelles would offers

great control for future optimization on the nanoparticles to be transfer printed into devices interlayer.

To summarize, mastering the technique of Raman characterization for the micelles system, together with the detection ability for the post-transferred system opened up more pathways for manipulating the interlayer that can ultimately benefit to the improvement on organic photovoltaics.

Bibliography

(1) *Global Warming of 1.5 °C–An IPCC special report on the impacts of global warming of 1.5 °C above pre-industrial levels and related global greenhouse gas emission pathways, in the context of strengthening the global response to the threat of climate chang*; tech. rep.; 2018.

(2) Kenning, T. Global solar deployment to grow in 2018 despite China cuts – SolarPower Europe., 2018.

(3) Ostroverkhova, O., *Handbook of Organic Materials for Optical and (Opto)Electronic Devices: Properties and Applications*, 2013.

(4) Mazzio, K. A.; Luscombe, C. K. *Chemical Society Reviews* **2015**, *44*, 78–90.

(5) Huang, W.; Cheng, P.; Yang, Y. M.; Li, G.; Yang, Y. *Advanced Materials* **2018**, *30*, DOI: 10.1002/adma.201705706.

(6) Pearson, G. L.; Fuller, C. S. *Proceedings of the I.R.E.* **1954**, *40*, DOI: 10.1097/IAE.0B013E3182437EA4.

(7) Kippelen, B.; Brédas, J.-L. *Energy & Environmental Science* **2009**, *2*, 251.

(8) Werner, J. H. *Advances in Solid State Physics* **2004**, *66*, 172.

(9) Slaoui, A.; Collins, R. T. *MRS Bulletin* **2007**, *32*, 211–218.

(10) Tang, C. W. *Applied Physics Letters* **1986**, *48*, 183.

(11) Clarke, T. M.; Durrant, J. R. *Chem. Rev.* **2010**, *110*, 6736–6767.

(12) Park, J. H.; Lee, T.-W.; Chin, B.-D.; Wang, D. H.; Park, O. O. *Macromolecular rapid communications* **2010**, *31*, 2095–108.

(13) Cheng, P.; Li, G.; Zhan, X.; Yang, Y. *Nature Photonics* **2018**, *12*, 131–142.

(14) Liu, Z. et al. *Advanced Materials* **2008**, *20*, 3924–3930.

(15) Baral, J.; Izquierdo, R.; Packirisamy, M.; Truong, V.-V. *The European Physical Journal Applied Physics* **2011**, *55*, 30202.

(16) Turak, A. *RSC Advances* **2013**, *3*, 6188.

(17) Jayawardena, K. D.G. I. et al. *Journal of Materials Chemistry A* **2013**, *1*, 9922–9927.

(18) Aytun, T.; Turak, A. Z.; Baikie, I.; Halek, G.; Ow-yang, C. W. *Nano letters* **2011**, *12*, 39–44.

(19) Yin, Z. et al. *ACS Nano* **2010**, *4*, 5263–5268.

(20) Yin, Z. et al. *Advanced Energy Materials* **2014**, *4*, 1–19.

(21) Li, S.-s.; Tu, K.-h.; Lin, C.-c.; Chen, C.-w.; Chhowalla, M. *ACS nano* **2010**, *4*, 3169–3174.

(22) Smith, C. T. G. et al. *Applied Physics Letters* **2014**, *105*, DOI: 10.1063/1.4893787.

(23) Wu, J. et al. *ACS nano* **2010**, *4*, 43–48.

(24) Wu, J. et al. *Applied Physics Letters* **2008**, *92*, DOI: 10.1063/1.2924771.

(25) Park, H.; Howden, R. M.; Barr, M. C.; Bulovi, V.; Al, P. E. T. *ACS nano* **2012**, DOI: 10.1021/nn301901v.

(26) Wang, D. H. et al. *Angewandte Chemie - International Edition* **2013**, *52*, 2874–2880.

(27) Kakavelakis, G.; Konios, D.; Stratakis, E.; Kymakis, E. *Chemistry of Materials* **2014**, *26*, 5988–5993.

(28) Konios, D. et al. *Journal of Materials Chemistry A* **2016**, *4*, 1612–1623.

(29) Kim, B. J. et al. *Nature Communications* **2016**, *7*, 1–9.

(30) Beliatis, M. J. et al. *Advanced Materials* **2014**, *26*, 2078–2083.

(31) Feng, X. et al. *Carbon* **2015**, *87*, 78–86.

(32) Liu, Y.; Yang, Z.; Liu, S. F. *Advanced Science* **2018**, *5*, DOI: 10.1002/advs.201700471.

(33) Kojima, A.; Teshima, K.; Shirai, Y.; Miyasaka, T. *Journal of the American Chemical Society* **2009**, *131*, 6050–6051.

(34) Snaith, H. J. *Journal of Physical Chemistry Letters* **2013**, *4*, 3623–3630.

(35) Hsiao, Y.-C. et al. *J. Mater. Chem. A* **2015**, *3*, 15372–15385.

(36) NREL Efficiency Chart 2018., 2018.

(37) Yang, D. et al. *Nature Communications* **2018**, *9*, DOI: 10.1038/s41467-018-05760-x.

(38) Snaith, H. J. *Nature Materials* **2018**, *17*, 372–376.

(39) Brittman, S.; Adhyaksa, G. W. P.; Garnett, E. C. *MRS Communications* **2015**, *5*, 7–26.

(40) Ruf, F. et al. *Applied Physics Letters* **2018**, *112*, DOI: 10.1063/1.5017943.

(41) Glaser, T. et al. *The Journal of Physical Chemistry Letters* **2015**, *6*, 2913–2918.

(42) Xie, L. Q. et al. *Journal of the American Chemical Society* **2017**, *139*, 3320–3323.

(43) Schmidt, L. C. et al. *Journal of the American Chemical Society* **2014**, *136*, 850–853.

(44) Zheng, K. et al. *Journal of Physical Chemistry Letters* **2015**, *6*, 2969–2975.

(45) Tilchin, J. et al. *ACS Nano* **2016**, *10*, 6363–6371.

(46) Amgar, D.; Aharon, S.; Etgar, L. *Advanced Functional Materials* **2016**, *26*, 8576–8593.

(47) Polavarapu, L.; Nickel, B.; Feldmann, J.; Urban, A. S. *Advanced Energy Materials* **2017**, *7*, 1–9.

(48) Wang, L. et al. *ACS Nano* **2017**, *11*, 2689–2696.

(49) De Roo, J. et al. *ACS Nano* **2016**, *10*, 2071–2081.

(50) Yakunin, S. et al. *Nature Communications* **2015**, *6*, 1–8.

(51) Protesescu, L. et al. *Nano Letters* **2015**, *15*, 3692–3696.

(52) Zhang, F. et al. *ACS Nano* **2015**, *9*, 4533–4542.

(53) Xing, J. et al. *ACS Nano* **2016**, *10*, 6623–6630.

(54) Levchuk, I. et al. *Chemical Communications* **2017**, *53*, 244–247.

(55) Sun, S.; Yuan, D.; Xu, Y.; Wang, A.; Deng, Z. *ACS Nano* **2016**, *10*, 3648–3657.

(56) Hintermayr, V. A. et al. *Advanced Materials* **2016**, *28*, 9478–9485.

(57) Huang, H. et al. *ACS Applied Materials and Interfaces* **2015**, *7*, 28128–28133.

(58) Akkerman, Q. A. et al. *Journal of the American Chemical Society* **2015**, *137*, 10276–10281.

(59) Jang, D. M. et al. *Nano Letters* **2015**, *15*, 5191–5199.

(60) Hassan, Y. et al. *Advanced Materials* **2016**, *28*, 566–573.

(61) Li, X. et al. *Advanced Functional Materials* **2016**, *26*, 2435–2445.

(62) Ananthakumar, S.; Kumar, J. R.; Babu, S. M. *Journal of Photonics for Energy* **2016**, *6*, 042001.

(63) Tenuta, E.; Zheng, C.; Rubel, O. *Scientific Reports* **2016**, *6*, 1–8.

(64) Zheng, C.; Rubel, O. *Journal of Physical Chemistry C* **2017**, *121*, 11977–11984.

(65) Vybornyi, O.; Yakunin, S.; Kovalenko, M. V. *Nanoscale* **2016**, *8*, 6278–6283.

(66) Eaton, S. W. et al. *Proceedings of the National Academy of Sciences* **2016**, *113*, 1993–1998.

(67) Aharon, S.; Etgar, L. *Nano Letters* **2016**, *16*, 3230–3235.

(68) Zhu, H. et al. *Nature Materials* **2015**, *14*, 636–642.

(69) Herrera, A. P.; Resto, O.; Briano, J. G.; Rinaldi, C. *Nanotechnology* **2005**, *16*, S618–S625.

(70) Zhang, H.; Li, H.; Li, D.; Meng, S. *Journal of Colloid and Interface Science* **2006**, *302*, 509–515.

(71) Lin, J.; Zhou, W.; O'Connor, C. J. *Materials Letters* **2001**, *49*, 282–286.

(72) Jiang, J. et al. *Chemical communications (Cambridge, England)* **2013**, *49*, 1912–4.

(73) Aizawa, M.; Buriak, J. M. *Chemistry of Materials* **2007**, *19*, 5090–5101.

(74) Förster, S.; Antonietti, M. *Advanced Materials* **1998**, *10*, 195–217.

(75) Turak, A.; Aytun, T.; Ow-Yang, C. W. *Applied Physics Letters* **2012**, *100*, 253303.

(76) O'Reilly, R. K. *Philosophical transactions. Series A, Mathematical, physical, and engineering sciences* **2007**, *365*, 2863–2878.

(77) Khullar, P. et al. *Journal of Physical Chemistry B* **2013**, *117*, 3028–3039.

(78) Spatz, J. P. et al. *Langmuir* **2000**, *16*, 407–415.

(79) Perl, A.; Reinhoudt, D. N.; Huskens, J. *Advanced Materials* **2009**, *21*, 2257–2268.

(80) Hur, S.-H.; Khang, D.-Y.; Kocabas, C.; Rogers, J. a. *Applied Physics Letters* **2004**, *85*, 5730.

(81) Carter, K. R. *ACS Nano* **2010**, *4*, 595–598.

(82) Moonen, P. F.; Yakimets, I.; Huskens, J. *Advanced Materials* **2012**, *24*, 5526–5541.

(83) Xia, Y.; Whitesides, G. M. *Angewandte Chemie,International Edition* **1998**, *37*, 550–575.

(84) Odom, T. W.; Love, J. C.; Wolfe, D. B.; Paul, K. E.; Whitesides, G. M. *Langmuir* **2002**, *18*, 5314–5320.

(85) Simeone, F. C.; Albonetti, C.; Cavallini, M. *The Journal of Physical Chemistry C* **2009**, *113*, 18987–18994.

(86) Kim, T.-h. et al. *Nature Photonics* **2011**, *5*, 176–182.

(87) Jeong, J. W. et al. *Advanced materials (Deerfield Beach, Fla.)* **2012**, *24*, 3526–31.

(88) Vitos, L.; Ruban, A.; Skriver, H.; Kollár, J. The surface energy of metals., 1998.

(89) Johnson, K. L.; Kendall, K.; Roberts, A. D. Surface Energy and the Contact of Elastic Solids., 1971.

(90) Tan, C. P.; Craighead, H. G. *Materials* **2010**, *3*, 1803–1832.

(91) Wang, S.; Zhang, Y.; Abidi, N.; Cabrales, L. *Langmuir : the ACS journal of surfaces and colloids* **2009**, *25*, 11078–81.

(92) Wang, X.; Ederth, T.; Inganäs, O. *Langmuir* **2006**, *22*, 9287–9294.

(93) Haubert, K.; Drier, T.; Beebe, D. *Lab on a chip* **2006**, *6*, 1548–1549.

(94) Ma, Y.; Cao, X.; Feng, X.; Ma, Y.; Zou, H. *Polymer* **2007**, *48*, 7455–7460.

(95) Gotoh, K.; Kobayashi, Y.; Yasukawa, A.; Ishigami, Y. *Colloid and Polymer Science* **2012**, *290*, 1005–1014.

(96) Abdelsalam, M. E.; Bartlett, P. N.; Kelf, T.; Baumberg, J. *Langmuir* **2005**, *21*, 1753–1757.

(97) Bhattacharya, S.; Datta, A.; Berg, J. M.; Gangopadhyay, S. *Journal of Microelectromechanical Systems* **2005**, *14*, 590–597.

(98) Berthier, E.; Young, E. W. K.; Beebe, D. *Lab on a chip* **2012**, *12*, 1224–37.

(99) Tsougeni, K.; Vourdas, N.; Tserepi, A.; Gogolides, E.; Cardinaud, C. *Langmuir* **2009**, *25*, 11748–11759.

(100) Klauk, H. et al. *Journal of Applied Physics* **2002**, *92*, 5259–5263.

(101) Kim, T.-H. et al. *Nature communications* **2013**, *4*, 2637.

(102) Kim, J.-W.; Yang, K.-Y.; Hong, S.-H.; Lee, H. *Applied Surface Science* **2008**, *254*, 5607–5611.

(103) Bietsch, A.; Michel, B. *Journal of Applied Physics* **2000**, *88*, 4310–4318.

(104) Vesel, A.; Mozetic, M. In *Vacuum*, 2012; Vol. 86, pp 634–637.

(105) Meng, E.; Li, P.-Y.; Tai, Y.-C. *J. Micromech. Microeng.* **2008**, *18*, 1–13.

(106) Young, T. J. et al. *Measurement Science and Technology* **2011**, *22*, DOI: 10.1088/0957-0233/22/12/125703.

(107) Hassler, C.; Von Metzen, R. P.; Ruther, P.; Stieglitz, T. *Journal of Biomedical Materials Research - Part B Applied Biomaterials* **2010**, *93*, 266–274.

(108) Park, H. et al. *Small* **2014**, *10*, 52–59.

(109) Armani, D.; Liu, C.; Aluru, N. *Technical Digest. IEEE International MEMS 99 Conference. Twelfth IEEE International Conference on Micro Electro Mechanical Systems* **1999**, DOI: 10.1109/MEMSYS.1999.746817.

(110) Kim, K. S. et al. *Nature* **2009**, *457*, 706–710.

(111) Li, X. et al. *Nano Lett.* **2009**, *9*, 4359–4363.

(112) Liang, X. et al. *ACS nano* **2011**, *5*, 9144–53.

(113) Kawano R Poplavskyy, D Nelson, J Bradley, DDC Durrant, JR, K. P. *Solar Energy Materials and Solar Cells* **2006**, *90*, 3530.

(114) Suk, J. W. et al. *Nano letters* **2013**, *13*, 1462–7.

(115) Martins, L. G. P. et al. *Proceedings of the National Academy of Sciences of the United States of America* **2013**, *110*, 17762–7.

(116) Kim, M. et al. *2D Materials* **2017**, *4*, DOI: 10.1088/2053-1583/aa780d.

(117) Lee, C. H.; Kim, D. R.; Zheng, X. *Proceedings of the National Academy of Sciences of the United States of America* **2010**, *107*, 9950–9955.

(118) Kang, J.; Shin, D.; Bae, S.; Hong, B. H. *Nanoscale* **2012**, *4*, 5527–5537.

(119) Wang, C. et al. *Applied Physics Letters* **2008**, *93*, DOI: 10.1063/1.2956677.

(120) Ryu, K. et al. *Nano Letters* **2009**, *9*, 189–197.

(121) Caldwell, J. D. et al. *ACS Nano* **2010**, *4*, 1108–1114.

(122) Weiss, E. A. et al. *Langmuir* **2007**, *23*, 9686–9694.

(123) Khabbaz Abkenar, S. et al. *Nanoscale* **2017**, *9*, 2969–2973.

(124) Paredes, J. I.; Martinez-Alonso, a; Tascon, J. M. D. *Journal of Materials Chemistry* **2000**, *10*, 1585–1591.

(125) Nguyen, T.; Le Rendu, P.; Dinh, N.; Fourmigué, M.; Mézière, C. *Synthetic Metals* **2003**, *138*, 229–232.

(126) Calchera, A. R.; Curtis, A. D.; Patterson, J. E. *ACS Applied Materials and Interfaces* **2012**, *4*, 3493–3499.

(127) Hartney, M. A. *Journal of Vacuum Science & Technology B: Microelectronics and Nanometer Structures* **1989**, *7*, 1.

(128) Donnelly, V. M.; Kornblit, A. *Journal of Vacuum Science & Technology A: Vacuum, Surfaces, and Films* **2013**, *31*, 050825.

(129) Gu, Y.; St-Pierre, J.; Ploehn, H. J. *Langmuir : the ACS journal of surfaces and colloids* **2008**, *24*, 12680–9.

(130) Bayley, F. A.; Liao, J. L.; Stavrinou, P. N.; Chiche, A.; Cabral, J. T. *Soft matter* **2014**, *10*, 1155–66.

(131) Nania, M.; Matar, O. K.; Cabral, J. T. *Soft Matter* **2015**, 3067–3075.

(132) Tserepi, A.; Gogolides, E.; Tsougeni, K.; Constantoudis, V.; Valamontes, E. S. *Journal of Applied Physics* **2005**, *98*, DOI: 10.1063/1.2136421.

(133) Mao, H.; Wang, R.; Zhong, J.; Zhong, S.; Chen, W. *Carbon* **2014**, *76*, 212–219.

(134) Feng, T. et al. *Materials Letters* **2012**, *73*, 187–189.

(135) Kim, D. C. et al. *Nanotechnology* **2009**, *20*, 375703.

(136) Liang, X.; Fu, Z.; Chou, S. Y. *Nano Letters* **2007**, *7*, 3840–3844.

(137) Starodub, E.; Bartelt, N. C.; McCarty, K. F. *Journal of Physical Chemistry C* **2010**, *114*, 5134–5140.

(138) Childres, I.; Jauregui, L. A.; Tian, J.; Chen, Y. P. *New Journal of Physics* **2011**, *13*, DOI: 10.1088/1367-2630/13/2/025008.

(139) Gokus, T. et al. *ACS nano* **2009**, *3*, 3963–3968.

(140) Shin, Y. J. et al. *Langmuir* **2010**, *26*, 3798–3802.

(141) Zandiatashbar, A. et al. *Nature communications* **2014**, *5*, 3186.

(142) Cardinaud, C.; Peignon, M.-c.; Tessier, P.-y.; Materiaux, L.-i. *Applied Surface Science* **2000**, *164*, 72–83.

(143) Seah, C. M.; Vigolo, B.; Chai, S. P.; Mohamed, A. R. *Carbon* **2016**, *105*, 496–509.

(144) Jimenez-Cervantes, E.; López-Barroso, J.; Martínez-Hernández, A. L.; Velasco-Santos, C. *Recent Advances in Graphene Research* **2016**, DOI: 10.5772/64001.

(145) Jung, J.; Lim, H.; Oh, J.; Kim, Y. **2014**, 2–5.

(146) Lin, L. C.; Grossman, J. C. *Nat Commun* **2015**, *6*, 8335.

(147) Bagri, A. et al. *Nature chemistry* **2010**, *2*, 581–587.

(148) Ferrari, A. C. *Solid State Communications* **2007**, *143*, 47–57.

(149) Liu, L. et al. *Nano Letters* **2008**, *8*, 1965–1970.

(150) Hui, L. S.; Whiteway, E.; Hilke, M.; Turak, A. *Faraday Discuss.* **2014**, *173*, 79–93.

(151) Long, D. A., *The Raman effect: a unified treatment of the theory of Raman scattering by molecules. 2002*, 2002.

(152) Ferraro, J. R.; Nakamoto, K.; Brown, C. W., *Introductory Raman Spectroscopy*, 2003, pp 406–421.

(153) Nakamoto, K. In *Wiley, Hoboken, New Jersey*, 2009.

(154) Gardiner, D. J.; Graves, P. R.; Luck, W. A. P. *Berichte der Bunsengesellschaft für physikalische Chemie* **1990**, DOI: 10.1002/bbpc.19900940938.

(155) Colthup, N. B.; Daly, L. H.; Wiberley, S. E., *Introduction to Infrared and Raman Spectroscopy*, 1990.

(156) Aroyo, M. I. et al. *Bulgarian Chemical Communications* **2011**, DOI: 10.1107/S205327331303091X.

(157) Perez-Mato, J. M. et al. Bilbao Crystallographic Server. 2013., 2015.

(158) Aroyo, M. I. et al. In *Zeitschrift fur Kristallographie*, 2006.

(159) Aroyo, M. I.; Kirov, A.; Capillas, C.; Perez-Mato, J. M.; Wondratschek, H. In *Acta Crystallographica Section A: Foundations of Crystallography*, 2006.

(160) Connell, G. A. N.; Nemanich, R. J.; Tsai, C. C. *Applied Physics Letters* **1980**, *36*, 31–33.

(161) Solonenko, D et al. *Journal of Physics D: Applied Physics* **2016**, *49*, 115502.

(162) Shoute, L. C. T.; Bergren, A. J.; Mahmoud, a. M.R. M.; Harris, K. E.N. D.; Creery, R. L.M. C. **2009**, *63*, 133–140.

(163) Fleischmann, M.; Hendra, P. J.; McQuillan, A. J. *Chemical Physics Letters* **1974**, *26*, 163–166.

(164) Yang, Y. et al. *Applied Surface Science* **2013**, *280*, 343–348.

(165) Yang, Y. et al. *Journal of Applied Physics* **2012**, *111*, 3–7.

(166) Tsai, W. H.; Boerio, F. J.; Clarson, S. J.; Parsonage, E. E.; Tirrell, M *Macromolecules* **1991**, *24*, 2538–2545.

(167) Wang, X. et al. *Chem. Soc. Rev.* **2017**, *46*, 4020–4041.

(168) Bailo, E.; Deckert, V. *Chemical Society reviews* **2008**, *37*, 921–930.

(169) Deckert, V. *Journal of Raman Spectroscopy* **2009**, *40*, 1336–1337.

(170) Wang, X. et al. *Applied Physics Letters* **2007**, *91*, 1–4.

(171) Poliani, E. et al. *Journal of Physical Chemistry Letters* **2017**, *8*, 5462–5471.

(172) Gucciardi, P. G. et al. *Nanotechnology* **2008**, *19*, DOI: 10.1088/0957-4484/19/21/215702.

(173) Szymanski, H., *Raman Spectroscopy Theory and Practice*; Springer US: 1967, pp X, 256.

(174) Ramsteiner, M; Wild, C; Wagner, J *Applied optics* **1990**, DOI: 10.1364/AO.28.004017.

(175) Nemanich, R. J.; Tsai, C. C.; Connell, G. A. N. *Physical Review Letters* **1980**, *44*, 273–276.

(176) Ferrari, A. C.; Basko, D. M. *Nature Nanotechnology* **2013**, *8*, 235–246.

(177) Ferrari, a. C. et al. *Physical Review Letters* **2006**, *97*, 187401.

(178) Schmucker, S. W. et al. *Carbon* **2015**, *93*, 250–257.

(179) Kudin, K. N. et al. *Nano letters* **2008**, *8*, 36–41.

(180) Banhart, F.; Kotakoski, J.; Krasheninnikov, A. V. *ACS nano* **2011**, *5*, 26–41.

(181) Papagno, M. et al. *ACS Nano* **2012**, *6*, 9299–9304.

(182) Yu, V.; Whiteway, E.; Maassen, J.; Hilke, M. *Physical Review B* **2011**, *84*, 205407.

(183) Malard, L.; Pimenta, M.; Dresselhaus, G.; Dresselhaus, M. *Physics Reports* **2009**, *473*, 51–87.

(184) Luo, Z. et al. *ACS nano* **2009**, *3*, 1781–8.

(185) Wojtaszek, M. et al. *Journal of Applied Physics* **2011**, *110*, 063715.

(186) Bernard, S.; Whiteway, E.; Yu, V.; Austing, D. G.; Hilke, M. *Physical Review B* **2012**, *86*, 085409.

(187) Li, X. et al. *Science* **2009**, *324*, 1312–4.

(188) Casiraghi, C. et al. *Nano Letters* **2009**, *9*, 1433–1441.

(189) Sun, Z. et al. *Nature* **2010**, *468*, 549–52.

(190) Wofford, J. M.; Nie, S.; McCarty, K. F.; Bartelt, N. C.; Dubon, O. D. *Nano letters* **2010**, *10*, 4890–6.

(191) Eckmann, A. et al. *Nano Letters* **2012**, *12*, 3925–3930.

(192) Ferrari, A.; Robertson, J. Interpretation of Raman spectra of disordered and amorphous carbon., 2000.

(193) MacHala, L.; Tuček, J.; Zbořil, R. *Chemistry of Materials* **2011**, *23*, 3255–3272.

(194) Sakurai, S.; Namai, A.; Hashimoto, K.; Ohkoshi, S.-i. *Journal of the American Chemical Society* **2009**, *131*, 18299–18303.

(195) Zhu, W. et al. *The Journal of Physical Chemistry C* **2016**, *120*, 14854–14862.

(196) Dar, M. I.; Shivashankar, S. A. *RSC Advances* **2014**, *4*, 4105–4113.

(197) Bersani, D; Lottici, P. P.; Montenero, a *Journal of Raman Spectroscopy* **1999**, *30*, 355–360.

(198) Chamritski, I.; Burns, G. *Journal of Physical Chemistry B* **2005**, *109*, 4965–4968.

(199) Liang, Y.; van de Krol, R. *Chemical Physics Letters* **2009**, *479*, 86–90.

(200) Kumar, C. S., *Raman spectroscopy for nanomaterials characterization*, 2012; Vol. 9783642206, pp 1–645.

(201) López-Sánchez, J. et al. *Chemistry of Materials* **2016**, *28*, 511–518.

(202) Kanno, H.; Hiraishi, J. *Journal of Raman Spectroscopy* **1982**, *12*, 224–227.

(203) Murata, K.; Irish, D. *Spectrochimica Acta* **1988**, *44*, 739–743.

(204) Caswell, N.; Solin, S. A. *Solid State Communications* **1978**, *27*, 961–967.

(205) Hill, P. S.; Schauble, E. A. *Geochimica et Cosmochimica Acta* **2008**, *72*, 1939–1958.

(206) Zhao, W. J.; Tan, P. H.; Liu, J.; Ferrari, A. C. *Journal of the American Chemical Society* **2011**, *133*, 5941–5946.

(207) De Faria, D. L. A.; Venâncio Silva, S.; de Oliveira, M. T. *Journal of Raman Spectroscopy* **1997**, *28*, 873–878.

(208) Jubb, A. M.; Allen, H. C. *ACS Applied Materials and Interfaces* **2010**, *2*, 2804–2812.

(209) Casula, M. F. et al. *Journal of the American Chemical Society* **2006**, *128*, 1675–1682.

(210) Natta, G.; Corradini, P.; Bassi, I. W. *Il Nuovo Cimento Series 10* **1960**, DOI: 10.1007/BF02731861.

(211) Greis, O.; Xu, Y.; Asano, T.; Petermann, J. *Polymer* **1989**, *30*, 590–594.

(212) De Rosa, C. *Macromolecules* **1996**, *29*, 8460–8465.

(213) Hong, P. P.; Boerio, F. J.; Tirrell, M.; Dhoot, S; Guenoun, P *Macromolecules* **1993**, *26*, 3953–3959.

(214) Tazuke, S.; Sato, N.; Okamura, S. *Journal of Polymer Science: Part A-1* **1966**, *4*, 2461–2478.

(215) Sageshima, Y.; Noro, A.; Matsushita, Y. *Journal of Polymer Science, Part B: Polymer Physics* **2014**, *52*, 377–386.

(216) Mavi, H. S.; Shukla, A. K.; Abbi, S. C.; Jain, K. P. *Journal of Applied Physics* **1989**, *66*, 5322–5326.

(217) Yang, S. et al. *Journal of Raman Spectroscopy* **2013**, DOI: 10.1002/jrs.4338.

(218) Stuart, B. *Kirk-Othmer Encyclopedia of Chemical Technology* **2015**, 1–18.

(219) Krantz, M.; Luty, F. *Physical Review B* **1985**, *31*, 2599–2601.

(220) Burstein, E.; Johnson, F. A.; Loudon, R. *Physical Review* **1965**, *139*, DOI: 10.1103/PhysRev.139.A1239.

(221) McHargue, C. J.; Snyder, Jr., W. B. *Proceedings of the SPIE* **1993**, *2018*, 135–142.

(222) Porto, S. P.; Krishnan, R. S. *The Journal of Chemical Physics* **1967**, *47*, 1009–1012.

(223) Wan, K. S.; Tochino, S.; Zhu, W. L.; Ohtsuka, S.; Pezzotti, G. *Journal of Physics D: Applied Physics* **2010**, *43*, DOI: 10.1088/0022-3727/43/20/205501.

(224) Thomas, K. J.; Sheeba, M.; Nampoori, V. P. N.; Vallabhan, C. P. G.; Radhakrishnan, P. *Journal of Optics A: Pure and Applied Optics* **2008**, *10*, DOI: 10.1088/1464-4258/10/5/055303.

(225) Kaniyoor, A.; Ramaprabhu, S. *AIP Advances* **2012**, *2*, DOI: 10.1063/1.4756995.

(226) Steele, J. A. et al. *ACS Nano* **2017**, acsnano.7b02777.

(227) Han, Q. et al. *Advanced Materials* **2016**, *28*, 2253–2258.

(228) Quarti, C. et al. *Journal of Physical Chemistry Letters* **2014**, *5*, 279–284.

(229) Brivio, F. et al. *Physical Review B - Condensed Matter and Materials Physics* **2015**, *92*, 1–8.

(230) Pistor, P.; Ruiz, A.; Cabot, A.; Izquierdo-Roca, V. *Scientific Reports* **2016**, *6*, 35973.

(231) Lee, J.-W.; Seol, D.-J.; Cho, A.-N.; Park, N.-G. *Advanced Materials* **2014**, DOI: 10.1002/adma.201401137.

(232) Eperon, G. E. et al. *Energy and Environmental Science* **2014**, *7*, 982–988.

(233) Pellet, N. et al. *Angewandte Chemie - International Edition* **2014**, DOI: 10.1002/anie.201309361.

(234) Wang, K.-h.; Li, L.-c.; Shellaiah, M.; Sun, K. W. *Scientific Reports* **2017**, *7*, 1–14.

(235) Horcas, I. et al. *Review of Scientific Instruments* **2007**, *78*, DOI: 10.1063/1.2432410.

(236) Baalousha, M.; Lead, J. R. *Environmental Science and Technology* **2012**, *46*, 6134–6142.

(237) Yu, H.; Turak, A. *Canadian Journal of Physics* **2014**, *92*, 797–801.

(238) Voulgaris, D.; Tsitsilianis, C.; Esselink, F. J.; Hadziioannou, G. *Polymer* **1998**, *39*, 6429–6439.

(239) Boyde, A.; Mccorkell, F. A.; Taylor, G. K.; Bomphrey, R. J.; Doube, M. *Microscopy Research and Technique* **2014**, *77*, 1044–1051.

(240) Jeon, S. M.; Lee, S. H.; Yoo, S. I.; Sohn, B. H. *Langmuir* **2011**, *27*, 12191–12196.

(241) Yoo, S. I.; Sohn, B. H.; Zin, W. C.; Jung, J. C.; Park, C. *Macromolecules* **2007**, *40*, 8323–8328.

(242) Bumstead, M.; Liang, K.; Hanta, G.; Hui, L.; Turak, A. *Scientific Reports* **2018**, *8*, DOI: 10.1038/s41598-017-18894-7.

(243) Ow-Yang, C. W. et al. *Thin Solid Films* **2014**, *559*, 58–63.

(244) Mizuno, H.; Kaneko, T.; Sakata, I.; Matsubara, K. *Chemical communications (Cambridge, England)* **2014**, *50*, 362–4.

(245) Gu, X.; Qiu, T.; Zhang, W.; Chu, P. K. **2011**, 1–12.

(246) Atwater, H. a.; Polman, A. *Nature materials* **2010**, *9*, 205–13.

(247) Ji, S.; Liu, C.-C.; Liu, G.; Nealey, P. F. *ACS nano* **2010**, *4*, 599–609.

(248) Ozbay, E. *Science* **2006**, *311*, 189–193.

(249) Kästle, G. et al. *Advanced Functional Materials* **2003**, *13*, 853–861.

(250) Zheng, G. et al. *ACS applied materials & interfaces* **2013**, *5*, 10288–93.

(251) Sojoudi, H.; Baltazar, J.; Tolbert, L. M.; Henderson, C. L.; Graham, S. *ACS applied materials & interfaces* **2012**, *4*, 4781–6.

(252) Gorantla, S. et al. *Nanoscale* **2014**, *6*, 889–96.

(253) Lee, S. et al. *Carbon* **2015**, *93*, 286–294.

(254) Hui, L. S. et al. *Carbon* **2017**, *125*, 500–508.

(255) King, A. A. K. et al. *Scientific reports* **2016**, *6*, 19491.

(256) Jung, I. et al. *Journal of Physical Chemistry C* **2008**, *112*, 8499–8506.

(257) Beadie, G; Brindza, M.; Flynn, R. A.; Rosenberg, A.; Shirk, J. S. *Applied optics* **2015**, *54*, 139–143.

(258) Willis, H. A.; Zichy, V. J.; Hendra, P. J. *Polymer* **1969**, *10*, 737–746.

(259) Xingsheng, X.; Hai, M.; Qijing, Z.; Yunsheng, Z. *Journal of Optics A: Pure and Applied Optics* **2002**, *4*, 237–242.

(260) Reese, M. O. et al. *Solar Energy Materials and Solar Cells* **2008**, *92*, 746–752.

(261) Tsoi, W. C. et al. *Journal of the American Chemical Society* **2011**, *133*, 9834–9843.

(262) Klimov, E.; Li, W.; Yang, X.; Hoffmann, G. G.; Loos, J. *Macromolecules* **2006**, *39*, 4493–4496.

(263) Nakamoto, K., *Infrared and Raman Spectra of Inorganic and Coordination Compounds, Applications in Coordination, Organometallic, and Bioinorganic Chemistry (Google eBook)*, 2009, p 400.

(264) Sastry, N. V.; Hoffmann, H *Aspects* **2004**, *250*, 247–261.

(265) Lagerwall, J. P. F.; McCann, J. T.; Formo, E.; Scalia, G.; Xia, Y. *Chemical Communications* **2008**, 5420–5422.

(266) Cornell, R. M.; Schwertmann, U, *The Iron Oxides : Structure, Properties, Reactions, Occurences and Uses*, 2003.

(267) Lu, A. H.; Salabas, E. L.; Schüth, F. *Angewandte Chemie - International Edition* **2007**, *46*, 1222–1244.

(268) Laurent, S. et al. *Chemical Reviews* **2008**, *108*, 2064–2110.

(269) Gupta, A. K.; Gupta, M. *Biomaterials* **2005**, *26*, 3995–4021.

(270) Hyeon, T. *Chemical Communications* **2003**, *3*, 927–934.

(271) Prosini, P. P.; Carewska, M.; Loreti, S.; Minarini, C.; Passerini, S. *International Journal of Inorganic Materials* **2000**, *2*, 365–370.

(272) Široký, K.; Jirešová, J.; Hudec, L. *Thin Solid Films* **1994**, *245*, 211–214.

(273) Klahr, B. M.; Martinson, A. B.; Hamann, T. W. *Langmuir* **2011**, *27*, 461–468.

(274) Wang, K. et al. *ACS Applied Materials and Interfaces* **2013**, *5*, 10325–10330.

(275) Wang, K. et al. *Scientific Reports* **2015**, *5*, 1–9.

(276) Liong, M. et al. *ACS Nano* **2008**, *2*, 889–896.

(277) Tuçek, J.; Kemp, K. C.; Kim, K. S.; Zboril, R. *ACS Nano* **2014**, *8*, 7571–7612.

(278) Li, Z.; Wei, L.; Gao, M.; Lei, H. *Advanced Materials* **2005**, *17*, 1001–1005.

(279) Na, H. B.; Song, I. C.; Hyeon, T. *Advanced Materials* **2009**, *21*, 2133–2148.

(280) Cui, H.; Liu, Y.; Ren, W. *Advanced Powder Technology* **2013**, *24*, 93–97.

(281) Kang, Y. S.; Risbud, S.; Rabolt, J. F.; Stroeve, P. *Chemistry of Materials* **1996**, *8*, 2209–2211.

(282) Morales, M. P.; Serna, C. J.; Bødker, F.; Mørup, S. *Journal of Physics Condensed Matter* **1997**, *9*, 5461–5467.

(283) Morales, M. P. et al. *Chemistry of Materials* **1999**, *11*, 3058–3064.

(284) Darbandi, M. et al. *Journal of Physics D: Applied Physics* **2012**, *45*, DOI: 10.1088/0022-3727/45/19/195001.

(285) Hu, H.; Gopinadhan, M.; Osuji, C. O. *Soft Matter* **2014**, *10*, 3867–3889.

(286) Cummins, C.; Ghoshal, T.; Holmes, J. D.; Morris, M. A. *Advanced Materials* **2016**, 5586–5618.

(287) Wiedwald, U.; Han, L.; Biskupek, J.; Kaiser, U.; Ziemann, P. *Beilstein Journal of Nanotechnology* **2010**, *1*, 24–47.

(288) Yun, S. H. et al. *Langmuir* **2005**, *21*, 6548–6552.

(289) Krishnamoorthy, S.; Pugin, R.; Brugger, J.; Heinzelmann, H.; Hinderling, C. *Advanced Functional Materials* **2006**, *16*, 1469–1475.

(290) Bennett, R. D. et al. *Macromolecules* **2005**, *38*, 10728–10735.

(291) Leslie-Pelecky, D. L.; Rieke, R. D. *Chemistry of Materials* **1996**, *8*, 1770–1783.

(292) Lee, M. M.; Tuescher, J.; Miyasaka, T.; Murakami, T. N.; Snaith, H. J. *Science* **2012**, *338*, 643–648.

(293) Wu, L.; Mendoza-Garcia, A.; Li, Q.; Sun, S. *Chemical Reviews* **2016**, *116*, 10473–10512.

(294) Chourpa, I. et al. *The Analyst* **2005**, *130*, 1395.

(295) Jacintho, G. V. M.; Corio, P.; Rubim, J. C. *Journal of Electroanalytical Chemistry* **2007**, *603*, 27–34.

(296) Clark, R. J. et al. *Inorganic Chemistry* **1977**, *16*, 84–89.

(297) Shebanova, O. N.; Lazor, P. *Journal of Solid State Chemistry* **2003**, *174*, 424–430.

(298) Zhu, H.; Deng, J.; Chen, J.; Yu, R.; Xing, X. *Journal of Materials Chemistry A* **2014**, *2*, 3008–3014.

(299) Chernyshova, I. V.; Hochella Jr, M. F.; Madden, A. S. *Physical Chemistry Chemical Physics* **2007**, *9*, 1736.

(300) Wang, C.; Ecker, B. R.; Wei, H.; Huang, J.; Gao, Y. *The Journal of Physical Chemistry C* **2018**, acs.jpcc.7b12740.

(301) Aytun, T. *MSc. Thesis* **2010**.

(302) Sichert, J. A. et al. *Nano Letters* **2015**, *15*, 6521–6527.

(303) Ohmann, R. et al. *Journal of the American Chemical Society* **2015**, *137*, 16049–16054.

(304) Gadelha, G. et al. *Desalination* **2014**, *354*, 97–106.

(305) Aloisi, G. G.; Beggiato, G.; Mazzucato, U. *Trans. Faraday Soc.* **1970**, *66*, 3075–3080.

(306) Xie, L.-Q. et al. *Phys. Chem. Chem. Phys.* **2016**, *18*, 18112–18118.

(307) Lindenmaier, R. et al. *Journal of Molecular Structure* **2017**, *1149*, 332–351.

(308) Maes, G.; zeegers Hugsrens, T. *Spectroscopy Letters* **1975**, *8*, 475–481.

(309) Vinogradov, N. A. et al. *Evolution* **2011**, 9568–9577.

(310) Larciprete, R. et al. *J. Am. Chem. Soc.* **2011**, *133*, 17315–17321.

(311) Zhou, M. et al. *Chemistry - A European Journal* **2009**, *15*, 6116–6120.

(312) Huang, X. et al. *Small* **2011**, *7*, 1876–1902.

(313) Lu, G.; Ocola, L. E.; Chen, J. *Nanotechnology* **2009**, *20*, 445502.

(314) Chen, Y.; Zhang, B.; Liu, G.; Zhuang, X.; Kang, E.-T. *Chemical Society Reviews* **2012**, *41*, 4688.

(315) Lenglet, M et al. *Materials Research Bulletin* **1995**, *30*, 393–403.

(316) Jones, J. D. et al. *Applied Physics Letters* **2010**, *97*, 233104.

(317) Lee, G.-H. et al. *Science (New York, N.Y.)* **2013**, *340*, 1073–6.

(318) Cancado, L. G. et al. *Nano Letters* **2011**, *11*, 3190–3196.

(319) Gao, L.; Guest, J. R.; Guisinger, N. P. *Nano letters* **2010**, *10*, 3512–6.

(320) Cho, J. et al. *ACS nano* **2011**, *5*, 3607–13.

(321) Yang, D. et al. *Carbon* **2009**, *47*, 145–152.

(322) Khan, M. et al. *Nanoscale research letters* **2015**, *10*, 281.

(323) Dave, K.; Park, K. H.; Dhayal, M. *RSC Adv.* **2015**, *5*, 95657–95665.

(324) Morimoto, N.; Kubo, T.; Nishina, Y. *Scientific reports* **2016**, *6*, 21715.

(325) Kidambi, P. R. et al. *Nano letters* **2013**, *13*, 4769–4778.

(326) Siokou, A. et al. *Applied Surface Science* **2011**, *257*, 9785–9790.

(327) Schultz, B. J. et al. *RSC Advances* **2014**, *4*, 634–644.

(328) Hontoria-Lucas, C.; López-Peinado, a. J.; López-González, J. D.d. D.; Rojas-Cervantes, M. L.; Martín-Aranda, R. M. *Carbon* **1995**, *33*, 1585–1592.

(329) Jernigan, G. G.; Somorjai, G. a. *Journal of Catalysis* **1994**, *147*, 567–577.

(330) Duong, D. L. et al. *Nature* **2012**, *490*, 235–239.

(331) Luo, B. et al. *Chemistry of Materials* **2016**, *28*, 3789–3795.

(332) Chen, S. et al. *ACS nano* **2011**, *5*, 1321–7.

(333) Wlasny, I. et al. *Applied Physics Letters* **2013**, *102*, DOI: 10.1063/1.4795861.

(334) Schriver, M. et al. *ACS Nano* **2013**, *7*, 5763–5768.

(335) Johnson, P. B.; Christy, R. W. *Physical Review B* **1972**, *6*, 4370–4379.

(336) Querry, M. R. *Contractor Report CRDC-CR-85034* **1985**.

(337) Seo, J.; Chang, W. S.; Kim, T. S. *Thin Solid Films* **2015**, *584*, 170–175.

(338) Lee, C.; Wei, X.; Kysar, J. W.; Hone, J. *Science (New York, N.Y.)* **2008**, *321*, 385–388.

(339) Dedkov, Y. S.; Fonin, M.; Rudiger, U.; Laubschat, C. *Applied Physics Letters* **2008**, *93*, 022509.

(340) Novoselov, K. S. et al. *Science (New York, N.Y.)* **2004**, *306*, 666–9.

(341) Wang, Y.; Tong, S. W.; Xu, X. F.; Ozyilmaz, B.; Loh, K. P. *Advanced materials (Deerfield Beach, Fla.)* **2011**, *23*, 1514–8.

(342) Jeong, Y. J. et al. *ACS applied materials & interfaces* **2014**, *6*, 6816–24.

(343) Zhong, S. et al. *ACS applied materials & interfaces* **2012**, *4*, 3134–40.

(344) Stylianakis, M. M.; Stratakis, E.; Koudoumas, E.; Kymakis, E.; Anastasiadis, S. H. *ACS applied materials & interfaces* **2012**, *4*, 4864–70.

(345) Wu, Q.-H.; Hong, G.; Ng, T. W.; Lee, S. T. *Applied Physics Letters* **2012**, *100*, 161603.

(346) Berman, D.; Erdemir, A.; Sumant, A. V. *Materials Today* **2014**, *17*, 31–42.

(347) Sutter, E.; Albrecht, P.; Camino, F. E.; Sutter, P. *Carbon* **2010**, *48*, 4414–4420.

(348) Bunch, J. S. et al. *Science (New York, N.Y.)* **2007**, *315*, 490–3.

(349) Filleter, T. et al. *Physical Review Letters* **2009**, *102*, 086102.

(350) Shin, Y. J. et al. *Carbon* **2011**, *49*, 4070–4073.

(351) Egberts, P.; Han, G. H.; Liu, X. Z.; Johnson, A. T. C.; Carpick, R. W. *ACS nano* **2014**, DOI: 10.1021/nn501085g.

(352) Yoon, T. et al. *Nano letters* **2012**, *12*, 1448–52.

(353) Liu, X.-Z.; Li, Q.; Egberts, P.; Carpick, R. W. *Advanced Materials Interfaces* **2014**, *1*, DOI: 10.1002/admi.201300053.

(354) Wang, X. et al. *Chemical Vapor Deposition* **2009**, *15*, 53–56.

(355) Liu, W.; Li, H.; Xu, C.; Khatami, Y.; Banerjee, K. *Carbon* **2011**, *49*, 4122–4130.

(356) Zhang, Y. et al. *ACS nano* **2011**, *5*, 4014–4022.

(357) Zhu, W. et al. *Nano letters* **2012**, *12*, 3431–6.

(358) Zhao, L. et al. *Solid State Communications* **2011**, *151*, 509–513.

(359) Yoon, D.; Son, Y. W.; Cheong, H. *Physical Review Letters* **2011**, *106*, 1–4.

(360) Nix, F.C. and MacNair, D. *Physical Review B* **1941**, *60*, 597.

(361) Tian, J. et al. *Nano letters* **2012**, *12*, 3893–9.

(362) Bai, J.; Zhong, X.; Jiang, S.; Huang, Y.; Duan, X. *Nature nanotechnology* **2010**, *5*, 190–4.

(363) Wang, Y.; Shao, Y.; Matson, D. W.; Li, J.; Lin, Y. Nitrogen-Doped Graphene and Its Application in Electrochemical Biosensing., 2010.

(364) Matei, D. G. et al. *Advanced materials (Deerfield Beach, Fla.)* **2013**, *25*, 4146–51.

(365) Pocsik, I.; Hundhausen, M.; Koos, M.; Ley, L. *Journal of Non-Crystalline Solids* **1998**, 1083–1086.

(366) Tuinstra, F.; Koenig, J. L. *The Journal of Chemical Physics* **1970**, *53*, 1126.

(367) Akhavan, O. *Carbon* **2010**, *48*, 509–519.

(368) Bunch, J. S. et al. *Nano letters* **2008**, *8*, 2458–2462.

(369) Iijima, J. et al. *Applied Surface Science* **2006**, *253*, 2825–2829.

(370) Shao, Y. et al. *Journal of Materials Chemistry* **2010**, *20*, 7491.

(371) Diankov, G.; Neumann, M.; Goldhaber-Gordon, D. *ACS nano* **2013**, *7*, 1324–32.

(372) Herron, J. T.; Green, D. S. *Plasma Chemistry and Plasma Processing* **2001**, *21*.

(373) Manos, D.M. Flamm, D., *Plasma Etching, and Introduction*, 1989, pp 91–183.

(374) Riccardi, C.; Barni, R.; Fontanesi, M. *Journal of Applied Physics* **2001**, *90*, 3735.

(375) Hojabri, a; Haghighian, N; Yasserian, K; Ghoranneviss, M *IOP Conference Series: Materials Science and Engineering* **2010**, *12*, 012004.

(376) Taylor, G. N.; Wolf, T. M. *Polymer Engineering and Science* **1980**, *20*, 1087–1092.

(377) Cabrera, N.; Mott, N. F. *Reports on Progress in Physics* **1949**, *12*, 163–184.

(378) Rhodin, T. N. *Journal of the American Chemical Society* **1950**, *72*, 5102–5106.

(379) Ye, Z.; Tang, C.; Dong, Y.; Martini, A. *Journal of Applied Physics* **2012**, *112*, 116102.

(380) Mattevi, C. et al. *Advanced Functional Materials* **2009**, DOI: 10.1002/adfm.200900166.

(381) Kumar, P. V.; Bernardi, M.; Grossman, J. C. *ACS Nano* **2013**, *7*, 1638–1645.

(382) Chien, C. T. et al. *Angewandte Chemie - International Edition* **2012**, DOI: 10.1002/anie.201200474.

(383) McEvoy, N.; Nolan, H.; Ashok Kumar, N.; Hallam, T.; Duesberg, G. S. *Carbon* **2013**, DOI: 10.1016/j.carbon.2012.11.040.

(384) Li, Z. et al. *Nature Materials* **2013**, *12*, 925–931.

(385) Martinez-Martin, D. et al. *Carbon* **2013**, DOI: 10.1016/j.carbon.2013.04.056.

(386) Panchal, V. et al. *2D Materials* **2016**, DOI: 10.1088/2053-1583/3/1/015006.

(387) Smith, P. J.; Lindley, P. M. *The 1998 international conference on characterization and metrology for ULSI technology* **1998**, *133*, 133–139.

(388) Afshari, A.; Gunnarsen, L.; Clausen, P. A.; Hansen, V. *Indoor Air* **2004**, *14*, 120–128.

(389) Sun, P.; Ayre, C.; Wallace, M. *AIP Conference Proceedings* **2003**, *245*, 1–34.

(390) Lisi, N. et al. *Scientific Reports* **2017**, DOI: 10.1038/s41598-017-09811-z.

(391) Eng, A. Y. S. et al. *Advanced Functional Materials* **2017**, *27*, DOI: 10.1002/adfm.201605797.

(392) Ţucureanu, V.; Matei, A.; Avram, A. M. *Critical Reviews in Analytical Chemistry* **2016**, *46*, 502–520.

(393) Aria, A. I. et al. *The Journal of Physical Chemistry C* **2016**, *120*, acsnano.6b00643.

(394) Luongo, J *Journal of Polymer Science* **1960**, *XLII*, 139–150.

(395) Corbella, C.; Grose-Kreul, S.; Von Keudell, A. *Plasma Processes and Polymers* **2015**, DOI: 10.1002/ppap.201400188.

(396) Moss, S. J.; Jolly, A. M.; Tighe, B. J. *Plasma Chemistry and Plasma Processing* **1986**, *6*, 401–416.

(397) Coburn, J. W. *Journal of Vacuum Science and Technology* **1979**, DOI: 10.1116/1.569958.

(398) Von Keudell, A.; Corbella, C. *Journal of Vacuum Science & Technology A: Vacuum, Surfaces, and Films* **2017**, DOI: 10.1116/1.4983275.

(399) Comelles, J. et al. *Journal of Organic Chemistry* **2004**, *69*, 6834–6842.

(400) Mohiuddin, T. M. G. et al. *Physical Review B - Condensed Matter and Materials Physics* **2009**, *79*, 1–8.

(401) Wang, Y. Y. et al. *Journal of Physical Chemistry C* **2008**, *112*, 10637–10640.

(402) Spjut, H.; Faux, D. A. *Surface Science* **1994**, *306*, 233–239.

(403) Rosei, F.; Rosei, R. *Surface Science* **2002**, *500*, 395–413.

(404) Frerichs, R. *Physical Review* **1961**, *121*, 991–996.

(405) Bruna, M. et al. *ACS nano* **2014**, *8*, 7432–41.

(406) Stolterfoht, M. et al. *Energy and Environmental Science* **2017**, *10*, 1530–1539.

(407) Correa-Baena, J. P. et al. Promises and challenges of perovskite solar cells., 2017.

(408) Ling, Y. et al. *Advanced Materials* **2016**, *28*, 305–311.

(409) Lin, K. et al. *Nature* **2018**, *562*, 245–248.

(410) Chen, Q. et al. *Nature* **2018**, *561*, 88–93.

(411) Dursun, I.; Shen, C.; Ooi, B. S.; Bakr, O. M. *SPIE Newsroom* **2017**, 9–11.

(412) Kojima, A.; Ikegami, M.; Teshima, K.; Miyasaka, T. *Chemistry Letters* **2012**, *41*, 397–399.

(413) Buin, A. et al. *Nano Letters* **2014**, *14*, 6281–6286.

(414) Jeon, N. J. et al. *Nature* **2015**, *517*, 476–480.

(415) Malgras, V. et al. *Journal of the American Chemical Society* **2016**, *138*, 13874–13881.

(416) Hu, H.; Salim, T.; Chen, B.; Lam, Y. M. *Scientific Reports* **2016**, *6*, 33546.

(417) Strickler, S. J.; Berg, R. A. *The Journal of Chemical Physics* **1962**, *37*, 814–822.

(418) Kim, H. S. et al. *Scientific Reports* **2012**, *2*, 1–7.

(419) Kim, J.; Lee, S. H.; Lee, J. H.; Hong, K. H. *Journal of Physical Chemistry Letters* **2014**, *5*, 1312–1317.

(420) Chirvony, V. S.; Martínez-Pastor, J. P. *Journal of Physical Chemistry Letters* **2018**, *9*, 4955–4962.

(421) Green, M. A.; Ho-Baillie, A.; Snaith, H. J. *Nature Photonics* **2014**, *8*, 506–514.

(422) Liang, K.; Mitzi, D. B.; Prikas, M. T. *Chemistry of Materials* **1998**, *10*, 403–411.

(423) Stavis, S. M.; Fagan, J. A.; Stopa, M.; Liddle, J. A. *ACS Applied Nano Materials* **2018**, acsanm.8b01239.

(424) Moerman, D.; Eperon, G. E.; Precht, J. T.; Ginger, D. S. *Chemistry of Materials* **2017**, *29*, 5484–5492.

(425) Bekenstein, Y.; Koscher, B. A.; Eaton, S. W.; Yang, P.; Alivisatos, A. P. *Journal of the American Chemical Society* **2015**, *137*, 16008–16011.

(426) Huang, H.; Susha, A. S.; Kershaw, S. V.; Hung, T. F.; Rogach, A. L. *Advanced Science* **2015**, *2*, 1–5.

(427) Li, M. et al. *Journal of Alloys and Compounds* **2017**, *706*, 395–400.

(428) Zhao, L. et al. *ACS Nano* **2017**, *11*, 3957–3964.

(429) Haider, M. A.; Capizzi, A. J.; Murayama, M.; McIntosh, S. *Solid State Ionics* **2011**, *196*, 65–72.

(430) Hou, S.; Guo, Y.; Tang, Y.; Quan, Q. *ACS Applied Materials and Interfaces* **2017**, *9*, 18417–18422.

(431) Lignos, I. et al. *Nano Letters* **2016**, *16*, 1869–1877.

(432) Kim, Y. et al. *ACS Applied Materials and Interfaces* **2015**, *7*, 25007–25013.

(433) Dokukin, M. E.; Sokolov, I. *Langmuir* **2012**, *28*, 16060–16071.

(434) Hughes, D.; Kelly, J. *Physical Review* **1953**, *92*, 1145–1150.

(435) El-Atwani, O. C. et al. *Langmuir* **2010**, *26*, 7431–7436.

(436) Jin, J.; Wu, J.; Frischknecht, A. L. *Macromolecules* **2009**, *42*, 7537–7544.

(437) Agnew, N. H. *Journal of Polymer Science* **1976**, *14*, 2819–2830.

(438) Dimitry, O. I. H.; Mazrouaa, A. M.; Saad, A. L. G. *Journal of Applied Polymer Science* **2006**, *101*, 3537–3549.

(439) Libera, M. R.; Egerton, R. F. *Polymer Reviews* **2010**, *50*, 321–339.

(440) Sawyer, L. C.; Grubb, D. T.; Meyers, G. F., *Polymer Microscopy*, 2013.

(441) Reiling, S.; Besnard, M.; Bopp, P. A. *The Journal of Physical Chemistry A* **1997**, *101*, 4409–4415.

(442) Ahn, N. et al. *Journal of the American Chemical Society* **2015**, *137*, 8698–8699.

(443) Ivanov, I. L. et al. *Journal of Chemical Thermodynamics* **2018**, *116*, 253–258.

(444) Whitham, P. J. et al. *Journal of Physical Chemistry C* **2016**, *120*, 17136–17142.

(445) Marchioro, A. et al. *Journal of Physical Chemistry C* **2016**, *120*, 27040–27049.

(446) Kahmann, S. et al. *Advanced Electronic Materials* **2018**, *4*, DOI: `10.1002/aelm.201700348`.

(447) Tong, Y. et al. *ACS Nano* **2016**, *10*, 10936–10944.

(448) Tanaka, K. et al. *Solid State Communications* **2003**, *127*, 619–623.

(449) Alharbi, N. D.; Salah, N.; Habib, S. S.; Alarfaj, E. *Journal of Physics D: Applied Physics* **2013**, *46*, 035305.

(450) Liu, F. et al. *Applied Physics Letters* **1995**, *66*, 523.

(451) Sharma, T. P.; Kirby, R. D.; Jaswal, S. S. *Physical Review B* **1974**, *9*, 1971–1974.

(452) Huang, H. et al. *NPG Asia Materials* **2016**, *8*, e328.

(453) Gonzalez-Carrero, S.; Galian, R. E.; Pérez-Prieto, J. *Journal of Materials Chemistry A* **2015**, *3*, 9187–9193.

(454) Du, X. et al. *RSC Adv.* **2017**, *7*, 10391–10396.

(455) Kim, H. S.; Park, N. G. *Journal of Physical Chemistry Letters* **2014**, *5*, 2927–2934.

(456) Jeon, N. J. et al. *Nature Materials* **2014**, *13*, 897–903.

(457) Yang, W. S. et al. *Science (80-.).* **2015**, *348*, 1234–1237.

(458) Derjaguin, B. V.; Muller, V. M.; Toporov, Y. P. *Journal of Colloid and Interface Science* **1975**, *53*, 314–326.

Part IX

Appendix

13.9 Supplementary information for Raman study of Methylammonium Lead Bromide Nanoparticles Complexation with Reverse Micelles Nanoreactor

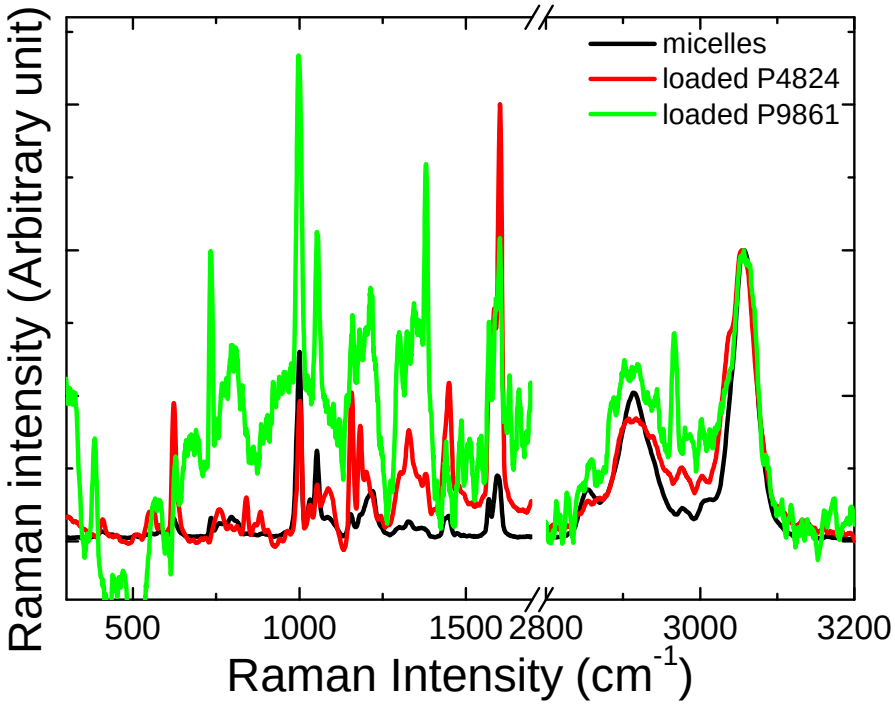

Figure 13.8: Full Raman spectra of $MAPbBr_3$ loaded P9861 and P4824 micelles and control empty P9861 in o-xylene.

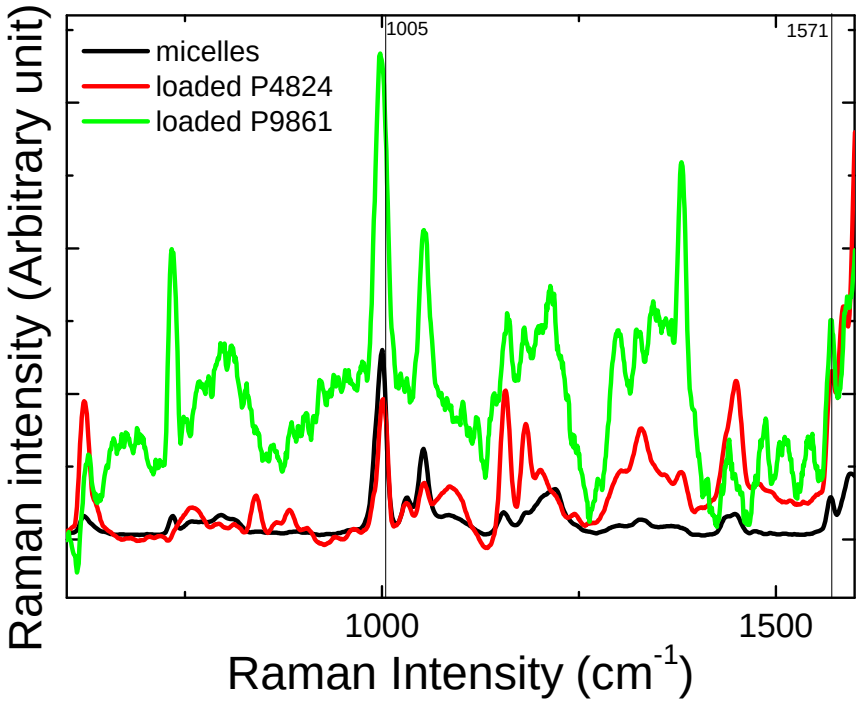

Figure 13.9: Raman spectra of $MAPbBr_3$ loaded P9861 (green curve) and P4824 (red curve) micelles and control empty P9861 micelles (black curve) in o-xylene in Raman shift region 600-1600 cm^{-1}. Solid line indicates the non-bromide-complexated free pyridine modes.

13.10 Supplementary information for Substrate-assisted Transfer of Nanoparticles by Graphene Oxide on Metal-organic Interface

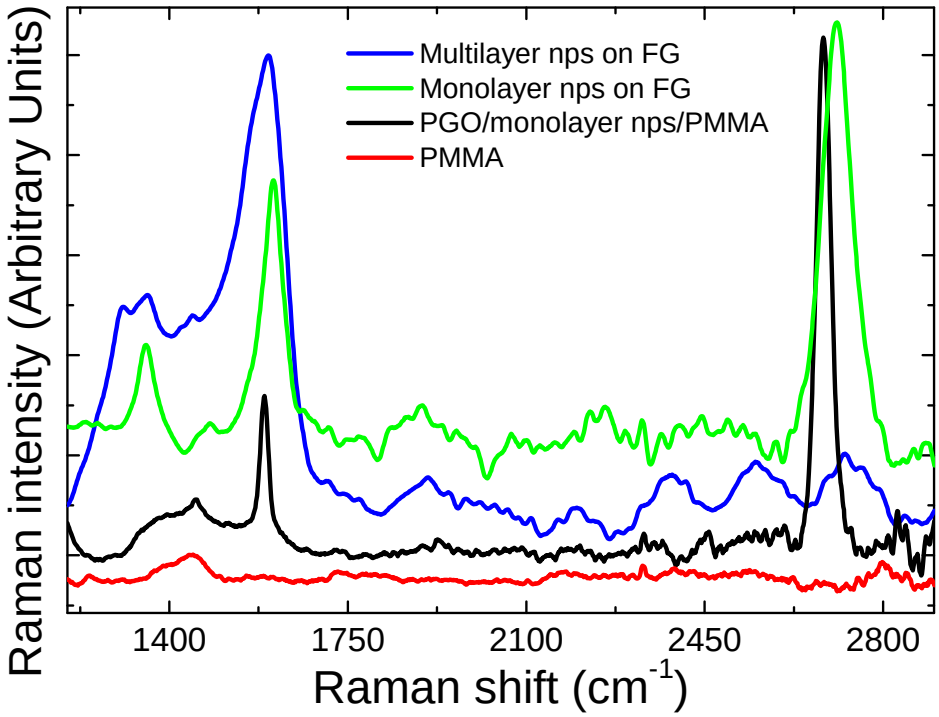

Figure 13.10: Comparison of Raman spectra for multilayer (blue line) and monolayer (green line) nanoparticles on full graphene before the transfer process; post-transferred partial graphene oxide with monolayer nanoparticles on PMMA 9black line) and the PMMA background (red line).

13.11 Supplementary information for Structure tunability from manipulation of reverse micelle deposition: single crystalline maghemite (γ-Fe_2O_3) nanoparticles with tunable coercivity

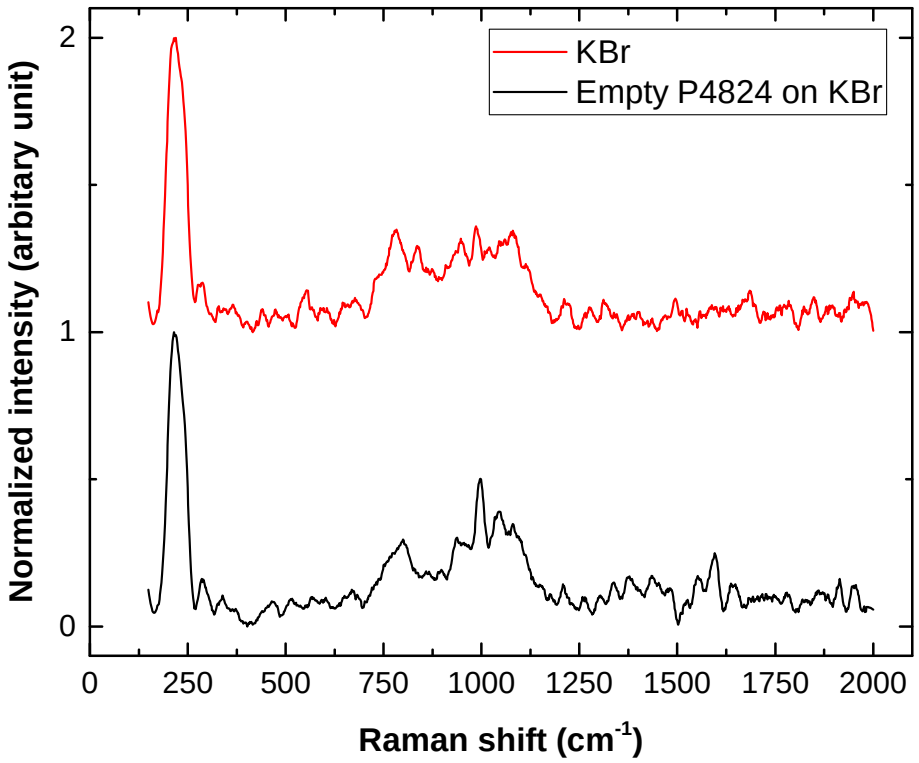

Figure 13.11: Raman spectra of KBr for background subtraction and unsubtracted P4824 empty micelles coated KBr.

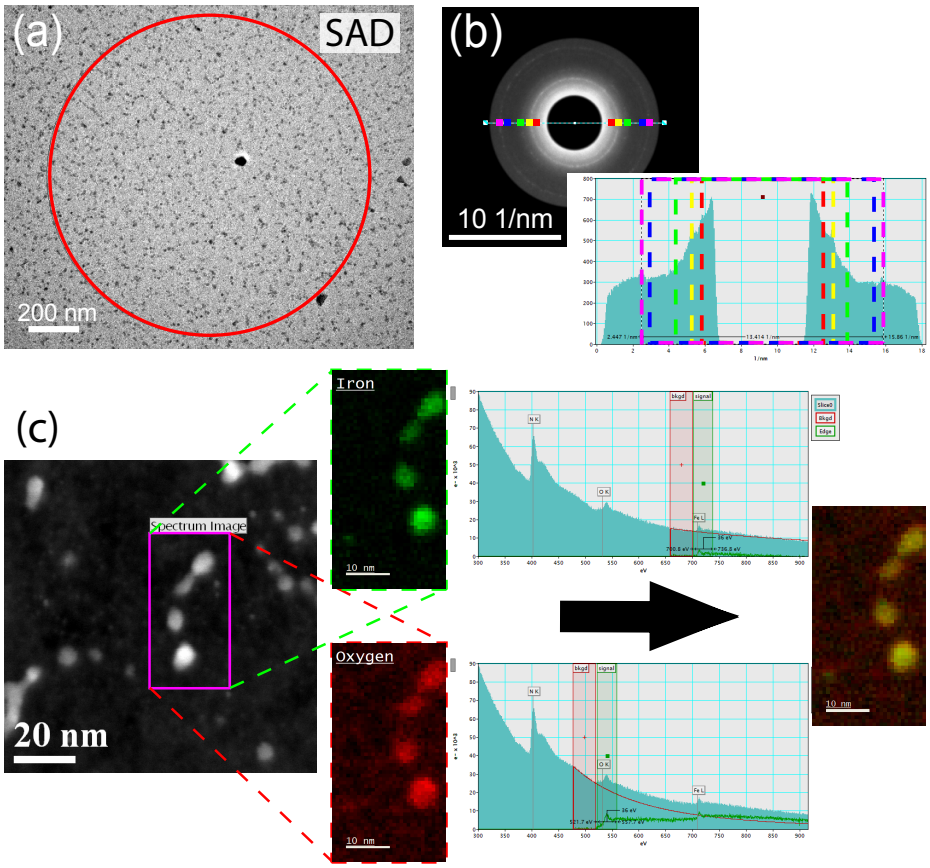

Figure 13.12: Selected area electron diffraction and chemical fingerprint of iron oxide nanoparticles. (a) TEM micrograph with selected area for electron diffraction, (b) electron diffraction pattern, with the line intensity profile (c) TEM micrograph of iron oxide nanoparticles with Fe and O elemental maps determined by energy selective filtering of the energy loss spectrum (EELS). Overlays of image, Fe and O maps show excellent correspondence. The loss spectra contain no features other that Fe and O from the particles, and N from the support grid. The lack of C and Cl signals suggest complete removal of the polymeric micelles and complete conversion of the FeCl

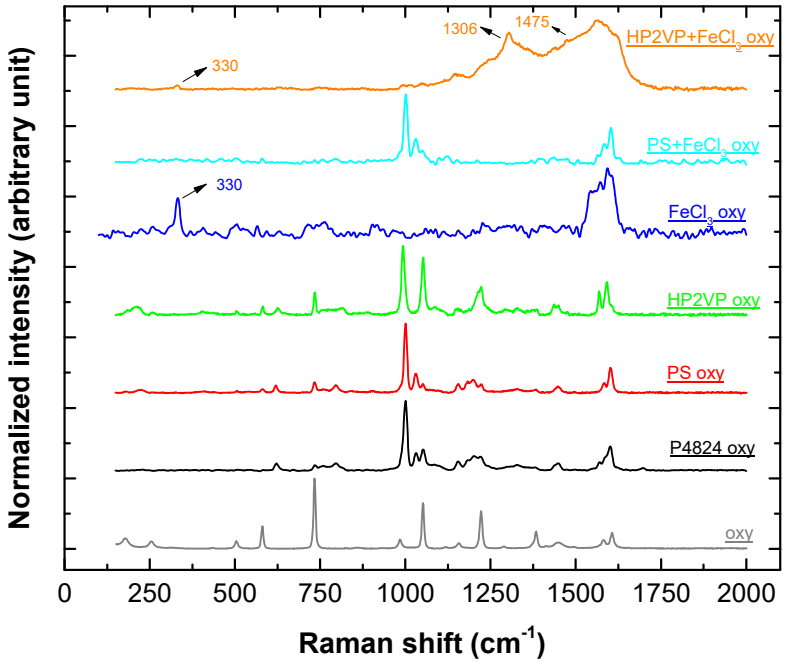

Figure 13.13: Raman spectra of pristine precursors, solvent and polymers used for control experiments.

13.12 Supplementary information for Synthesizing Monodispersed Methylammonium Lead Iodide Perovskite Nanoparticles by Reverse Micelles Templating

13.12.1 Perovskite nanoparticles dispersion comparision

Perovskite nanoparticles have been made using several different methods, and molecules. The results for are outlined below, split into multiple categories. Due to applications taking advantage of light-emission, MAPBr particles are more common in this field, as shown by the number of published papers found. A convenient way to express the distribution of particle sizes for particles of varying average diameter is the relative standard deviation in the particle size, i.e. normalized by the particle diameter, yielding a polydispersity index[237]. The particle size distributions were determined by randomly selecting particles in the micrograph images. More than 100 particles were analyzed, if available, to obtain a statistical representation of the entire population. Gaussian distribution functions were fitted to eliminate unexpected small and large particles to obtain precise statistical values. Table 13.3 is not exhaustive of all papers discussing these nanoparticles, as only papers showing an image appropriate for the determination of the PDI of the sample are referenced.

NEW

Method	Molecule	Average ϕ (nm)	PDI	Source
Nanoparticles and nanorods				
Micelle Templated	**$MAPbI_3$**	**6.82**	**0.0999**	**This Work**
Ligand-assisted	**$MAPbI_3$**	**59.42**	**0.2440**	**This Work**
Ligand-assisted	$MAPbI_3$	2.60	0.1538	Wang et al., 2017[167]
Nanocrystal-in-matrix	$MAPbI_3$	5.37	0.2250	Zhao et al., 2017[428]
Ligand-assisted	$MAPbI_3$	8.10	0.3161	Li et al., 2017[427]
Hot Injection	$MAPbI_3$	8.34	0.6520	Schmidt et al, 2014[43]
Ligand-assisted	$MAPbI_x$	10.11	0.2874	Aharon et al., 2016[67]
Ligand-assisted	$MAPbBr_3$	2.56	0.2900	Huang et al., 2016[452]
Emulsion	$MAPbBr_3$	3.32	0.2200	Huang et al., 2015[57]
Emulsion	$MAPbBr_3$	4.05	0.2120	Huang et al., 2015[57]
Emulsion	$MAPbBr_3$	5.33	0.2179	Huang et al., 2015[57]
Ligand-assisted	$MAPbBr_3$	6.11	0.3390	Gonzalez-Carrero et al., 2015[453]
Ligand-assisted	$MAPbBr_3$	6.58	0.1957	Xing et al., 2016[53]
Ligand-assisted	$MAPbBr_3$	7.37	0.3143	Huang et al., 2015[57]
Ligand-assisted	$MAPbBr_3$	10.46	0.2721	Amgar et al., 2016[46]
Nanocrystalline Films				
Ligand-assisted	$MAPbI_3$	5.37	0.3248	Zhao et al., 2017[428]
Ligand-assisted	$MAPbI_3$	12.65	0.2549	Levchuk et al., 2017[54]
Ligand-assisted	$CsPbBr_3$	4.68	0.1386	Du et al., 2017[454]
Hot-injection	$CsPbBr_3$	8.13	0.0887	Huang et al., 2016[51]
Emulsion	$CsPbBr_3$	15.23	0.2133	Huang et al., 2015[57]
Crystalline Films				
Sequential deposition	$MAPbI_3$	126.0	0.3046	Kim et al., 2014[455]
Sequential deposition	$MAPbI_3$	160.6	0.2288	Kim et al., 2014[455]
Sequential deposition	$MAPbI_3$	258.4	0.4009	Kim et al., 2014[455]
Solvent washing	$MAPbI_3$	314.8	0.3839	Jeon et al., 2014[456]
Ion exchange	$FAPbI_3$	247.9	0.4729	Yang et al., 2015[457]
Ion exchange	$FAPbI_3$	422.3	0.4507	Yang et al., 2015[457]

Table 13.3: Comparison of nanoparticle material, diameter and PDI of metal/organic halide perovskites using various approaches

We successfully produced nanoparticles of MAPI, MAPBr and FAPI as shown in the main text Fig. 13.6. Though MAPI and FAPI showed no evidence of quantum confinement effects, the MAPBr nanoparticles produced by micelle templating showed some shift of the PL spectrum, as shown in Fig. 13.14. The PL peak asymmetry results from the excitation of subband states. The first peak at 534nm comes from the dominant band-to-band transition and the second broadband at 542nm is from trap states recombination on the crystal surface below the optical gap [234]. Due to the nanoparticle size, the surface states are more prominent relative to the band to band transitions compared to large single crystals of MAPBr perovskites.

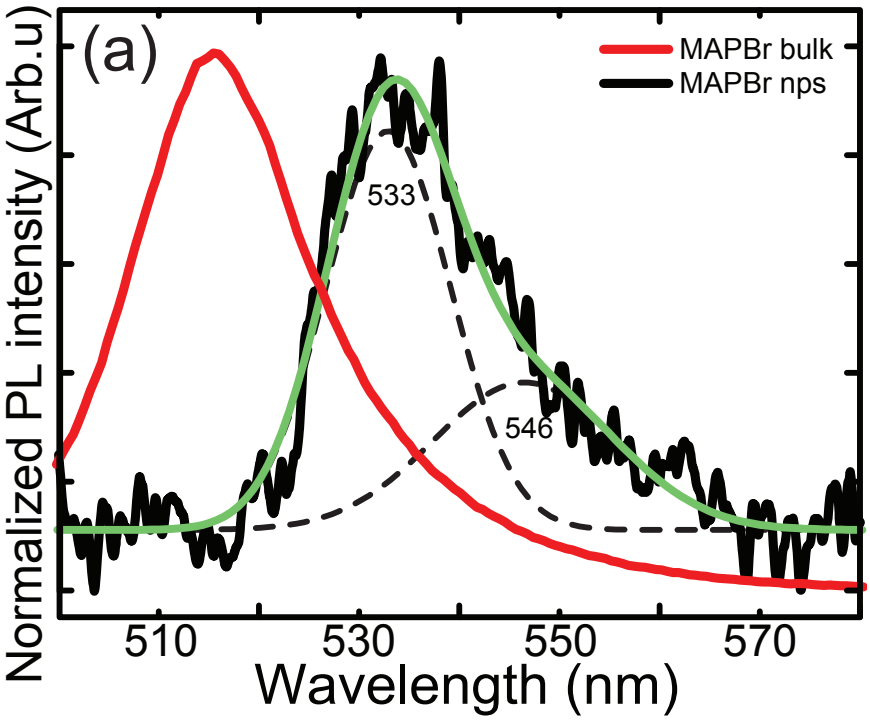

Figure 13.14: Photoluminescence measurements of $MAPbBr_3$ bulk particle in solution and $MAPbBr_3$ diblock copolymer micelle templated nanoparticle film spin coated onto Si wafers. The film shows an asymmetric PL peak, which can be deconvoluted into two components due to the band-to-band transition and trap states recombination on the crystal surface below the optical gap.

This is different from the excess particles centrifuged out in normal loading procedures. They are excess because the micelles has reached its loading limit that the MAI salt can no longer get in, the excess MAI binds with some of the PbI_2 salt in the sequential loading steps and forms the excess $MAPbI_3$ that never goes into the

micelles, while the remaining PbI_2 infiltrates the MAI-loaded-micelles.

13.12.2 Spatial statistics of optimized micelle templated MAPI nanoparticles

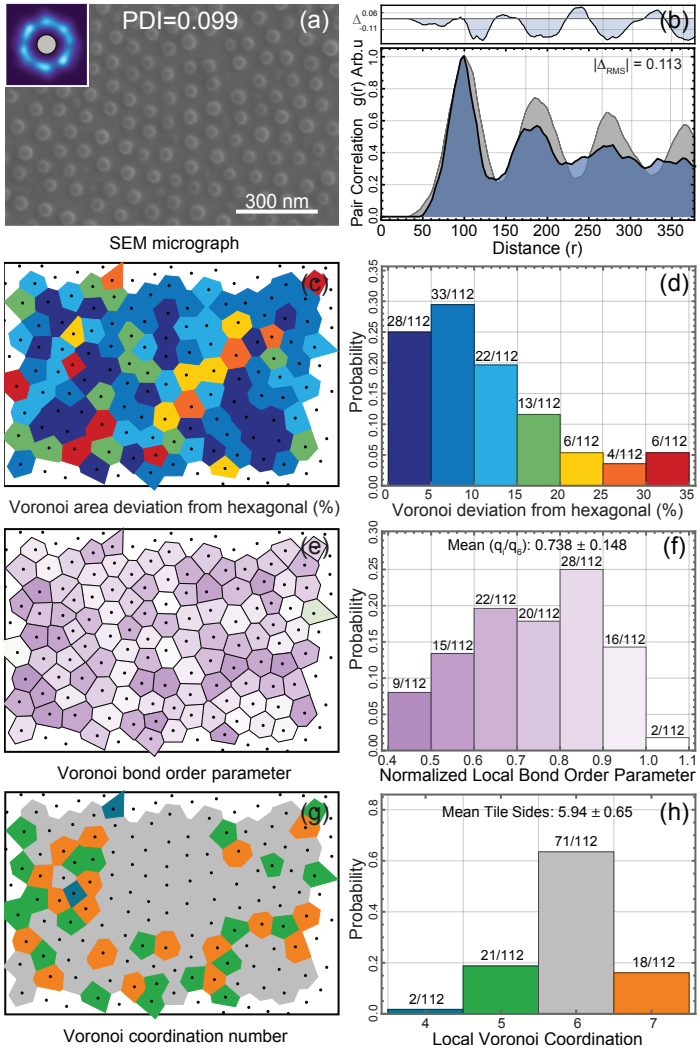

Figure 13.15: SEM micrograph of $MAPbI_3$ nanoparticles synthesized by micelle-templated approach with inset of entropic force map of first neighbour (b) Pair correlation function of micelle-templated $MAPbI_3$. (c) Voronoi tessellations of the micelle centroids coloured by percent deviation of the expected cell produced from hexagonal packing. (d) Histogram of the probabilities of various percent deviations of the Voronoi cell areas from those produced from hexagonal packing. (e) Voronoi tessellations of the micelle centroids coloured by the normalized bond order parameter. Whiter areas indicate particles that have high angular order in a hexagonal (q_6) symmetry basis. (f) Histogram of the probabilities for various values of the bond order parameter. (g) Voronoi tessellation of the micelle centroids coloured by the number of shared facets (coordination number). (h) Histogram of the probabilities for each coordination number.

13.12.3 Iodine interaction with micelles

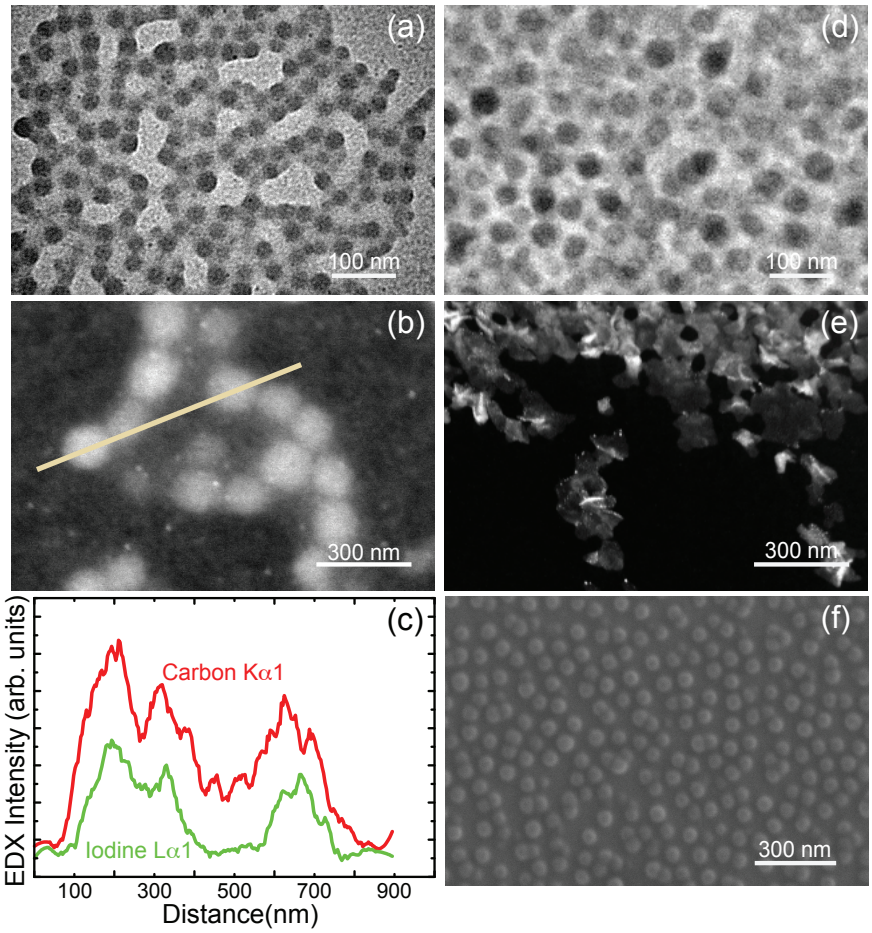

Figure 13.16: (a) TEM and (b) STEM micrographs of methylammonium iodide loaded micelles (c) EDX line profile of I (green line) and C (red line) across MAI loaded micelles (yellow line). (d) TEM micrographs of iodine stained micelles (e) STEM micrographs of PbI_2 loading destruction of micelles (f) SEM micrograph of centrifuged micelles 48hr after simultaneously loading of MAI and PbI_2 salts into solution. Micelles are essentially unloaded due to the immediate reaction of the salts in the surrounding organic solvent without infiltration.

13.12.4 Quantitative nanomechanical property mapping (QNM)

Quantitative nanomechanical property mapping (QNM) AFM was done using a Bruker Bioscope Catalyst with an RTESPA probe. For each round of measurements, the probe

was calibrated using a relative method of calibration with a sample of known modulus. The calibration first involved the calculation of the deflection sensitivity by ramping the probe into a clean sapphire substrate. A minimum of three ramps were done and the average deflection sensitivity was used. The probe was then withdrawn from the substrate and a thermal tune was preformed to calculate the spring constant. Lastly, a polystyrene sample of known modulus provided was loaded and imaged. The tip radius was adjusted until the measured modulus agreed with the known modulus. The elastic modulus was determined by taking a line profile through 100 micelles by matching the coordinates in the topography channel to the elastic modulus channel in WSxM. Due to the variability in Young's modulus within a micelle, the elastic modulus for each micelle was determined by taking the average of the centre points of the line profile. The number of points averaged to determine the modulus also varied due to a range in the size of micelles measured. Typically, 10 points were taken for each micelle. The modulus measurements for each micelle were fit using a Gaussian approximation to calculate the average modulus value and error for the unloaded and loaded micelles. The QNM sample preparation is similar to the AFM sample preparation procedures, with the exception for the spin speed being 8000 rpm to promote sparse dispersion.

To confirm the formation of the perovskite nanoparticles within the reverse micelles, hardness maps were generated using the QNM AFM mode provided by the Bruker Nanoscope software. The hardness maps were created by calculating the elastic modulus at each AFM interaction point using the Derjaguin-Müller-Toporov (DMT) model. The DMT model calculates the reduced elastic modulus by fitting the DMT model to the unloading portion of the force-indentation curve (Eq. (13.1)).[106, 458]

$$F_{tip} = \frac{4}{3} E^* \sqrt{R d^3} + F_{adh} \tag{13.1}$$

Where E^* is the reduced elastic modulus, F_{tip} is the force on the AFM tip, F_{adh} is the adhesion force between the AFM tip and the sample (the lowest point on the retract curve), R is the radius of the AFM tip, and d is deformation depth.[106, 458]

The reduced elastic modulus (E^*) can be related to the sample elastic modulus (E_s) by

$$E^* = \frac{(1-\nu_t^2)}{E_t} + \frac{(1-\nu_s^2)}{E_s} \tag{13.2}$$

In Eq. (13.2), E_t is the elastic modulus of the AFM tip, ν_t is the Poisson's ratio of the AFM tip, and ν_s is the Poisson's ratio of the sample.[106, 458] As the AFM tip is

much stiffer than the sample, assuming E_t to be infinite, the first term of the equation becomes negligible.[106] The resulting modulus maps produced by the Bruker QNM technique present the sample elastic modulus (E_s).

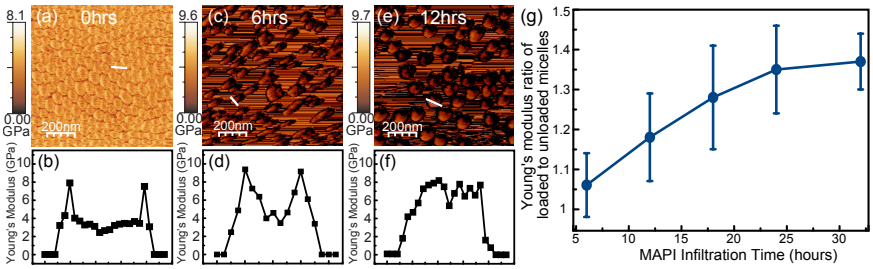

Figure 13.17: Young's Modulus map measured by QNM of (a) empty micelles and (c,e) loaded micelles; and the Young's Modulus line profile of one single (b) empty micelle and (d,f) loaded micelle. (h) Change of the Young's modulus ratio of the loaded to unloaded micelles with different loading times showing the increasing infiltration of MAI into the micelle core. Average Young's modulus derived from 100 micelles per sample.